The Luminosity Function for White Dwarfs in the SuperCOSMOS Sky Survey

---

Nicholas Rowell

Institute for Astronomy
School of Physics and Astronomy

University of Edinburgh
Doctor of Philosophy

2010

Abstract

I present a magnitude and proper motion limited catalogue of $\sim 10,000$ white dwarf candidates, obtained from the SuperCOSMOS Sky Survey by means of reduced proper motion selection. This catalogue extends to $R \sim 19.75$ and $\mu \sim 0\farcs05$ yr^{-1}, and covers more than three quarters of the sky. Spectroscopic follow-up observations have been obtained for a subsample of objects, and are used to assess the reliability of the selection procedure and contamination of the final catalogue. Photometric parallaxes provide distance estimates accurate to $\sim 50\%$.

This catalogue is used to measure the luminosity function (LF) for white dwarfs in the Solar neighbourhood over the range $4 \leq M_{bol} \leq 18$. A new technique is devised to separate the LFs for disk and spheroid stars, which allows all stars to contribute to the LF even at tangential velocities where the populations overlap. The disk LF shows a sharp decline at $M_{bol} = 15.75$, in agreement with other studies, and extends over a magnitude fainter than previously determined. The spheroid LF has a sharp peak at $M_{bol} = 15.75$, then levels out and shows no sign of a drop off at faint magnitudes, as expected for a considerably older population.

By simulating white dwarf LFs for stellar populations with a range of star formation histories, I measure the age of the local disk and spheroid. The disk age of $9.13^{+0.66}_{-0.67}$ Gyr agrees with that measured in similar studies, and with the basic picture of galaxy formation in a cosmological context. No reliable solution is found for the spheroid age. By integrating the LFs, I investigate the local mass density of spheroid white dwarfs, with particular reference to their contribution to the baryonic dark matter content of the Galaxy. I also place an upper limit on their contribution to the possible MACHO population and the microlensing events observed towards the LMC.

Table of Contents

List of Tables

List of Figures

CHAPTER 1

Introduction

White dwarfs are the second most common type of star in the Galaxy, and represent the final stage in the evolution of the vast majority of all stars. Their application to the study of the formation history of the Galaxy and stellar populations more generally has undergone something of a renaissance in recent years, due to the confluence of improvements in the theoretical understanding of their evolution, and their discovery in large numbers both in modern wide angle sky surveys and deep imaging. In this chapter I review some of the milestones in the recent history of white dwarf science, both on the theoretical and observational frontiers, and present some of the basic concepts that inform the field.

1.1 Introduction

The identification of white dwarfs as a distinct class of star was made in the early decades of the twentieth century. The location in the Hertzsprung-Russell diagram of 40 Eridani B set it apart from the rest of the 'normal' stars, the key distinction being its extreme subluminosity compared to other stars of the same spectral type (see Figure 1.1(a)). The small radius inferred by Stefan's law, combined with the colour of these white-hot objects, earned them the name 'white dwarf'. The existence of a subluminous companion to the star Sirius A had been deduced by its perturbed motion across the sky; eventual direct observation of the companion revealed it to be a member of this emerging class - see Figure 1.1(b). Analysis of the binary orbital parameters of the Sirius system placed the mass of the white dwarf at $\sim 1M_{\odot}$. Indeed, a common rule-of-thumb concerning white dwarfs is that they have a mass roughly equal to that of the Sun, and a size roughly equal to that of the Earth. The extreme conditions that characterise the internal structure of such an object were met with some disbelief in the scientific community (not least from Eddington; see Koester and Chanmugam 1990), however the theory of the equation of state as laid down by Chandrasekhar (1939) was eventually accepted, and is recognised as a major advance in the field of stellar evolution. White dwarfs are formed from the burnt out remains of low- and intermediate-mass main sequence stars, following ejection of the envelope at the tip of the asymptotic giant branch. The intermediate phase is that of a *planetary nebula*, so called due to the resemblance to a planet when viewed through early telescopes. These are interesting objects in their own right, lit up as they are by ionizing radiation from the exposed stellar core (see Figure 1.2). Most of the mass of the original star is ejected in this process, and is returned to the interstellar medium enriched with heavier elements produced by nucleosynthesis. It is thought that white dwarfs represent the final stage in the evolution of stars less massive than $\sim 7-9$ times that of the Sun. This includes the great majority of all stars; all but the most massive few percent are expected to eventually become white dwarfs. Now devoid of nuclear energy sources, the evolution of these objects is that of a slow cooling process, during which the residual thermal energy of the core is radiated away through the outer layers, and the star gradually

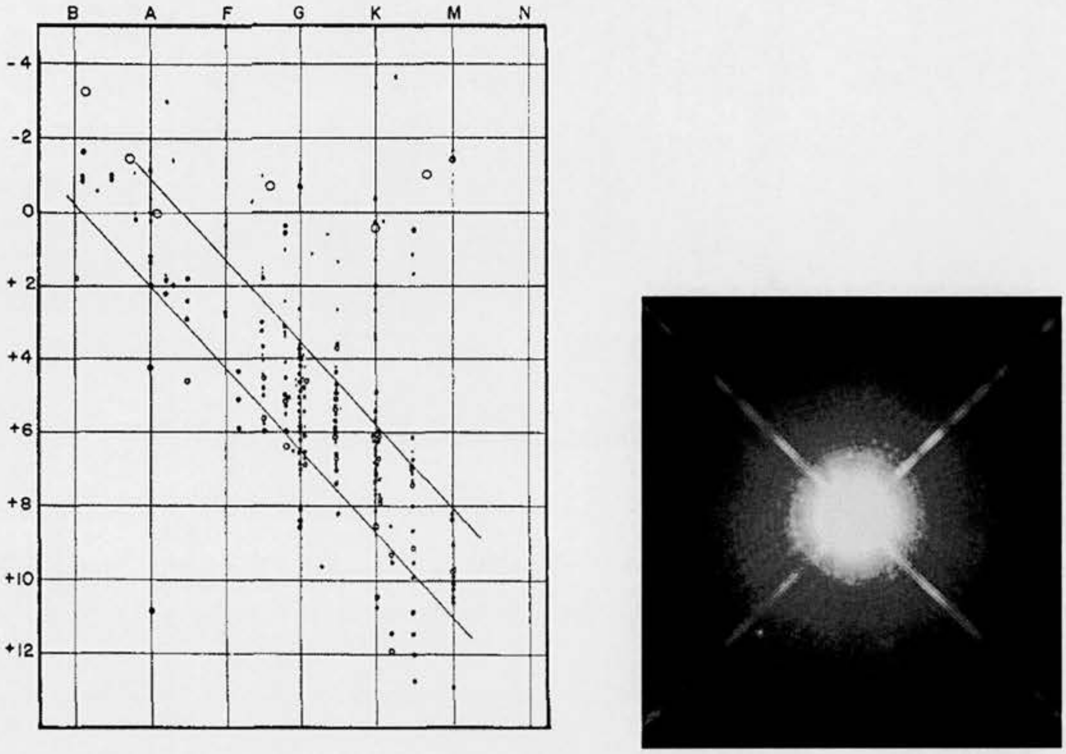

(a)

(b)

Figure 1.1: (a) An early HR diagram showing the position of 40 Eridani B, stuck out from the main locus of stars at a visual magnitude of 11 and spectral type A. Figure reproduced from Koester and Chanmugam (1990). (b) Sirius A - the 'Dog Star' - along with its 'pup' at lower left, the white dwarf Sirius B. Credit: NASA, H.E. Bond & E. Nelan (STScI) and M. Barstow

fades over many billions of years. White dwarfs are numerous both in Galactic star clusters and the Solar neighbourhood, where they account for about ten percent of nearby stars[1], though they are sufficiently faint that none can be seen with the naked eye. Their relative abundance, combined with their long evolutionary timescales, makes them suitable probes of the formation history of the various star populations within the Galaxy. They do, however, have a whole host of applications in other areas of astrophysics, including plasma physics, gravitational waves, dark matter and exoplanet

---

[1] `www.chara.gsu.edu/RECONS/TOP100.posted.htm` - "The 100 nearest star systems", courtesy of the Research Consortium on Nearby Stars (RECONS)

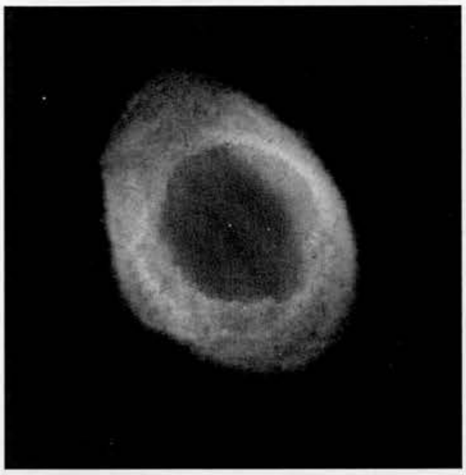

Figure 1.2: The Ring nebula, M57. The ejected photosphere is ionised by ultraviolet photons from the exposed stellar core, and shines in a dazzling array of colours due to the emission of intense line radiation. Credit: The Hubble Heritage Team

searches to name but a few, and as the apparent progenitors of type 1a supernovae, their role in the understanding of the evolution of the Universe has been profound.

1.2 Observational properties

1.2.1 Spectral classification and taxonomy

The high surface gravity of white dwarfs has two important effects on the spectral energy distribution. Typically, only a single element is present in the spectrum, due to the compositional stratification of the atmosphere, and absorption lines are highly pressure-broadened compared to non-degenerate stars. Most white dwarfs can be categorised according to a simple spectral classification scheme - those showing only hydrogen lines (DA type) and those showing only helium lines (rare DOs at high temperatures, and more common DBs at $T_{\text{eff}} \leq 30,000K$), with DAs outnumbering DBs by roughly four to one at moderate temperatures. A rare type that has had considerable attention recently in the literature, due to the discovery of several objects at high effective temperature (Dufour et al., 2007), shows only carbon features - these are the DQs. At low effective temperatures atomic lines disappear, and a substantial number of white dwarfs that may previously have appeared as one of these types now show spectra entirely devoid of features. These are classified as DC types. An example of each type can be found in Appendix C; SSSJ0903+0412 is a DA, SSSJ1821+1441 is a DB, SSSJ2318+2019 is a DC, and SSSJ0235+0729 is a cool DQ showing the molecular C_2 Swann bands.

The relationship between these types can be broadly understood in terms of the occurence (or not) of late thermal pulses during the ejection of the photosphere (Herwig et al., 1999). Such an event may entirely strip the outer H or He layers, and mix material from the core into the photosphere. However, the connection between the spectral type and the composition of the atmosphere is not quite as straightforward as it may appear. There is good empirical evidence that white dwarfs change spectral type throughout their evolution, and the existence of several ranges in effective temperature in which certain spectral types are found in very small number is well documented. This represents an important limitation in current white dwarf age estimates - see Section 1.3.3 for details.

Many white dwarfs show metal lines in their spectra; these are the DZ types. As metals are expected to sink rapidly below the photosphere, any features present must be due to the continual accretion of metals, either from the interstellar medium or asteroid impacts. Spectra with evidence of a magnetic field (e.g. Zeeman splitting) are given the DH classification.

Finally, it is worth pointing out that the features defining each of the spectral types are not necessarily mutually exclusive (this obviously does not apply to DCs), and objects that show a variety of spectral features will be designated an amalgamation of the different classes, ordered according to the relative strengths (e.g. DZA for a star with stronger metal lines than hydrogen).

1.2.2 Mass and luminosity distribution

The very tight mass distribution of white dwarfs is a well known feature of this class of star. Figure 1.3 shows the mass distribution for 1859 DA white dwarfs in the SDSS, measured by Kepler et al. (2007). This is strongly peaked at around $0.6M_{\odot}$, with secondary peaks at low and high mass. The main peak represents typical C/O core degenerates, evolving as isolated objects. The stars at lower masses are thought to have formed through close binary star evolution, as there has not been sufficient time for single low mass main sequence stars to produce these. The high mass component (which makes a larger contribution when volume-corrected) is thought to represent O/Ne core degenerates descended from high mass main sequence stars.

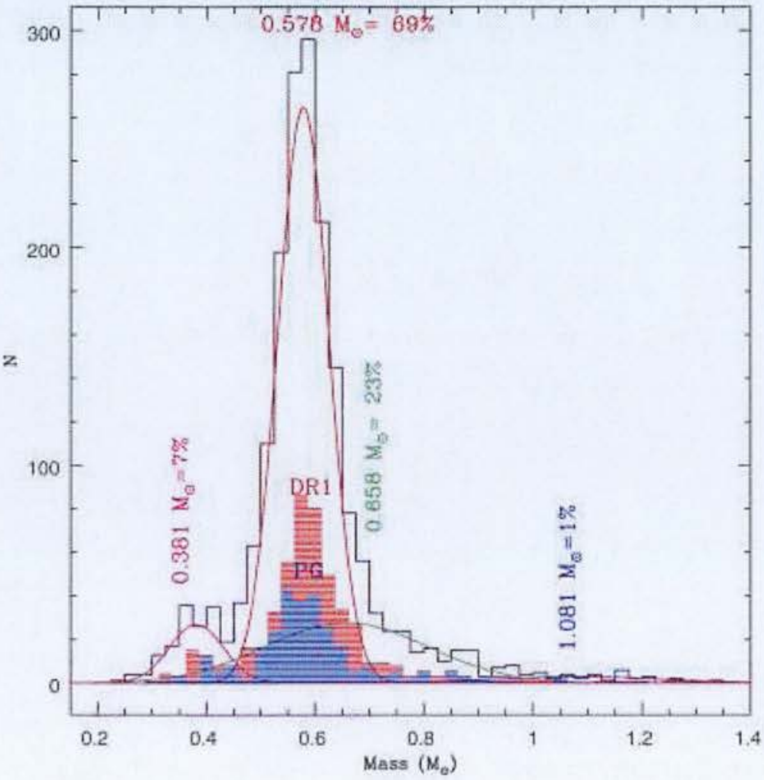

Figure 1.3: The distribution of masses for DA stars hotter than $T_{\text{eff}} = 12,000K$ and brighter than $g = 19$ in data release 4 of the Sloan Digital Sky Survey, reproduced from Kepler et al. (2007).

Considering the wide range of main sequence stellar masses that have had time to contribute white dwarfs to the local population ($\sim 1.1 \rightarrow 8M_{\odot}$), the fact that the white dwarf masses show such a tight distribution is very interesting indeed. It suggests that the various competing processes controlling mass loss are sufficiently finely tuned that a remnant of approximately the same mass is left behind consistently. It also reveals that most of the mass of a star is returned to the interstellar medium during this event. The ejected material is enriched with carbon, nitrogen and oxygen, and white dwarf progenitors play a significant role in the chemical evolution of the Galaxy. The relation between the initial main sequence mass and the mass of the resulting white dwarf (the initial-final mass relation, IFMR) is an important quantity in understanding the evolution of stars and stellar populations. The IFMR is constrained both theoretically, using stellar models exploring the mass of the degenerate core at the first thermal pulse, and empirically using clusters, where the masses of white dwarfs and their associated cooling times are compared to the age of the cluster to measure the main sequence lifetime of their progenitors, thus constraining their original main sequence mass (Weidemann, 2000; Kalirai et al., 2009).

The luminosity function for white dwarfs has a morphology that is determined mainly by the age of the stellar population, though cooling rates as a function of luminosity also play a significant role - see Chapter 4 for an in-depth analysis. In the solar neighbourhood, the luminosity function is well determined at all but the faintest magnitudes. Harris et al. (2006) and Krzesinski et al. (2009) used the SDSS to measure the faint and bright ends of the luminosity function respectively, achieving good constraint across a wide range $0 \leq M_{bol} \leq 16$. Their combined results are presented in Figure 1.4.

1.2.3 Selection and identification

Proper motion

The fact that the proper motions of nearby stars correlate with their line-of-sight distances can be used to estimate their intrinsic luminosity. The statistic used to do this is called the *reduced proper motion*, H, and a plot of H against colour can be used to identify white dwarfs in much the same way as with the classical HR diagram - by their extreme faintness at a given colour. Chapter 2 describes this technique in detail, with particular reference to proper motions derived from the SuperCOSMOS Sky Survey.

Early white dwarf samples compiled in this manner were derived from the star catalogues of Willem Luyten, in particular the Luyten Half Second (LHS) catalogue of objects with proper motions in excess of $0\farcs5$ yr^{-1}. The study of Liebert et al. (1988)

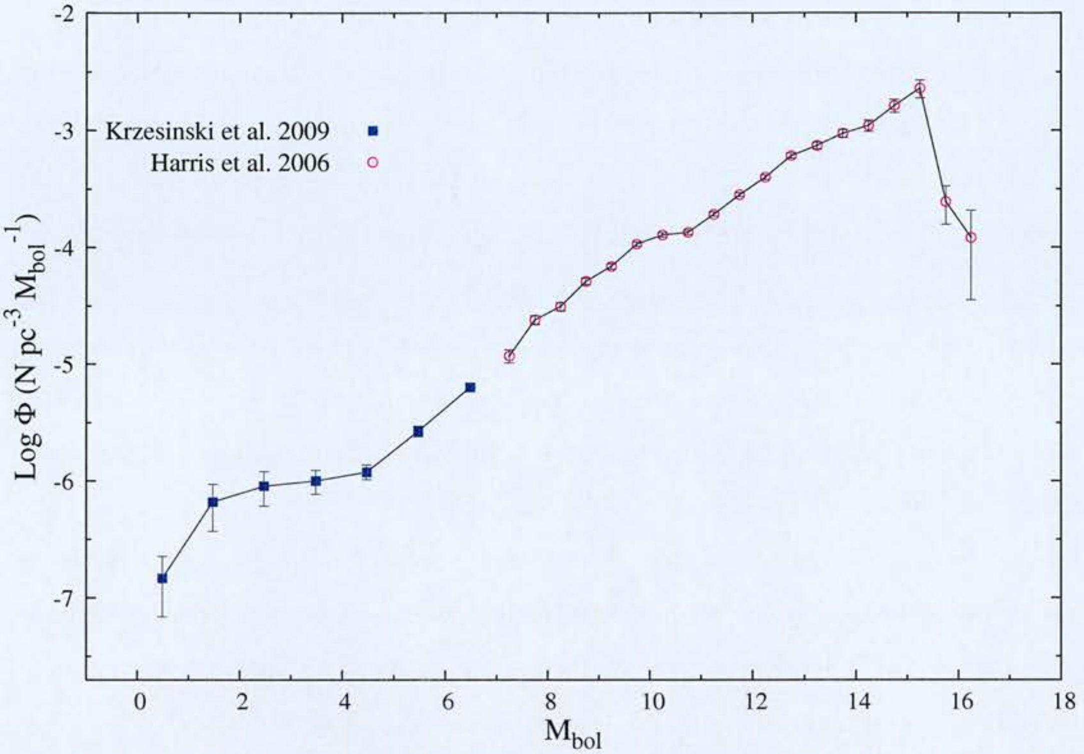

Figure 1.4: The luminosity function for solar neighbourhood white dwarfs, obtained from the SDSS by Harris et al. (2006) and Krzesinski et al. (2009).

used 43 white dwarfs from the LHS catalogue, and constructed the first luminosity function to detect the paucity of solar neighbourhood white dwarfs at faint magnitudes.

Modern digital surveys can reach much fainter than older surveys, such as those of Luyten, that were based on photographic plates. With the aid of computerised pairing algorithms and better resolution, much lower proper motions can be detected and considerably larger samples compiled. Having said that, photographic material has been crucial in extending modern proper motion sensitivity to the lowest limits, by providing an early epoch of observation so that slow-moving objects show a larger displacement. For example, Kilic et al. (2006) use a pairing of SDSS with USNO-B photographic astrometry to identify several thousand white dwarfs.

Colour

Due to the lack of atmospheric metals, white dwarfs are relatively bright in the UV with respect to disk main sequence stars, and they stand apart from the main stellar locus in a two-colour plot employing the U band - see Figure 1.5. While there may be contamination by metal-poor subdwarfs, colour selected samples can at least be used as input for a spectroscopic follow up campaign. The Palomar-Green survey of UV excess objects was used in this manner to derive the luminosity function of white dwarfs by Fleming et al. (1986). However, white dwarfs cooler than $\sim 8000K$ overlap with the A and F stars in colour, and so tend to be excluded from colour-selected samples.

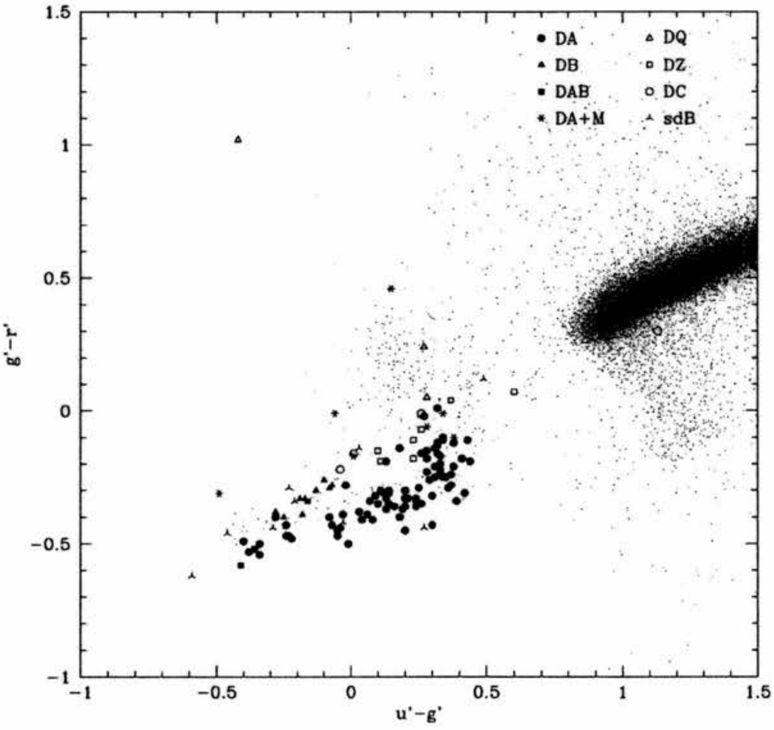

Figure 1.5: Selection of white dwarf candidates according to blue colours. The dense region on upper right is the main sequence; various white dwarf spectral types are identified by the symbols. The three pointed stars are subdwarfs, indicating the overlap with this population. Figure reproduced from Hansen and Liebert (2003).

Spectroscopy

The most widely accepted way to confirm the identity of a white dwarf, short of obtaining a trigonometric parallax, is by spectroscopy. The highly pressure-broadened absorption lines easily distinguish this class of star from lower gravity objects. Most large white dwarf surveys include some spectroscopy component, either to test the reliability of the selection method, or as a major part of the analysis, as line profiles allow direct measurement of the surface gravity. Large catalogues of spectroscopically confirmed white dwarfs have been produced from the SDSS in recent years. Eisenstein et al. (2006) checked *all* spectroscopically observed objects in DR4 that fell within a selected colour range, finding over nine thousand white dwarfs. This catalogue was used by De Gennaro et al. (2008) to investigate the luminosity function, with the eventual aim of using the spectroscopically determined masses to measure this function in restricted mass ranges. However, this study was hampered by the fact that most white dwarfs selected for SDSS spectroscopic follow up are done so inadvertently, when the imaging pipeline mistakes them for quasars. This leads to a complex selection probability that is hard to correct for. Also, the colour selection restricts the effective temperature range of their sample, as noted before.

1.3 Theoretical framework

1.3.1 Basic properties

Certain general properties of white dwarf stars as a class can be obtained from a simple analysis, using several fundamental observational parameters measured accurately for a single example. Note that most of the following derivation is adapted from Koester and Chanmugam (1990); Kippenhahn and Weigert (1994); Rose (1998). The star Sirius B was one of the first white dwarfs to be discovered, and while its proximity to Sirius A rendered its stellar parameters highly uncertain for many years, recent space based observations have significantly improved matters. Holberg et al. (1998) collate the results of several diverse investigations including parallax, gravitational redshift and extreme ultraviolet observations to redetermine the mass, radius and effective temperature of

Parameter	Value
Mass ($M_\odot$)	1.034 ± 0.026
Radius ($R_\odot$)	0.0084 ± 0.00025
$\mathrm{T_{eff}}$ (K)	$24,790 \pm 100$

Table 1.1: Fundamental stellar parameters of Sirius B, as determined by Holberg et al. (1998).

Sirius B. Their values are summarised in Table 1.1. It should be pointed out that Sirius B is not strictly representative of white dwarfs in general, being of extremely high mass, but as it is believed to possess a carbon core (in common with the vast majority of white dwarfs), it is suitable for the following analysis.

Pressure ionisation and electron degeneracy

The mass and radius of Sirius B suggest a mean density of $\sim 2.5 \times 10^9$ kg m^{-3}. The interiors of white dwarfs are generally believed to be composed of the products of He burning, specifically some ratio of carbon and oxygen, and assuming a pure C composition implies a nuclear separation of $\sim 2 \times 10^{-12}$ m. By contrast, the Bohr radius of a carbon ion with only one remaining electron is $\sim 8 \times 10^{-12}$ m, and the interior must be entirely *pressure ionised.*

Using the effective temperature as a zeroth-order estimate of the interior temperature, one calculates a de Broglie wavelength of $\sim 6.85 \times 10^{-10}$ m for the (free) electrons, several orders or magnitude greater than their mean separation of 9.85×10^{-13} m. Therefore, any attempt to understand the internal structure must involve a quantum mechanical explanation for the electronic component. By contrast, the de Broglie wavelength of the ions, $\sim 4.63 \times 10^{-12}$ m, is only about twice their average separation, and we expect a classical description of their behaviour to suffice.

The equation of state

The equation of state for the degenerate electronic component can be derived by first considering the density of quantum states $g(p)$, defined in phase space as

$$g(p)\ \mathrm{d}p\mathrm{d}V = \frac{8\pi}{h^3}p^2\ \mathrm{d}p\mathrm{d}V.$$

This includes the degeneracy factor of two for electrons of opposite spin states. The distribution of particles amongst the quantum states obeys Fermi-Dirac statistics, which states that the average occupation of a state of energy ϵ is given by

$$f(\epsilon) = \frac{1}{exp[\frac{\epsilon-\mu}{kT}]+1}.$$

Microscopically, pressure is defined as the flux of momentum through a unit surface. If we consider a surface element of area $\mathrm{d}\sigma$ with normal $\underline{\mathbf{n}}$, we can derive an expression for the pressure by considering how many electrons pass through it per second into an element of solid angle $\mathrm{d}\Omega$, in the direction $\underline{\mathrm{s}}$, in the momentum range $p \rightarrow p+\mathrm{d}p$ (Figure 1.6). The number density of states in the vicinity of $\mathrm{d}\sigma$ is given by $g(p)\mathrm{d}p$, and these are occupied according to $f(\epsilon)$. Each electron carries a momentum equal to $p\cos(\theta)$ in the direction $\underline{\mathbf{n}}$, and crosses the surface $\mathrm{d}\sigma$ with a velocity $v(p)\cos(\theta)$. As the distribution function is isotropic, the fraction of electrons passing into $\mathrm{d}\Omega$ is equal to $\frac{\mathrm{d}\Omega}{4\pi}$. Finally, to get the pressure on the surface, we divide out $\mathrm{d}\sigma$ and integrate over one hemisphere and all momentum states:

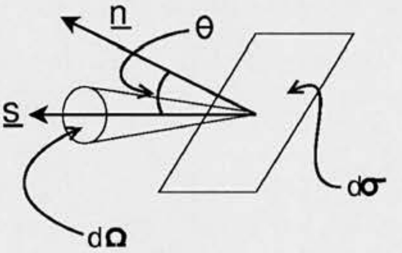

Figure 1.6: The equation of state is derived by considering the flux of momentum across surface element $\mathrm{d}\sigma$ in the direction $\underline{\mathbf{n}}$

$$P = \int_{\theta=0}^{\frac{\pi}{2}}\int_{\phi=0}^{2\pi}\int_{p=0}^{\infty}\frac{8\pi p^3}{h^3}\frac{1}{exp[\frac{\epsilon(p)-\mu}{kT}]+1}\cos(\theta)^2 v(p)\mathrm{d}p\frac{\mathrm{d}\Omega}{4\pi}.$$

Integrating out the angular dependency leaves:

$$P = \frac{4\pi}{3h^3}\int_{p=0}^{\infty}\frac{p^3}{exp[\frac{\epsilon(p)-\mu}{kT}]+1}v(p)\mathrm{d}p.$$

where $v(p)$ and $\epsilon(p)$ are the relativistic expressions for the velocity and energy of a given momentum state, respectively. μ has dimensions of energy and is called the *chemical potential.* In this context it is related to the degree to which the interior is degenerate. This formula cannot be solved analytically for all possible conditions in the white dwarf interior. However, there are several limiting cases in which this is possible, and these can be used to demonstrate certain properties that extend into the analytically intractible regimes.

Fully degenerate configurations

When all quantum states are occupied up to some momentum, and none above this, the electron gas is said to be *fully degenerate.* The momentum of the highest occupied states is denoted p_f and called the *Fermi momentum*, with the corresponding *Fermi energy* ϵ_f. This is equivalent to assuming a temperature of zero for the interior. This is obviously unphysical, and any thermal energy will promote electrons to higher momentum states. In reality, the interior of a white dwarf is only partially degenerate, and hydrostatic equilibrium is maintained by a complex mixture of degeneracy pressure and a small but finite thermal pressure. However, this assumption greatly simplifies the solution to the equation of state, as in this regime the distribution function takes the following form:

$$f(\epsilon) = \begin{cases} 1 & : \quad \epsilon \leq \epsilon_f \\ 0 & : \quad \epsilon > \epsilon_f \end{cases}$$

The pressure integral now becomes:

$$P = \frac{4\pi}{3h^3}\int_{p=0}^{p_f} p^3 v(p)\mathrm{d}p.$$

For the velocity, we rearrange the relativistic expression for momentum $p = \gamma(v)mv$ to obtain

$$v(p) = c\frac{\frac{p}{m_e c}}{\sqrt{(\frac{p}{m_e c})^2+1}}$$

which, when substituted into the above formula, allows us to write for the equation of state:

$$P = \frac{4\pi m_e^4 c^5}{3h^3} \int_{\xi=0}^{x} \frac{\xi^4}{\sqrt{1+\xi^2}} \mathrm{d}\xi$$

where we have used the substitutions $\xi = \frac{p}{m_e c}$ and $x = \frac{p_f}{m_e c}$. x is called the *relativity parameter* and appears widely in degeneracy pressure calculations. This integral has the following solution:

$$P = \frac{\pi m_e^4 c^5}{6h^3} \left[x(2x^2 - 3)\sqrt{(1+x^2)} + 3\sinh^{-1}(x) \right].$$

This is the general formula for the pressure at all values of the relativity parameter, for the fully degenerate case. Now, the number density of electrons can be expressed as a function of the Fermi momentum p_f by integrating the density of states in phase space over all possible values of the momentum ($p = 0 \rightarrow p_f$). This gives:

$$n_e = \frac{8\pi}{h^3} \int_{p=0}^{p_f} p^2 \mathrm{d}p = \frac{8\pi}{3h^3} p_f^3$$

which can be expressed in terms of x as

$$n_e = \frac{8\pi m_e^3 c^3}{3h^3} x^3$$

which allows one to express the pressure directly in terms of the number density of electrons. Before making this substitution, we may further simplify the equation of state by considering as two limiting cases the regimes of *non-relativistic degeneracy* ($x \rightarrow 0$) and *relativistic degeneracy* ($x \rightarrow \infty$). The parameter x is a measure of the momentum of the electrons in the highest populated energy states, and thus measures the importance of relativistic effects. In these two cases the general equation of state reduces to the following forms:

$$P \rightarrow \begin{cases} \frac{8\pi m_e^4 c^5}{30h^3} x^5 & x << 1 \\ \\ \frac{\pi m_e^4 c^5}{3h^3} x^4 & x >> 1 \end{cases}$$

Now substituting in the number density of electrons:

$$P = \frac{1}{40} \left(\frac{3}{\pi}\right)^{\frac{2}{3}} \frac{h^2}{m_e} n_e^{\frac{5}{3}}$$

$$P = \frac{1}{16}\left(\frac{3}{\pi}\right)^{\frac{1}{3}} hcn_e^{\frac{4}{3}}$$

These expressions give approximations to the equation of state for completely degenerate stellar configurations, in the limiting regimes of non-relativistic and relativistic degeneracy.

The Mass-Radius relation and the Chandrasekhar mass limit

Putting the equation of state for the non-relativistic, fully degenerate white dwarf interior into the equation for hydrostatic equilibrium yields the following approximate result:

$$P \sim \left(\frac{M^2}{R^4}\right) \sim \left(\frac{M}{R^3}\right)^{\frac{5}{3}}$$

which has the solution:

$$R \sim \frac{1}{M^{\frac{1}{3}}}.$$

Thus more massive white dwarfs are expected to be *smaller*, a property not observed in main sequence stars. High and low mass white dwarfs are correspondingly under- and over-luminous with respect to their normal mass counterparts.

The relativistic 'softening' of the equation of state has profound implications for the *maximum* mass of white dwarf stars, as first noted by Chandrasekhar in 1931. Specifically, the reduction in stiffness gives rise to a *limiting mass* for highly relativistic white dwarfs. Repeating the above argument for the relativistic-degenerate configuration gives the relation:

$$P \sim \left(\frac{M^2}{R^4}\right) \sim \left(\frac{M}{R^3}\right)^{\frac{4}{3}}$$

$$\frac{M^{\frac{6}{3}}}{R^4} \sim \frac{M^{\frac{4}{3}}}{R^4}$$

R cancels out, implying the existence of a unique mass for relativistic white dwarfs, above which hydrostatic equilibrium cannot be maintained and the star starts to collapse. This unique mass is called the Chandrasekhar Mass, and has the definition given by Chandrasekhar (1939):

$$M_{Ch} = 5.75\mu_e^{-2} M_{\odot}$$

where μ_e is the number of nucleons per electron. M_{Ch} has the value $1.44 M_\odot$ for a composition of pure carbon.

Decoupling of mechanical and thermal properties

It was shown earlier that the ions present in the interior of the star behave, to a good approximation, like an ideal classical gas, and the electrons as an ideal Fermi gas. How does the pressure in each component contribute to hydrostatic support? Using data for Sirius B presented in Table 1.1, we can estimate the pressure of the ions and electrons separately. The equation of state for the ions is $P_i = n_i k_B T$, and for the electrons $P_e = \frac{1}{40}\left(\frac{3}{\pi}\right)^{\frac{2}{3}} \frac{h^2}{m_e} n_e^{\frac{5}{3}}$, where $n_e = 12 n_i$ for an internal composition of pure carbon. Putting the numbers in leads to the following ratio for the relative magnitude of the pressures:

$$\frac{P_e}{P_i} = 2.148 \times 10^{-18} n_i^{\frac{2}{3}}.$$

Given the mean density of Sirius B, one calculates an ion number density of $n_i = 1.25 \times 10^{35}$ m^{-3}. Putting this into the above ratio gives:

$$\frac{P_e}{P_i} = 5.37 \times 10^5.$$

Thus the mechanical properties of white dwarfs are completely dominated by the degenerate electron gas.

The thermal properties can be explored by considering the heat capacities of the two components, defined at constant volume as $C_v = \frac{\partial U}{\partial T}\big|_v$. The internal energy of both the ideal classical gas of ions and ideal Fermi gas of electrons satisfies $U \propto P$. However, the equation of state for the electrons has no T dependency in the fully degenerate limit, and the total combined heat capacity of the interior is found to be:

$$\begin{aligned} C_v &= \left.\frac{\partial U_i}{\partial T}\right|_v + \left.\frac{\partial U_e}{\partial T}\right|_v \\ &= \frac{3}{2} n_i k \end{aligned}$$

The heat capacity of the degenerate electrons is equal to zero; the thermal energy content of the star is dominated by the ions.

1.3.2 Modern evolutionary models

Basic picture

The basic picture of a white dwarf is that of an isolated, degenerate, isothermal core containing all of the energy of the star and nearly all of the mass, surrounded by an insulating non-degenerate photosphere that regulates the energy flow from the interior, thus controlling the cooling rate and appearance. It is thought that the core is normally composed of the products of helium burning in the progenitor, namely an admixture of carbon and oxygen distributed according to some unknown abundance profile. High mass progenitors may produce high mass white dwarfs with oxygen-neon-magnesium cores, though these are rare. Stars that experience sufficient mass loss to avoid the helium flash, either due to binary interactions or possibly an extremely metal-rich environment (see Meng et al., 2008; Kalirai et al., 2007), result in a low mass helium core white dwarf.

The large surface gravity causes lighter elements to float to the surface on short timescales, giving rise to a highly stratified photosphere composed of any light elements remaining after ejection of the envelope. Even tiny amounts of lighter elements are sufficient to cloak the star and conceal the underlying layers, and it is for this reason that most white dwarfs show nothing but hydrogen in their spectrum. The approximate thickness of the H/He layers has a strong effect on the cooling rate, and while current wisdom favours 'thick' layers of $q_H \equiv \frac{M_H}{M_*} = 10^{-4}$ and $q_{He} = 10^{-2}$, it is known from pulsating white dwarfs that this does not hold in all cases.

The early evolution of a white dwarf is driven by energy released from a variety of processes, including gravitational contraction and residual nuclear burning. Energy loss due to neutrino emission may be orders of magnitude larger than radiative losses at early times. Settling of the photosphere causes changes in the surface composition and spectral type, as sedimentation is followed by convective mixing at high effective temperatures. However, these processes are relatively short-lived, and the main evolutionary phase of a white dwarf is characterised by the slow transfer of residual thermal energy from the degenerate core to the surface through the insulating outer layers. To reflect this, the terms *evolution* and *cooling* are often used interchangeably in white dwarf literature.

A significant event in the later stages of evolution is the onset of crystallisation in the core. This is a first order phase transition, and the accompanying release of latent heat slows the cooling process. Also, the crystallised material is oxygen-rich compared to the original C/O mixture, and in the high gravitational field the release of energy associated with the sedimentation of the heavier element can be substantial. The magnitude of these effects depends closely on the precise C/O composition and abundance profile, something that is not currently well understood.

Next generation models

Before the late nineties, the standard reference white dwarf models were those of Bergeron et al. (1995), used by e.g. Oswalt et al. (1996) and Knox et al. (1999) to investigate the age of the Galactic disk via the white dwarf luminosity function. These coupled the evolutionary models of Wood (1995), describing the structure and energy content of the star, to atmosphere models describing the radiative transfer through the outer non-degenerate layers, thus linking stellar colours to cooling ages.

However, the treatment of the core and photosphere as essentially separate entities resulted in some built-in deficiencies in the models. The fact that the crystallisation of the core could not penetrate into the photosphere meant that ages had to be extrapolated for the coolest ($T_{\text{eff}} \leq 4000K$) objects. Also, the surface convection zone extends into the degenerate region at low luminosities, increasing energy transport through the outer layers and significantly reducing the cooling rate ('convective coupling'). The importance of this process was not recognised until new models were developed around 2001.

A significant milestone was reached by Hansen (1998), who successfully extended his models down to $T_{\text{eff}} = 1500K$. This revealed that the collision induced opacity of H_2 molecules in the cool, high density atmospheres of hydrogen rich white dwarfs causes a strong departure from a blackbody form for the emergent flux. This is in stark contrast to helium atmospheres, which cool as blackbodies to the lowest temperatures (see Figure A.3). The optical colours of hydrogen rich white dwarfs, which were thought to become redder with age, thus turn back to the blue cooler than $T_{\text{eff}} \sim 3000K$. With the subsequent identification of faint blue objects in the Hubble deep field (Méndez and Minniti, 2000), and the suggestion of a large population of faint, $\sim 0.5 M_{\odot}$ objects in the Galactic halo from microlensing results (Alcock et al., 2000), this discovery caused quite a stir.

The current generation of white dwarf models were developed by the Montreal group, and presented to the astronomical community in a review paper (Fontaine et al., 2001) and a comprehensive study of a large sample of cool white dwarfs (Bergeron et al., 2001). Their evolutionary code included the full structure of the star from the centre to the top of the photosphere, and was thus able to track both the advancement of crystallisation into the photosphere, and the extension of the superficial convection zone into the degenerate core. This revealed that the convective coupling of the photosphere and core introduces a significant delay in the cooling rate, resulting in a strong feature in the theoretical luminosity function that had not previously been identified. These models remain the standard reference in the field, and have been used throughout this work.

1.3.3 Current frontiers

In the opinion of Fontaine et al. (2001), there are no fundamental limitations to the application of white dwarf cosmochronology. However, they identify several deficiencies in the current understanding of white dwarf evolution that, at present, render the technique less accurate than other methods, such as the main sequence turn-off age for clusters. Some of these are long standing problems; others have only recently been identified. In this section I outline some of the present limitations on white dwarf cosmochronology, with reference to the theoretical understanding of their evolutionary timescales.

Photosphere layer thickness

The current 'standard model' for the outer photosphere of a hydrogen white dwarf has a helium layer of mass fraction $q_{He} = 10^{-2}$ surrounded by a hydrogen layer of $q_H = 10^{-4}$. However, seismology of pulsating ZZ Ceti stars would appear to indicate a wide range of thicknesses, e.g. Castanheira and Kepler (2009) find $q_H = 10^{-6.3\pm1.6}$. As the cooling time to a given luminosity depends sensitively on the layer thicknesses (e.g. changing q_{He} to 10^{-3} results in a factor of ~ 19 difference in cooling time to $M_{bol} \sim 16$; Fontaine et al. 2001), this must be regarded as a significant source of systematic error in the cooling ages.

Initial chemical profile

The exact C/O composition of the core at birth, and the distribution of elements therein, has an effect on the cooling rate in a number of ways. All other things begin equal, increasing the C content increases the total specific heat, leading to longer cooling times to a given luminosity. The liberation of energy during the crystallisation process is influenced by the distribution of C and O in the core, and while the amount of energy released is small, the fact it generally occurs at low luminosity can considerably delay the cooling time. Salaris et al. (1997) found that uncertainty in the C/O profile was due mainly to uncertainty in the $^{12}\mathrm{C}(\alpha,\gamma)^{16}\mathrm{O}$ reaction rate in the progenitor star, with cooling ages at $M_{bol} \sim 16.5$ differing by as much as a Gyr depending on whether a low or high rate was adopted.

Spectral evolution

The existance of effective temperature ranges in which certain white dwarf spectral types are found in very small numbers is well known. The 'DB gap' at high effective temperatures is understood to be a consequence of a very thin H layer masking a larger He layer in a purely radiative atmosphere; when convective mixing sets in below $\sim 30,000K$, the H is sufficiently diluted into the He layer that it disappears from the spectrum, and the star becomes a DB type. A second DB gap is seen from $T_{\text{eff}} \sim 6000K$ to $T_{\text{eff}} \sim 5000K$; this one is not quite so well understood. An explanation in terms of a difference in cooling times between H and He atmosphere white dwarfs cannot be reconciled with the reappearance of He-rich white dwarfs below $\sim 5000K$. Bergeron et al. (1997) hypothesise an elaborate accretion/quenching mechanism to explain this, whereby small amounts of hydrogen could be concealed in the high-pressure atmosphere of a helium rich star, only to appear at around $\sim 6000K$ due to a drop in atmospheric pressure.

Regardless of the precise interplay between convective mixing, sedimentation, accretion and energy-level quenching in photospheres of varying layer thickness, the point is that the cooling age at a given luminosity is determined by the entire spectral history, rather than the present appearance. For example, a $0.6M_{\odot}$ star that has cooled with a He photosphere until reaching $6000K$ and is then observed as a DA at $5500K$ will have its cooling age underestimated by ~ 1 Gyr. The unknown spectral evolution history of a white dwarf therefore introduces a large uncertainty in the cooling age.

Ultracool white dwarfs

The coolest white dwarfs currently observed show unusual optical spectra with large flux suppresion at red wavelengths. This is broadly understood to be a consequence of collision-induced absorption by neutral H_2 molecules (H2CIA). However, the handful of stars currently studied in detail show spectral energy distributions that deviate significantly from models incorporating H2CIA (e.g. Bergeron and Leggett, 2002), with the atmospheric composition particularly difficult to estimate. As these stars are crucial in constraining age estimates of the local Galactic populations, addressing this problem is of fundamental importance.

1.4 Applications

1.4.1 Cosmochronology

The fact that white dwarfs cool at a rate that can be calculated from theory makes them suitable for use as chronometers. The total integrated cooling time of a white dwarf depends mainly on its present luminosity, with the mass and atmosphere composition important second parameters, especially at low luminosities. In order to obtain accurate age estimates for *individual* objects it is therefore necessary to measure all three of these, which requires a range of high quality data including high resolution spectroscopy and broadband photometry extending into the infra-red. Trigonometric parallaxes are desirable in order to provide superior mass constraint to spectral line fitting. The time spent evolving as a main sequence star has to be included; this is obtained using an IFMR to estimate the main sequence mass, and another relation for the corresponding lifetime. Studies that have used stellar ages obtained in this manner include that of Monteiro et al. (2006), who used the white dwarf components of two subdwarf-white dwarf binaries to assign a thick disk origin to each system. Analysis of a control object suggested an external accuracy of $\sim 10\%$ for the ages.

Larger studies typically lack the broad observational base necessary to date individual stars, and instead focus on groups of stars with a common origin, using only the distribution in luminosity to constrain the age of the population as a whole. The notion that the star formation history of a stellar population is encoded in the luminosity distribution of its white dwarf members was introduced by Schmidt (1959). In Chapter 4, I explore in detail the development of the underlying theory over the last few decades to the level of practical application; in this Section I provide a brief review of important works and areas of research.

With respect to the Galactic disk, the first such study was that of Winget et al. (1987), who used a preliminary version of the Liebert et al. (1988) luminosity function to estimate a disk age of 9.3 ± 2.0 Gyr. This work revealed the need for deep observations, as only the faintest few luminosity bins show sensitivity to the absolute age. Brighter bins can indicate the occurence of bursts in star formation in the more recent past, as investigated from a theoretical point of view by Noh and Scalo (1990). The sample of Liebert et al. (1988) was later revisited by Leggett et al. (1998), who used updated white dwarf models and theoretical luminosity function techniques to redetermine the disk age at 8 ± 1.5 Gyr. Oswalt et al. (1996) used measurements of 50 white dwarfs found in binary systems to place a lower limit on the age of the disk of 9.5 Gyr. By integrating the luminosity function, they measure a total local density of 5.3×10^{-3}

pc^{-3} for white dwarfs in binaries, and 7.6×10^{-3} pc^{-3} for all white dwarfs by adding those single members of the Liebert et al. (1988) sample. A similar number of stars were used by Knox et al. (1999) to obtain a disk age of 10^{+3}_{-1} Gyr, with the rather large uncertainty due to a significant difference in age estimates depending on which of two independent sets of theoretical luminosity functions were used.

An important testbed for white dwarf cosmochronology is the Galactic cluster population, where this technique can be checked against ages derived in other ways, often in the same study. Indeed, Fontaine et al. (2001) suggest that the most fruitful application of white dwarf cosmochronology at present is likely to be in comparing ages derived by different means, due to several sources of uncertainty in white dwarf evolutionary models. A recent example from the literature concerns the open cluster NGC 6791, which has independent age estimates from isochrone fits to an eclipsing binary (Grundahl et al., 2008) and the main sequence turn off (Bedin et al., 2008a), and from a luminosity function fit to the white dwarf members (also Bedin et al., 2008a). The unexpectedly bright peak in the white dwarf luminosity function, and the existence of a secondary peak at fainter magnitudes, led to an age younger by up to a factor 3 than that obtained from the main sequence stars. This fact, along with the observation of several He core white dwarfs suggested that extreme mass loss driven by the cluster's high metallicity ($[\frac{Fe}{H}] \sim +0.4$) may be forming He core white dwarfs in large numbers. As these stars cool ~ 3 times slower than their C/O counterparts, this hypothesis naturally explains the age discrepancy. However, follow up observations with *Spitzer* failed to find the large quantities of circumstellar dust that this scenario predicted (van Loon et al., 2008). Bedin et al. (2008b) showed that a high binary fraction naturally explained the form of the luminosity function, and when properly accounted for removed most of the age difference. They note that the remaining difference may be accounted for by updated white dwarf models using a new estimate of the $^{12}\mathrm{C}(\alpha,\gamma)^{16}\mathrm{O}$ reaction rate.

The application of this technique can be observationally challenging, due to the requirement of observing the faintest white dwarfs. However, younger clusters have cooling sequences that terminate at brighter magnitudes, and are therefore more accessible to this approach. Also, the morphology of the lumiosity function changes more rapidly for younger populations, and the uncertainties in white dwarf evolutionary models increase with age, so younger populations can be dated more accurately. Bedin et al. (2010) measure the age of NGC 2158 using both the main sequence turn off method and luminosity function fits to the white dwarfs, finding nice agreement with ages of 1.9 ± 0.2 Gyr and between ~ 1.8 and 2.0 Gyr, respectively.

Jeffery et al. (2007) suggest that the morphology of the white dwarf cooling sequence at the *hot* end may be used to constrain the age. This is an attractive idea as it avoids the need to observe the faintest white dwarfs, thus opening the technique up to older and more distant clusters. However, it is worth pointing out that this method relies on the fact that in a single burst cluster population, the masses of newly forming white dwarfs are unique. This precludes any application to the cosmochronology of the disk, because as a continuous population newly forming disk white dwarfs have a range of masses. This method has yet to be applied in the field.

1.4.2 Galactic structure

The contribution to the local mass density from Galactic disk white dwarfs is relatively well known, at around $\sim 0.002 - 0.003\ M_{\odot}\ \mathrm{pc}^{-3}$ (Leggett et al. 1998; Knox et al. 1999; Harris et al. 2006). Halo white dwarfs are not quite so well understood, due partly to the small samples that most studies are based on, but also the fact that the uncertain kinematic properties and lack of metallicity measurements make secure identification of white dwarfs among the known Galactic populations difficult. Liebert et al. (1989) measure $\sim 1.5 \times 10^{-5}\ M_{\odot}\ \mathrm{pc}^{-3}$ from a sample size of five; a more modern value is $\sim 2.5 \times 10^{-5}\ M_{\odot}\ \mathrm{pc}^{-3}$ from Harris et al. (2006), based on around twenty stars.

Great interest in halo white dwarfs was stirred around the year 2000, when several lines of evidence suggested the existance of a vast and hitherto undetected halo population. The observation of excess microlensing events in the direction of the LMC, above that expected from the canonical thick disk and stellar halo, was attributed to compact stellar mass objects residing in a halo surrounding the Galaxy (Alcock et al., 1997). A second epoch of observation in the Hubble deep field identified two faint, blue objects with significant proper motions, and a further three marginal detections (Ibata et al., 1999). Given that Hansen (1998) showed that the colours of ancient, cool white dwarfs turn back to the blue, the identification of these stars as white dwarfs would naturally explain the microlensing observations. Such a population could also account for the entire missing dynamical mass of the Galaxy - the dark matter. Though not 'dark matter' in the strict sense of the phrase, these objects would count as such having been missed in previous luminous mass inventories of the Galaxy. These objects would also be found in the solar neighbourhood, and the proper motion survey of Oppenheimer et al. (2001) claimed the discovery of a substantial population of old white dwarfs too faint to have been detected in previous surveys. 38 of these objects were assigned halo membership, which indicated a local mass density of $1.3 \times 10^{-4} M_{\odot}\mathrm{pc}^{-3}$, an order of magnitude higher than that expected from subdwarf starcounts and a standard initial mass function.

However, most of these conclusions were later revised in the light of new studies. A third epoch in the Hubble deep field north failed to confirm any of the previous proper motion claims (Kilic et al., 2004), and found instead two disk white dwarfs. The local halo white dwarf sample of Oppenheimer et al. (2001) was analysed by several authors; Reid (2005) concluded that the prograde orbits of most of these stars indicated a thick disk origin, and that no additional Galactic component was required to explain them. Flynn et al. (2003) reached the same conclusions based on a simulation of the Oppenheimer et al. (2001) survey in conjunction with a model of the existing Galactic populations. While the microlensing events still stand, the optical depth of the lensing population has been revised downwards by a factor ~ 2, and it is thought that a substantial fraction of the events are due to self-lensing by stars in the LMC, rather than objects in a dark milky way halo (Calchi Novati et al., 2006).

Still, the list of confirmed halo white dwarfs remains sparse, and further investigation of a larger sample is required before firm conclusions can be drawn.

1.4.3 Broader context

Extrasolar planets

Several surveys have been carried out to look for planetary companions to white dwarf stars (Hogan et al. 2009; Kilic et al. 2010; Friedrich et al. 2005), and more are planned (e.g. Subasavage, 2010). White dwarfs probe an interesting range of progenitor mass ($M_{\rm MS} \geq 2M_{\odot}$), in which all present observing techniques fail, but where planets are expected to be found in significant number based on the correlation observed at lower mass between stellar mass and the existance of planetary systems (Johnson et al., 2007; Gould and Kilic, 2008). However, at present there have been no confirmed detections.

All current surveys use either ground- or space-based IR imagers, and employ quite different observing techniques to main sequence exoplanet searches. This is because the broad absorption lines of white dwarfs are unsuitable for measuring small radial velocity shifts, and their small projected radii greatly reduce the probability of transiting planets. Instead, the expected properties of white dwarf planetary systems enable direct detection of the planetary component.

White dwarfs are up to 10^4 times fainter than their main sequence progenitors, which greatly improves the contrast and makes young, massive planets ($\geq 5M_{\rm Jup}$) detectable as a photometric excess in the IR, where the planet spectrum peaks. Also, planets with white dwarf primaries have significantly larger orbits than those around main sequence stars, due to close-in planets ($a \leq 3 - 5$ AU) being swallowed up during the red giant phase, and any further out migrating to larger orbits ($\frac{a_{\rm final}}{a_{\rm intial}} = \frac{M_{\rm MS}}{M_{\rm WD}}$) during ejection of the envelope. This makes the planets potentially resolveable; at 20pc, a 20AU orbit has a projected radius of around an arcsecond. The Leicester group have been pioneering the ground-based search for resolved, IR planetary companions (e.g. Hogan et al.; Burleigh et al. 2006), and have used their non-detections around 23 stars to place an upper limit of $\leq 5\%$ on the number of white dwarfs with $T_{\rm eff} \geq 500K$, $a \sim 60 - 200$AU substellar companions.

From space, *HST* and *Spitzer* have been used to look for planets around Hyades white dwarfs (Friedrich et al., 2005) and pulsating white dwarfs (Mullally et al., 2009).

Mullally et al. obtained the most convincing detection of a planet so far, by measuring a sinusoidal variation in the arrival times of stellar pulsations. However, attempts at directly imaging the planet in the IR found no evidence of a companion.

Supernovae 1a progenitors

The existence of an upper mass limit on the range of stable white dwarf configurations (the Chandrasekhar mass) is well established. It is thought that if a white dwarf exceeds this limit, it will be disrupted in a supernova explosion of type 1a (SN1a). The intrinsic luminosity of these events correlates with the decay timescale from peak brightness, and SN1a provide an important standard candle that can be seen across vast distances. For this reason they are important cosmological probes (e.g. Perlmutter et al., 1999). Mechanisms that have been proposed to describe how a white dwarf might exceed the Chandrasekhar limit include the accretion of matter from an evolved secondary, and the coalesence of binary white dwarfs after orbital decay. Understanding the nature of the progenitors of SN1a would help to constrain systematics in their use as a distance indicator, and to explain the origin of inhomogeneities in their detonations (e.g. the progenitor of supernova 2003fg, at $\sim 2M_{\odot}$, appears to have been considerably above the Chandrasekhar limit).

The Supernova Progenitor surveY (SPY - Napiwotzki et al. 2003) is a systematic radial velocity search for SN1a progenitors that follow the double-degenerate formation channel. They have checked over 1000 supposedly single white dwarfs for evidence of a degenerate companion. Double line binaries allow the total mass of the system to be measured, as well as the orbital decay time, which in turn allows the identification of supernova progenitors by the criteria that the total mass exceeds the Chandrasekhar limit, and that the binary system merges within a Hubble time. Recent results (Napiwotzki et al., 2007) reveal no firm detections, though several single-lined binaries fall in the selection region as SN1a progenitors when the average inclination angle is used to solve the orbit.

Gravitational wave sources

Short period binaries consisting of double white dwarfs are expected to be strong sources of gravitational wave radiation. Indeed, the orbital energy loss associated with this emission is what causes the eventual merger of SN1a progenitors discussed in the preceeding Section. The next generation of space-based gravitational wave observatories are expected to routinely observe gravitational waves emitted by double white dwarf binaries, which the Laser Interferometer Space Antenna (LISA) should observe as both resolved sources and unresolved Galactic foreground emission (Liu, 2009).

The interstellar medium

The exceptionally unpolluted spectra of white dwarfs makes them ideal background sources for studies of the local interstellar medium. Due to their highly stratified atmospheres, species heavier than hydrogen are generally not present in the photosphere, and any absorption lines that appear are due to interstellar material. The column densities of different elements can be obtained by analysis of the line profiles, allowing both the chemical and ionization structure of the local interstellar medium to be investigated. Moos et al. (2002) measured the relative abundance of deuterium, nitrogen and oxygen along seven lines of sight, five of which were towards hot DA and DO type white dwarfs. They suggest that the constant ratio of D/H within 100pc of the Sun can be used to place constraints on the rate of supernovae, given various assumptions about mixing timescales within the local bubble, and that the variation across larger distances may reveal significantly different histories of nucleosynthesis.

OVI is widely believed to form along the interface between hot ($\sim 10^6 K$) and cool ($\sim 10^4 K$) gas clouds. The number of clouds in the vicinity of the sun is such that the lines of sight towards nearby (50-100pc) white dwarfs should intersect several clouds. Oegerle et al. (2005) observed 29 white dwarfs, finding a wide range in interstellar OVI abundance in different directions. In particular, they find no increase in column density for stars closer to the wall of the local bubble, which they find hard to reconcile with any existing model of OVI formation. However, recent work by Barstow et al. (2009) has discovered that OVI may be present in white dwarf spectra after all. They observed OVI absorption in the direction of 18 white dwarfs, and managed to determine the origin by measuring the velocity shift of the line relative to both the star and ISM. In all but 4 cases, the OVI was found to reside in the star, casting into doubt previous studies that use OVI, and even the whole question of the presence of hot gas in the local bubble.

Astroparticle physics

The emission of neutrinos is an important energy sink in white dwarfs at $M_{bol} \leq 9$, where the neutrino luminosity can be orders of magnitude higher than the photon luminosity. The transition from neutrino dominated cooling to photon dominated cooling causes a distinct change in slope of the luminosity function. Extending this idea, it is thought that the extreme conditions in the interior of white dwarfs may create other types of weakly interacting particles, which may be indirectly observed as a change in the cooling rate compared to that expected from standard theory.

One potential candidate for detection by this method is the 'axion'. These would be produced in a variety of astrophysical environments including the interiors of white dwarfs and non-degenerate stars. Zioutas et al. (2005) observed the Sun for six months using a laboratory based 'axion helioscope' in an attempt to directly detect solar axions, but found no signal above the background. Isern et al. (2008) investigated the effect on the cooling of white dwarfs by axion emission, finding a slight change in the slope of the luminosity function at intermediate magnitudes ($M_{bol} \leq 12$). They rule out axion masses greater than 10 meV, finding a best fit to the luminosity function of Harris et al. (2006) for a mass of ~5 meV. However, the changes in the luminosity function are within the range of uncertainty in cooling rates due to conventional physics, e.g. core composition profiles and photospheric layer thickness. Improvements in the input physics for white dwarf evolutionary models would be required before the reliable detection of a new cooling mechanism can be claimed.

1.5 Summary

White dwarfs are the most common endpoint in the evolution of stars, and are highly numerous in the solar neighbourhood where they represent the fossil remains of intermediate to high mass stars. With recent advances in the theoretical understanding of their evolution, and the advent of wide-angle surveys and deep pencil-beam imaging, their application in the fields of Galactic structure and formation has reached maturity.

CHAPTER 2

A Catalogue of White Dwarfs in the SuperCOSMOS Sky Survey

Wide angle proper motion surveys provide a great resource for identifying white dwarfs in the solar neighbourhood. Photometry to faint magnitudes combined with sensitive proper motion enables the identification of large numbers of these stars, and the homogeneous nature of wide-field data can be exploited to construct large, statistically complete catalogues. In this chapter, I describe in detail the construction of such a catalogue, including the techniques used in survey astronomy and the considerations involved in maximising catalogue size while ensuring completeness and reliability.

2.1 The SuperCOSMOS Sky Survey

Introduction

The SuperCOSMOS Sky Survey (SSS) was compiled by digitizing several generations of photographic Schmidt plate surveys. The source material includes the second generation POSSII-B, R, I and SERC-$J/EJ, ER, I/$AAO-R surveys, observed by the Palomar Oschin Schmidt Telescope in the northern hemisphere and the United Kingdom Schmidt Telescope in the south. These were performed in the photographic b_J r_{59F} i_N bands. The subscripts refer to particular combinations of filter and photographic emulsion used by the surveys; we ignore the small differences in response between the northern and southern hemisphere. While photography cannot compete with CCD astronomy in terms of photometric accuracy, it has been noted in the literature (e.g. Salim et al., 2004) that insofar as digitized photographic surveys go, SSS photometry is of the highest quality with uncertainties as low as $\sigma_m \sim 0.07$.

The first generation POSSI-E and ESO-R surveys provide an early epoch for astrometric constraint. The photometry is mostly redundant due to a similar response to r_{59F}, but we will nevertheless refer to magnitudes in these surveys as r_{103aE} and r_{63F} when distinction has to be made. Note that r_{103aE} and r_{63F} are identical in response, but we do expect differences in the survey characteristics due to different copying history etc. These surveys cross over at $\delta \sim -18°$, thus the sky is divided into three regions of common photographic material. This has implications for the charcteristics of the digitized survey. Over 1700 fields are required to cover the whole sky, with each field being observed in each of the four photographic bands to a depth of $r \sim 21$. Relevant technical details of these bands are provided in Appendix A and references therein. The four observations in each field are spread over a wide time baseline in the latter half of the twentieth century, with up to fifty years between epochs in the extreme.

Digitization scheme

Schmidt plates were digitized by the SuperCOSMOS scanning machine, scanning at 0.67 arcsecond pixel size and 15 bit digitization. SuperCOSMOS was operated at the

Royal Observatory of Edinburgh - see Hambly et al. (2001a) for an introduction to SuperCOSMOS and brief historical census of scanning programs. In some cases, glass or film copies of survey plates were scanned rather than originals. This includes the entire northern hemisphere. The use of copies was not thought to significantly degrade the quality of the scanned data, however we regard each of the surveys as having independent completeness and contamination characteristics in case any differences arise due to the copying history. Image Analysis Mode software was used to convert the raw pixel data into parameterised object catalogues, which were then merged across the four epochs to measure proper motion and colours.

Data access & technical info

The SSS data are housed in a relational database at the Wide Field Astronomy Unit, Royal Observatory of Edinburgh. The original SSS is now contained within the SuperCOSMOS Science Archive, with access provided via a web-based SQL query form at `http://surveys.roe.ac.uk/ssa/`. Parametrised object information is dispensed from two large tables; the `detection` table contains roughly 6.4 billion individual object detections, which are merged into around 1.9 billion multi-colour, multi-epoch observations in the `source` table. A comprehensive description, user-guide and technical notes for the SSS were released in a series of three papers - see Hambly et al. 2001a,b,c.

2.1.1 Low proper motion data

As described in Hambly et al. 2001c, a pairing radius of 6 arcseconds was applied to all objects in the merged source catalogue. This results in a maximum proper motion limit that varies from field to field, depending on the epoch difference of the corresponding four observations. As outlined in Section 2.1.2, we have access to a superior high proper motion catalogue based on SSS data that covers motions greater than $0\farcs18$ yr^{-1}. We therefore impose our own maximum proper motion limit of $0\farcs18$ yr^{-1} on data drawn from the SuperCOSMOS Science Archive, although note that fields with long time baselines between epochs may have limits lower than this.

We impose a lower proper motion limit on our catalogue such that all objects have at least a $5\sigma_\mu$ proper motion detection, defined by

$$\mu \quad > \quad 5\sqrt{\left(\frac{\mu_\alpha cos(\delta)}{\mu}\right)^2 \sigma^2_{\mu_\alpha cos(\delta)} + \left(\frac{\mu_\delta}{\mu}\right)^2 \sigma^2_{\mu_\delta}} \quad = \quad 5\sigma_\mu, \qquad (2.1)$$

where $\mu_{\alpha cos(\delta)}$ and μ_δ are the angular motions parallel and perpendicular to the equator. This is desirable in order to reduce scatter in the reduced proper motion diagram that is used to select WD candidates. Due to a spread in the proper motion errors of objects, many $> 5\sigma_\mu$ detections fail the lower proper motion limit, an unfortunate consequence of demanding catalogue completeness. The appropriate lower proper motion limit is set on a field-by-field basis by analysing the proper motion errors, as explained in detail later. These limits define our low proper motion sample of stars.

2.1.2 High proper motion data

We base our high proper motion catalogue on the results of a large automated search for high proper motion objects described in Hambly et al. (2004). The search algorithm works on a field-by-field basis, and starts with the complete set of parameterized object detections on each of the four plates. Any sources that have been succesfully merged and included in the default SSS catalogue at motions lower than the selected limit of $0\overset{''}{.}18$ yr^{-1} are thrown away. The remaining objects are then paired in all possible combinations within a search radius set by the upper proper motion limit of $10\overset{''}{.}0$ yr^{-1} and the epoch difference between plates. The primary pairing is between the two r epochs, which are subject to a magnitude limit of $r_{59F} < 19.75$, but any detections in b_J and i_N are also folded into the analysis to improve the astrometric solution. To produce an all sky catalogue, we take the entire object catalogue and purge multiple observations appearing in plate overlap regions, keeping whichever appears closest to its respective field centre in order to match the seaming of the low proper motion catalogue. This is far more rigorous than the object pairing in the low proper motion catalogue, and is designed to maximise completeness of high proper motion objects at the expense of introducing large numbers of spurious objects. Judicious selection of astrometric and image statistics is necessary to reduce the contamination to a tolerable level.

2.1.3 Detections

Detections on at least b_J, r_{59F} and i_N plates are required in order to obtain photometric parallaxes for WD candidates. In the case of the high proper motion stars, the primary object pairing is between the two r epochs, so in effect all objects are required to have 4 plate detections. This is also true for the low proper motion stars, because objects not detected on the $r_{63F/103aE}$ plate have much larger proper motion errors.

2.1.4 Image quality criteria

The Image Analysis Mode (IAM) software used to convert digitized Schmidt plate data into object catalogues measures a set of 32 parameters for each detected image. We restrict several of these in order to ensure that objects in our final sample have reliable, high quality stellar images. The criteria applied are as follows.

Profile classification statistic

The *profile classification statistic* η provides a magnitude-independent measure of the 'stellarness' of each image (but check the caveat in Section 2.2.2). It quantifies the deviation of the radial profile slope from that of a mean stellar template, calculated during an earlier stage of image classification. η is given in terms of a unit Gaussian statistic, and we accept images with $|\eta| \leq 4\sigma$.

Blend number

The IAM software checks for blended images by looking for image fragmentation over a range of intensity thresholds, and employs a deblending algorithm to separate blended objects. However, the deblending process introduces systematic defects in the image parameters that may be large (~ 0.6 mag) for objects of high contrast (Beard et al., 1990). We therefore reject any objects that have been deblended, indicated by non-zero values of the *blend number*.

Quality number

The *quality number* is an integer that indicates various situations encountered during image analysis, such as proximity to a bright star or plate boundary, that may adversely affect the image quality. It is set such that increasingly severe circumstances are assigned higher values. We restrict this parameter to values less than 128.

Ellipticities

Previous studies utilising digitized Schmidt plate data have placed cuts on the ellipticities e of images, in order to limit contamination from faint galaxies and noise. However, we have found that the ellipticities fitted by the IAM software are extremely noisy at intermediate to faint magnitudes, and that any intuitively sensible cut will result in a seriously incomplete sample of stars. For example, real stellar images in the b_J band are often assigned $e > 0.5$ within two magnitudes of the plate detection limit. This may be a consequence of the eight-fold nearest neighbour pixel connectivity employed by the IAM software. Therefore, we have decided to ignore this parameter when constructing our catalogue of stars.

2.1.5 Sky coverage

Individual field areas

The pointings used for the ~ 1700 fields comprising the SSS use the ESO/SERC system of field centres, which is based on a 5° pitch angle plus some small adjustments to allow for locating guide stars. This results in $\sim 0.5°$ overlap between neighbouring fields, given the $\sim 6° \times 6°$ field of view of Schmidt plates. Objects observed multiple times in overlap regions are assigned to the field whose centre they are closest to along a Great Circle, providing a 'seamless' catalogue. However, the POSS-I survey adopted the Palomar system of field centres, which uses a 6° pitch and results in very little overlap between fields. POSS-I data are 're-mossaiced' onto the ESO/SERC field system for inclusion in the SSS, resulting in $\delta > -18°$ r_{63F} fields that are really a composite of several pointings. This has implications for measurement of the completeness limits of SSS fields.

I have measured the solid angle for all SSS fields, based on the ESO/SERC field system. This was done numerically by dividing the sky into small elements of solid angle, accounting for any excluded regions close to the plane, and assigning each element to the field it lies closest to along a Great Circle. The average field of view for fields in the SSS is ~ 0.007 sr, with a significant spread as shown in Figure 2.1.

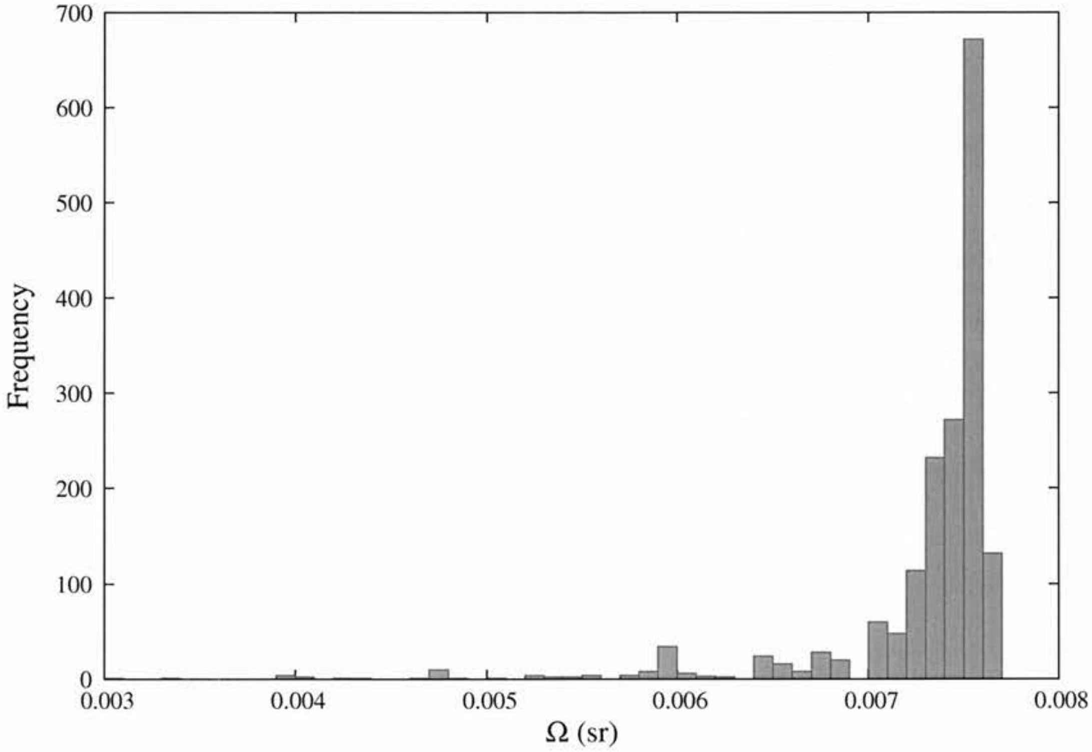

Figure 2.1: Frequency of SSS field areas in seamless catalogue.

Bright star haloes and diffraction spikes

Certain structures within the telescope give rise to spurious 'ghost' images associated with each real star, mostly attributed to internal reflections within the optical system. Bright stars are accompanied by large haloes and diffraction spikes arising from, respectively, reflections within the Schmidt plate itself and the spider arms supporting the plateholder assembly.

These images effectively 'drill out' regions of sky from the survey, and must be accounted for in order to accurately calculate the survey volume. The *drilling fraction* is measured exclusively from the b_J plates, on which these images have the greatest areal extent, and ranges from a few percent at high Galactic latitude to more than 50% in the plane.

Rejection of crowded fields

The SSS nominally covers the entire sky. However, in dusty regions at low Galactic latitude the photometric calibration can be adversely affected by differential extinction across the field. Also, the process by which merged images are deblended into separate catalogue objects is dubious, and results in unreliable stellar parameters. Image pairing across epochs is also tricky in crowded regions, where mis-pairings can result in large amounts of contamination.

For these reasons, we avoid the Galactic plane by 10° and the Galactic centre by 20°. We also reject 49 fields lying slightly outside this region that show a large amount of contamination, manifest in highly dense regions of stars bounded by field edges. Seven fields centred on the cores of the Magellanic clouds are also excluded.

Rejection of fields with a poor epoch spread from high proper motion survey

In most fields, the earliest epoch of observation is $r_{63F/103aE}$. The remaining three epochs are distributed over a ~ 10 to 20 year period with a varying spread in time. The primary object pairing is between the two r epochs, and if the b_J and i_N observations are taken very close to the r_{59F} observation, they provide very little astrometric constraint. For example, in northern field 103 the r_{63F} observation is made in July 1952, and b_J, r_{59F} and i_N are all taken within three weeks of each other in April 1991. In such cases, a large number of first-epoch pairings are generated for every real high proper motion object, as the search algorithm proceeds through every possible combination within the search radius, and the single correct image pairing is swamped by noise.

This is not a problem with the low proper motion catalogue, as the search radius for image pairing is much smaller. For certain fields in the high proper motion catalogue however, the effect is catastrophic. We therefore reject from our high proper motion

Survey	Ω(sr)	Fraction of whole sky
$\mu < 0\farcs18$ yr^{-1}	9.86	0.78
$\mu > 0\farcs18$ yr^{-1}	9.52	0.76

Table 2.1: Total sky coverage of the low and high proper motion surveys.

catalogue any fields that have b_J,r_{59F} and i_N plates taken within 1.5 years. 58 fields fall into this category, and are excluded.

Total sky coverage

The total sky footprint contained in both the low and high proper motion surveys is given in Table 2.1. This excludes the Galactic plane and centre regions, accounts for the stellar halo drilling fraction, and all fields rejected from each of the two surveys.

2.2 Proper motion completeness limits

2.2.1 The low proper motion stars

Upper proper motion limits

The low proper motion data are limited to motions less than $0\farcs18$ yr^{-1}. However, individual fields in the SSS may be incomplete at motions lower than this, due to the epoch spread and pairing radius combination, as explained in Section 2.1.1. To locate the upper proper motion completeness limit in each field, we look at the cumulative number counts as a function of proper motion, which drop off as $\log(N) \propto -3\log(\mu)$ towards high proper motions for a uniform, complete sample. We allow for non-uniformity by measuring the gradient in each field, and fit a straight line to the distribution over the mid range where the number counts are assumed complete. We compare the observed number counts towards high proper motions to the expected counts based on our power-law extrapolation, and fix the proper motion limit at the point where the ratio of observed to expected counts falls below or above a certain threshold, indicating incompleteness or extreme contamination. The threshold was set to 0.8 and 0.8^{-1} for

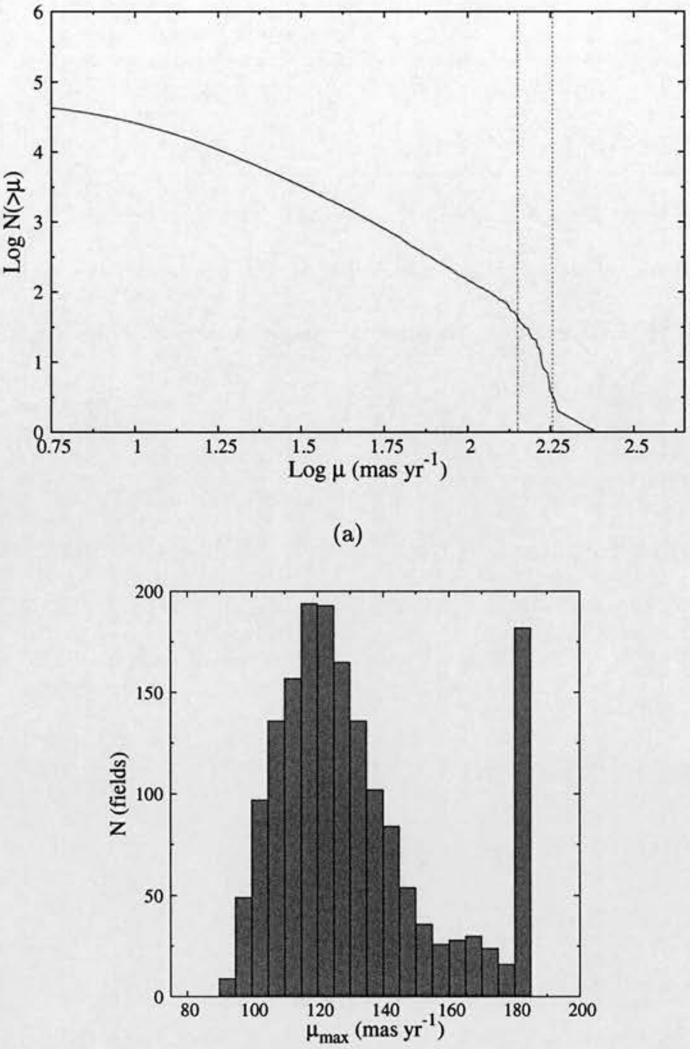

(a)

(b)

Figure 2.2: 2.2(a) above shows field 259N from the low proper motion survey. The blue line corresponds to the external high proper motion limit of $0''.18\ \mathrm{yr}^{-1}$ applied across all fields; the green line is the completeness limit for proper motion in this field, measured according to the method is Section 2.2.1. 2.2(b) shows the upper proper motion limit frequency histogram for all fields in the low proper motion survey.

the two cases.

Lower proper motion limits

The requirement of at least $5\sigma_\mu$ proper motion detection excludes non-moving objects from our catalogue, and limits scatter in reduced proper motion. However, we cannot simply select all objects with $\geq 5\sigma_\mu$ detections, because the proper motion errors show significant scatter at constant magnitude. The resulting survey volume limits at given tangential velocity would be unknown, as it would be impossible to measure the distance at which the star dropped below the required $5\sigma_\mu$ detection threshold. Therefore, we wish to find the *maximum* proper motion error as a function of magnitude, and use this to fix the lower proper motion limit. This guarantees that all objects that pass the limit also have $\geq 5\sigma_\mu$ detections. The proper motion error σ_μ varies from field to field, due to differences in plate quality and time baseline. It is also a strong function of magnitude, and at constant magnitude shows a significant spread. Figure 2.3(a) shows the distribution of σ_μ with b_J for a representative field. We use b_J for these figures because it is the highest quality photometry available. Objects in the upper locus have been missed at one of the four epochs, usually r_{63F}, and have inferior astrometric fits. For this reason we restrict our low proper motion sample to objects with four plate detections. To fix the proper motion limit, we fit functions to the upper boundaries of the b_J,σ_μ locus. The procedure for each field is as follows. We start at the bright end of the distribution, and bin objects on magnitude interactively so that all bins contain one hundred objects. The mean b_J and maximum σ_μ in each bin is located, after rejecting the top 5% of σ_μ as outliers. The full set of σ_μ^{max},$\langle b_J \rangle$ points defines the rough upper boundary of the locus, but shows considerable noise on small scales. The raw fit is then processed through one stage of smoothing to obtain the desired function. We use a Savitzky-Golay technique to smooth the data, generalized from their original prescription (Savitzky and Golay, 1964) to allow for non-uniform points on the abscissa. This removes small-scale noise while preserving any low-frequency features, such as the mid-magnitude turning point seen in most fields. Figure 2.3(b) shows the same field as (a), but restricted to four plate detections, and with the fitted functions shown. The final, smoothed function obtained for each field is denoted $\sigma_\mu^{max}(b_J)$, and is used to set

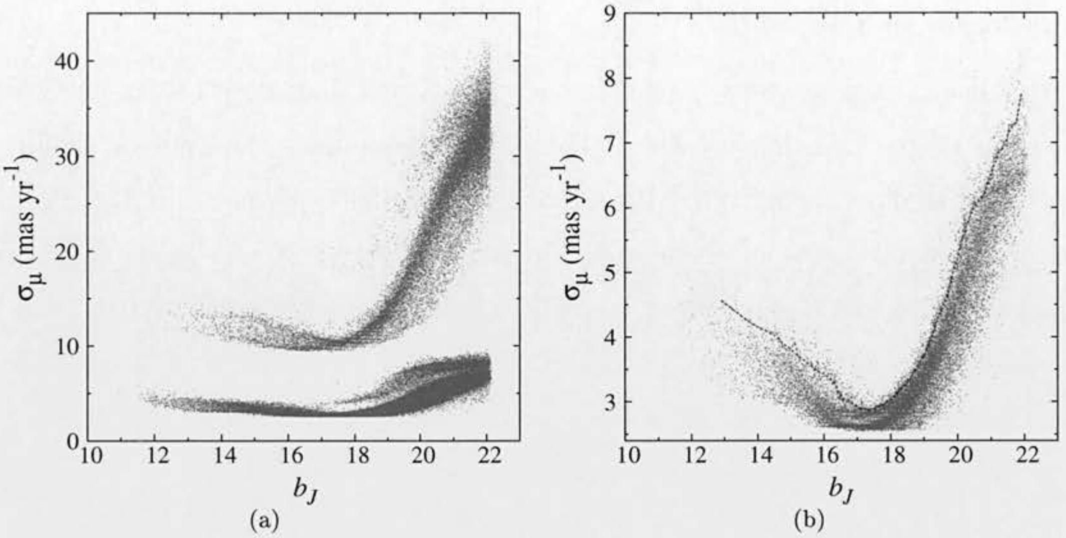

Figure 2.3: Field 772S proper motion errors and fitted $\sigma_\mu(b_J)$ function. (a) includes objects not detected at r_{63F}, which form the locus of points at higher σ_μ. (b) is restricted to objects with full four plate detections, and shows the function fitted to the upper boundary of the σ_μ, b_J locus.

the lower proper motion limit according to

$$\mu_{min}(b_J) = \quad 5\sigma_\mu^{max}(b_J). \tag{2.2}$$

The set of points defining $\sigma_\mu^{max}(b_J)$ is tabulated for each field, and interpolated using cubic splines to obtain the proper motion limit at arbitrary apparent magnitude. Thus the lower proper motion limit is a piecewise function of apparent magnitude, which complicates the measurement of the survey volume, but maximises the sample size by fully exploiting the variable proper motion accuracy. The mean lower proper motion limit across the survey is shown in Figure 2.4. This is divided into the three sky regions where the source photographic data are the same. It is interesting to note that the lower quality northern data attains a similar proper motion accuracy as the southern region that shares the same first epoch r material, that of the POSSI-E survey. The ESO-R survey has a much later average epoch, with the result that proper motion measurements are considerably more uncertain at equal μ.

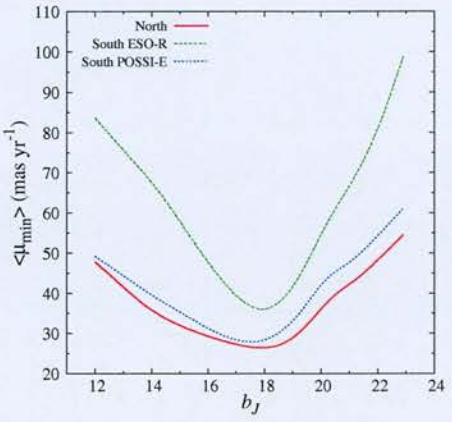

Figure 2.4: Mean lower proper motion limits in the three sky regions of uniform photographic source data.

2.2.2 Astrometric contamination of low proper motion data

The magnitude completeness limits defined in Section 2.3.3 (later on) were used to draw an initial catalogue of stars. Upon early analysis of the reduced proper motion diagram, it was apparent that the low proper motion catalogue was highly contaminated at faint magnitudes by objects with erroneous proper motion measurements. A significant fraction of stars have spurious large proper motions, which cause the highly numerous disk main sequence stars to scatter to high values of reduced proper motion, completely swamping the region where we expect to find cool white dwarfs. As can be seen in Figure 2.5(a), objects start to scatter from the dense disk main sequence locus at around the colour of the old disk turnoff. Redwards of this, the Galactic stellar populations merge in reduced proper motion (RPM), as RPM no longer correlates with distance.

We selected a sample of objects from the highly contaminated region to investigate ways to exclude them. The proper motion errors for these objects are of the same order as those for well-measured objects, but the distribution of astrometric residuals shows a highly non-χ^2 form, indicating that the assumption of Gaussian positional errors is breaking down as presumably the image centroiding is being compromised. Analysis of the image statistics for these objects shows a tendency towards a larger η than expected for point sources, indicative of a shallower radial profile. The contamination is significantly worse in the north, where the data are of lower quality, but is also present in the south at intolerable levels and with the same characteristics. We investigated whether undetected blended objects were responsible, by comparing equal size regions of sky in opposite Celestial hemispheres, but at equal Galactic longitude and absolute latitude $|b|$ to ensure similar levels of crowding. Number counts show a consistently larger number of blended objects in the south than the north, suggesting that the source of contamination may be blended objects that have not been detected as such. The image parameters and astrometry for such an object are likely to be significantly affected. Getting rid of these objects proved to be tricky. They are found at magnitudes well within the completeness limits of the Schmidt plates, and at a wide range of proper motion. We investigated whether a combination of η and astrometric χ^2 per degree of freedom (χ^2_ν) could be used to devise a new statistic to identify these objects, but

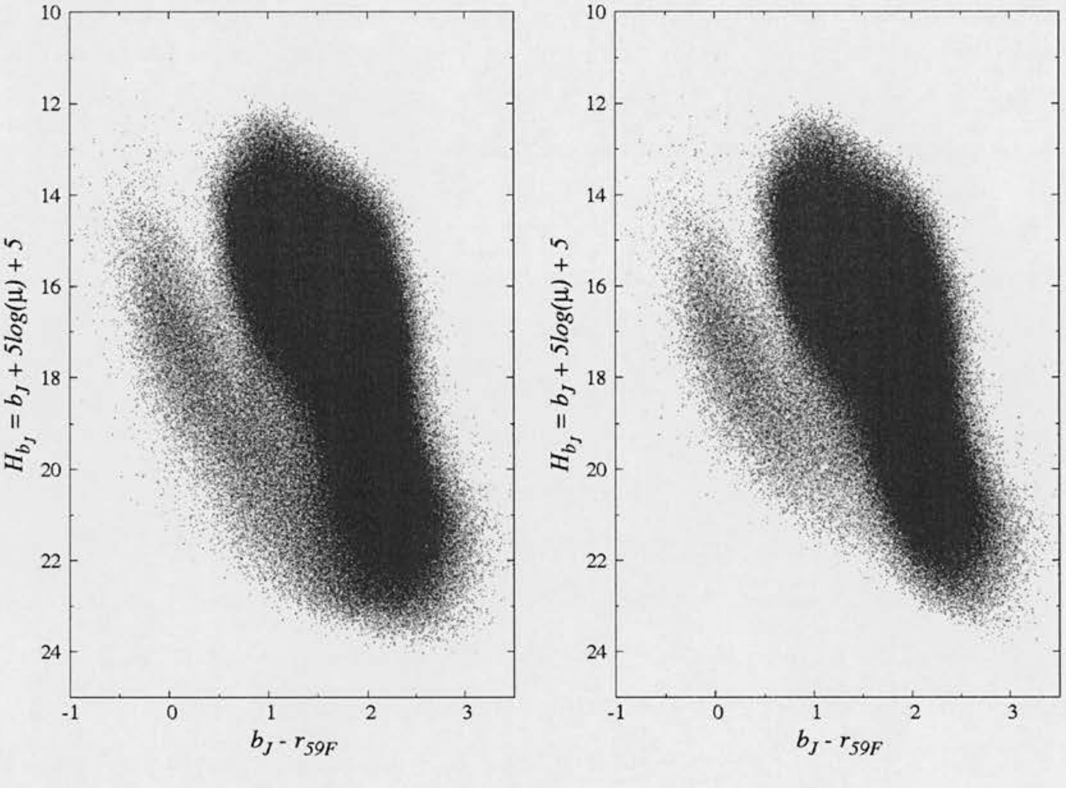

(a)

(b)

Figure 2.5: (a) Depicts an early reduced proper motion diagram showing significant contamination redwards of $b_J - r_{59F}$. In (b) we have applied a $r_{59F} < 19.75$ cut and restricted the astrometric residuals in order to weed out the contaminating objects.

Statistic	Limit	P($<\chi^2_\nu$)
χ^2_ν, north	0.8	0.83
χ^2_ν, south	1.7	0.99

Table 2.2: Limits on χ^2_ν selected for low proper motion catalogue.

unfortunately it was discovered that η is slightly magnitude dependent and that any new statistic would select against faint stars. Tighter proper motion limits are not an option, because the contamination is present at all proper motions to some extent, and reducing contamination to tolerable levels in this way results in a very small catalogue of stars.

The only remaining option is to limit the range of magnitude. We decided to use the same magnitude constraint as that applied externally to the high proper motion catalogue, which shows no sign of this contamination. Thus, we restrict r_{59F} to magnitudes brighter than 19.75. This removes nearly all of the contamination while maintaining a suitable catalogue size. As a final constraint, residual contamination at brighter magnitudes is reduced by setting cuts on χ^2_ν. These cuts are different in the northern and southern hemispheres, and are set by checking the RPMD over a range of limits until contamination is judged to be tolerable. The adopted limits are given in Table 2.2. As a side note, we discovered that the χ^2_ν values given in the SSA are precisely half what they should be given the number of degrees of freedom in the astrometric fit, so the third column in the table gives the corresponding fraction of real stars that pass the adopted χ^2_ν limit, given the halved statistic. In the end, spectroscopic analysis of a sub-sample of RPM selected objects is required to judge overall contamination.

2.2.3 The high proper motion stars

Low proper motion limit

The high proper motion catalogue is constructed using a rigorous object pairing algorithm, and we expect completeness around the $0\farcs18$ yr^{-1} transition between the low and high μ catalogues to be much better on the high μ side. Indeed, all-sky cumulative proper motion counts for the high μ catalogue show 100% completeness right down to $0.''18$ yr^{-1} (see Figure 2.6). We fix this as the low proper motion limit across all fields.

High proper motion limit

It is apparent from Figure 2.6 that spurious detections are creeping into the high proper motion catalogue above $\sim 1.''5$ yr^{-1}. We fix the all-sky upper proper motion limit in an identical fashion as for individual fields in the low proper motion catalogue. A straight line is fitted to the low proper motion range of the log-number counts, and used to extrapolate the expected observed counts to high proper motions. The proper motion limit is set at the point where the ratio of observed to expected counts passes below 0.8 or above 0.8^{-1}. This occurs at a proper motion of $\sim 1.''485$ yr^{-1}, and is adopted as the upper proper motion limit for the survey.

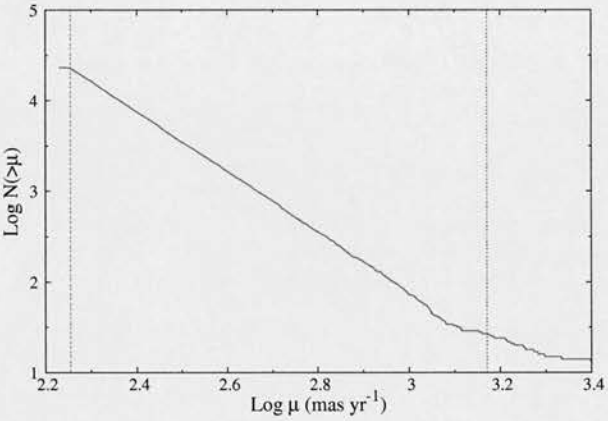

Figure 2.6: Proper motion completeness of high μ catalogue. The green line shows the $0.''18$ yr^{-1} boundary between the low and high proper motion catalogues, used as the lower proper motion limit. Beyond $\sim 1.''5$ yr^{-1}, contamination starts to appear. The blue line corresponds to $\sim 1.''485$ yr^{-1} and is the upper proper motion limit chosen for the high μ survey.

2.3 Magnitude completeness limits

The SSS literature provides completeness estimates for a selection of b_J and r_{59F} plates in the first SSS data release, the South Galactic Cap (SGC). These are measured by comparing SSS star and galaxy counts with those obtained from deeper prime-focus and

CCD data in overlapping regions, and estimate near 100% completeness within ~ 1.5 mags of the plate detection limits. However, our all-sky survey uses northern Schmidt plate data not included in the SGC, those of the POSS-I and POSS-II surveys. Also, the $r_{63F/103aE}$ and i_N plates are shallower and of lower signal to noise than b_J and r_{59F}, and, given the colours of the objects we are interested in, will likely determine the overall completeness limits of the SSS fields when considering objects detected on all four plates.

Therefore, it was necessary to estimate new completeness limits for all plates used in the SSS. We obviously cannot obtain deeper imaging for all fields, and so an alternative approach is required. We decided to follow the method of Tinney et al. (1993); this involves simulating star and galaxy counts along the line of sight, and comparing these to observed counts derived from the corresponding plate material.

We assume that the completeness characteristics of plates within the same photographic survey are identical, due to uniform quality control, emulsion grade and copying history prior to digitization. This allows us to restrict our analysis to a representative sample of plates from each of the eight photographic surveys used in the SSS. Although the plate detection limit varies within each survey, we assume that the plates have a common *completeness function*, which we define as the ratio of detected objects to real objects as a function of magnitude relative to the plate detection limit. We decided to analyse five plates from each survey, drawn from five fields in each of the celestial hemispheres. A summary of the fields selected for analysis is given in Table 2.3.

2.3.1 Synthetic star and galaxy counts.

Stars

Differential star counts along the line of sight to each field are obtained using the Besançon Galaxy model (see Robin et al., 2003). This employs a population synthesis approach to produce a self-consistent model of the Galactic stellar populations, which can be 'observed' to obtain theoretical data sets useful for testing various Galactic structure and formation scenarios. We use the coordinates, solid angles and passbands of our selected fields as inputs, and select an output number count range that goes

Field	b	Ω	Surveys
411S	-86.89	0.00756	SERC – J/EJ SERC – R/AAO – R SERC – I ESO – R
350S	-80.18	0.00749	
241S	-69.38	0.00538	
149S	-60.60	0.00591	
237S	-50.23	0.00731	
507N	87.85	0.00759	POSSI – E POSSII – B POSSII – R POSSII – I
382N	80.98	0.00751	
270N	70.38	0.00750	
273N	59.44	0.00750	
135N	49.36	0.00723	

Table 2.3: Fields used to measure the completeness function for each photographic survey. b and Ω are the Galactic latitude and solid angle subtended by each field.

several magnitudes fainter than the plate limits. The SuperCOSMOS filter system is not included in the Besançon model; instead we use the CFHT Megacam bands g and r to approximate b_J and $r_{59F/63F/103aE}$, and Johnson-Cousins I to approximate i_N. The similarity between the filter response curves is demonstrated in Appendix A.

Galaxies

Within a few magnitudes of the plate limits, galaxies appear as unresolved, point-like objects and have image parameters that overlap with stars. We therefore have to include galaxies in our synthetic number counts. Galaxy counts to faint magnitudes are well determined from many independent studies. We use counts provided by the Durham Cosmology Group that combine their own results (see e.g. Jones et al., 1991; Metcalfe et al., 1991) with those of many other authors. These are available online at `http://astro.dur.ac.uk/~nm/pubhtml/counts/counts.html`, along with transformations to photographic bands. They are provided in terms of log-number counts per square degree per half-magnitude; we fit straight lines to obtain functional forms for the galaxy counts in each band, and transform these to 0.1M for comparison to our observed counts. Note that the ~ 25 square degree field of view of each Schmidt plate smooths out any anisotropies in the faint galaxy counts. The fitted functions are given in Equations 2.3 to 2.6 ($r \equiv r_{59F/63F/103aE}$). We multiply these functions by the solid angle of each field, then add them to the star counts to obtain our theoretical counts for each plate.

$$\log(N_{b_J}\mathrm{deg}^{-2}0.1\mathrm{M}^{-1}) = 0.471\ b_J - 7.890 \qquad (16 < b_J < 26) \tag{2.3}$$

$$\log(N_r\mathrm{deg}^{-2}0.1\mathrm{M}^{-1}) = 0.379\ r - 5.351 \qquad (17 < r < 25) \tag{2.4}$$

$$\log(N_{i_N}\mathrm{deg}^{-2}0.1\mathrm{M}^{-1}) = 0.606\ i_N - 9.132 \qquad (12 < i_N < 17.75) \tag{2.5}$$

$$= 0.346\ i_N - 4.397 \qquad (17.75 < i_N < 25) \tag{2.6}$$

2.3.2 Observed star and galaxy counts.

For each field selected for analysis, we obtain object counts to the detection limit on all four plates, binned at 0.1 magnitude intervals server-side using an efficient SQL query on the SSA interface. We widen the η and e range to include partially resolved galaxies, though at the plate limits everything is pointlike.

2.3.3 Completeness functions

In Figure 2.7 we show observed and modelled differential object counts for field 270 in the north and 149 in the south. The ratio of these quantities relative to the detection limit gives the completeness function; these are inlaid for comparison. Total model counts are normalised to the observed number at two magnitudes above the detection limit, where the plates are assumed 100% complete. The superior quality of SERC-J and SERC-R is evident, due to the use of original glass survey plates in the SuperCOSMOS scanning program. These plates show $\sim 100\%$ completeness to within a few tenths of a magnitude of the detection limit. All other surveys were copied photographically at least once before digitizing, which has resulted in noise creeping in within a magnitude of the plate limit. This makes completeness assessment difficult due to real detections being indistinguishable from spurious ones. The POSSII-I survey was copied *twice* before scanning, and the noise is noticeably worse on this plate. The POSSI-E plate shows large numbers of spurious detections within up to two magnitudes of the detection limit. A double peak is often seen in the distribution; this is due to the mosaicking of two or more Palomar fields onto one ESO-SERC field for inclusion in the SSS catalogue. To estimate the global completeness function for each survey, we repeat the above analysis for five fields and take an unweighted average of the individual completeness functions. These are shown in Figure 2.8.

As mentioned above, the noise at faint magnitudes makes completeness assesment of the plates tricky. Real objects are often dwarfed in number by spurious detections, seriously compromising any star catalogue drawn from this magnitude range on an individual plate. However, by restricting our white dwarf catalogue to objects that have been detected on all four plates in a field, contamination by noise can be considerably reduced, as noise is eliminated by the image pairing criterion. This allows us to push our catalogue magnitude limits into the noisy regions, and investigate the completeness of the catalogue as a whole using statistical methods. We avoid the worst of the noise just above the plate limit, and set a *plate limit offset* for each survey that will define the field-by-field magnitude limits for our WD catalogue. The magnitude offsets chosen, and the resulting mean depths for each survey, are given in Table 2.4.

2.3.4 Bright magnitude limits

The selection of the bright limits on apparent magnitude is not as important, due to the low probability of white dwarfs being found at these magnitudes. We fix the bright limits at 12 for all bands and across all fields. This is within the complete range of the Schmidt plates.

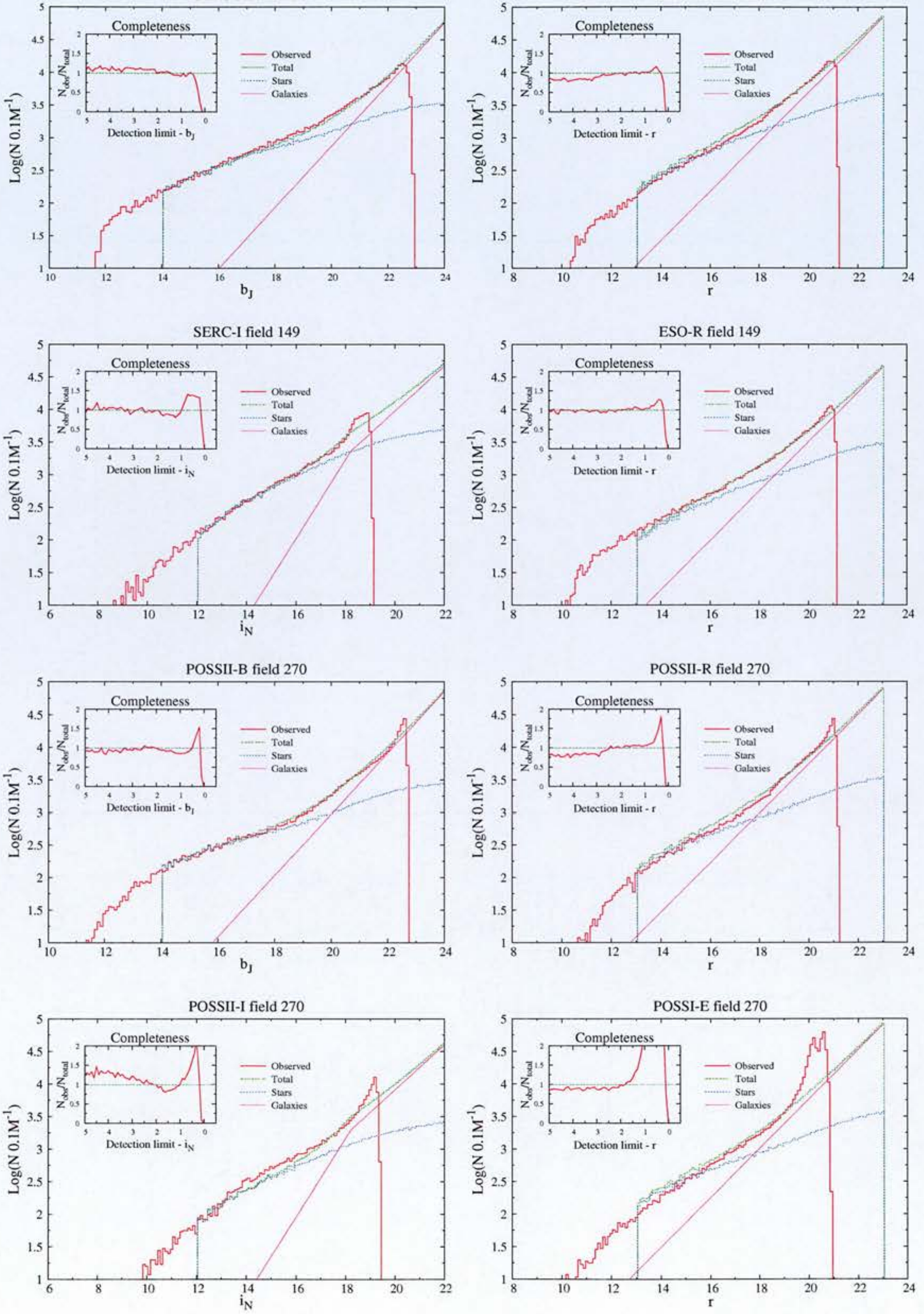

Figure 2.7: Example completeness analysis for two fields in the SSS, covering all eight of the constituent photographic surveys.

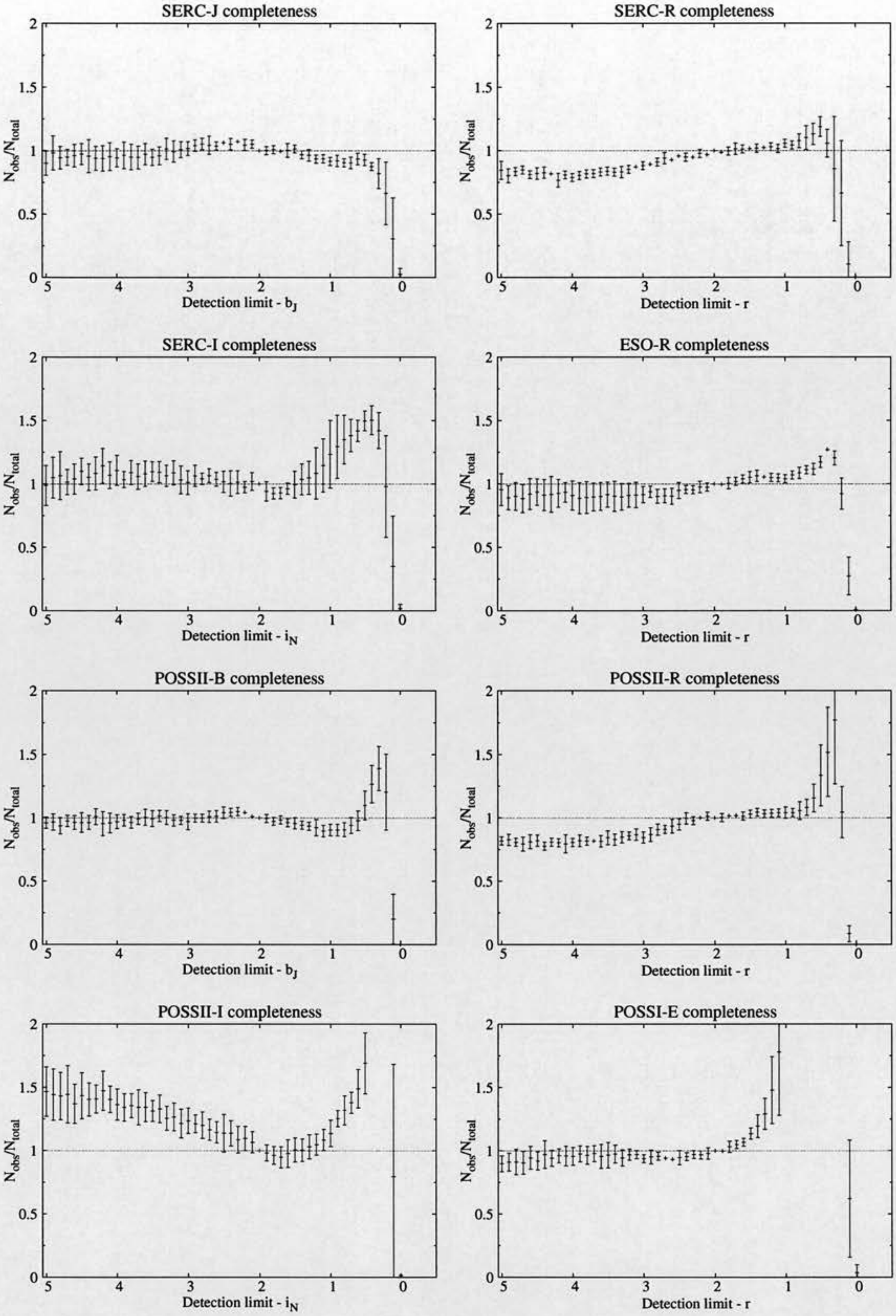

Figure 2.8: Completeness functions averaged over five plates in each photographic survey.

Survey	m_{offset}	Mean mag limit	
Northern hemisphere:			
POSSI-E	1.0	19.7	
POSSII-B	0.4	22.2	
POSSII-R	0.5	20.6	(19.7)
POSSII-I	0.8	18.8	
Southern hemisphere:			
ESO-R	0.7	20.2	
SERC-J	0.4	22.4	
SERC-R	0.3	20.7	(19.7)
SERC-I	0.8	18.5	

Table 2.4: Offsets defining the magnitude limit for each field in the eight constituent photographic surveys. Column three gives the average survey magnitude limit on applying these offsets globally. The number in brackets is the corresponding average when the $r_{59F} < 19.75$ constraint is applied to the second epoch r data, as explained in Section 2.2.2.

2.4 Survey methods

2.4.1 Identification of white dwarf candidates

Reduced proper motion

The proper motions of nearby stars correlate with distance, in the sense that closer objects are more likely to show large angular velocities. The proper motion can be combined with apparent magnitude to obtain a statistic called the *reduced proper motion* H, which provides a crude estimate of the absolute magnitude.

$$H_m = m + 5\log_{10}\mu + 5 \tag{2.7}$$

$$= M + 5\log_{10}V_T - 3.38 \tag{2.8}$$

Although useless for obtaining accurate stellar distances, H is sufficient to distinguish populations of stars with distinctly different luminosity calibrations or kinematic properties. The classical tool for exploiting this is the *reduced proper motion diagram* (RPMD), which plots colour against H. The RPMD is topologically equivalent to the HR diagram, though with considerable vertical scatter due to the weak correlation between H and M. At around ten magnitudes fainter than main sequence stars of the same colour, white dwarfs are ideally suited to identification based on H.

Tangential velocity selection

Equation 2.8 suggests that with an appropriate colour-magnitude relation, regions of the RPMD inhabited by white dwarfs of different tangential velocity can be isolated. This allows us to perform rigorous selections on H to produce catalogues of white dwarf candidates within a well-defined tangential velocity range. However, cool, low velocity white dwarfs can have identical colours and H values to high velocity subdwarfs from the Galactic halo, and these two populations overlap to some extent in the RPMD. Contamination by subdwarfs can be reduced by applying a minimum tangential velocity threshold to stars identified as white dwarf candidates. This produces a cleaner sample of white dwarfs by restricting selection to regions of the RPMD more widely separated from the subdwarf locus. Figure 2.9 demonstrates the selection of white dwarf candidates based on reduced proper motion. The fact that low velocity white dwarfs are lost from the survey is of course a drawback of this technique; however, the fraction of stars that fall below the chosen threshold can be calculated, if the kinematic properties of the population are known. This is done in each field by projecting the velocity ellipsoid onto the tangent plane, correcting for the mean motion relative to the sun, and marginalising over the position angle to obtain the distribution in tangential velocity. This is covered in detail in Appendix B.

The values adopted for the mean reflex motions and velocity dispersion tensors are given in Table 2.5. These are derived by Hawley et al. (1996) for the thin disc and Chiba and Beers (2000) for the thick disk and halo. Mean motions are relative to the local standard of rest; the usual Galactic frame is used in which the velocity dispersion tensor is diagonal in σ_U^2, σ_V^2, σ_W^2. We use the Dehnen and Binney (1998b) determination of the solar motion from Hipparcos data.

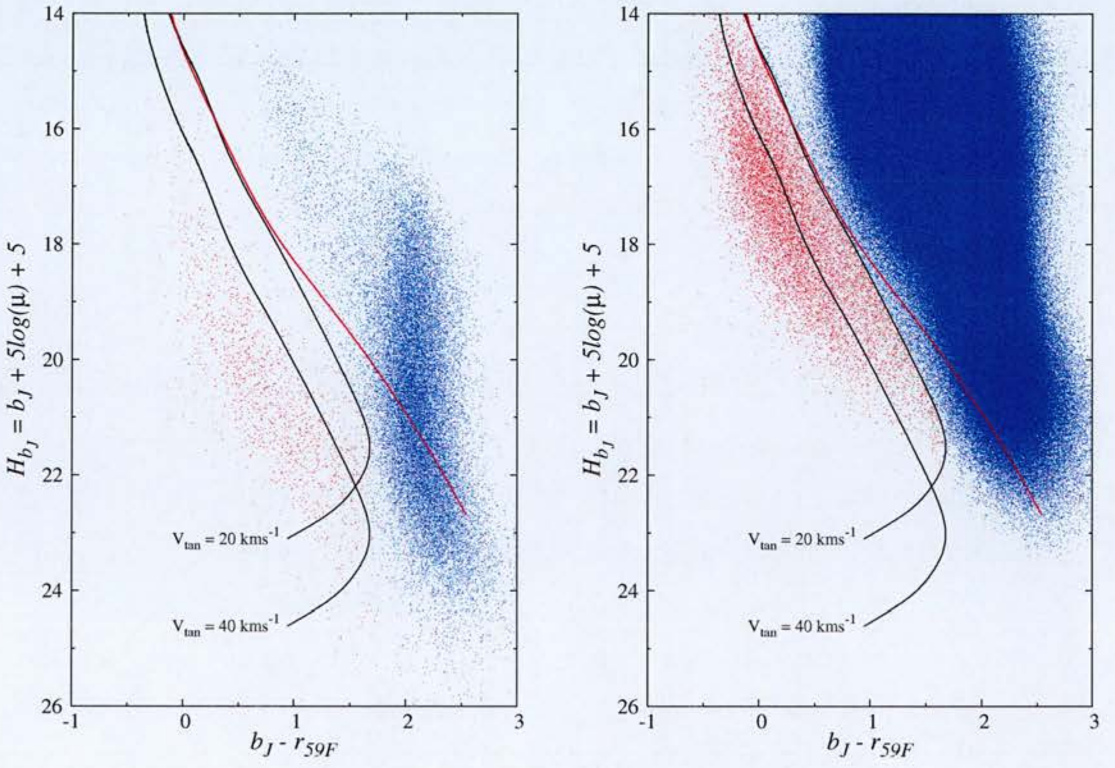

(a)

(b)

Figure 2.9: Reduced proper motion diagrams for high (a) and low (b) proper motion catalogues. Also shown are colour-magnitude relations in reduced proper motion for $0.6M_\odot$ H (black lines) and He (red line) white dwarfs, for two adopted values for the tangential velocity according to Equation 2.8. The $20kms^{-1}$ H track is used to select white dwarf candidates for our catalogue, which are indicated by red dots. Objects rejected based on RPM are indicated by blue dots.

Population	$\langle U \rangle$	$\langle V \rangle$	$\langle W \rangle$	σ_U	σ_V	σ_W
Thin disc	0.9	-18.0	-0.4	40.6	26.7	21.2
Thick disc	-1.0	-37.0	-5.0	50.0	56.0	34.0
Halo	-16.0	-194.0	-5.0	141.0	106.0	94.0
Sun	10.0	5.25	7.17	-	-	-

Table 2.5: Kinematic quantities adopted in this work. The usual Galactic coordinate axes UVW are used, with U pointing towards the Galactic centre, V in the direction of rotation, and W towards the NGP. The velocity dispersion tensor is assumed diagonal in this frame. Mean motions are relative to the local standard of rest.

2.4.2 Photometric parallaxes

Photometric distances are obtained by fitting the two-colour photometry to the white dwarf model atmospheres and cooling sequences described in Fontaine et al. (2001) and updated in Bergeron et al. (2001) and references therein (see also `http://www.astro.umontreal.ca/~bergeron/CoolingModels`). They were provided in the SuperCOSMOS bands by Dr. Bergeron on request. The models consist of cooling sequences for white dwarfs of different surface gravity and H/He atmosphere type. The gravity and atmosphere effect the fitted distances by changing the absolute magnitude at a given colour, but with only two data points each we cannot fit these for our stars. Instead, we assume $\log g = 8.0$ for all our stars, and fit both hydrogen and helium atmospheres. It is well known that the gravities of white dwarfs are tightly distributed about this value (for example, Bergeron et al. (2001) find $\langle \log g \rangle = 8.070 \pm 0.014$), a consequence of their tight mass distribution. Low and high mass white dwarfs exist in roughly equal numbers ($\sim 10\%$ and 15%), and fitting to $\log g = 8.0$ models has opposite effects on the photometric parallax.

Also, the H/He atmosphere type has very little effect on the luminosity above around $6,000K$ ($b_J - r_{59F} \sim 0.8$). Below this, the assumption of a H atmosphere for a He atmosphere star will cause the absolute magnitude to be considerably overestimated, and the distance underestimated. In general, optical spectra are useless for distinguishing the atmosphere type, because below around $5000K$ all the absorption lines are washed out. There is therefore some ambiguity over the nature of the coolest white dwarfs in our survey.

Fitting procedure

The best fitting $\log g = 8.0$ H and He atmospheres are found in a straightforward manner by variance-weighted least squares, after interpolating the models at $10K$ intervals. We fit the $b_J - r_{59F}, b_J - i_N$ photographic colours to the predictions of the models, with photometric uncertainty assigned according to the relation in Appendix A.1.2. The models corresponding to the upper and lower 1σ confidence boundaries are found by $\chi^2_{1\sigma} = \chi^2_{min} + 1$. We take no account of redenning, and do not expect it have a significant effect due to the proximity of our stars. Objects with $\chi^2_{min} > 5$ are rejected from the survey; these are mostly unresolved binaries as explained at the end of this section.

Overall distances are estimated by taking a minimum-variance combination of the estimates from each photometric band b_J, r_{59F} and i_N. Note that we avoid $r_{63F/103aE}$ in this calculation. Uncertainty on the overall distance estimate is assigned by averaging the upper and lower confidence boundaries. A two-colour diagram showing the location and status of our stars relative to the models is presented in Figure 2.10.

Calibration of photometric parallaxes

In order to measure the success, or otherwise, of our photometric parallaxes, we compare the photometric distances to those obtained by trigonometric parallax for a subset of our white dwarfs. Bergeron et al. (2001) presented an analysis of 152 cool white dwarfs with accurate trigonometric parallaxes ($\frac{\sigma_\pi}{\pi} < 0.3$), all but four of which fall within the proper motion and magnitude range of our high proper motion data. Of the remaining 148, 115 have SSS counterparts. We investigated the missing stars by searching individual plate records for proper-motion corrected positions; mostly stars are excluded due to lack of a detection at $r_{63F/103aE}$. Note that when cross identifying stars, we do not apply the completeness limits from Sections 2.2 and 2.3, as the identification is done manually and contamination is not a problem. We do, however, apply the usual restrictions on

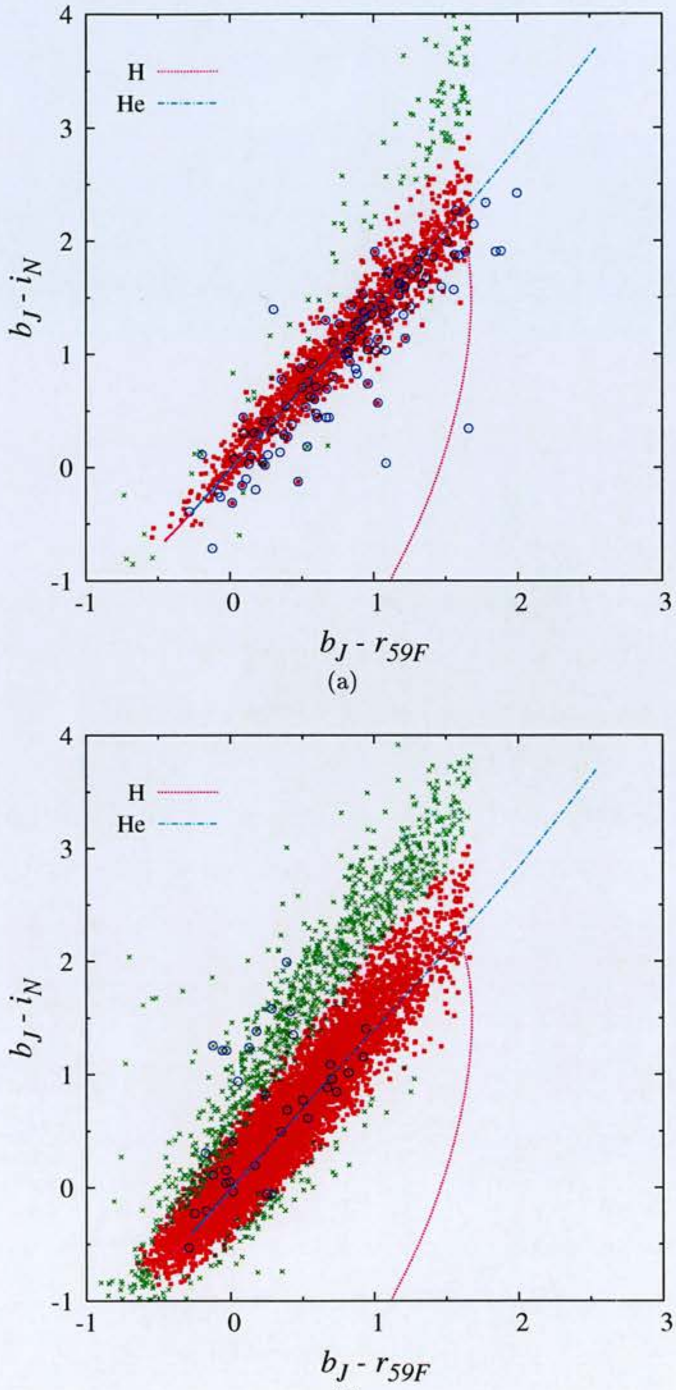

(a)

(b)

Figure 2.10: Two colour plots for high (a) and low (b) proper motion catalogues. Red squares indicate stars that pass the $\chi^2 < 5.0$ cut on the model atmosphere fit; green crosses indicate failures. Objects with spectroscopic follow-ups are marked with circles.

blend and quality number, as these directly affect the quality of the photometry. We also require stars to be detected at all four epochs, which is necessary for the fit. These constraints reduce the sample to 74 stars.

We fit atmosphere models to the remaining stars, in each case using the appropriate H/He atmosphere as measured by Bergeron et al. (2001). We place the same cut on the residuals as is used in the main survey, in order to remove any stars with spurious photometry. This results in a sample of 67 stars with adequately fitted photometric distances. A comparison of the distances obtained by the two methods is presented in Figure 2.11. The correlation between the two is $r = 0.76$, and $\frac{d_{trig}}{d_{phot}} = 1.07 \pm 0.54$. The error in $\frac{d_{true}}{d_{phot}}$ is likely to be lower than this, due to uncertainty in d_{trig}, and we estimate the accuracy of our photometric parallaxes $\sigma_{d_{phot}}$ to be around 50%.

We compared the results of fitting $(b_J - r_{59F}, r_{59F} - i_N)$ and $(b_J - r_{59F}, b_J - i_N)$ colours to the models. The $(b_J - r_{59F}, r_{59F} - i_N)$ colours resulted in a slightly worse fit ($r = 0.74$, $\frac{d_{trig}}{d_{photo}} = 1.09 \pm 0.55$) presumably due to the superior quality of b_J, so we adopt $(b_J - r_{59F}, b_J - i_N)$ for performing our photometric parallax fits. We also tried relaxing the χ^2 cut to 6 then 7; in both cases the sample was increased to 69 stars with $\frac{d_{trig}}{d_{photo}} = 1.07 \pm 0.53$. Therefore, all but a few percent of white dwarfs with reliable photometry will pass the survey $\chi^2 < 5.0$ threshold.

Cool white dwarf atmosphere types

At colours where the choice of atmosphere has a significant effect on the absolute magnitude, a dichotomy arises in the photometric distance estimate that must be addressed. Knox et al. (1999) deal with the unknown atmosphere type by assigning half of the stars H atmospheres and half He. However, as He WDs are brighter at a given colour they will be sampled over a larger volume and are expected to be present in greater numbers than a simple 50:50 ratio. Harris et al. (2006) use this fact to estimate the relative numbers of the two types they expect to find in their survey, in several bolometric magnitude bins. They also avoid strict atmosphere assignments for each object, choosing instead to attach a weight to each atmosphere and allow stars to contribute as both types.

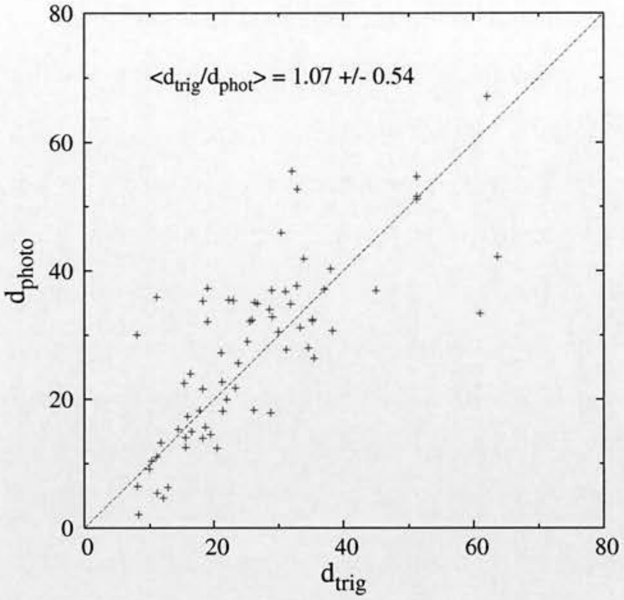

Figure 2.11: We compare the distances obtained by our photometric parallaxes to those obtained by trigonometric means, for a subsample of stars analysed by Bergeron et al. (2001).

We follow the lead of Harris et al. (2006), and assign weights to each star depending on colour. However, instead of using a few discrete magnitude ranges, we derive a continuous weight function based on the survey volume for each each type as a function of colour. The relative fraction of He to H stars at a given $b_J - r_{59F}$ colour is estimated from the corresponding absolute magnitudes R_H and R_{He} assuming a spherical survey volume and uniform density profile. We obtain the following formulae for the weights ω_H and ω_{He} for each type;

$$\omega_{He} = \frac{n_{He}}{n_{He} + n_H} \tag{2.9}$$

$$= \frac{1}{1 + \mathcal{C}^{-1} 10^{\frac{3}{5}(R_{He} - R_H)}} \tag{2.10}$$

$$\omega_H = 1 - \omega_{He} \tag{2.11}$$

where $\mathcal{C}$ is the ratio $\frac{n_{He}}{n_H}$ of helium to hydrogen white dwarfs. $\mathcal{C}$ is likely an evolving function of colour, due to spectral evolution (see e.g. Tremblay and Bergeron, 2008), however here we simply set it equal to 0.5. The helium weight as a function of colour is plotted in Figure 2.12(b) for several assumed values of $\mathcal{C}$, along with reference weights obtained if H and He white dwarfs did not diverge in absolute magnitude. The colour-magnitude relations used to calculate the weights are shown in Figure 2.12(a).

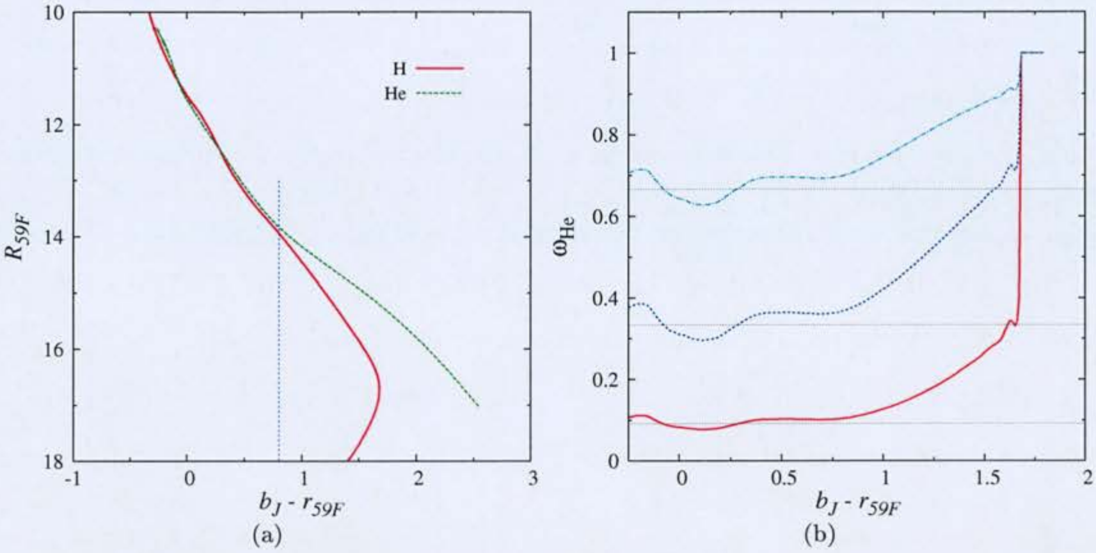

(a)

(b)

Figure 2.12: (a) Colour-magnitude relations for $0.6M_{\odot}$ H and He white dwarf models, showing the divergence beyond $b_J - r_{59F} \sim 0.8$. (b) Weights calculated for cool helium atmosphere white dwarfs, under different assumptions for the ratio $\frac{n_{He}}{n_H}$ in the solar neighbourhood. The curves correspond to $\mathcal{C} = 0.1, 0.5, 2.0$ (bottom to top), and the straight lines are the weights if the H and He colour-magnitude relations did not diverge.

Known ultracool white dwarfs

Of the dozen or so ultracool ($T_{\rm eff} < 4000K$) white dwarfs that have been reported in the literature, seven pass the survey constraints and are included in our white dwarf catalogue. These are LHS 3250 (Harris et al., 1999; Bergeron and Leggett, 2002), CE 51 (Ruiz and Bergeron, 2001), LHS 1402 (Bergeron et al., 2005), SDSSJ0947 (Gates et al., 2004), SSSJ1556 (Rowell et al., 2008), SDSSJ1452+45 and SDSSJ1632+24 (Harris et al., 2008). Our default photometric parallax method is inappropriate for these stars for two reasons. Firstly, although detailed analysis of stars of this class is currently, and necessarily, restricted to only a couple of examples, it is clear that their properties are quite different to what one would expect based on an extrapolation from higher temperatures. In particular, it would appear that most of these objects have extremely He rich atmospheres, which is difficult to reconcile with the expected accretion rates of

H from the interstellar medium. Also, the single object with a trigonometric parallax (LHS 3250) appears over-luminous for its temperature, and has been interpeted either as an unresolved double degenerate or an extremely low mass single white dwarf. Secondly, models fail to reproduce the SEDs of these objects for *any* set of parameters, indicating incomplete input physics. To quote Harris et al. (2008), writing with reference to their own objects but applicable more generally,

> "It is premature to add these new ultracool white dwarfs to any analysis of the space density and luminosity function of white dwarfs for two reasons: we do not yet have models to fit the spectra adequately to give accurate temperatures and H/He abundances, and we do not yet have distances to get luminosities, masses, and ages."

While this may be true, these stars are present in our survey and must be dealt with in some way. And so with these caveats, we proceed to estimate distances and luminsoties for these objects, though note that our adopted values should be treated with caution.

Of the seven white dwarfs, only three have anything close to a reliable distance estimate. LHS 3250 has a trigonometric parallax as noted above, and CE 51 and LHS 1402 have photometric parallaxes based on spectroscopy and multiband photometry, extending into the IR in the latter case. SSSJ1556 has a SED very similar to that of LHS 3250, and Rowell et al. (2008) invoked their similarity to assign a distance by assuming these stars also shared identical luminosities. Gates et al. (2004) performed a similar analysis for SDSSJ0947 using superior Sloan photometry. We continue in this way for the final two stars. SDSSJ1452+45 is closest in colour to LHS3250, though $r_{59F} - i_N$ differs by ~ 0.4 and this star is most likely warmer. SDSSJ1632+24 has identical colours to CE 51 (to ~ 0.01m), and we use this star as a reference in this case. The distances and bolometric magnitudes adopted for these objects are presented in Table 2.6. We have used SSS proper motions to calculate corresponding tangential velocities. Note that on the basis of this distance estimate, SDSSJ0947 has $\mathrm{v}_{tan} = 18$kms^{-1} and drops out of the sample. To be clear, it passes the $\mathrm{v}_{tan} > 20$kms^{-1} RPM threshold for the survey, but when the extra (dubious) distance information is added at this stage it falls

Star	distance	v_{tan}	M_{bol}	$T_{\rm eff}$	Method
CE 51	14.7	44	17.5	2730	Photometric π
LHS 3250	30.3	80	16.17	<4000	Trigonometric π
LHS 1402	25	58	16.8	3240	Photometric π
SSSJ1556	32	63	16.17	<4000	Reference to LHS 3250
J1632+24	23	38	17.5	<3000	Reference to CE-51
SDSSJ0947	47	18	16.17	<4000	Reference to LHS 3250 via SDSS colours
J1452+45	57	28	16.17	<4000	Reference to LHS 3250

Table 2.6: Distances and bolometric magnitudes for ultracool white dwarfs appearing in our survey.

below the cut.

Unresolved binaries

Selection of white dwarf candidates is made on b_J, r_{59F} and μ, so objects with unusual i_N magnitudes turn up at this point when their $b_J - i_N$ colours are compared to the models. The large populations of objects at red $b_J - i_N$ in Figure 2.10 show excess flux in i_N, due to an unresolved cool main sequence companion. Figure A.1 shows how the i_N band is sensitive to the flux from the cool star. These WD+dM binaries are ejected from the survey by the restriction on the photometric parallax residuals, as with at least one of three bands polluted no reliable white dwarf fit is possible. This therefore represents a source of incompleteness in the survey. Spectra of some of these objects were taken as part of our spectroscopic follow up program to confirm their nature; see Section 2.4.3. Similarly, Sirius-like systems consisting of a *hot* main sequence star and white dwarf will fail reduced proper motion selection as white dwarf candidates.

Unresolved double degenerates often have combined spectral energy distributions that closely resemble single stars of intermediate temperature. They will therefore be successfully fitted to the models and pass into the white dwarf catalogue as apparently single objects. However, with two stars contributing to the flux the derived photometric distance will be underestimated by up to a factor $\sqrt{2}$.

Indications from the local (20pc) white dwarf population are that $\sim 70\%$ of white dwarfs exist as single objects (Holberg, 2009). Around 20% are members of either a WD+dM or Sirius-like binary system, and so ejection of these may result in incompleteness of up to 20%, depending on what fraction are unresolved by SuperCOSMOS. Around 10% of white dwarfs exist in double degenerate binaries, which translates to a double degenerate-to-single star fraction of up to 7% among our catalogue objects, again depending on what fraction are not spatially resolved.

2.4.3 Evaluation of spectroscopic subsample

In order to assess the integrity of our survey method and white dwarf catalogue, we have undertaken a program of spectroscopic follow-up observations for a subset of objects selected from our catalogue. Our observations were made over four nights using the CTIO 4m Blanco telescope with the R-C spectrograph, eleven nights in total on the Isaac Newton Telescope using IDS, and eleven hours using the ISIS spectrograph on the William Herschel Telescope in service mode. All spectra were taken with a similar instrument set up, obtaining a resolution of ~ 5Å with a wavelength coverage of $\sim 3000 - 9000$Å. Data were reduced using standard IRAF packages. Briefly, using the `ccdproc` task, images were trimmed, corrected for overscan and bias, flatfielded and a slit illumination correction applied using twilight sky exposures. Spectra were extracted using the `apall` task, wavelength calibrated using appropriate arc lamp exposures, and flux calibrated with observations of spectrophotometric standards. Observations of early type stars were used to remove atmospheric absorption features (telluric correction). In most cases, three exposures were taken and combined in median to remove cosmic rays and reduce noise.

Of the 148 objects for which we measured spectra, 75 are included in our final white dwarf catalogue, and are presented in Appendix C. Of these, only three are identifiable as non-white dwarfs: SSSJ1126+1433 and SSSJ0206+1836 are M dwarfs, and SSSJ1717+3026 is a subdwarf. This suggests that our catalogue may be contaminated by non-white dwarf stars at the level of a few percent. The remaining stars show a wide range in spectral type, including hot hydrogen (e.g. SSSJ1248+4153, SSSJ1248+4153) and helium (e.g. SSSJ1248+4153) atmosphere stars (DA and DB types), featureless DC types (SSSJ1248+4153, SSSJ1248+4153, SSSJ1248+4153), DZ stars with only metal lines (SSSJ1248+4153) or DZAs with both hydrogen and metals (SSSJ1248+4153), stars with strong collision-induced absorption (SSSJ1556-0805) and a sole cool DQ showing only the Swann bands of carbon (SSSJ1248+4153).

The 73 stars that do not end end up in our final catalogue, and that are presented in Appendix D, were targeted for a number of reasons. Some were present in early catalogues before the survey limits were refined, and now lie outside the survey range. These are a mixture of bonafide white dwarfs (SSSJ1248+4153), expected subdwarf contaminants (SSSJ1248+4153) and objects that must have spurious photometry, e.g the catalclysmic variable SSSJ1248+4153. We also targeted a number of stars we suspected of being white dwarfs with unresolved, low mass main sequence companions. These tend to be selected as white dwarfs based on their $b_J - r_{59F}$ colour and reduced proper motion, but then fail the photometric fitting procedure due to excess flux at i_N. The spectra confirmed our suspisions - for example, SSSJ1248+4153, SSSJ1248+4153 and SSSJ1248+4153 show both the broad Balmer lines characteristic of the high temperature, high pressure atmospheres of white dwarfs, and the TiO bandheads associated with the low temperature, low pressure atmospheres of M dwarfs. The position of these features relative to our photographic filters is shown in Figure A.1.

2.5 Catalogue summary

To bring this chapter to a close, I briefly review the main results of the preceeding sections and summarise the final white dwarf catalogue. I have undertaken a proper motion and magnitude limited survey for white dwarfs in the SuperCOSMOS Sky Survey, using two distinct datasets of low and high proper motion stars. The high proper survey is limited mainly by the $0''.18\mathrm{yr}^{-1}$ low proper motion limit; the low proper motion survey, probing more distant stars, is limited mainly on i_N magnitude. In light of

Section 2.4.2, the catalogue may be up to 50% incomplete due to exclusion of blended objects and those for which no first epoch detection exists. However, Section 2.4.3 indicates that contamination of the final catalogue by non-white dwarfs is limited to a few percent. On applying a $v_{tan} > 20\text{kms}^{-1}$ cut in reduced proper motion, I obtain 10,929 white dwarf candidates with photometric parallaxes accurate to around 50%. Increasing the v_{tan} threshold results in a cleaner catalogue; $v_{tan} > 30\text{kms}^{-1}$ gives 8558 stars, and $v_{tan} > 40\text{kms}^{-1}$ gives 6463. Note that these numbers are based on reduced proper motion selected samples; later, I will draw velocity subsamples using the photometric parallaxes to determine velocities, and the numbers will be slightly different. Sky projections of white dwarf candidates that pass the $v_{tan} > 20\text{kms}^{-1}$ cut are shown in Figure 2.13. Tangential velocity and distance distributions are presented in Figures 2.14 and 2.15.

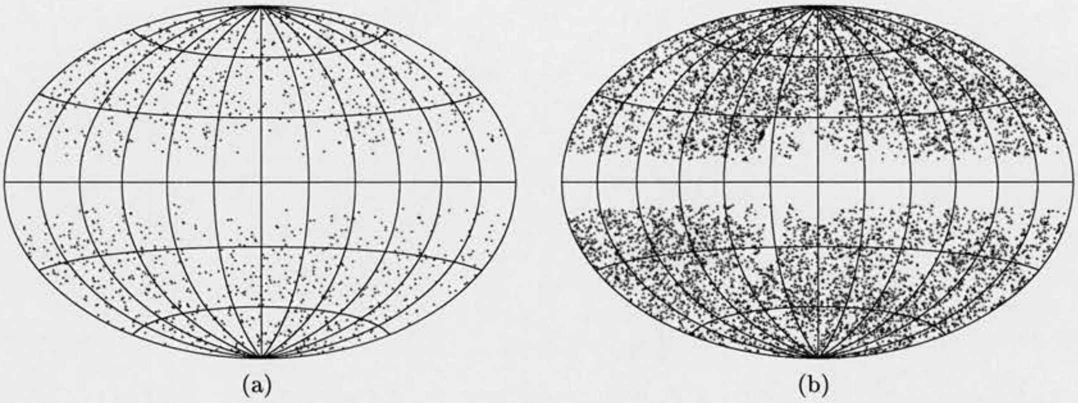
(a) (b)

Figure 2.13: Sky projection of white dwarfs in the high (a) and low (b) proper motion surveys.

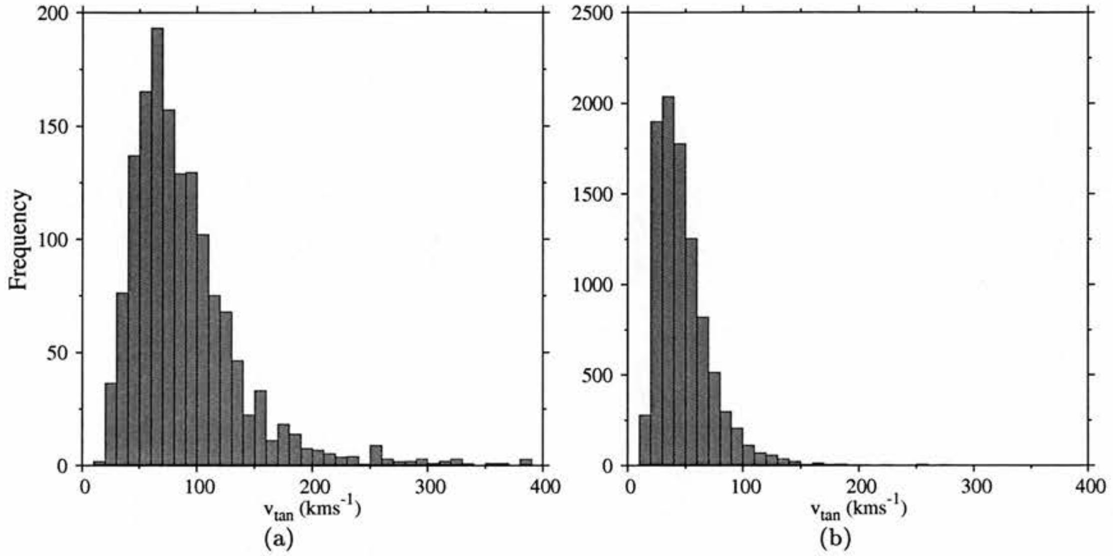

Figure 2.14: Tangential velocity distribution of white dwarfs in our high (a) and low (b) proper motion surveys.

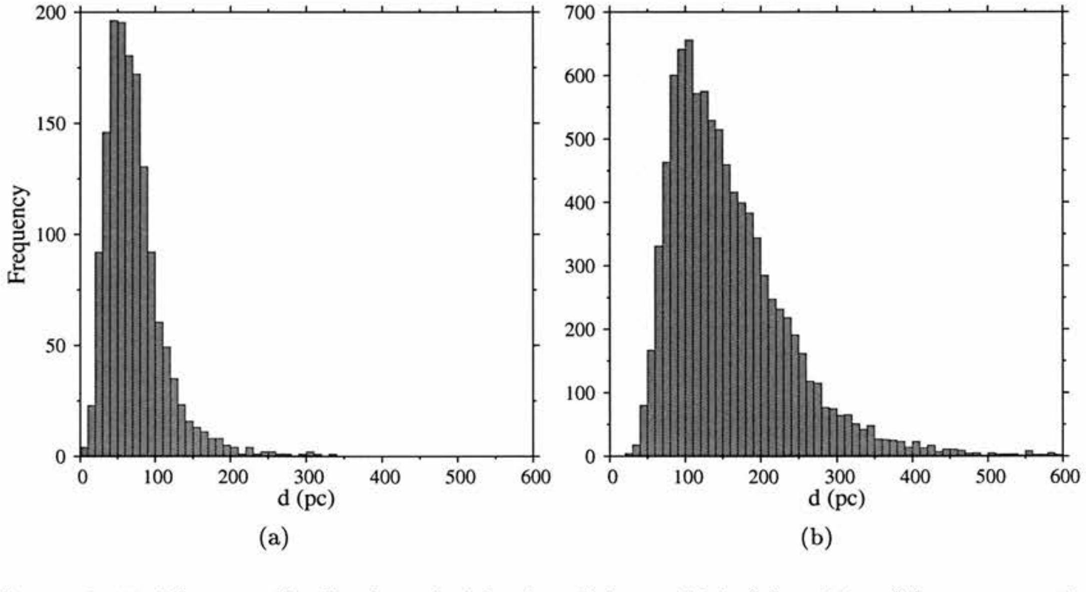

Figure 2.15: Distance distribution of white dwarfs in our high (a) and low (b) proper motion surveys.

CHAPTER 3

The Luminosity Function for White Dwarfs in the SuperCOSMOS Sky Survey

The white dwarf luminosity function is of fundamental importance in the cosmochronology of stellar populations. A whole host of astrophysical phenomena influence its morphology, including white dwarf cooling rates, the initial mass function and the star formation history for the population under study. Reconciling the observed luminosity function with that reconstructed from theory allows one to investigate the various parameters that go into the mix. However, it is usually the absolute age of the population that is of greatest interest. In this chapter, we focus on the measurement of the luminosity function using our catalogue of white dwarfs.

3.1 Luminosity function methods

3.1.1 The $\frac{1}{\mathrm{V_{max}}}$ density estimator

There exists a variety of statistical methods for estimating luminosity functions, including both parametric and non-parametric methods, maximum likelihood estimators and simple number counts. The $\frac{1}{V_{max}}$ technique (Schmidt, 1968) has been used in every major study of the white dwarf luminosity function, due largely to tradition and to the relative simplicity of the approach, although it has the advantage of easily incorporating proper motion selected samples, as well as the non-uniform distribution of objects within the Galactic disk. Its performance alongside other methods has been analysed by Geijo et al. (2006) and found to be satisfactory; it provides an unbiased estimate of the true density, and for large enough samples (≥ 300) accurately characterises both the rising slope and faint peak of the luminosity function. Its particular relevance to cosmochronology has also been investigated. Wood and Oswalt (1998) found that statistical uncertainty alone in $\frac{1}{V_{max}}$ luminosity functions resulted in 15% (10%) age uncertainty for 50 (200) point samples, and that uncertainties in white dwarf and Galactic evolutionary models contributed a further $10 - 15\%$. Therefore, using the $\sim 9,000$ objects with $v_t > 30$ kms^{-1}, we expect the uncertainty in age estimates arising from statistical uncertainty in the observed luminosity function to be negligible compared to the theoretical uncertainties associated with calculating the reconstructed luminosity function.

The $\frac{1}{V_{max}}$ method obtains an estimate for the number density of objects ϕ by summing the inverse of the maximum volume in which each object could reside and still be accessible to the survey,

$$\phi = \sum_{i=1}^{N} \frac{1}{V_{max,i}} \tag{3.1}$$

Uncertainties are conventionally assigned assuming Poisson statistics, where the standard error in each $\frac{1}{V_{max}}$ term is equal to the term itself (e.g. 1 ± 1 events). These are then summed in quadrature to obtain the error on ϕ,

$$\sigma_{\phi}^{2} = \sum_{i=1}^{N} \frac{1}{V_{max,i}^{2}} \tag{3.2}$$

A more accurate approach would be to use the Gehrels (1986) upper and lower confidence limits for Poisson statistics, which would result in a $1^{+2.3}_{-0.83}$ contribution from each star for a 68.27% confidence interval. It is to allow comparison with other studies that we adopt an uncertainty of ±1 on the number of stars; all previous measurements of the white dwarf luminosity function have used this.

Objects are binned on bolometric magnitude, and the density associated with each bin is calculated in this manner to obtain the luminosity function. As in Knox et al. (1999), we plot the luminosity function points at the mean magnitude of the objects in each bin. This is more realistic, and shifts the observed luminosity function slightly in regions where the number counts change rapidly with magnitude, such as at the downturn. We also assign horizontal error bars to each point, calculated by averaging the lower and upper bolometric magnitude errors separately, e.g.

$$\sigma_{up} = \sqrt{\frac{\Sigma_{i=1}^{N} \sigma_{up,i}^{2}}{N}} \tag{3.3}$$

with $\sigma_{up,i}$ and $\sigma_{low,i}$ assigned from the 1σ photometric models.

This method relies on being able to calculate the appropriate survey volume for each star, and correct for various sources of incompleteness introduced by the survey procedure. We turn to this now.

3.1.2 Calculating $\mathbf{V_{max}}$

Our survey is limited on both apparent magnitude and proper motion. The intrinsic stellar properties, namely the absolute magnitude and tangential velocity, lead to restrictions on the distance at which each star could reside and still pass the survey limits. The apparent magnitude limits are fixed in each field, and the corresponding distance limits are found according to

$$d^{m}_{max} = \min\left(10^{\frac{b_{J,max}-B_J}{5}}, 10^{\frac{r_{59F,max}-R_{59F}}{5}}, 10^{\frac{r_{63F,max}-R_{63F}}{5}}, 10^{\frac{i_{N,max}-I_N}{5}}\right) \tag{3.4}$$

$$d^{m}_{min} = \max\left(10^{\frac{b_{J,min}-B_J}{5}}, 10^{\frac{r_{59F,min}-R_{59F}}{5}}, 10^{\frac{r_{63F,min}-R_{63F}}{5}}, 10^{\frac{i_{N,min}-I_N}{5}}\right) \tag{3.5}$$

The high proper motion stars

Our high proper motion sample also has fixed proper motion limits, which are converted into distance limits similar to those above given above using the star's tangential velocity v_t by

$$d^{\mu}_{max} = \frac{v_t}{4.74 \quad \mu_{min}} \tag{3.6}$$

$$d^{\mu}_{min} = \frac{v_t}{4.74 \quad \mu_{max}} \tag{3.7}$$

where μ is in $''\!.\mathrm{yr}^{-1}$, v_t is in kms^{-1} and d is in parsecs. The overall distance limits are found by combining these with Equations 3.4, with the condition that the star has to pass both sets of limits to be included in the survey. V_{max} is then found by integrating the appropriate density profile along the line of sight

$$V_{max} = \sum_{f=1}^{N} \Omega \int_{r=d_{min}}^{d_{max}} \frac{\rho}{\rho_{\odot}} r^2.dr \tag{3.8}$$

where the summation is over all survey fields, and $\frac{\rho}{\rho_{\odot}}$ is the normalised density profile for the Galactic disk. This method for V_{max} follows that of Stobie et al. (1989), generalised to arbitrary Galactic latitudes by Tinney et al. (1993).

The low proper motion stars

Our low proper motion sample has lower proper motion limits that are piecewise functions of apparent magnitude in each field, and no simple expression (cf. Equation 3.6) for the corresponding distance limits can be derived. Indeed, if the lower limit changes rapidly with apparent magnitude there may even be several ranges of distance in which the star passes the survey limits. V_{max} must be calculated by integrating numerically along the line of sight between the magnitude distance limits (Equation 3.4), at each step evaluating whether the star passes the proper motion limits, which are calculated from the star's b_J magnitude at that distance. This leads to the integral

$$V_{max} = \sum_{f=1}^{N} \Omega \int_{r=d^m_{min}}^{d^m_{max}} \frac{\rho}{\rho_{\odot}} \quad \mathcal{P}(r) r^2.dr \tag{3.9}$$

where

$$\mathcal{P}(r) = \begin{cases} 1 & \text{if} \quad \mu_{min}(b_J(r)) \leq \frac{v_t}{4.74r} \leq \mu_{max} \\ 0 & \text{otherwise.} \end{cases}$$

Exponential density profiles

The density profile of disk stars in the solar neighbourhood is that of an exponential decay law in both perpendicular distance from the Galactic plane, and radial distance from the centre. The decay constants are called the scaleheight H and radial scalelength R_d, with H having a value of ≤ 100 to ~ 500pc depending on the spectral type and R_d about an order of magnitude larger.

As our stars are all within a few hundred parsecs, we expect to see no variation in density arising from the change in radial distance from the Galactic centre across the survey volume. However, the scaleheight has the effect of truncating the survey volume away from the Galactic plane, and will be observed given the distances involved in our survey. An appropriate form for $\frac{\rho}{\rho_\odot}$ is thus

$$\frac{\rho}{\rho_\odot} = \exp \frac{-|z_*|}{H} \tag{3.10}$$

$$= \exp \frac{-|r\sin(b) + z_\odot|}{H} \tag{3.11}$$

where b, r are the Galactic latitude and line of sight distance, and $z_\odot$ is the Galactic plane distance of the Sun.

Adopted $\mathbf{z_\odot}$ and H

We adopt a scaleheight of 250pc for the thin disk, which is in line with the result of Mendez and Guzman (1998) obtained for faint main sequence stars. These are likely of similar age to the white dwarfs in our catalogue and are expected to show a similar spatial distribution, having been subjected to the same kinematic heating. This is also the value used in most other studies of the white dwarf luminosity function, and thus allows more meaningful comparison with other works. There is some empirical evidence that the scaleheight of white dwarfs increases towards fainter magnitudes (see Harris et al., 2006) where the stars are on average older, but we ignore this here. Indeed, at the faintest magnitudes all observed white dwarfs are so close to the Sun that the chosen scaleheight makes very little difference.

The Solar distance from the Galactic plane, $z_{\odot}$, is often omitted in studies like this (e.g. Tinney et al., 1993), which is equivalent to setting its value equal to zero. However, the consensus of many star count investigations is that in fact $z_{\odot}$ lies close to $\sim$ 20pc (Reed, 2006). Therefore, we adopt this value in our density profile for the disk.

Corrections

Several steps in the compilation of our white dwarf catalogue have the side effect of excluding a fraction of target stars. We correct our density estimate for the ejected objects, under the assumption that the exclusion is uniform with luminosity and does not bias the survey towards bright/faint or blue/red stars. The fraction of stars that pass the lower tangential velocity threshold is called the *discovery fraction* and is usually denoted χ. It is calculated from the velocity ellipsoid and line of sight to the field in which the star was discovered, according to the method outlined in Appendix B. The contribution of each star to the total density is adjusted according to

$$\phi = \sum_{i=1}^{N} \frac{1}{\chi_i} \frac{1}{V_{max,i}} \tag{3.12}$$

A similar adjustment arises from the restriction on astrometric residuals. The fraction of stars that pass the cut can be calculated from the appropriate χ^2 distribution and the chosen threshold, and the correction is applied in an identical manner.

In order to account for the unknown H/He atmosphere types of cool white dwarfs, stars are allowed to contribute as *both* types, with a weight set by the probability of observing either type given the survey volume and relative luminosities. The contribution of each type to its respective luminosity function bin is multiplied by the appropriate ω_H/ω_{He} weight, calculated from the $b_J - r_{59F}$ colour according to Equation 2.9.

The $\langle \frac{\mathbf{V}}{\mathbf{V_{max}}} \rangle$ test

The $\frac{1}{V_{max}}$ method provides a useful statistic for checking the completeness of the sample. A complete catalogue has the property that objects are distributed uniformly within the observable survey volume V_{max} (provided that the correct density profile is used), and it follows that the statistic $\frac{V}{V_{max}}$ is drawn from $U[0,1]$. We therefore expect $\langle\frac{V}{V_{max}}\rangle = 0.5$, to within a statistical uncertainty of $\sigma = \frac{1}{\sqrt{12N}}$ for N objects.

For the 7315 stars in our low proper motion catalogue with $v_t > 30\text{kms}^{-1}$, $\langle\frac{V}{V_{max}}\rangle = 0.497 \pm 0.003$ and is consistent with being drawn from a complete sample. Note that the velocities used to define the subsamples drawn in this section are obtained from the full photometric parallax, rather than simply the reduced proper motion cuts. Also, stars are included if *either* their H or He atmosphere solution leads to a velocity that is included in the sample, and the weight for the corresponding atmosphere is non-zero.

The 1450 objects in our corresponding high proper motion catalogue show $\langle\frac{V}{V_{max}}\rangle = 0.532 \pm 0.008$, and would appear to be either incomplete (missing nearby stars) or contaminated by spurious objects masquerading as white dwarfs at large distances. We think the second explanation is correct, but that far from being spurious objects, the extra stars are in fact white dwarfs from an extended population that does not follow the 250pc decay of the thin disk. These objects would on average lie at large $\frac{V}{V_{max}}$. This would seem to be confirmed by the analysis of Section 3.3, which estimates that ~ 165 stars in the high proper motion catalogue are of spheroid origin.

3.2 The white dwarf luminosity function

In Figure 3.1 we present the luminosity functions measured for both the high and low proper motion catalogues, on adopting a 250pc scaleheight and minimum tangential velocity threshold of 30kms^{-1}. The high proper motion catalogue has fewer stars, but probes intrinsically fainter objects due to the large upper proper motion limit allowing nearby stars to enter the sample. This gives a better constraint on the luminosity function at fainter magnitudes around the peak and dropoff. The low proper motion catalogue contains objects of fainter *apparent* magnitude, due to relatively bright white dwarfs entering the sample at larger distances. This results in more uncertain photometric parallaxes, which is apparent in the wider horizontal errors bars on the low proper motion luminosity function. The structure in the luminosity function at the faint end is easily discernible - beyond the peak, there is a sharp drop off followed by a slow decline. Theory predicts that high mass white dwarfs cool faster than their normal mass counterparts, and, all other things being equal, fall in the region beyond the peak where the luminosity function for normal mass white dwarfs terminates. Good constraint in this region is vital for obtaining accurate age estimates, and the number of datapoints beyond the peak is encouraging. However, a quantitative analysis is only possible in conjunction with theoretical luminosity functions.

Figure 3.1(a) shows the effect on the luminosity function when the lower tangential velocity threshold is varied. Ideally, the discovery fraction of Section 3.1.2 corrects for the excluded stars and there would be no systematic difference. This is the case at brighter magnitudes, if we ignore random errors due to small number counts in a few bins. At the faint end, the $\mathrm{v}_t > 20\mathrm{kms}^{-1}$ luminosity functions rise slightly, indicating either over-correction due to an inappropriate velocity ellipsoid, or that contamination from subdwarfs is creeping in. As the $\mathrm{v}_t > 30, 40\mathrm{kms}^{-1}$ luminosity functions show agreement, we conclude that the $\mathrm{v}_t > 20\mathrm{kms}^{-1}$ sample is mildly contaminated by subdwarfs.

3.2.1 The luminosity function for high velocity white dwarfs

Any spheroid white dwarfs present in our catalogue may be identified by their large tangential velocities. Precisely how large a velocity is sufficient to reliably determine spheroid membership is a matter of some debate, as discussed in the following section. Figure 3.3 shows the tangential velocity distributions for the thin disk, thick disk and spheroid along the line of sight to one of our survey fields, as determined from M dwarfs and low metallicity stars (see Hawley et al., 1996; Chiba and Beers, 2000). A cut of $\mathrm{v}_t > 200\mathrm{kms}^{-1}$ is often considered to cleanly separate the spheroid and disk populations, and the luminosity function obtained on applying this cut to our catalogue is presented in Figure 3.4(a). The discovery fraction used to correct for the excluded low velocity stars is calculated from the spheroid velocity ellipsoid, and the density profile is that of a uniform population. The effect of varying the velocity threshold is investigated in

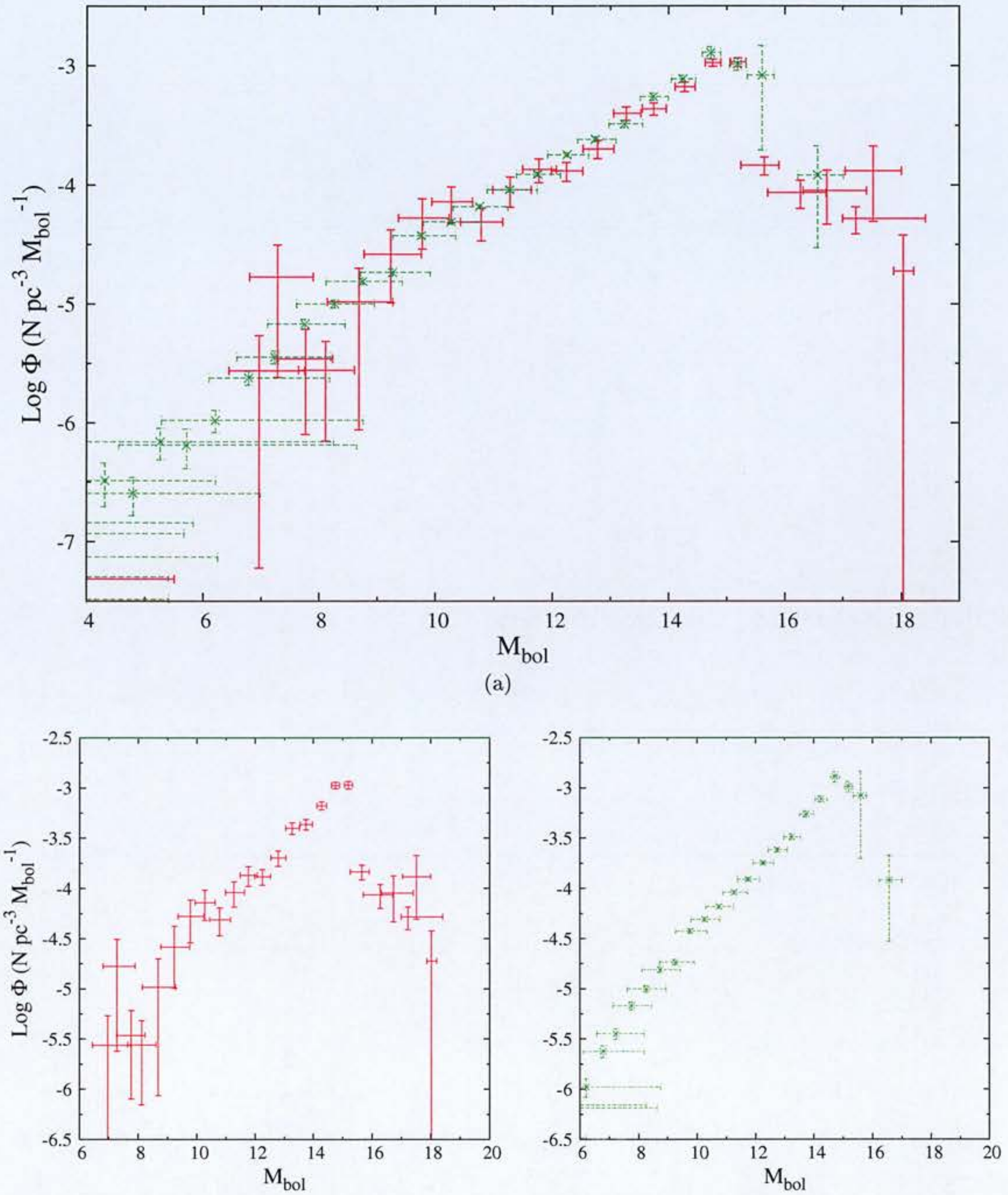

(a) (b) (c)

Figure 3.1: Luminosity functions for $v_t > 30\text{kms}^{-1}$ white dwarfs in the high (red points) and low (green points) proper motion surveys. Figures (b) and (c) show these separately for more clarity around the faint peak.

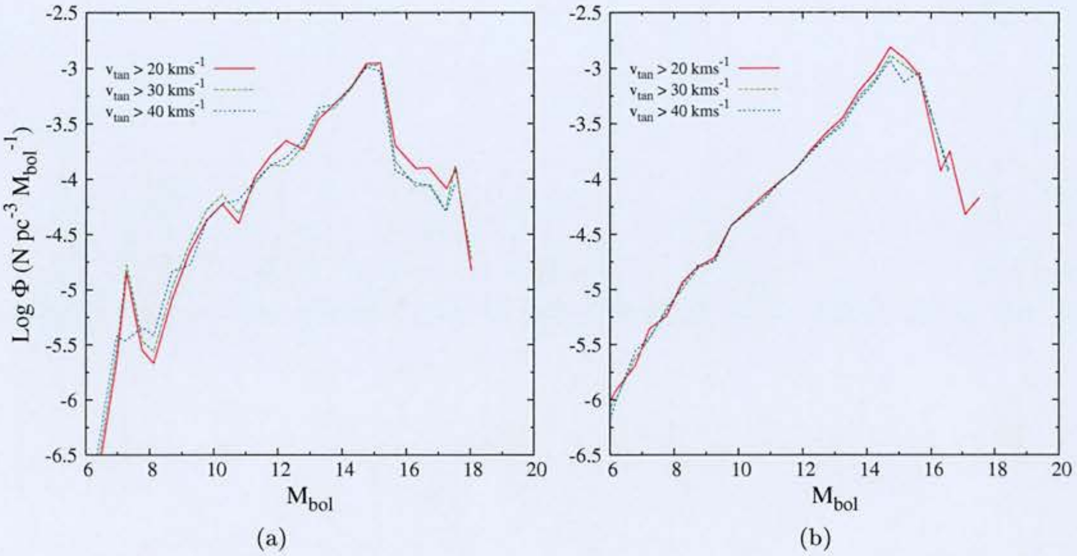

(a)

(b)

Figure 3.2: Luminosity functions for white dwarfs on adopting a range of lower tangential velocity cuts, for the high (a) and low (b) proper motion catalogues. The rise in the $v_t >$ 20kms^{-1} LF at faint magnitudes indicates that contamination from subdwarfs may be present, and that by $v_t > 30, 40$kms^{-1} this has disappeared.

Figure 3.4(b). The fact that the $v_t >$ 160kms^{-1} luminosity function sits at a slightly higher density suggests that there is some residual contamination from the disk even at these velocities.

The origin of the high velocity stars

Attributing individual stars to a particular kinematic population based on tangential velocity alone is tricky. The kinematic properties of cool white dwarfs are relatively uncertain, and it is possible that the high velocity tail of the disk population(s) overlaps considerably with the spheroid (see Reid, 2005). Ideally, radial velocities would complete the full 3D space motion in Galactic coordinates, allowing far better discrimination for individual stars. However, with only proper motions it is still possible to measure the *mean* motion in Galactic coordinates for the population as a whole, which is sufficient to distinguish a spheroid sample from one drawn from a rotating disk. This is done by deprojecting the proper motions, according to the method used by Dehnen and Binney (1998b) to analyse the kinematics of stars in the Hipparcos catalogue.

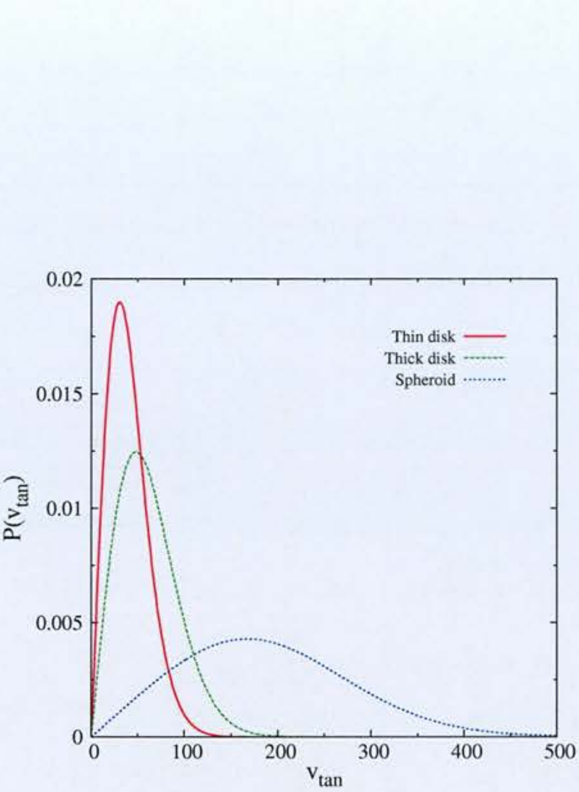

Figure 3.3: Tangential velocity distributions for the three major kinematic populations, along the line of sight to field 362 in the southern hemisphere. A cut of $v_t > 200\text{kms}^{-1}$ is often considered to cleanly separate the spheroid and disk populations.

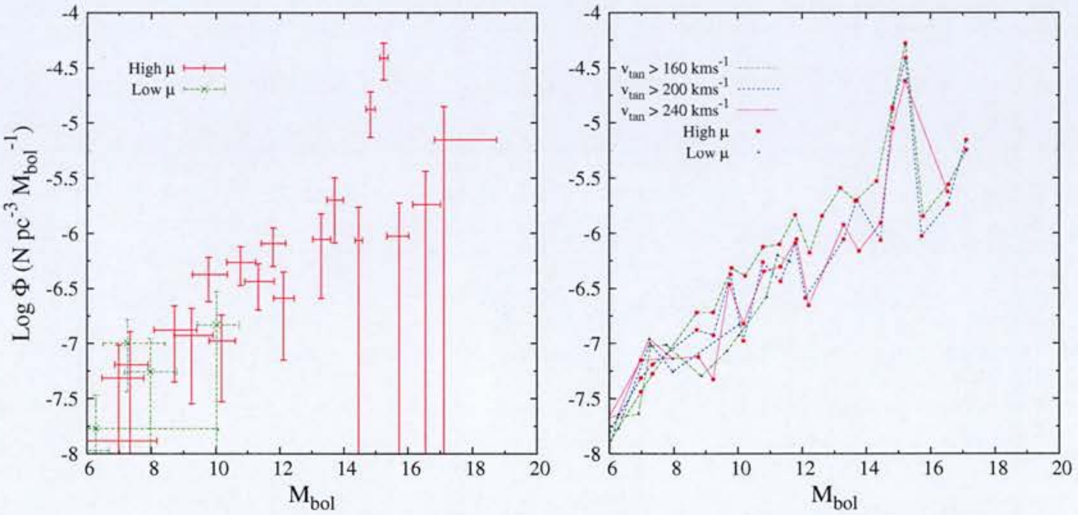

(a)

(b)

Figure 3.4: Luminosity functions for high tangential velocity white dwarfs. Figure (a) shows the LFs for $v_t > 200\text{kms}^{-1}$ stars in the high (red points) and low (green points) proper motion samples. Figure (b) compares the LFs obtained when the lower velocity limit is varied.

On doing so, we find that the 48 stars in the high proper motion catalogue with $v_t > 200\text{kms}^{-1}$ have $\langle UVW \rangle = (-51, -204, 12)$ kms^{-1}, and the 23 stars in the low proper motion catalogue have $\langle UVW \rangle = (-61, -162, -88)$ kms^{-1}. These would suggest that both samples are drawn from a non-rotating population, i.e. that of the spheroid. We therefore conclude that the luminosity function presented in Figure 3.4(a) is representative of the spheroid white dwarf population.

3.2.2 Local disk and spheroid white dwarf densities

Integrating the luminosity functions presented in Figures 3.1(b) and 3.1(c) give total local densities for white dwarfs in the solar neighbourhood of $(2.48 \pm 0.10) \times 10^{-3}\text{pc}^{-3}$ and $(2.88 \pm 0.34) \times 10^{-3}\text{pc}^{-3}$. A minimum variance combination of these obtains $(2.5 \pm 0.1) \times 10^{-3}\text{pc}^{-3}$

The spheroid white dwarf luminosity function of Figure 3.4(a) integrates out to $(3.4 \pm 0.9) \times 10^{-5}\text{pc}^{-3}$, resulting in a disk-to-spheroid ratio of 74 ± 20 disk stars to every spheroid star.

These densities are significantly lower than those obtained by other studies, e.g. Harris et al. (2006) find $4.6 \times 10^{-3}\text{pc}^{-3}$ and Leggett et al. (1998) find $3.4 \times 10^{-3}\text{pc}^{-3}$ for the local density of disk white dwarfs, and Harris et al. (2006) find $4 \times 10^{-5}\text{pc}^{-3}$ for those of the spheroid. If we recall from Sections 2.4.2 and 2.5, our catalogues may be up to 50% incomplete due to blended objects and those missed at first epoch r, which explains the disagreement between these numbers. This incompleteness is expected to be uniform with bolometric magnitude, and therefore will not affect the disk-to-spheroid ratio, nor will it affect any conclusions about the age of these two populations, as this is insensitive to the normalisation of the luminosity function.

3.3 Untangling the disk and spheroid

Section 3.2.1 indicates that white dwarfs from the Galactic spheroid are present in our catalogue, albeit in smaller numbers than those of the disk. As chemical tagging is not possible for white dwarfs, due to any photospheric metals sinking rapidly below the envelope, the only way to distinguish disk and halo stars is on their kinematics. Spheroid stars have, on average, much larger space velocities than disk stars, and as this population has no angular momentum about the Galactic centre they usually show a large rotational lag behind the local standard of rest. Working in projection, their high space velocities translate into mean tangential velocities much larger than disk stars, although the two populations overlap considerably at low speeds (cf. Figure 3.3). Velocities of $\sim 200\mathrm{kms}^{-1}$ are often used to separate a clean sample of spheroid stars from a mixed catalogue. Of course, the drawback of this approach is that many spheroid stars are thrown out with the disk stars, at tangential velocities where the two populations overlap. A spheroid luminosity function measured from a sample of stars drawn in this manner thus wastes lots of good information.

An alternative approach, one that avoids the use of severe tangential velocity cuts, is based on modelling the survey volume for each of the two populations. Varying the survey limits alters both the number of stars that are found and the sampled survey volume for each of the two populations. By using the change in the number of stars in conjunction with the change in the survey volume, it is possible to solve for the local number density of each population in a weighted least squares manner. This method is best described by considering how the two populations contribute stars to the survey. The total number of survey stars, N_*, is determined by the local number density multiplied by the sampled volume of space, separately for the two populations,

$$N_* = n_{disc} \times V_{disc} + n_{sph.} \times V_{sph.} \tag{3.13}$$

In a narrow range of magnitude, such as one of our luminosity function bins, the factor that determines V for each of the two populations is the tangential velocity distribution combined with the survey proper motion and tangential velocity limits. The magnitude limits are effectively decoupled from the analysis, because stars belonging to each population have identical absolute magnitudes over the small ranges considered. The kinematics differ considerably however, and for equal survey limits each population will be sampled over a different volume of space. By varying the survey tangential velocity limit, and recalculating V_{disc} and $V_{sph.}$ for the new N_*, a set of linear equations in the two unknowns n_{thin} and $n_{sph.}$ can be generated. In general, the equation set is non-singular and solvable by weighted least squares.

The power of this approach lies in the fact that individual stars are not assigned conclusively to either population. Instead, it simply measures the fraction of stars that belong to each population, as a function of v_t. Note that we will refer to this method further on as a 'two component decomposition' in order to distinguish it from the conventional $\frac{1}{V_{max}}$ approach.

3.3.1 Modelling $\mathbf{V_{disc}}$ and $\mathbf{V_{sph.}}$

The survey volumes used in this analysis are calculated in a rather different manner to V_{max} from Section 3.1.2. This is because neither the absolute magnitude nor tangential velocity are directly observed from the survey objects. Rather, the absolute magnitude is now the average for all stars in the LF bin (under the assumption that the LF is flat over the width of the bin), and we marginalise over the tangential velocity to obtain the volume for all stars that pass the v_t and μ limits.

The procedure for doing this is as follows. First, the mean absolute magnitudes of white dwarfs in each luminosity function bin are found by integrating synthetic $M(M_{bol})$ relations over the width of the bin. We use a standard $\log(g) = 8.0$ hydrogen rich model for this, and obtain the mean absolute magnitudes in each of the four SuperCOSMOS bands. These are then used in conjunction with the apparent magnitude limits in each survey field to place limits on the distance at which this hypothetical star could lie and still pass the magnitude limits. These are found according to

$$\begin{aligned} d^m_{max} &= \min\left(10^{\frac{b_{J,max}-\langle B_J\rangle}{5}}, 10^{\frac{r_{59F,max}-\langle R_{59F}\rangle}{5}}, 10^{\frac{r_{63F,max}-\langle R_{63F}\rangle}{5}}, 10^{\frac{i_{N,max}-\langle I_N\rangle}{5}}\right) \\ d^m_{min} &= \max\left(10^{\frac{b_{J,min}-\langle B_J\rangle}{5}}, 10^{\frac{r_{59F,min}-\langle R_{59F}\rangle}{5}}, 10^{\frac{r_{63F,min}-\langle R_{63F}\rangle}{5}}, 10^{\frac{i_{N,min}-\langle I_N\rangle}{5}}\right) \end{aligned}$$

We now compute the effective survey volume contained between these limits, under the assumption that the star belongs to each of the two populations, i.e. using the appropriate density profile to correct the disk volume for the scaleheight effect, and the appropriate velocity ellipsoid to correct for the fraction of recovered stars. The computation of the total survey volume is thus

$$V = \sum_{f=1}^{N} \Omega \int_{r=d^m_{min}}^{d^m_{max}} \frac{\rho}{\rho_\odot} r^2 \quad \chi(r).dr \tag{3.14}$$

where $\chi(r)$ is the *discovery fraction* of stars that pass the proper motion limits at distance r, and is calculated from the cumulative tangential velocity distribution by

$$\chi(r) = \begin{cases} \mathrm{cdf}(4.74\,\mu_{max}\,r) - \mathrm{cdf}(4.74\,\mu_{min}\,r) & \text{if} \quad 4.74\,\mu_{min}\,r \geq v_{min} \\ \mathrm{cdf}(4.74\,\mu_{max}\,r) - \mathrm{cdf}(v_{min}) & \text{otherwise} \end{cases}$$

The factor $\frac{\rho}{\rho_\odot}$ is the normalised stellar density profile, and is an exponential decay in $|z|$ in the case of the disk (cf. Section 3.1.2) and uniform (= 1) for the spheroid.

3.3.2 Solution for $\mathbf{n_{disk}}$ and $\mathbf{n_{sph}}$ by least squares

Adjusting v_{min} enables us to generate several instances of Equation 3.13, which can be used to solve for the unknowns. Investigations indicate that a suitable range of values is from 30 to 100kms^{-1} in steps of roughly 10-20kms^{-1}, then up to 200kms^{-1} in steps of ~50kms^{-1}, thus evenly sampling the range over which the relative contributions of each population change rapidly, and probing the region of pure spheroid stars at the extreme. The set of equations can be cast in matrix form like

$$\begin{bmatrix} V_{disc}(v_t > v_1) & V_{sph.}(v_t > v_1) \\ V_{disc}(v_t > v_2) & V_{sph.}(v_t > v_2) \\ V_{disc}(v_t > v_3) & V_{sph.}(v_t > v_3) \\ \vdots & \vdots \\ V_{disc}(v_t > v_m) & V_{sph.}(v_t > v_m) \end{bmatrix} \begin{bmatrix} n_{disk} \\ n_{sph.} \end{bmatrix} = \begin{bmatrix} N_*(v_t > v_1) \\ N_*(v_t > v_2) \\ N_*(v_t > v_3) \\ \vdots \\ N_*(v_t > v_m) \end{bmatrix} \tag{3.15}$$

where $v_{1,2,3...}$ are the chosen lower tangential velocity cuts. In short hand,

$$V\mathbf{n} = \mathbf{N} \tag{3.16}$$

The weighted least squares solution for $\mathbf{n}$, denoted $\hat{\mathbf{n}}$, is given by

$$\hat{\mathbf{n}} = (V^\dagger W V)^{-1}(V^\dagger W N) \tag{3.17}$$

where † denotes the matrix transpose (Martin, 1971). W is the matrix of weights, which we set according to

$$W = \begin{bmatrix} \frac{1}{\sigma^2_{N_1}} & 0 & 0 & \cdots & 0 \\ 0 & \frac{1}{\sigma^2_{N_2}} & 0 & & \\ 0 & 0 & \frac{1}{\sigma^2_{N_3}} & & \\ \vdots & & & \ddots & \\ 0 & & & & \frac{1}{\sigma^2_{N_m}} \end{bmatrix} \tag{3.18}$$

i.e. inverse variance weights, adopting Poisson statistics to estimate the noise on the observed number counts. The uncertainties on $\hat{\mathbf{n}}$ are obtained from the variance-covariance matrix $\mathcal{V}$ calculated

$$\mathcal{V} = (V^\dagger W V)^{-1} \tag{3.19}$$

and we adopt these as the formal uncertainties on the luminosity function points.

3.3.3 The disk and spheroid luminosity functions

The luminosity functions obtained on applying this technique to our white dwarf catalogues are presented in Figures 3.5(a) and 3.5(b), for the high and low proper motion samples respectively. The high proper motion luminosity functions show very good agreement with those obtained by conventional $\frac{1}{V_{max}}$ methods. The spheroid luminosity function in particular agrees on almost all datapoints to within the errors (Figure 3.6(b)), and has considerably smaller uncertainties due to the fact that low velocity stars are included in the density estimate. The sharp peak observed at $M_{bol} = 15.25$ appears to be confirmed by this analysis, and is the only structure in an otherwise monotonic rise towards fainter magnitudes. This will be an important feature when interpreting this luminosity function in terms of the age of the spheroid. The disk luminosity function deviates slightly over the mid luminosity range (Figure 3.6(a)), which could be due simply to statistical fluctuation, or to the fact that the $\frac{1}{V_{max}}$ luminosity function includes all spheroid stars and therefore is not a true representation of the disk. Nevertheless, the agreement is very good, and it is interesting to note that the peak of the luminosity function is adjusted slightly by the removal of a relatively large group of spheroid

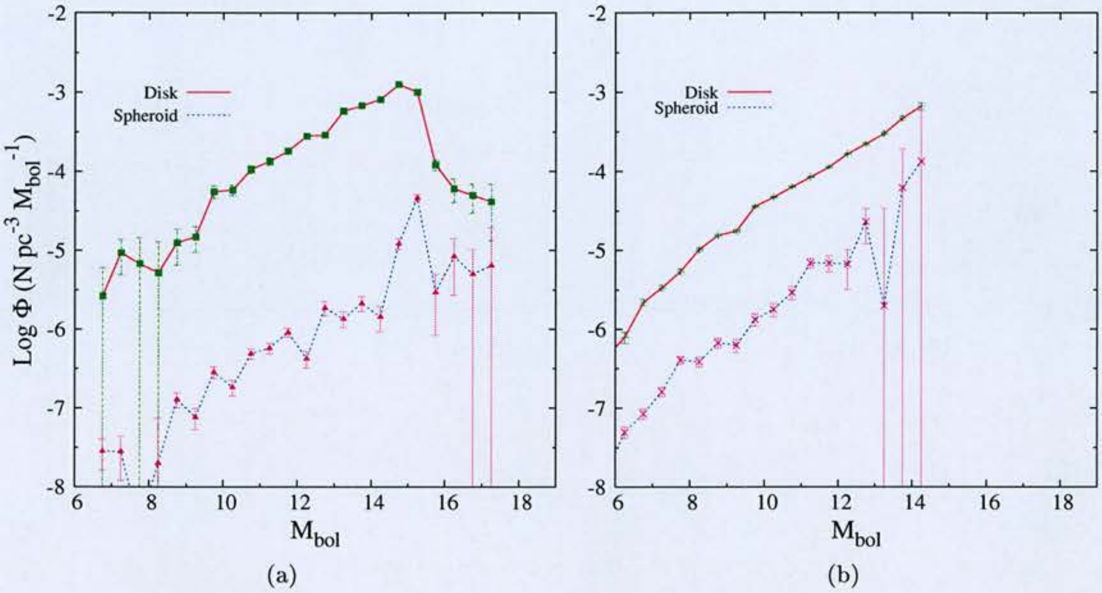

(a) (b)

Figure 3.5: Luminosity functions for the disk and spheroid in the high (a) and low (b) proper motion surveys, obtained by applying the two component decomposition technique described in the preceeding section.

stars that lie at the same luminosity. This may be of significance when comparing to theoretical luminosity functions.

In contrast, the low proper motion sample fails to obtain a reliable measurement of the spheroid luminosity function. This is perhaps unsurprising, as in light of Figures 2.14(b) and 3.3 any spheroid stars in the sample will be present at tangential velocities where they are heavily outnumbered by disk stars, and the small excess in the number counts at high v_t due to the spheroid component will be swamped by noise in the disk counts. Fainter than $M_{bol} = 13$ the uncertainty on $n_{sph.}$ is very large, due to the small survey volume for spheroid stars, and beyond $M_{bol} = 14.25$ the method fails altogether as the solutions for $n_{sph.}$ become negative. Although there appears to be good constraint at higher luminosities, the function deviates significantly from that obtained by either $\frac{1}{V_{max}}$ or this approach applied to the high proper motion sample. Our two component decomposition will generally be sensitive to whatever kinematic components are present, and we suspect that in the absence of significant numbers of spheroid stars, we are measuring instead an intermediate population between that of

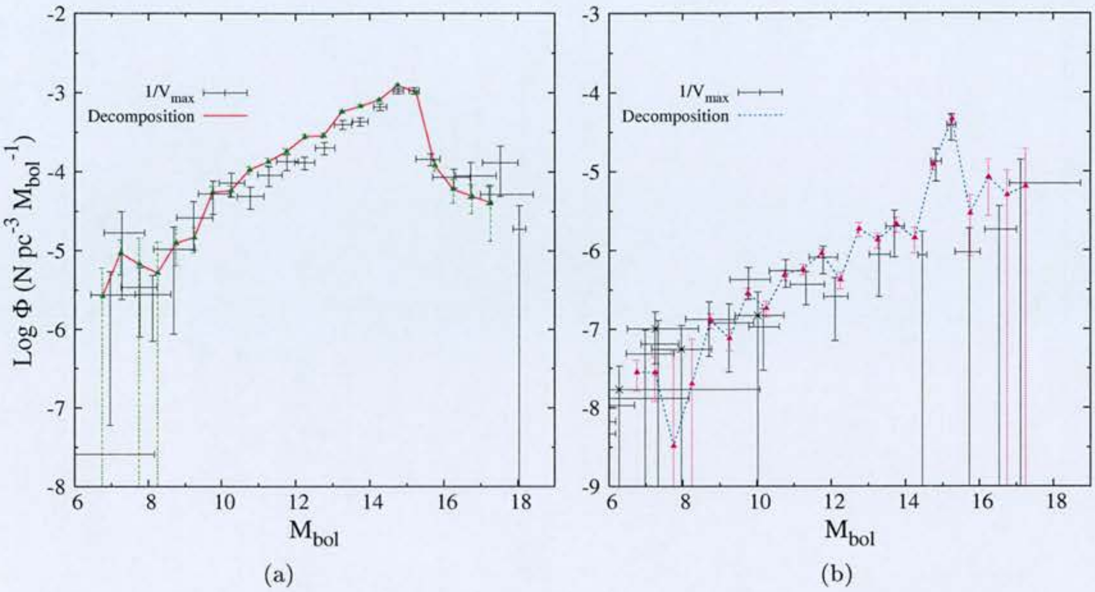

Figure 3.6: Comparison of luminosity functions for the disk (a) and spheroid (b) obtained from the high proper motion sample using both conventional $\frac{1}{V_{max}}$ and two component decomposition techniques.

the thin disk and spheroid, i.e. the thick disk. However, we repeated this analysis using thick disk parameters in place of the spheroid, and obtained very noisy results. This may indicate that the density profile and velocity ellipsoid we have adopted are not suitable for the white dwarf component of the thick disk (being closer to those of the spheroid), or that they are not present in sufficient numbers to be distinguishable from noise in the thin disk number counts. The disk luminosity function is therefore also unreliable, as the measured densities of the two components are coupled in the analysis.

3.4 Comparison to other works

The most directly comparable white dwarf luminosity function to this study, in terms of number of stars and survey technique, is that of Harris et al. (2006). These authors used proper motions derived from a combination of SDSS and USNO-B astrometry to obtain a sample of 6000 white dwarfs with $v_t > 30\text{kms}^{-1}$, with photometric parallaxes obtained from superior 5 band SDSS photometry. Their disk luminosity function is shown in Figure 3.7(a), alongside our own reproduced from Figure 3.1(a). Ignoring the vertical offset, which is due to the incompleteness of our sample discussed in Section 3.2.2, these functions agree very well. They agree on the location and depth of the drop off in the disk luminosity function, and on the slope at brighter magnitudes. This lends credence to our faintest luminosity function bins, which lie in a region that has not been probed before.

The spheroid luminosity function measured by Harris et al. (2006) is reproduced in Figure 3.7(b), alongside our own from Figure 3.5(a). Again these show good agreement on both the slope of the luminosity function and the location of the single notable feature - the sharp peak at $M_{bol} = 15$. Again, this would suggest that our fainter luminosity function bins are reliable.

3.5 Summary

Using our catalogue of 8765 white dwarfs with $v_t > 30\text{kms}^{-1}$, we have measured both the disk and spheroid luminosity functions to the faintest limits thus far obtained. These reach deeper than the next deepest study by 1.5 and 2.5 magnitudes respectively, due to our large survey volume for faint and high velocity stars, and the inclusion of most known ultracool white dwarfs. The downturn in the disk luminosity function at faint magnitudes is clearly resolved, and its location at $M_{bol} = 15.75$ is now surely a secure result. Structure in the spheroid luminosity function has been revealed by the extended depth of our study, and the sharp peak observed at $M_{bol} \sim 15$ will provide useful constraint on the age by anchoring theoretical luminosity functions. The sample of spheroid white dwarfs has been confirmed as such by their large tangential velocities and lack of a net rotation about the Galactic centre.

We have introduced a new technique for decomposing the luminosity function derived from a single mixed catalogue of stars into the contributions from each kinematic component separately. We have used this to obtain a spheroid luminosity function with greater accuracy than the conventional $\frac{1}{V_{max}}$ approach, due to the inclusion of low velocity spheroid stars in the density estimate. This technique relies rather heavily on

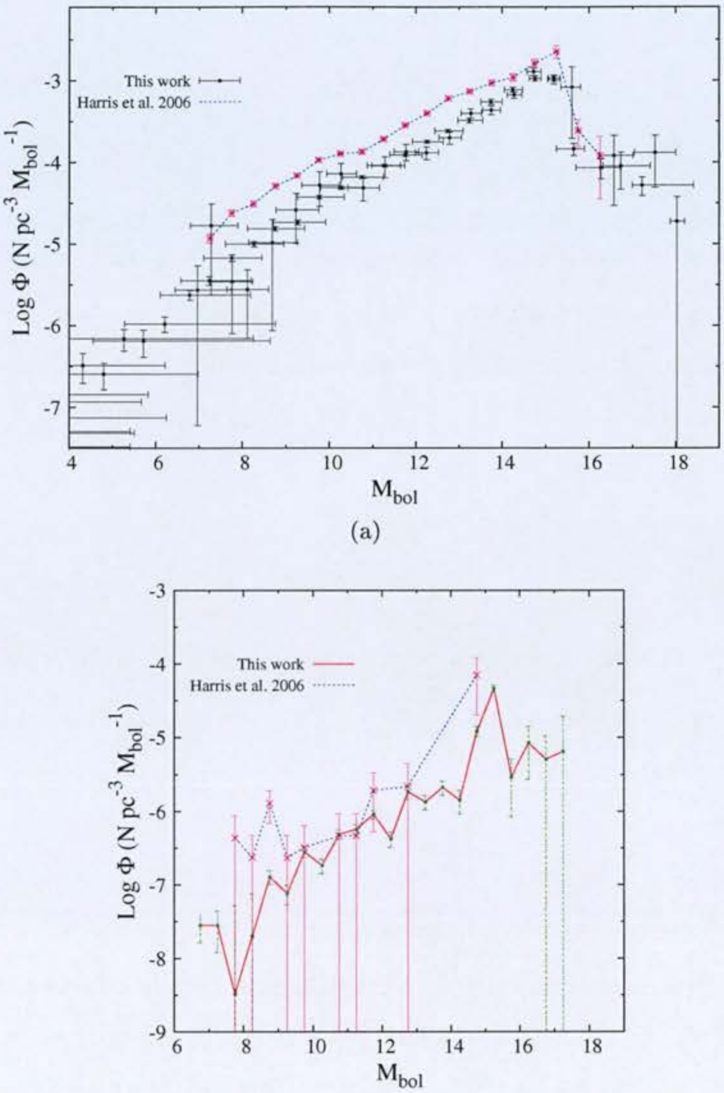

(a)

(b)

Figure 3.7: Comparison of the luminosity functions derived in this work with those of Harris et al. (2006). Figure (a) compares their $v_t > 30\text{kms}^{-1}$ luminosity function with ours obtained from both the high and low proper motion samples by conventional $\frac{1}{V_{max}}$ means. Figure (b) shows the Harris et al. (2006) luminosity function for white dwarfs with $v_t > 200\text{kms}^{-1}$, as well as our spheroid luminosity function measured from the high proper motion sample using the two component decomposition method.

knowing the density profile and velocity ellipsoid *a priori*, and the failure to obtain a thick disk luminsity function could be due to the uncertain properties of thick disk white dwarfs, or that they are simply too similar to their thin disk counterparts to prise these populations apart with $\sim 9,000$ stars.

The incompleteness of our catalogue gives rise to a vertical offset between our luminosity functions and those derived by other authors, and the integrated densities of $\sim 2.5 \times 10^{-3}\mathrm{pc}^{-1}$ are therefore underestimated by up to 50%. However, age estimates based on the luminosity function are insensitive to the normalisation, and the disk-to-spheroid ratio of ~ 70 is likewise unaffected.

CHAPTER 4

White Dwarf Cosmochronology of the Galactic Disk and Spheroid

The potential use of white dwarfs as chronometers was first recognised by Maarten Schmidt (Schmidt, 1959), who noted that basic cooling theory predicted a shortfall of stars at cooling times equal to the age of the Galaxy. Since then, much progress has been made on both the theoretical and observational fronts, and the cosmochronology of stellar populations using their white dwarf members is now an established field. In this chapter, I investigate the age of the Galactic disk and spheroid by applying the techniques of white dwarf cosmochronology to the catalogue of white dwarfs derived from the SuperCOSMOS Sky Survey.

4.1 Introduction

White dwarfs are typically much fainter than the main sequence turn off, especially the coolest objects that are vital for accurate age determination. They are also far less numerous. For example, in an 8 Gyr population the overwhelming majority of stars - all those less massive than $\sim 1.1M_{\odot}$ - are still on the main sequence. As such, they would not seem like an obvious choice for cosmochronology from either an observational or statistical point of view. However, white dwarfs are insensitive to several sources of random and systematic error that plague ages based on the main sequence turn off method. White dwarf age estimates have only a very weak dependency on the metallicity, the distance modulus (for clusters), and in particular the treatment of convection in the progenitor stars, which is currently the largest source of uncertainty in main sequence ages. The point is that for most populations, the cool white dwarfs are the remnants of high mass stars with relatively very short main sequence lifetimes, and the evolution of such objects is completely dominated by the white dwarf cooling phase. The existing sources of uncertainty, beyond the observational, are mainly systematic and arise from the detailed physics of white dwarf evolution, including the chemical abundance profile of the core at birth, the convective coupling of the outer layers and degenerate core during the late stages, and the spectral evolution of white dwarfs with unknown envelope thickness. Indeed, recent advances in evolutionary models have revealed the cooling of white dwarfs to be not quite the 'simple' process it was once considered. In a thorough review of the topic, Fontaine et al. (2001) note that the physics of white dwarf evolution is considerably more complex, and therefore more uncertain, than for main sequence and giant star evolution. As a result, white dwarf based age estimates are unlikely to yield measurements more accurate than those derived from main sequence stars or other methods until some of these problems are addressed, either by observation (e.g. asteroseismology to measure envelope layer thickness) or theory (e.g. improvements on the $C^{12}(\alpha,\gamma)O^{16}$ reaction rate to constrain the initial core composition). At present, it is the comparison of this approach with others that is providing the most interesting results - see Section 1.4.1 for some examples from the literature.

4.2 Theoretical luminosity functions

The white dwarf luminosity function (WDLF) is the standard diagnostic tool for investigating the star formation history of a stellar population based on its degenerate component. The WDLF is an evolving function of time, with a precise morphology determined by a number of important inputs. Several authors have investigated methods for modelling the WDLF, including Winget et al. (1987) who used their models in conjunction with an observed WDLF derived from the LHS catalogue to obtain the first estimate of the age of the Galaxy using this method. However, their models assumed a constant rate of white dwarf production, and obtained the white dwarf mass distribution as a function of magnitude by evolving the present-day mass distribution for hot white dwarfs to faint magnitudes. They then added the cooling time of their faintest populated LF bin to the main sequence lifetime for the mean mass in this bin to obtain their estimate of the disk age. Although a groundbreaking study, the method of Winget et al. (1987) was criticised for failing to take into account mass-dependent progenitor lifetimes, which will affect both the rate of white dwarf production and the mass distribution of newly forming white dwarfs, both of which evolve over time for a given rate of main sequence star production.

A holistic approach was laid down by Iben and Laughlin (1989), who included the past rate of star formation, the initial mass function and the relation between the progenitor and white dwarf mass (initial-final mass relation) explicitly in the models. This revealed structure in the WDLF beyond the downturn, at magnitudes where high mass and helium atmosphere white dwarfs, which cool faster, tend to accumulate. A useful derivation of the Iben & Laughlin model was presented by Noh and Scalo (1990), who examined the WDLF with particular reference to the star formation history of the Milky Way, showing that it is more sensitive to changes in the rate of star production than changes in the initial mass function. We now reproduce the Noh & Scalo formula for the theoretical WDLF, with a couple of small changes;

$$n(M_{bol}) = \int\limits_{M=M_l}^{M_u} \frac{dt_{cool}}{dM_{bol}}[M_{bol}, m(M)]\, \psi[T_0 - t_{cool}(M_{bol}, m(M)) - t_{MS}(M, Z)]\, \phi[M]\, dM \tag{4.1}$$

The WDLF is parameterized in terms of the progenitor mass M, the white dwarf mass m, the star formation rate $\psi(t)$ as a function of time, and the initial mass function $\phi(M)$. t_{cool} refers to the time taken for a white dwarf of mass m to cool to bolometric magnitude M_{bol}. The cooling *rates* are also an important input, and here $\frac{dt_{cool}}{dM_{bol}}$ is taken inside the integral as it is a function of the white dwarf mass, and hence progenitor mass. t_{MS} is the total pre-WD evolutionary time for progenitors of mass M, and we include the metallicity Z here as we are interested in modelling the low-metallicity spheroid. Finally, T_0 is the age of the stellar population, or more correctly, the time since the onset of major star formation.

The integral is over the progenitor mass, from the highest mass star capable of producing a white dwarf, to the lowest mass star that has had time to contribute a white dwarf of the given bolometric magnitude. The quantity $T_0 - t_{cool}(M_{bol}, m(M)) - t_{MS}(M, Z)$ is simply the time after the onset of star formation that progenitors of mass M must form in order to produce white dwarfs of magnitude M_{bol}, and M_l is calculated by solving the equation

$$T_0 - t_{cool}(M_{bol}, m(M_l)) - t_{MS}(M_l, Z) = 0 \tag{4.2}$$

i.e. stars of mass M_l would have to have formed at t=0 in order to have had time to complete their main sequence evolution and cool as white dwarfs to magnitude M_{bol}. Stars with masses lower than M_l have not had time to contribute white dwarfs of magnitude M_{bol}, and are not included in the integral.

4.2.1 Forward modelling the luminosity function

The integral equation presented in Equation 4.1 is of a general form encountered commonly across all branches of the physical sciences - namely, the data ($n(M_{bol})$) are the integral of some desired function (in this case the star formation rate, $\psi(t)$) multiplied by a known, or at least estimated, kernel (in this case, the initial mass function and WD cooling rates). The smoothing effect of the kernel causes information to be lost, which makes the *inverse problem*, that of obtaining the desired function from the data, ill-posed. This is particularly true when the data are discretely sampled, as is the case with our WDLF. Specifically, a given choice of model parameters ($\psi(t)$) results in a single solution for the observed data, while any given data set can generally be produced by a range of model parameters, and the inverse problem has no unique solution. Also, small changes in the data, such as those introduced by noise, may lead to large changes in the solution. While the literature on solving inverse problems is extensive, each distinct equation has its own pitfalls and method of solution, and a suitable technique for the WDLF has not been investigated. For the purposes of this study, I use the *forward modelling* approach, where a set of model parameters is adopted and used to model the data. The integrity of the adopted parameters can then be assessed by comparing the model to the observations. In the context of the WDLF, the model parameter(s) concern the star formation rate, which I parameterise in terms of the time since the onset of star formation and a particular time-dependent functional form. I also assume certain relations concerning white dwarf and main sequence evolutionary timescales, and other values relating to the kernel. All quantities adopted in modelling the luminosity function are described in the next few paragraphs.

The main sequence stars: lifetimes and mass

I use the stellar evolutionary tracks of Girardi et al. (2000) to provide total pre-white dwarf lifetimes for stars as a function of mass. The models extend from $0.15M_{\odot}$ to $7.0M_{\odot}$, in steps of $0.05M_{\odot}$ at low masses increasing to $1.0M_{\odot}$ towards the high mass end. I consider the pre-white dwarf phase to last from the zero age main sequence to either the first thermal pulse or the onset of carbon burning, depending on mass. For low mass stars I include the time spent on the horizontal branch. I adopt the mass of the most massive model, $7.0M_{\odot}$, as the maximum mass for white dwarf formation. This forms the upper integration limit for all of my models. The lower mass limit varies, as described previously, but never falls below $0.6M_{\odot}$ for the range of population ages considered.

The main sequence stars: metallicity

The Girardi et al. (2000) models are computed for a number of different metallicities, and for the disk models we adopt a constant value of $Z = 0.019$, i.e. solar metallicity. For the spheroid, I adopt the value $Z = 0.001$ used by the TRILEGAL population synthesis code (Girardi et al., 2005), which is based on the same stellar models. This value is derived from an [Fe/H] of -1.6, with an α enhancement of 0.3 dex.

The white dwarfs: masses

The initial-final mass relation (IFMR) is constrained observationally using a handful of nearby binaries and star clusters, where the masses of recently formed WDs are compared to those of the most massive stars still on the main sequence. Open clusters supply points at progenitor masses above $\sim 1M_{\odot}$ (Weidemann, 2000); a single point at $0.8M_{\odot}$ is contributed by the globular cluster M4 (Kalirai et al., 2009). The existing data are well fitted within the uncertainties by a straight line, and here I adopt the linear fit of Kalirai et al., which includes the globular cluster point at low mass:

$$m_f = 0.101 m_i + 0.463 \tag{4.3}$$

It is worth pointing out that below $m_i \sim 0.52M_{\odot}$ this relation returns a final WD mass greater than the initial MS mass, and therefore breaks down. However, stars of this mass have main sequence lifetimes well in excess of the age of the universe, and do not contribute white dwarfs to any of the theoretical luminosity functions.

The white dwarfs: cooling times and atmosphere type

I use the white dwarf evolutionary models of Pierre Bergeron to provide cooling tracks as a function of mass. These are based on the same code as those used in Chapters 2 and 3, and again were provided in the SuperCOSMOS bands by Dr. Bergeron on request. The H/He atmosphere type has a strong effect on the cooling age at a given magnitude, altering the morphology of the luminosity function at the faint end where the difference is greatest. In order to include both atmosphere types, I synthesise luminosity functions for pure H and pure He white dwarf populations, then obtain that for a mixed population by taking a weighted average of the two. I use a 50:50 ratio of hydrogen to helium atmospheres, identical to that used in Section 2.4.2 in the observational determination of the luminosity function.

The initial mass function

The initial mass function (IMF) is well determined over the range of masses of relevance to this study - namely, those main sequence stars that form white dwarfs within a Hubble time. I adopt the IMF of Kroupa (2001), which is a three segment power law with index -2.3 for masses larger than $0.5M_{\odot}$. This covers the entire range of interest.

The star formation rate

I consider three possibilities for the star formation rate (SFR): (1) a single burst of constant amplitude and duration 1 Gyr, (2) an exponentially decaying formation rate with a decay constant of 1 Gyr, and (3) a rate that is constant over the entire history of the population. These cover the main paradigms of star formation in the Galaxy, with the single burst model appropriate for the spheroid, and the exponentially decaying and constant rates two possibilities for the disk.

4.2.2 Method for solution

The main sequence lifetime at arbitrary mass is obtained by cubic spline interpolation within the range of available stellar models. The white dwarf cooling time at arbitrary mass and bolometric magnitude is obtained by bi-cubic spline interpolation within the two dimensional grid of cooling tracks. Equation 4.2 for the lower mass integration limit is transcendental, and is solved using an efficient interval-halving approach that rapidly converges on the unique solution. Figure 4.1 displays the solution for M_l graphically. The integral in Equation 4.1 is, of course, non-analytic, and must be solved by numerical means. I investigated two ways to do this. The first used a Monte Carlo method that involved simulating a population of stars endowed with properties (mass, formation time etc.) drawn from appropriate PDFs, and tracking their evolution over time via an object-based Java program. The second method was to directly solve the integral, using

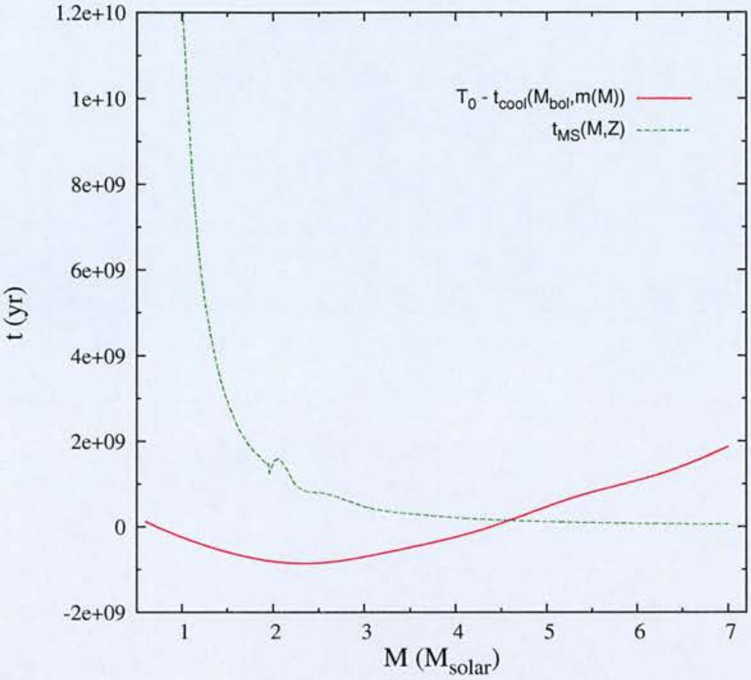

Figure 4.1: The solution to Equation 4.2 lies at the mass where $T_0 - t_{cool}(M_{bol}, m(M)) = t_{MS}(M, Z)$. The solution can be found to arbitrary precision using an interval-halving approach.

the trapezium rule with extrapolation to reduce higher order errors. The Monte Carlo approach avoids the need to solve Equation 4.2, but requires many more interpolations to evaluate each luminosity function. This proved to be very time consuming to compute to the necessary precision, and gave results that agreed well with the (considerably faster) trapezium method, so I adopted the trapezium method with extrapolation to solve the theoretical luminosity function integral.

4.2.3 Results

I present some representative examples of my theoretical luminosity functions. Figure 4.2 shows the solar-metallicity models appropriate for the Galactic disk, covering both constant and exponentially decaying star formation rates. These are normalised at $M_{bol} = 12$. The vertical scale is dimensionless, and will be calibrated to number density per magnitude on normalisation to the observed luminosity function. The constant SFR models are plotted at 0.5 Gyr intervals from 6-14 Gyrs; the exponentially

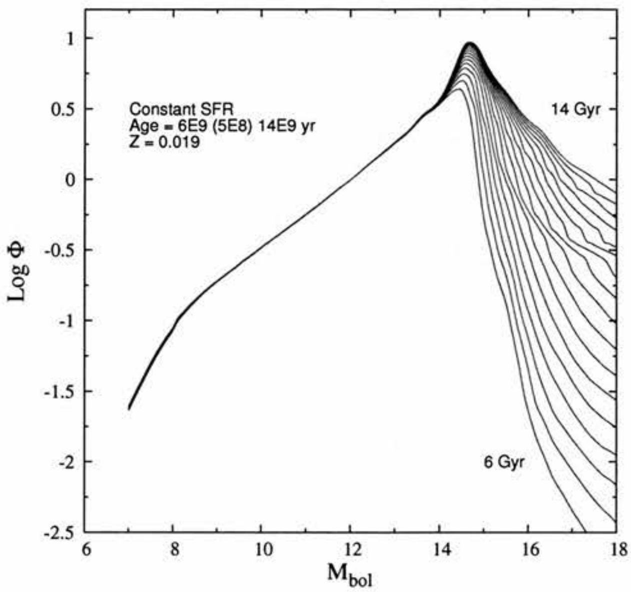

(a)

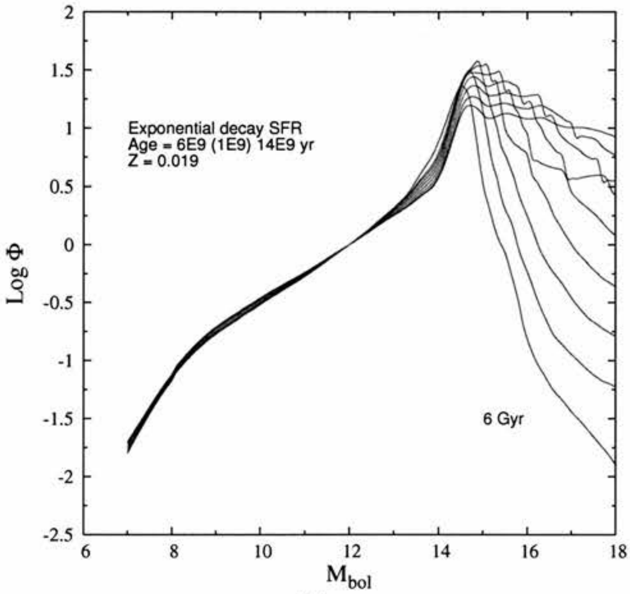

(b)

Figure 4.2: Theoretical luminosity functions for constant (a) and exponentially decaying (b) star formation rates, as described in text.

decaying models, which overlap more, are plotted every 1 Gyr. Figure 4.3 shows the low-metallicity, single burst models appropriate for the Galactic spheroid, plotted at 1 Gyr intervals from 6-16 Gyrs. It is evident from these plots that the slope of the

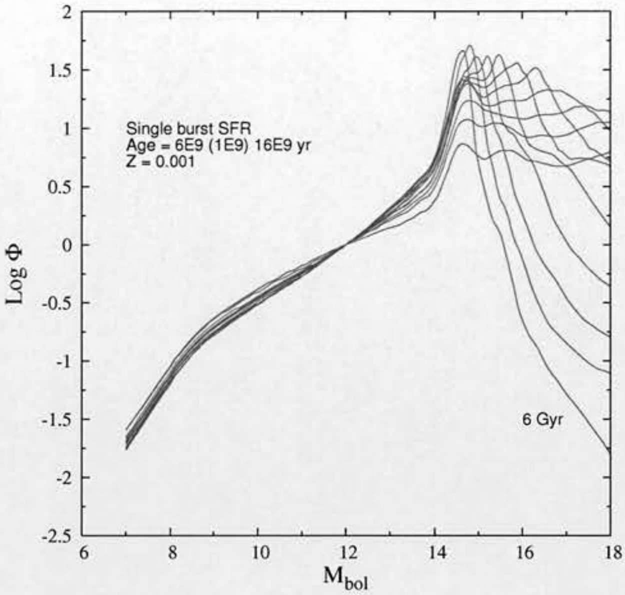

Figure 4.3: Theoretical luminosity functions for single burst star formation rate, as described in text.

luminosity function on the bright side of the peak is degenerate with age. This unfortunately means that all of the age constraint available in the observational luminosity function is at faint magnitudes, where the data are most uncertain. The sharp rise seen around $M_{bol} = 14$ in the theoretical luminosity functions coincides with the convective coupling of the photosphere and degenerate core, which slows the rate of cooling and causes white dwarfs to pile up in the fainter magnitude bins. This feature is somewhat less apparent in the constant star formation rate models, because the bright slope is constantly replenished with white dwarfs and the rise does not stand out as clearly.

The drop at faint magnitudes occurs when the cooling sequence for normal mass white dwarfs terminates. High mass white dwarfs cool faster and tend to populate the region beyond the peak, but in relatively low numbers due to their intrinsic rarity. The cooling of massive white dwarfs is very rapid once the core is fully crystallised, and leads to a flattening in the luminosity function at faint magnitudes.

A similar effect arises from the differing opacities of H and He atmospheres at faint magnitudes. The relative contributions of H and He atmosphere white dwarfs to the total luminosity function is presented in Figure 4.4. At moderate to high temperatures,

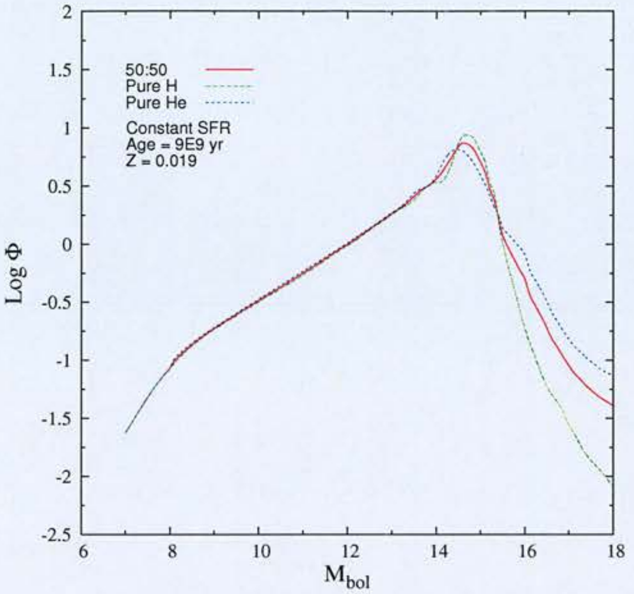

Figure 4.4: Relative contributions of H and He white dwarfs to the total luminosity function.

the bolometric magnitudes and cooling rates of these objects are almost identical, and very little difference is seen in the pure H and pure He luminosity functions. At lower temperatures, the formation of atmospheric H_2 molecules raises the opacity and slows the cooling rate of H white dwarfs relative to their He counterparts, causing a sharper drop off in the pure H luminosity function. As a result, He atmosphere white dwarfs dominate at the faintest magnitudes.

4.3 The age of the Galactic disk and halo

4.3.1 Weighting scheme and the star formation rate

A straightforward fit of these models to the data results in a large χ^2_ν statistic, due to structure in the bright luminosity function that is not reproduced in the models. In order to extract meaningful age estimates from the data, this discrepancy has to be understood and a suitable workaround devised. The inability of my theoretical LFs to synthesise short period features in the observed LF is, most likely, due to the simplistic model of the star formation history of the Galaxy. In the case of the disk, although a constant SFR is commonly assumed when modelling the WDLF, independent studies of the SFR using, for example, chromospheric age distributions (e.g. Rocha-Pinto et al., 2000) indicate an irregular rate characterised by a series of bursts and lulls of varying duration. The SFR can likely only be considered constant if the WDLF is insensitive to bursts shorter than several Gyr. Noh and Scalo (1990) investigated the effect of bursts on the morphology of the WDLF, finding that bursts of strength $\frac{\psi_{burst}-\psi_{quiescent}}{\psi_{quiescent}} = 10$ and duration 0.1 Gyr lead to features in the rising side of the WDLF of amplitude $\Delta \log \Phi \sim 0.3$ and width $\Delta M_{bol} \sim 1$. Bursts of this nature are consistent with the observed SFR of Rocha-Pinto et al. (2000) (given that their age resolution of 0.4 Gyr would tend to smooth over shorter duration bursts), and features fitting this description are indeed seen in both the disk and spheroid WDLFs. Interestingly, the study of Iben and Laughlin (1989) found that the shape of the WDLF at luminosities fainter than the peak is virtually independent of any changes in the SFR after the earliest epoch. This would suggest that the best way to extract an age estimate from the observed WDLF is to simply ignore the rising side altogether. However, this region is important for fixing the normalization of the model LF, and if disregarded completely in the fit results in a model that diverges wildly from the observations. Although the small scale structure in the observed LF brighter than the peak is not reproduced by the models, I expect the overall form to be correct. Therefore, I proceed by artificially inflating the error bars on the bright side of the peak, which reduces sensitivity to small scale irregularities in this region while maintaining a good overall fit. At the faint end, where the models are likely a true representation of the WDLF structure, I leave the errors alone in order to maximise the constraint.

4.3.2 Fitting technique and age estimates

The adopted forms for the observed disk and spheroid WDLFs are those of Section 3.3.3, Figure 3.5, derived from the high proper motion catalogue by means of the two population decomposition method. These were chosen because they are deeper than those from the low proper motion catalogue, and isolate the disk and spheroid populations more successfully than a simple tangential velocity cut. Theoretical WDLFs were generated at 100Myr intervals, and fitted in turn to the observed WDLFs using a

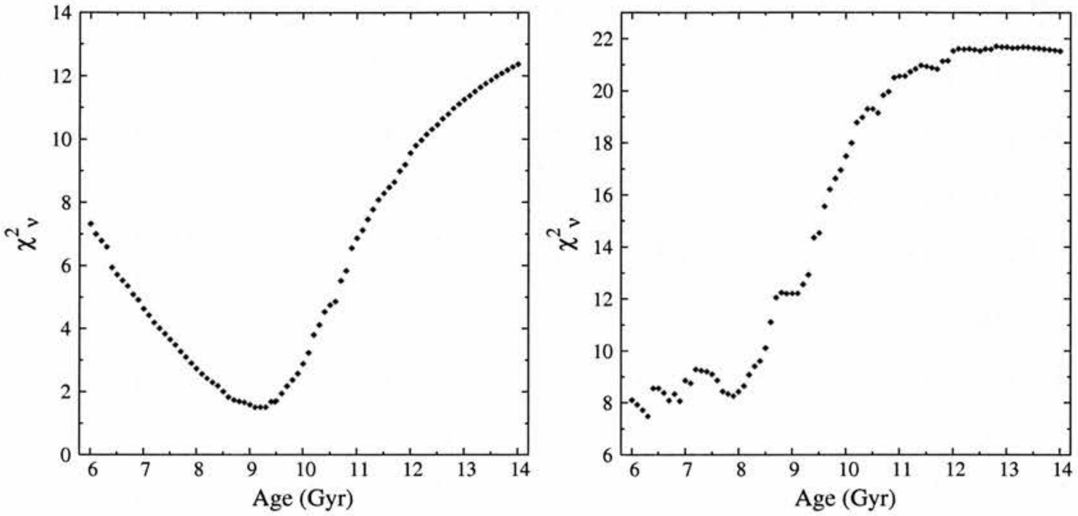

(a) (b)

Figure 4.5: Residuals for the fits of our $Z = 0.019$ models to the disk WDLF, for a constant (a) and exponentially decaying (b) SFR. A clear minimum is seen in (a); no such feature is apparent in (b), and an exponentially decaying SFR can be ruled out on this basis.

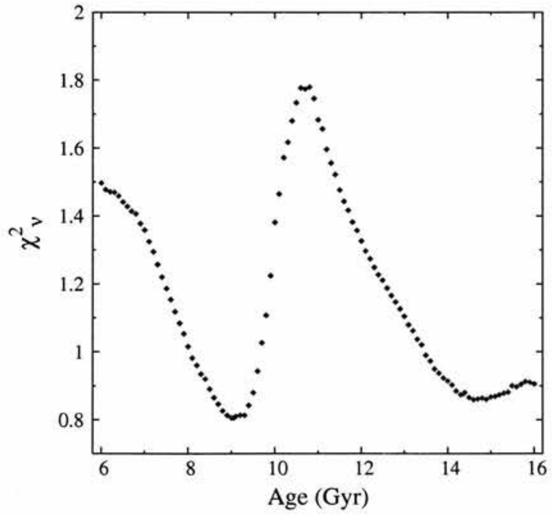

Figure 4.6: Residuals for the fits of our single burst, $Z = 0.001$ models to the spheroid WDLF. Two distinct minima are seen at roughly equal χ^2_ν.

minimum χ^2 approach. The errors on points brighter than $M_{bol} = 15.5$ were inflated by a factor 3, decreasing the (inverse-variance) weight assigned to these points by a factor 9. The distributions of reduced χ^2 for each of the two disk models are shown in Figure 4.5. It is clear that the assumption of a constant SFR is far more consistent with the data than an exponentially decaying rate, for which no convincing minimum in the (considerably larger) residuals is seen. I therefore adopt the constant SFR models for my investigation of the disk age, and proceed no further with the exponentially decaying models. The distribution of the residuals for the single-burst, low metallicity models fitted to the spheroid WDLF is shown in Figure 4.6. Two distinct minima with roughly equal χ^2_ν are seen, indicating a degeneracy in the age estimate. This is investigated further later on.

The best fitting ages are obtained by interpolating the residuals around the minima using cubic polynomials, and 68% confidence regions are assigned using $\Delta\chi^2 = 2.3$ for my two parameter models (normalisation and age). For the disk, I find a best fit age of $9.13^{+0.27}_{-0.29}$ Gyr for a constant SFR - but see below for the inclusion of systematic errors. A plot of this fit is shown in Figure 4.7. In the case of the spheroid, I treat each minima separately and obtain ages of $9.08^{+0.45}_{-0.64}$ Gyr and $14.8^{\geq 1.2}_{-1.2}$ Gyr. Note that no upper age limit on the old spheroid solution is found within the range considered. Older than ~ 16 Gyr, the models start to break down as certain evolutionary tracks have to be extrapolated beyond their computed range. The fits of these models to the data are shown in Figure 4.8. It is clear that the age degeneracy arises from the uncertain status of the faintest WDLF points. Although the young solution fits the peak of the WDLF better than the old solution, it should be born in mind that this region may still contain the signatures of starbursts ocurring after the intitial epoch of formation.

4.3.3 Systematic errors

The errors on the age estimates quoted in the previous Section are simply the statistical uncertainties in the fits of our luminosity function models to the data. As is well known (see Section 1.3.3), white dwarf based age estimates are subject to a number of systematic errors that must be considered. The thickness of the hydrogen layer is one

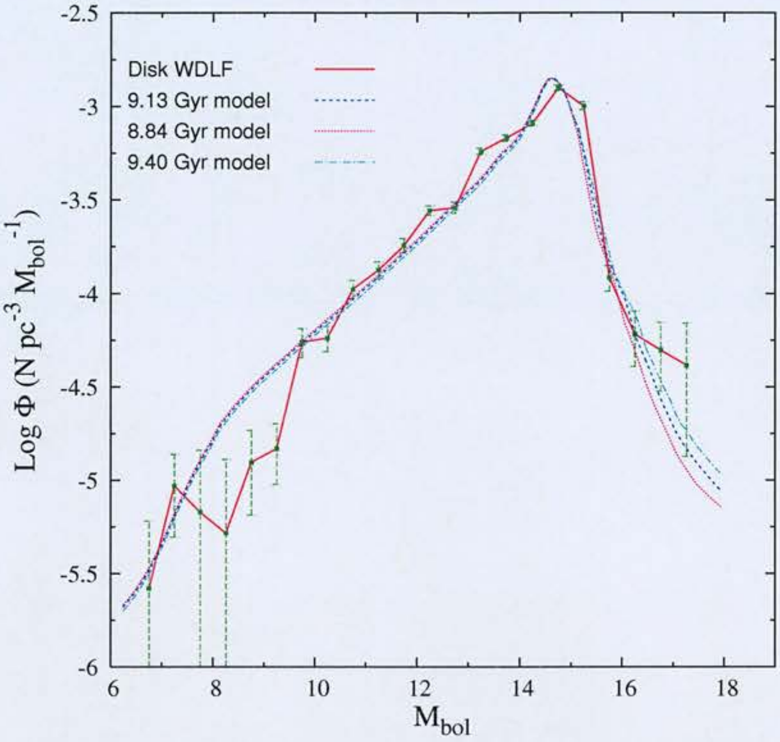

Figure 4.7: The observed disk WDLF, including the best fitting model (blue) and upper/lower one sigma confidence limits (cyan/magenta). Note that the error bars on the observed points have not been inflated in this plot.

of the main sources; Bergeron et al. (2001) find a difference of $\sim$ 2 Gyr in the ages of their oldest models depending on whether thin ($q_H = 10^{-10}$) or thick ($q_H = 10^{-4}$) hydrogen layers are used. It is worth noting, however, that there is good observational evidence (e.g. Castanheira and Kepler, 2009) that the mean layer thickness is closer to the $q_H = 10^{-4}$ assumed in this study. The rate of the $^{12}\mathrm{C}(\alpha,\gamma)^{16}\mathrm{O}$ reaction and the initial chemical profile of the core also affect the age; Salaris et al. (1997) find a difference of $\sim$ 0.4 Gyr in the ages of their oldest models depending on whether a high or low rate is assumed. I conclude that an outside estimate of the systematic uncertainty on these ages is $\sigma \sim 1.0$ Gyr, but may be as low as $\sigma \sim 0.6$ assuming some of these effects wash out when averaged over a large sample. Indeed, it is for this reason that the changing spectral signature of a white dwarf, which introduces a large uncertainty on individual age estimates, has a limited effect on the luminosity function age for an

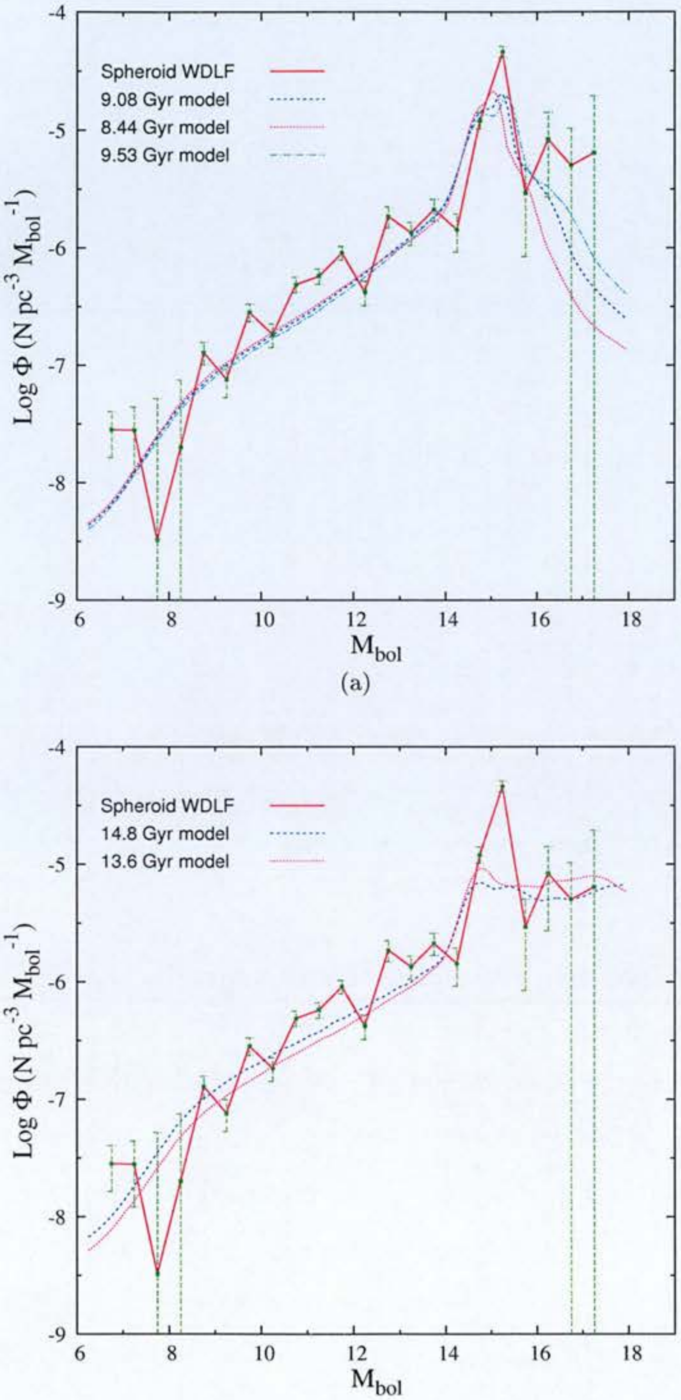

(a)

(b)

Figure 4.8: The observed spheroid WDLF, with the young (a) and old (b) solution. The best fitting models (blue) are plotted along with the upper/lower one sigma confidence limits (cyan/magenta). The old solution finds no upper age limit in the range of available models. Again, the error bars on the observed points have not been inflated in these plots.

ensemble of stars. The high σ agrees with that considered by Wood and Oswalt (1998) in their analysis of white dwarf luminosity function ages, but considerable progress has been made since then in addressing some of the sources of error that they considered (e.g. crystallisation, sedimentation), and the low estimate derived here is probably more realistic.

4.4 Summary

In this chapter I have identified an appropriate integral equation for the white dwarf luminosity function, and forward modelled my observations using a variety of adopted inputs and assumptions concerning the star formation history of the Galactic disk and spheroid. I find that exponentially decaying and single burst models of star formation lead to WDLFs more strongly peaked than those obtained for a constant rate. This is consistent with the observations, which reveal a smoothly rising WDLF for the disk and a sharply peaked WDLF for the spheroid. I also find that He atmosphere white dwarfs tend to dominate the number counts at the faint end, where most of the age information lies.

The simple star formation histories considered result in smooth model luminosity functions that fail to reproduce small scale irregularities in the observations at bright magnitudes. By shifting the weight to the faint end, where the form of the luminosity function is independent of the star formation rate after the earliest times, I fit an age for the local Galactic disk of $9.13^{+0.66}_{-0.67}$ Gyr, including several sources of systematic error that affect white dwarf age estimates. This is likely to be representative of an annulus in the disk centred on the Solar radius, assuming that stars remain at roughly their birth radii throughout their lifetime. For the spheroid, I find two roughly degenerate age solutions of $9.08^{+0.75}_{-0.88}$ Gyr and $14.8^{>1.2}_{-1.3}$ Gyr. This degeneracy could be broken either by improved constraint at the faint end of the WDLF where the number counts are low and distances uncertain, or by an improved model of the star formation history, which would indicate whether the peak in the WDLF is a relic from the earliest period of star formation or the result of a later burst.

CHAPTER 5

Conclusions

5.1 The SuperCOSMOS white dwarf catalogue

I have conducted a wide angle magnitude and proper motion limited survey for white dwarfs, using data from the SuperCOSMOS Sky Survey. This survey covers $\sim 75\%$ of the sky to $R \sim 19.75$ and $\mu \sim 50$ mas yr^{-1}, and identifies over ten thousand white dwarf candidates based on reduced proper motion. Follow up spectroscopy indicates a contamination rate by non-degenerate stars of around a few percent. Although it appears that the catalogue may be up to 50% incomplete due to the exclusion of blended objects, the incompleteness is uniform with colour and bolometric magnitude, and does not bias the selection towards any particular type of white dwarf. Photometric parallaxes are obtained by fitting the photographic colours to grids of atmosphere models, and have been shown to be accurate to $\sim 50\%$. The unknown atmosphere type of each white dwarf is accounted for by fitting both types, and attaching a weight proportional to the likely contribution to the survey from each type as a function of colour. Most known ultracool white dwarfs are present in this catalogue, and have had distances estimated by a variety of techniques due to the failure of photometric parallaxes for these stars.

This white dwarf catalogue is significantly larger than that obtained from the SDSS DR4 by reduced proper motion selection (Kilic et al. 2006, Harris et al. 2006), due to the fact that identification in the USNO-B survey was required for their survey technique. SDSS has identified a large number (≥ 9000) of white dwarfs spectroscopically (Eisenstein et al., 2006), although these are generally only observed accidentally because of their similar colours to QSOs, and the problem of estimating the detection probability and completeness has restricted their usefulness for measuring derived statistical quantities. Other compilations of white dwarfs gathered from a variety of sources (e.g. the Villanova catalogue, McCook and Sion 1999) suffer the same limitation. It is therefore likely that this will remain the largest homogenous white dwarf sample until a later data release of SDSS is paired with USNO-B.

5.2 The white dwarf luminosity function

The white dwarf luminosity function presented in this work is measured using the largest homogenous sample of white dwarfs to date (8765 with $v_t > 30\text{kms}^{-1}$). The large sample size is due mostly to the large footprint of the SuperCOSMOS Sky Survey (see Figure 2.13 (a) and (b)). For example, Harris et al. (2006) have significantly wider proper motion limits over the same range in magnitude, but cover just one sixth of the area of the present study and find 6000 white dwarfs with $v_t > 30\text{kms}^{-1}$. The large survey volume for faint stars allows nearly all known ultracool white dwarfs to be included in the complete catalogue (Table 2.6), pushing the luminosity function to the deepest magnitudes yet obtained.

5.2.1 The disk

The drop in the disk luminosity function at the faint end has the same position ($\sim M_{bol} = 15.75$) and magnitude ($\Delta \log \Phi \sim 1.0$) as found by other surveys (e.g. Liebert et al. 1988, Harris et al. 2006) - see Figure 3.7 (a). The identification of this drop in the local density of degenerate stars with that predicted by Schmidt (1959) is now beyond doubt. This feature is a result of both the finite age of the Galaxy, and the rapid cooling experienced by white dwarfs at fainter magnitudes. The morphology beyond the peak bears a direct imprint of the earliest epoch of star formation in the disk, and the luminosity function is essentially unexplored at these magnitudes; the observations presented here are the first to investigate this region at any appreciable level of constraint, and I feel that this is one of the main results of this work. At brighter magnitudes, the slope of the luminosity function agrees well with that of the two studies cited previously, and is punctuated by features that may correspond to bursts in star formation in the recent history of the Galaxy. However, the accuracy of our photometric parallaxes is such that these features are probably not sufficiently resolved to draw any firm conclusions. Finally, as pointed out by Reid (2005), the thick disk is expected to dominate the number counts in the faintest luminosity bins, due to its white dwarfs having ~ 1 Gyr longer to cool. Therefore, cosmochronology of the disk using the turnover in the white dwarf luminosity function likely measures the age of the thick disk, not the thin disk.

5.2.2 The spheroid

The measurement of a separate luminosity function for the spheroid is an important result. The large upper proper motion limit of our survey enables many high velocity stars to enter the catalogue, and our $v_t > 200\text{kms}^{-1}$ sample has nearly three times as many objects as the previous largest study (Harris et al., 2006). Deprojecting the proper motions of these stars (Dehnen and Binney, 1998b) suggests an origin in a non-rotating population, thus confirming their spheroid membership. This has been a particularly contested point in previous studies claiming to detect spheroid white dwarfs (Oppenheimer et al. 2001, Reid 2005). The luminosity function agrees qualitatively with that of Liebert et al. (1989) and Harris et al. (2006), while achieving considerably better constraint and extending 2.5 magnitudes fainter. I have improved the accuracy of the spheroid luminosity function by introducing a new survey technique that allows *all* spheroid stars to be used to measure the density, including those at tangential velocities that overlap considerably with the disk. This allows more information to be extracted from a proper motion catalogue than traditional means. Application of this technique reveals structure in the spheroid white dwarf luminosity function that has not been seen before, in particular a distinct peak at $\sim M_{bol} = 15.25$ and no sign of a drop off at the faintest magnitudes unlike for the disk, as shown in Figure 3.5 (a). The introduction of this technique and the measurement of the spheroid white dwarf luminosity function are significant results.

5.2.3 Incompleteness

Incompleteness in the underlying white dwarf catalogue causes a vertical offset of $\Delta \log \Phi \sim 0.5$ between the luminosity functions measured in the present work, and those obtained by others (Figure 3.7). This is due to the rejection of blended objects and those missed at the first observation epoch. The incompleteness is uniform with M_{bol} and can be corrected for where necessary by normalisation to other studies, although the luminosity function ages and disk-to-spheroid ratio are insensitive to the incompleteness, assuming it is the same between the two populations.

5.2.4 Caveats

I feel there are two important caveats that should be attached to these luminosity functions. The first concerns the method by which white dwarfs are selected based on their reduced proper motion. White dwarfs with helium dominated atmospheres cool as blackbodies to the faintest magnitudes, and their colours do no turn back to the blue as with hydrogen dominated atmospheres (see Figure A.3). They are also brighter at a given colour, and at cool effective temperatures overlap considerably in reduced proper motion with both spheroid subdwarfs and disk main sequence stars. As this survey, along with all others that perform a rigorous reduced proper motion selection, uses a hydrogen atmosphere cooling track to select white dwarf candidates, helium atmosphere white dwarfs will not be selected once they have reached redder colours than the reddest point in the cooling track. This occurs at $b_J - r_{59F} \sim 1.6$, which corresponds to $T_{\mathrm{eff}} \sim 4500K$ and $M_{bol} \sim 15.4$ for a helium atmosphere. It is for this reason that the prototypical old halo white dwarf WD 0346+246 (Hambly et al. 1997, Bergeron 2001) is not included in our survey. Although it is likely that most cool white dwarfs have enough hydrogen in their atmospheres to undergo the blue turn (see Bergeron, 2001, and arguments therein), and that excluding pure helium stars likely has little effect on the luminosity function, it is worth pointing out that this survey method is not sensitive to them.

Secondly, the faintest luminosity bins are inhabited by stars whose stellar parameters are rather more uncertain than those consituting the bulk of the sample. These are the 'ultracool' white dwarfs, with $T_{\mathrm{eff}} \leq 4000K$. As no atmosphere models can convincingly reproduce the unusual spectral energy distributions of these objects, their bolometric magnitudes and distances have been estimated by the rather ad-hoc means presented in Section 2.4.2. While their status as the faintest white dwarfs in the survey is sound, their true parameters may be sufficiently different to the estimates that the morphology of the faintest ~3 or 4 bins is changed significantly when better values become available.

5.3 The age of the disk and spheroid

The age of the disk obtained in Section 4.3 is $9.13^{+0.66}_{-0.67}$ Gyr. This agrees well with several other white dwarf luminosity function based age estimates, for example Winget et al. (1987) (9.3 ± 2.0 Gyr), Oswalt et al. (1996) ($9.5^{+1.1}_{-0.8}$ Gyr), Leggett et al. (1998) (8.0 ± 1.5 Gyr) and Knox et al. (1999) (10^{+3}_{-1} Gyr). It is also consistent with that obtained by a range of independent methods - Lineweaver (1999) conducted a meta-analysis of five studies and calculated a disk age of 8.7 ± 0.4 Gyr. A disk ~ 9 Gyr old fits into the broad picture of Galaxy formation in the ΛCDM paradigm (Freeman and Bland-Hawthorn 2002, Lineweaver 1999). In this picture, the Big Bang occured ~ 13.4 Gyr ago, followed by formation of the spheroid roughly a Gyr later. Around ~ 3.5 Gyr after that, dissipation caused most of the baryons to settle into a rotating disk, creating the stars that would eventually make their way into our proper motion survey as white dwarfs.

For the spheroid, two degenerate age solutions of $9.08^{+0.75}_{-0.88}$ and $14.8^{>1.2}_{-1.3}$ Gyr are found. This is the first time that any significant number of white dwarfs have been used to date the spheroid , and the results are somewhat ambiguous. The young solution is highly inconsistent with the age estimate of Lineweaver (1999) (12.2 ± 0.5 Gyr) based on main sequence ages and isotope analysis. It also disagrees with the only other white dwarf based age estimate, the tentative result of ~ 13 Gyr claimed by Fontaine et al. (2001), and is impossible to reconcile with the current understanding of Galaxy formation, in which stellar haloes certainly form before disks. The old solution certainly shows better agreement with these predictions, and while it is tempting to accept this as a valid age estimate, the only firm conclusion we can draw is that we cannot distinguish between the two with the data available. Better constraint in the observed luminosity function at the faintest magnitudes is required before this degeneracy can be broken.

Most of the uncertainty on the disk age is systematic, as detailed in Section 4.3. The statistical error is only $\sim 3\%$ percent, which broadly agrees with the predictions of Wood and Oswalt (1998), who examined the statistical uncertainty in white dwarf luminosity function age estimates that employ the $\frac{1}{V_{max}}$ method. An extrapolation of their results to our sample size predicts $\leq 1\%$ statistical uncertainty. Finally, the spheroid age errors are rather smaller than those predicted by the Wood and Oswalt (1998) investigation ($\sim 5 - 8\%$ compared to $\geq 10\%$). This may be due to the fact that Wood et al. restricted their analysis to disk luminosity functions, but may also be down to the use of the least-squares decomposition method to derive the observed spheroid luminosity function. Either this method achieves greater statistical accuracy than a straightforward application of $\frac{1}{V_{max}}$, or, more likely, it underestimates the errors due to overlapping v_{tan} ranges not providing independent star count estimates. See the Further Work section at the end of this chapter.

5.4 Galactic structure

5.4.1 Disk to spheroid normalisation

The total integrated number densities for disk and spheroid white dwarfs in the solar neighbourhood are $(2.5 \pm 0.1) \times 10^{-3}\text{pc}^{-3}$ and $(3.4 \pm 0.9) \times 10^{-5}\text{pc}^{-3}$, respectively. These are taken from Section 3.2.2; the disk number density quoted here is a variance-weighted combination of the two independent measures. Due to incompleteness these are likely underestimated by up to 50%, however the *relative* number density should not be affected by this. We thus obtain a total disk-to-spheroid ratio of 74 ± 20 by number. This is significantly lower than for non-degenerate stars, and is a direct result of the greater age of the spheroid population - a larger fraction of its stars have moved off the main sequence. For example, a brief review of the literature finds a wide range of density normalisations for main sequence stars; combining Stobie et al. (1989) and Digby et al. (2003) gives $(\frac{n_{disk}}{n_{sph}})_{MS} \sim 200$, Tinney et al. (1993) and Gould et al. (1998) give $(\frac{n_{disk}}{n_{sph}})_{MS} \sim 700$ and Robin et al. (2003) find $(\frac{n_{disk}}{n_{sph}})_{MS} \geq 1500$, although in the latter two cases the local spheroid density is inferred from deep star counts, and is perhaps not truly representative of the solar neighbourhood.

5.4.2 Spheroid white dwarf number and mass density

The local number density of disk white dwarfs is well constrained by other studies, and we can use this in conjunction with our disk-to-spheroid normalisation to correct the spheroid number density for incompleteness. Using the value of $(4.6 \pm 0.5) \times 10^{-3}\mathrm{pc}^{-3}$ obtained by Harris et al. (2006), we find a corrected local number density for spheroid white dwarfs of $(6.2 \pm 1.8) \times 10^{-5}\mathrm{pc}^{-3}$. This is consistent with the value of $5 \times 10^{-5}\mathrm{pc}^{-3}$ argued for by Reid (2005); this is mid way between the low value of $2.2 \times 10^{-5}\mathrm{pc}^{-3}$ predicted by the spheroid model of Gould et al. (1998), and the $7.6 \times 10^{-5}\mathrm{pc}^{-3}$ estimated by Reid using the local subdwarf density and intial mass function. This value disagrees with the $1.8 \times 10^{-4}\mathrm{pc}^{-3}$ measured by Oppenheimer et al. (2001), due to the more rigorous exclusion of thick disk white dwarfs employed here. The spheroid white dwarf density measured in the present work has the advantage of being calculated from a directly observed sample of stars, and thus supercedes previous estimates based on star count models.

This number density translates to a mass density of $(3.7 \pm 1.1) \times 10^{-5} M_{\odot}\mathrm{pc}^{-3}$, on adopting a mass of $0.6M_{\odot}$ for spheroid white dwarfs. This equates to 0.4% to 0.7% of the local dark matter density, assuming $\rho_{DM} = 0.005 - 0.01 M_{\odot}\mathrm{pc}^{-3}$ (Weber and de Boer, 2009). I thus find no evidence for a significant contribution to the local dark matter density from a population of ancient white dwarfs, and do not need to invoke extra Galactic components to explain my observations.

5.4.3 White dwarf contribution to the MACHO observations

A long standing controversy has surrounded the question of to what extent halo white dwarfs are responsible for the observed microloensing events towards the LMC. Proper motion surveys have placed upper limits on the likely contribution, but these are often based on the non-detection of halo white dwarfs in a relatively small survey volume (e.g. Goldman et al., 2002, find a 5% upper limit). With this large survey, I can place tighter constraints on the white dwarf microlensing contribution.

If the microlensing events are due to MACHOs in the Galactic halo, Alcock et al. (2000) estimate that they constitute 20% to the dark matter, and that the total mass in MACHOs out to 50 kpc is $9^{+4}_{-3} \times 10^{10} M_{\odot}$. Assuming the high velocity white dwarfs this survey has detected are part of an extended 'dark halo' population, their total mass out to 50 kpc can be estimated using the halo density law (model 'S') of Alcock et al., normalised to the solar neighbourhood density measured in this work. This gives a total mass of $M_{R<50kpc} \sim 1.9 \times 10^9 M_\odot$ for dark halo white dwarfs. If, more likely, these white dwarfs are regular stellar halo objects, I estimate their total mass using the spheroid density law of Dehnen and Binney (1998a) (model 2b, so that the adopted $R_\odot$ matches that of Alcock et al., and with a flattening parameter $\epsilon = 0.76$) to be

$$M_{R<50kpc} \sim 1.2 \times 10^9 M_\odot$$

Therefore, an extended population of white dwarfs may contribute to the MACHO microlensing events at the level of $\sim 1\%$ with an upper limit of $\sim 2-3\%$, allowing for the possibility of a more extended density profile and the existance of extremely faint objects that have cooled beyond the detection limit of our survey (see Section 5.5.2).

5.5 Discussion

5.5.1 Scaleheight and kinematics

It seems appropriate to report a null result from another measurement I attempted to make on this white dwarf catalogue. The scaleheight of the disk is a parameter that appears in the density profile used to calculate the generalised volume for each star (Section 3.1.2). The scaleheight is relatively well known for main sequence stars - it is a function of spectral type, and increases from $\sim$ 100pc for OB stars (Kong and Zhu, 2008) to $\sim$ 250pc for M dwarfs (e.g. Mendez and Guzman, 1998). This increase is well understood in terms of kinematic heating of the disk; the fainter stars are older and have experienced more heating. However, it is not clear what value is appropriate for white dwarfs, or how the scaleheight changes with luminosity, and it is typical to adopt a value measured for main sequence stars. I therefore attempted to measure this quantity for the white dwarfs in each luminosity function bin using star count modelling techniques, i.e. for each bin, I calculated the distribution of generalised survey volume as a function of distance from the plane *and* scaleheight, and fitted these models to my data to see which scaleheight most closely matched the observed distribution of stars. Unfortunately, I could not get enough constraint from the data to obtain a convincing result at any luminosity. At bright magnitudes there are too few stars to get much of a signal, and at faint magnitudes the stars are all too close to the Sun for the scaleheight to have a significant effect on the number counts. At the least, an encouraging conclusion from this is that the luminosity function is rather insensitive to the adopted scaleheight, and is unlikely to change much when an appropriate value is measured.

The kinematic properties assumed (velocity ellipsoids and mean motions) in the analysis of these white dwarfs also had to be 'borrowed' from main sequence stars, as a large analysis of the motions of white dwarfs has not been conducted. Unfortunately, the minimum tangential velocity threshold probably rules out reduced proper motion selected white dwarf samples from a statistical analysis of velocities, especially for disk stars. Also, once all spectral lines have disappeared below $T_{\text{eff}} \sim 5000K$, radial velocities are unobtainable - although deprojection of proper motions could recover the velocity moments. Hypothetically, if a large, statistically complete sample of white dwarfs with full 3D (or even 2D) velocity measurements were available, it would be interesting to look for a feature equivalent to Parenago's discontinuity in main sequence stars (Dehnen and Binney, 1998b), where the velocity dispersion saturates redwards of the old disk turn off at $B - V \sim 0.6$. A similar feature could be expected to appear in a plot of the velocity dispersion against bolometric magnitude for white dwarfs (for which colour does not necessarily correlate with age). A significant difference to the main sequence equivalent would be that beyond the discontinuity, all white dwarfs would be of a uniform age, and would correspond to stars created right at the onset of star formation in the disk. This could be used to date the disk in a manner independent of the luminosity function.

5.5.2 Looking beyond the survey limits

It is interesting to speculate, at this point, on the possible existence of white dwarfs even fainter than those detected in our survey. The spheroid white dwarf luminosity function measured in this work does not appear to turn over like that of the disk, and presumably extends beyond the faintest detected objects to magnitudes where our survey volume is very small. I can estimate the probable numbers of these objects using the same techniques employed to model the theoretical luminosity function. Although it is not possible to predict the morphology of the luminosity function beyond $M_{bol} \sim 18$, because the input evolutionary tracks are not computed further than around this magnitude, it is still possible to calculate the number of stars that have cooled fainter than this. To do this, I used the Monte Carlo code mentioned in Section 4.2.2 to simulate a population of stars, and measured how many of the resulting white dwarfs cooled beyond $M_{bol} = 18$ in 9.08 and 14.8 Gyr. These correspond to the two degenerate age solutions for the spheroid. I found that for a 9.08 Gyr population, 99% of all white dwarfs are brighter than $M_{bol} = 18$. For a 14.8 Gyr population, this figure is 60%, meaning that nearly half of all white dwarfs have cooled to magnitudes undetectable by current surveys, and that the local density may be almost double that calculated from $M_{bol} < 18$ stars. However, neither of these ages are standard for the spheroid. Using the age of 12.2 Gyr calculated by Lineweaver (1999), I find that 93% of white dwarfs have $M_{bol} < 18$ and are likely to be included in the density estimate measured above. Therefore, the existence of a substantial population of white dwarfs lying beyond the detection limits of this survey is unlikely.

5.6 Further work

5.6.1 Faint white dwarfs

The most pressing extension to this work is a thorough observational analysis of the white dwarfs at the faint end of the luminosity function, where all of the age information lies. High mass and helium atmosphere white dwarfs are expected to dominate at this end, and the application of our photometric parallax method to these stars will give results far more error prone than for objects at brighter magnitudes. Optical spectroscopy, combined with CCD photometry from the B band to the infra red JHK bands would provide the effective temperature, surface gravity and atmospheric composition for these objects. Note that IR photometry for some stars may soon be available 'for free' from the VISTA Hemisphere Survey and the UKIDSS Large Area Survey, in particular the ultracool white dwarf SSSJ1556-0806 which was discovered in the course of this survey, and the various ultracool objects discovered in the SDSS. In conjunction with trigonometric parallaxes, these observations would enable mass and bolometric magnitude estimates, greatly improving the constraint on the faint luminosity function.

5.6.2 The luminosity function inverse problem

The formula for the luminosity function presented in Equation 4.1 is a classic inverse problem (Press et al. e.g. 2007, see Chapter 19; Binney and Merrifield 1998, Appendix C). In this work, I have investigated the star formation rate by *forward modelling* the luminosity function, where a particular star formation rate model is assumed and used to predict the data, which in turn is used to falsify the model. The *inverse problem* - that of using the data to measure the star formation rate - is considerably more challenging, and typically requires high quality data and a unique method of solution tailored to the precise form of the problem. Many different types of inverse problem exist, each with their own methods of solution. It would be interesting to investigate a solution to Equation 4.1 that would allow the star formation rate to be directly measured from the white dwarf luminosity function.

5.6.3 Decomposition of the luminosity function

The technique of measuring the survey volume separately for different kinematic populations, and recovering the local density of each by checking the star counts against varying survey limits, is worthy of some closer analysis. An investigation similar to that applied to the straightforward $\frac{1}{V_{max}}$ method by Wood and Oswalt (1998) might be a good place to start. This would involve simulating several distinct but overlapping populations of stars, endowing them with positions and velocities drawn from different underlying distributions, then 'observing' this population synthetically and testing how well the luminosity function technique recovers the numbers of stars contributed by each population to the total observed sample. In the same way, it would be possible to investigate what size of sample is required to separate significantly overlapping populations such as the thin and thick disks.

A review of the method itself could possibly improve the results it obtains. The matrix equation that provides the density estimate might be better solved by singular value decomposition rather than straightforward inversion, especially considering that when star counts are low the design matrix becomes ill-conditioned. Also, at present the varying survey limits overlap each other, which might result in underestimated or correlated errors in the luminosity function. For example, instances of Equation 3.13 are generated using $v_t \geq 20, 30, 40...\mathrm{kms}^{-1}$ cuts to vary the survey volume and number of stars. However, because e.g. the $v_t > 20\mathrm{kms}^{-1}$ sample includes all stars present in the $v_t > 30\mathrm{kms}^{-1}$ sample, they are not truly independent. Distinct ranges such as $20\mathrm{kms}^{-1} \leq v_t < 30\mathrm{kms}^{-1}$, $30\mathrm{kms}^{-1} \leq v_t < 40\mathrm{kms}^{-1}$ etc. might be better. Also, as the local density of each population cannot be negative, some form of constrained least squares might provide a better solution when the number counts are low.

5.6.4 Future surveys

Looking ahead, it is interesting to ask what kind of advances might be made in this field based on the data products of certain sky surveys that are planned for the near future.

PanSTARRS

The prototype telescope for the *PanSTARRS* (Panoramic Survey Telescope & Rapid Response System) project has begun observations from Hawai'i. While its primary mission is to detect potentially hazardous objects in the Solar System, it will produce huge amounts of data suitable for a whole host of astrophysical science purposes. As part of the PS1 3π survey, over the next ~ 3.5 years the telescope will observe the entire sky north of $\delta \sim -30^\circ$, returning to each location 12 times in each of 5 filters (Magnier et al., 2008). The final set of co-added images will reach a limiting magnitude (5σ) of $m_r \sim 23$, and measure proper motions to an accuracy of $\mu \sim 1.2$ mas yr^{-1}.

It is possible to estimate what kind of increase in star counts might be achieved over the present survey. The increase in survey depth on extending the magnitude and proper motion limits is

$$\begin{aligned}\left(\frac{d_{PS1}}{d_{SSS}}\right)_m &= 10^{\frac{m_{PS1}-m_{SSS}}{5}} \\ \left(\frac{d_{PS1}}{d_{SSS}}\right)_\mu &= \frac{\mu_{SSS}}{\mu_{PS1}}\end{aligned}$$

where $m_{SSS} = 19.75$ and $\mu_{SSS} = 0\farcs04\ \mathrm{yr}^{-1}$ are the approximate limits of the present survey. $m_{PS1} = 20.3$ is the approximate single-epoch magnitude limit of PS1, which is appropriate for proper motion objects, and $\mu_{PS1} = 0\farcs01\ \mathrm{yr}^{-1}$ is a conservative estimate of the proper motion limit for a secure detection. The 3π survey subtends a solid angle roughly equal to this survey, so the expected number of disk white dwarfs is $N_{PS1} \sim N_{SSS} \times \left(\frac{d_{PS1}}{d_{SSS}}\right)_m^2 \times \left(\frac{d_{PS1}}{d_{SSS}}\right)_\mu^2$, with the exponent of 2 arising from the scaleheight effect. Spheroid white dwarfs have a uniform spatial distribution, and will have an exponent of 3 in this formula. Putting the numbers into these equations, and adopting 9000 and 100 as the number of disk and spheroid white dwarfs in the present survey, I find

$$\begin{aligned}N_{\text{disk WDs}} &\sim 25 \times 10^4 \\ N_{\text{spheroid WDs}} &\sim 1.4 \times 10^4\end{aligned}$$

for the number of disk and spheroid white dwarfs obtainable from the PS1 3π survey, by means of reduced proper motion selection. These should be interpreted both as lower limits, given that the SSS counts are probably $\sim 50\%$ incomplete, and a first order estimate, as many contributing factors have been omitted. A more accurate estimate could be obtained by Monte Carlo analysis of a Galactic model, taking into account extinction, differential rotation and detailed density profiles, similar to that carried out by Garcia-Berro et al. (2005) for the Gaia satellite. Assuming the statistics of Wood and Oswalt (1998) hold to this limit, the sample sizes derived here would translate to disk and spheroid statistical age uncertainties of $\sim 0.2\%$ and $\sim 1\%$, respectively.

Gaia

The Gaia[1] astrometric satellite is due for launch in 2012, and over 5-6 years will produce an incredibly precise three dimensional map of around one billion stars in the Milky Way. It will measure positions, proper motions, parallaxes and spectra for stars down to $m_V \sim 20$ with unprecedented accuracy, with radial velocities for a subset to $m_V \sim 17$ (Lindegren, 2010). The number of white dwarfs expected to be found by Gaia is around 4×10^5, including nearly 100% of objects within 100pc (Garcia-Berro et al., 2005; Jordan, 2007). While these will undoubtedly be interesting from a luminosity function point of view, the real breakthrough will come from the parallax measurements, which will provide accurate mass determinations. These will allow extensive tests of the theoretical mass-radius relation, focusing in particular on how it varies with surface temperature and composition.

---

[1] `http://www.esa.int/science/gaia`

APPENDIX A

SuperCOSMOS Photometry

A.1 Photographic passbands

A.1.1 Transmission functions

Transmission functions for the photographic bands used in the SuperCOSMOS Sky Survey have been obtained from Evans (1989) (b_J) and Bessell (1986) ($r_{63F/103aE}$, r_{59F} and i_N). The two first epoch r bands r_{63F} and r_{103aE} are assumed to be identical in response. These are plotted in Figure A.1, along with the spectrum of SSSJ1016-0109. This WD+dM binary was discovered by our survey, and is included in the plot to show how the unresolved MS companion contributes flux to the i_N filter.

The Besançon Galaxy model does not include these photographic bands in it's selection of filter systems. This is fairly common for modern astronomical applications (e.g. TRILEGAL) which are designed to complement CCD surveys. Therefore it is useful to identify certain photoelectric bands that closely resemble the photographic bands. Figure A.2 depicts the bands adopted as SSS proxies in this work, for use with the Besançon model.

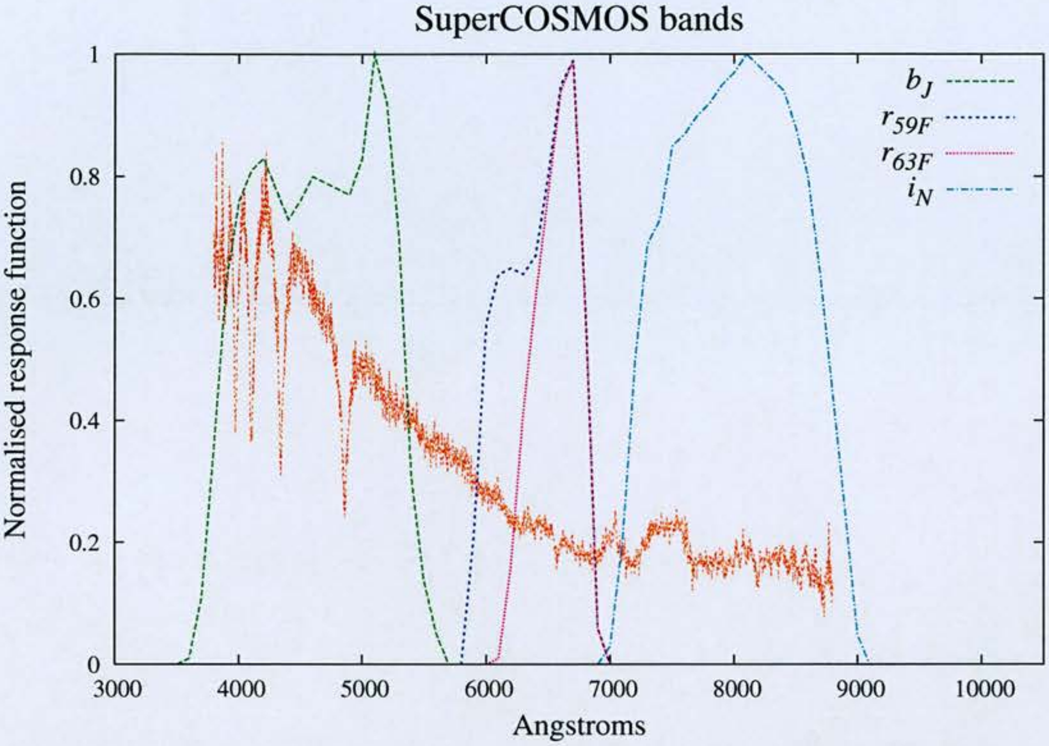

Figure A.1: SSS filter functions. Also shown is the spectrum of the WD+dM binary SSSJ1016-0109.

A.1.2 Photometric uncertainty

Rough estimates of the external error on the photographic *colours* at $b_J \sim 16.5$ and $b_J \sim 20$ are given in Hambly et al. (2001b). We fit a straight line for the error at intermediate and fainter magnitudes, and use the uncertainty at $b_J \sim 16.5$ for all brighter magnitudes. The relation we obtain is

$$\sigma_{b-r,b-i}(b_J) = \begin{cases} 0.07 & \text{if } b_J \leq 16.5 \\ 0.026 b_J - 0.35 & \text{otherwise.} \end{cases}$$

Due to the particular way in which the photometric scale is calibrated, colours are more accurate than single magnitudes (see Hambly et al. (2001b) for details). Uncertainty in single passbands is necessary however for deriving minimum-variance estimates of the photometric distance, by comparing model and observed magnitudes. These are taken from Table 12 in Hambly et al. (2001b).

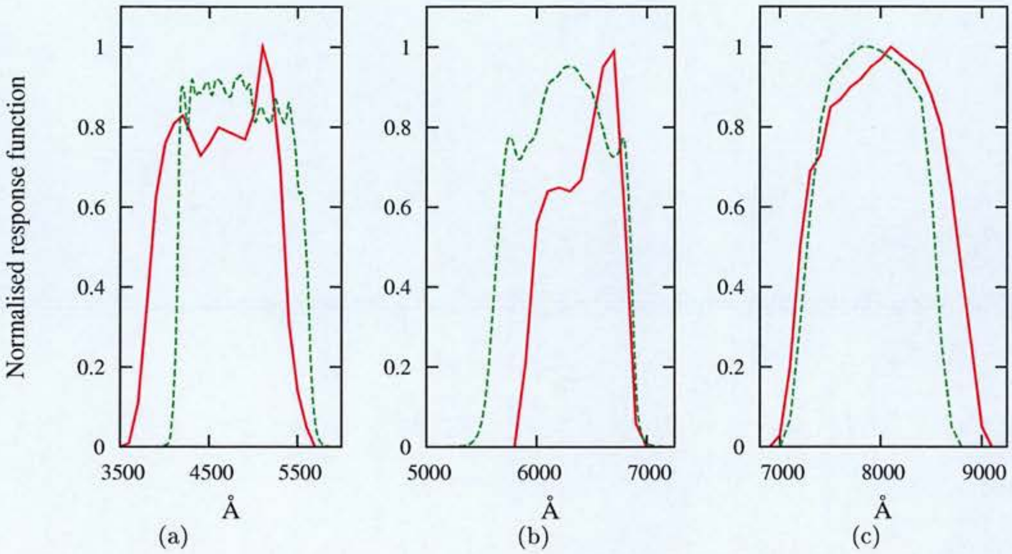

Figure A.2: CCD bands used to approximate SSS photographic bands. (a) shows the CFHT g band (green line) alongside b_J, (b) shows CFHT r alongside r_{59F} and (c) shows Cousins I alongside i_N.

A.2 Synthetic photometry

The magnitude in a given band can be synthesised from the spectral energy distribution, and vice-versa, by means of synthetic photometry. The integrated flux in band m is denoted f_λ^m and is calculated from the wavelength flux density $f_\lambda(\lambda)$ and associated transmission function $S_m(\lambda)$ according to

$$f_\lambda^m = \frac{\int_0^\infty f_\lambda(\lambda) S_m(\lambda).d\lambda}{\int_0^\infty S_m(\lambda).d\lambda} \tag{A.1}$$

This is placed on the magnitude scale by

$$m = -2.5\log(f_\lambda^m) + c_m$$

where c_m is a constant that sets the zero point of the scale and remains to be determined.

A.2.1 Vega flux constants

SSS magnitudes are defined on a Vega-type photometric scale, such that A0 type stars have all colours zero. We use the Vega spectrum from Bohlin and Gilliland (2004),

Band	c_m
b_J	-20.624
$r_{63F/103aE}$	-21.724
r_{59F}	-21.629
i_N	-22.342

Table A.1: Magnitude zeropoints for SuperCOSMOS photographic passbands.

used to calibrate *HST* spectrophotometry and accurate in absolute flux to $\sim 1\%$. The constants c_m are determined from the Vega spectrum via

$$f^m_{\lambda,Vega} = \frac{\int_0^\infty f_{\lambda,Vega}(\lambda) S_m(\lambda).d\lambda}{\int_0^\infty S_m(\lambda).d\lambda}$$

$$c_m = -2.5\log(f^m_{\lambda,Vega})$$

The values we determine for the photographic passbands used in the SuperCOSMOS Sky Survey are given in Table A.1.

A.2.2 Blackbody colours

With knowledge of c_m, the photographic colours of a blackbody source can be calculated by replacing the stellar spectral energy distribution in Equation A.1 with the Planck function for the desired temperature. It is instructive to compare in colour space the cooling track of a blackbody with that of the synthetic white dwarf models used in this work. As can be seen in Figure A.3, at high temperatures white dwarf colours very closely resemble that of a blackbody at the same temperature. Below $5000K$ they start to diverge, and cooler than around $4000K$ the optical spectra of H atmosphere white dwarfs become highly non-Planckian, as collisionally induced absorption extends to visible wavelengths.

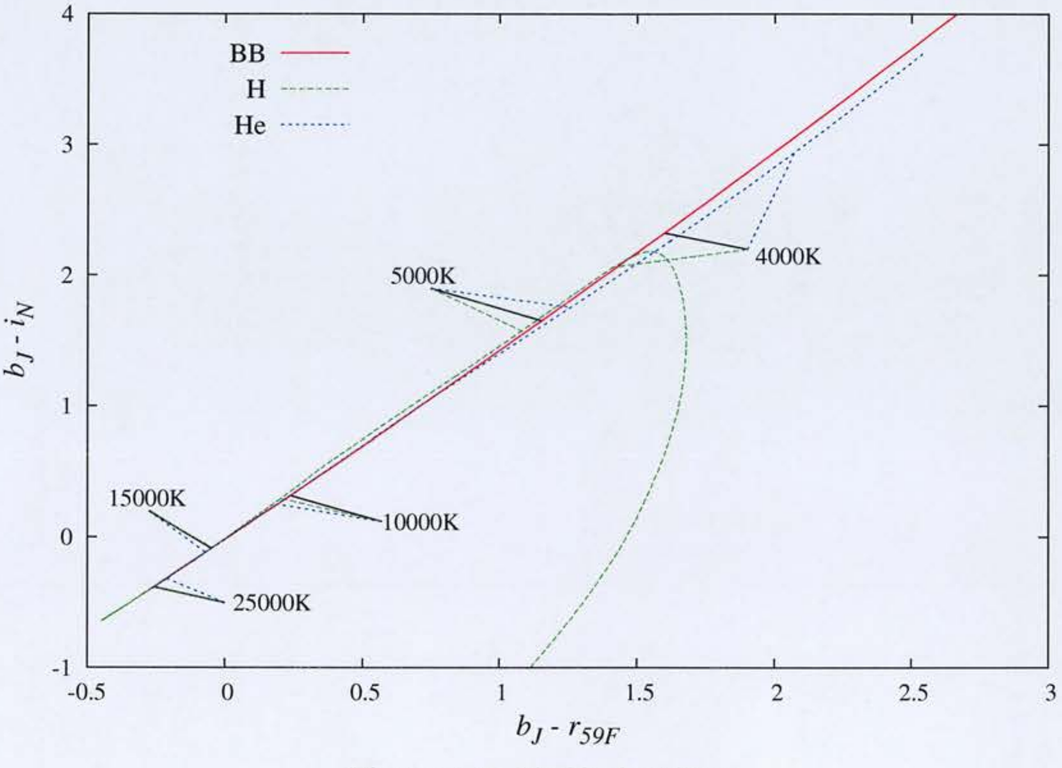

Figure A.3: Blackbody colours

APPENDIX B

Tangential Velocity Distributions

B.1 Coordinate systems

A number of different coordinate systems are used in this work. The Galactic coordinate system is defined by the 'Galactic triad' of unit vectors $[UVW]$, denoted $\mathbf{G}$. U points to the Galactic centre, V in the direction of rotation and W to the north Galactic pole. Positions on the sky can be specified in terms of the Galactic latitude and longitude b and l. The equatorial coordinate system is defined by the 'Normal triad' $[lmn]$, denoted $\mathbf{N}$. l points to the vernal equinox, n to the north celestial pole and m completes the set. They are related by the orthogonal transformation

$$\mathbf{N}^{\dagger}\mathbf{G} = \begin{bmatrix} \cos(\alpha_{\mathrm{GC}})\cos(\delta_{\mathrm{GC}}) & \begin{array}{c}\sin(\delta_{\mathrm{GC}})\sin(\alpha_{\mathrm{NGP}})\cos(\delta_{\mathrm{NGP}})- \\ \sin(\delta_{\mathrm{NGP}})\sin(\alpha_{\mathrm{GC}})\cos(\delta_{\mathrm{GC}})\end{array} & \cos(\alpha_{\mathrm{NGP}})\cos(\delta_{\mathrm{NGP}}) \\ \sin(\alpha_{\mathrm{GC}})\cos(\delta_{\mathrm{GC}}) & \begin{array}{c}\sin(\delta_{\mathrm{NGP}})\cos(\alpha_{\mathrm{GC}})\cos(\delta_{\mathrm{GC}})- \\ \cos(\alpha_{\mathrm{NGP}})\cos(\delta_{\mathrm{NGP}})\sin(\delta_{\mathrm{GC}})\end{array} & \sin(\alpha_{\mathrm{NGP}})\cos(\delta_{\mathrm{NGP}}) \\ \sin(\delta_{\mathrm{GC}}) & \cos(\delta_{\mathrm{GC}})\cos(\delta_{\mathrm{NGP}})\sin(\alpha_{\mathrm{GC}} - \alpha_{\mathrm{NGP}}) & \sin(\delta_{\mathrm{NGP}}) \end{bmatrix}$$

The Normal coordinate system is defined by the triad of unit vectors $[pqr]$, denoted $\mathbf{R}$. r points along the line of sight, and pq lie in the tangent plane with p pointing to the

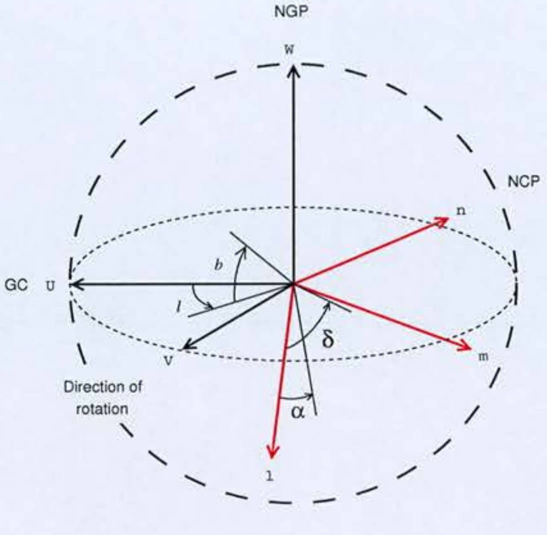

Figure B.1: Galactic and Equatorial triads

north celestial pole and q parallel to the equator with positive east. The transformation

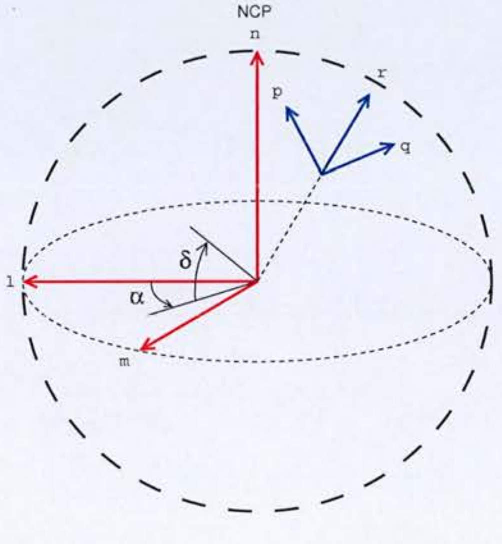

Figure B.2: Equatorial and Normal triads

between the normal and equatorial systems varies according to the line of sight, and is defined in terms of the equatorial coordinates (α_{TP},δ_{TP}) of the chosen tangent point by

$$\mathbf{N}^{\dagger}\mathbf{R} = \begin{bmatrix} -\sin(\alpha_{\mathrm{TP}}) & -\sin(\delta_{\mathrm{TP}})\cos(\alpha_{\mathrm{TP}}) & \cos(\delta_{\mathrm{TP}})\cos(\alpha_{\mathrm{TP}}) \\ \cos(\alpha_{\mathrm{TP}}) & -\sin(\delta_{\mathrm{TP}})\sin(\alpha_{\mathrm{TP}}) & \cos(\delta_{\mathrm{TP}})\sin(\alpha_{\mathrm{TP}}) \\ 0 & \cos(\delta_{\mathrm{TP}}) & \sin(\delta_{\mathrm{TP}}) \end{bmatrix}$$

B.2 The distribution of stellar velocities in the Solar neighbourhood

Ignoring the effect of differential rotation, the peculiar velocity of a star relative to the LSR can be expressed as the sum of a mean velocity and a residual velocity:

$$\underline{v} = \langle \underline{v} \rangle + \underline{\eta}$$

The mean velocity vector differs between the kinematic populations within the Galaxy, and is characterised mainly by an *asymmetric drift*, the tendency for the mean rotation velocity of stars to lag behind that of the LSR. The residual velocity vector $\underline{\eta}$ is assumed to follow a Schwarzschild distribution of the form

$$\mathcal{S}(\underline{\eta}) = \left(\frac{1}{2\pi}\right)^{\frac{3}{2}} \left(\frac{1}{|\mathbf{\Sigma}|}\right)^{\frac{1}{2}} \exp(\frac{-1}{2}\underline{\eta}^{\dagger}\mathbf{\Sigma}^{-1}\underline{\eta}) \tag{B.1}$$

where $\mathbf{\Sigma}$ denotes the covariance matrix for the components of the residual velocity, and defines the *velocity ellipsoid* for a given kinematic population. In a frame constructed from unit vectors pointing along the axes of the velocity ellipsoid, $\mathbf{\Sigma}$ is diagonal. It is conventional to assume that the principal axes of the velocity ellipsoid point along the axes of the Galactic coordinate system. Any difference is referred to as *vertex deviation*, and is likely to be small. In this case, $\mathbf{\Sigma}$ is diagonal in the Galactic frame, and can be written

$$\mathbf{\Sigma} = \mathbf{G} \begin{bmatrix} \sigma_U^2 & 0 & 0 \\ 0 & \sigma_V^2 & 0 \\ 0 & 0 & \sigma_W^2 \end{bmatrix} \mathbf{G}^{\dagger}$$

It is worth pointing out that in the case where $\sigma_U^2 = \sigma_V^2 = \sigma_W^2$, $\mathcal{S}(\underline{\eta})$ reduces to the Maxwell-Boltzmann velocity distribution.

B.3 Obtaining the velocity ellipse in the tangent plane

Transforming $\underline{\eta}$ and $\mathbf{\Sigma}$ to the normal triad gives the distribution of residual velocities along the line of sight and in the tangent plane, written as

$$\underline{\eta} = \mathbf{R} \begin{bmatrix} \eta_p \\ \eta_q \\ \eta_r \end{bmatrix} \qquad \mathbf{\Sigma} = \mathbf{R} \begin{bmatrix} C_{pp} & C_{pq} & C_{rp} \\ C_{pq} & C_{qq} & C_{qr} \\ C_{rp} & C_{qr} & C_{rr} \end{bmatrix} \mathbf{R}^{\dagger} \tag{B.2}$$

Because $\mathbf{\Sigma}$ has trixial asymmetry, different lines of sight see different velocity distributions. The bivariate distribution of η_p and η_q in the tangent plane is called the *velocity ellipse*, and is obtained by marginalising $\mathcal{S}(\underline{\eta})$ over the radial velocity η_r. Explicitly,

$$\mathcal{S}(\underline{\eta}) = \left(\frac{1}{2\pi}\right)^{\frac{3}{2}} \left(\frac{1}{|\mathbf{\Sigma}|}\right)^{\frac{1}{2}} \exp\left(\frac{-1}{2} \begin{bmatrix} \eta_p & \eta_q & \eta_r \end{bmatrix} \begin{bmatrix} c_{pp} & c_{pq} & c_{rp} \\ c_{pq} & c_{qq} & c_{qr} \\ c_{rp} & c_{qr} & c_{rr} \end{bmatrix} \begin{bmatrix} \eta_p \\ \eta_q \\ \eta_r \end{bmatrix}\right)$$

where c_{ij} denote elements of the matrix $\mathbf{\Sigma}^{-1}$ referred to the triad $\mathbf{R}$. This can be written

$$\mathcal{S}(\underline{\eta}) = \left(\frac{1}{2\pi}\right)^{\frac{3}{2}} \left(\frac{1}{|\mathbf{\Sigma}|}\right)^{\frac{1}{2}} \exp\left(\frac{C_{qq}\eta_p^2 + C_{pp}\eta_q^2 + 2C_{pq}\eta_p\eta_q}{2(C_{pq}^2 - C_{pp}C_{qq})}\right) \exp\left(\frac{-c_{rr}}{2}\left(\eta_r + \frac{c_{qr}\eta_q + c_{rp}\eta_p}{c_{rr}}\right)^2\right)$$

which can be integrated over all η_r to obtain the velocity ellipse

$$\mathcal{S}_{pq} = \left(\frac{1}{C_{pp}C_{qq} - C_{pq}^2}\right)^{\frac{1}{2}} \frac{1}{2\pi} \exp\left(\frac{C_{qq}\eta_p^2 + C_{pp}\eta_q^2 + 2C_{pq}\eta_p\eta_q}{2(C_{pq}^2 - C_{pp}C_{qq})}\right)$$

B.4 Correcting for the mean motion and obtaining $\mathbf{P}(v_{tan})$

The mean motion of the Sun relative to a given kinematic population is simply the difference between the solar motion and the mean population velocity relative to the LSR;

$$\langle \underline{v_{\odot}} \rangle = \underline{v_{\odot}} - \langle \underline{v} \rangle$$

The contribution to the tangent plane velocity of a star that arises from the relative solar motion can be found by referring $\langle \underline{v_{\odot}} \rangle$ to the normal triad

$$\langle \underline{v_{\odot}} \rangle = \mathbf{R} \begin{bmatrix} \langle \underline{v_{\odot}} \rangle_p \\ \langle \underline{v_{\odot}} \rangle_q \\ \langle \underline{v_{\odot}} \rangle_r \end{bmatrix}$$

The velocity ellipse is now transformed to P(v_{tan}, θ), the bivariate distribution of tangential velocity and position angle, using the prescription

$$\eta_p \longrightarrow v_{tan} \sin(\theta) + \langle \underline{v_{\odot}} \rangle_p$$
$$\eta_q \longrightarrow v_{tan} \cos(\theta) + \langle \underline{v_{\odot}} \rangle_q,$$

and the distribution over v_{tan} can be obtained by marginalising over θ

$$P(v_{tan}) = \int_0^{2\pi} P(v_{tan}, \theta).d\theta$$

In practise this must be done numerically, and is implemented in this work using the trapezium rule with Richardson's extrapolation to reduce higher order errors.

APPENDIX C

Spectroscopic Data for Catalogue Objects

In this Appendix I present astrometric, photometric and spectroscopic data, including spectral classifications where possible, for 75 objects included in my observational follow-up campaign that are present in the final white dwarf catalogue.

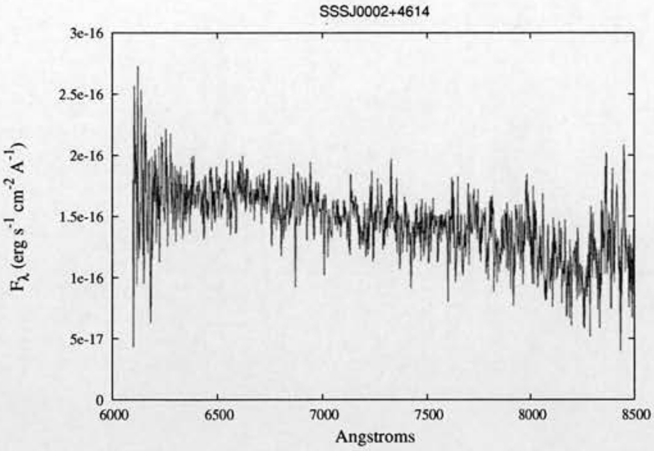
SSSJ0002+4614

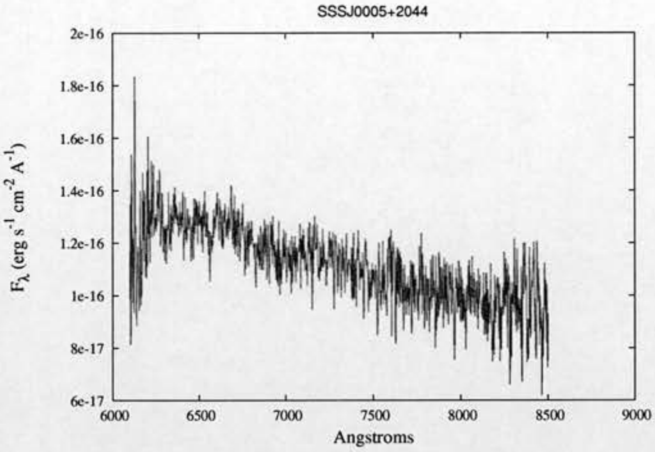
SSSJ0005+2044

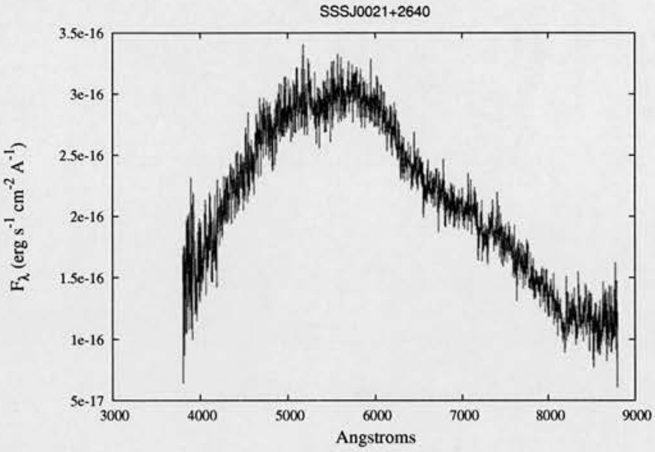
SSSJ0021+2640

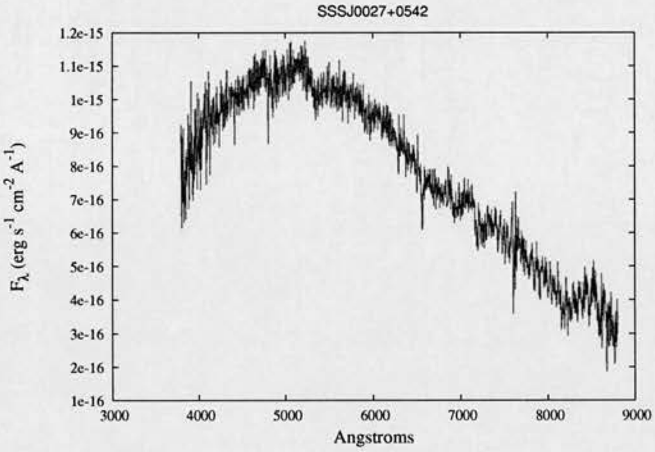
SSSJ0027+0542

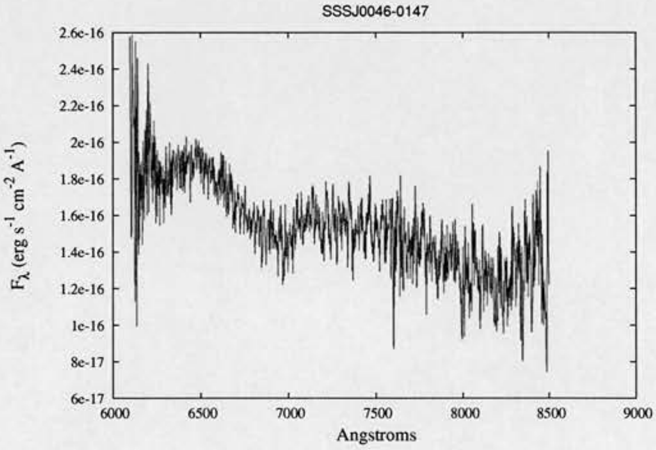
SSSJ0046-0147

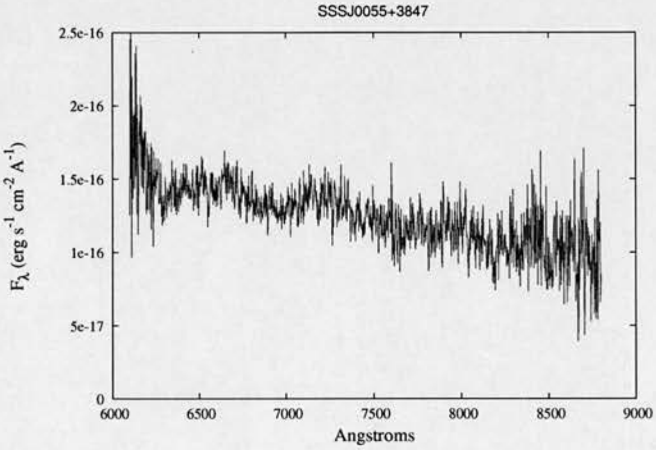
SSSJ0055+3847

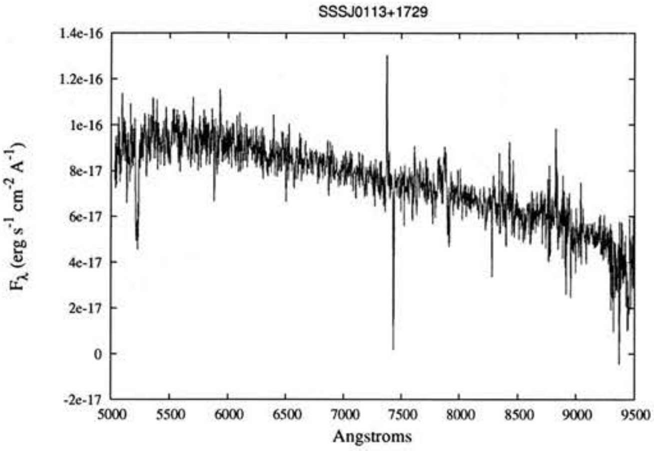
SSSJ0113+1729

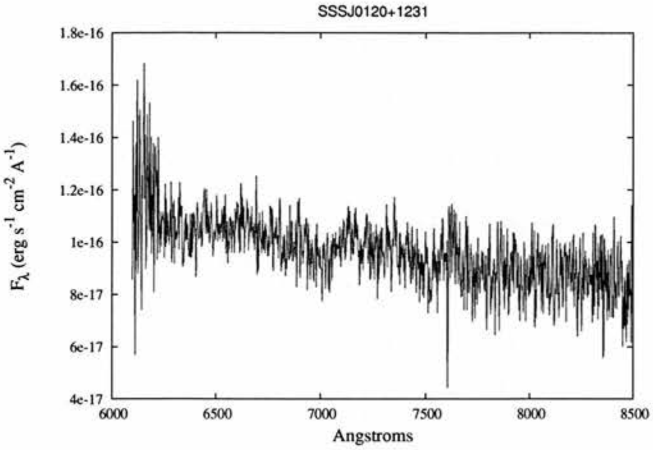
SSSJ0120+1231

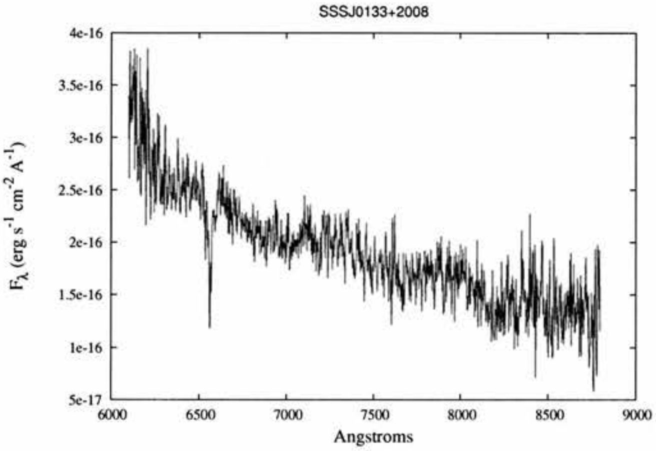
SSSJ0133+2008

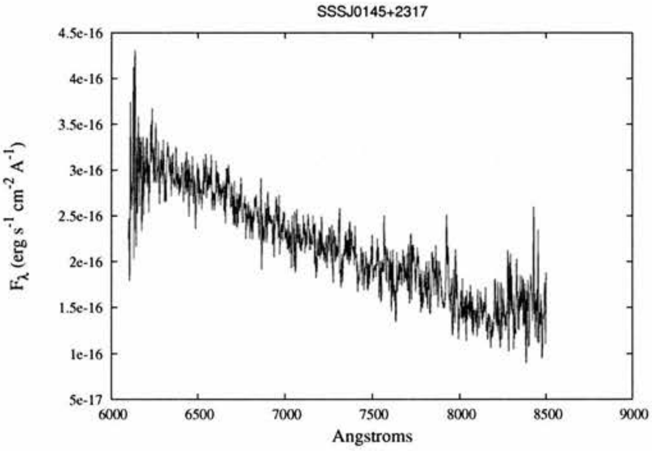
SSSJ0145+2317

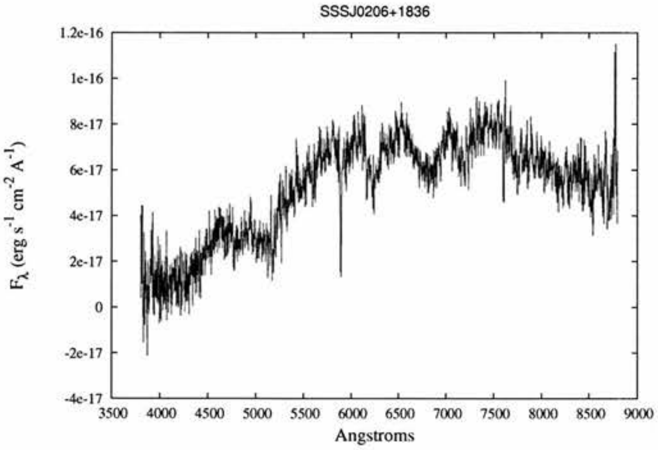
SSSJ0206+1836

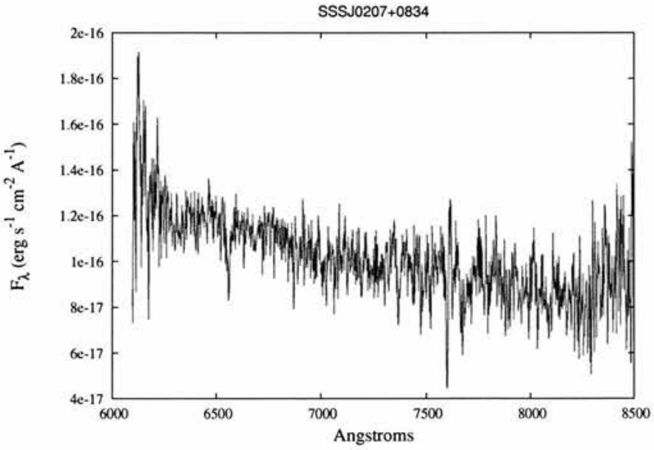
SSSJ0207+0834

SSSJ0207+1111

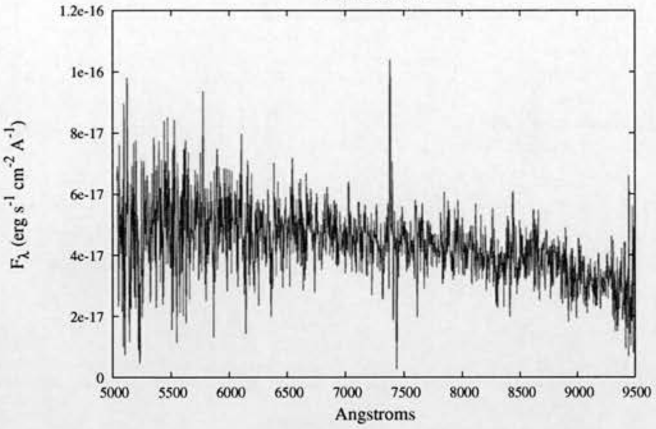

SSSJ0224-2854

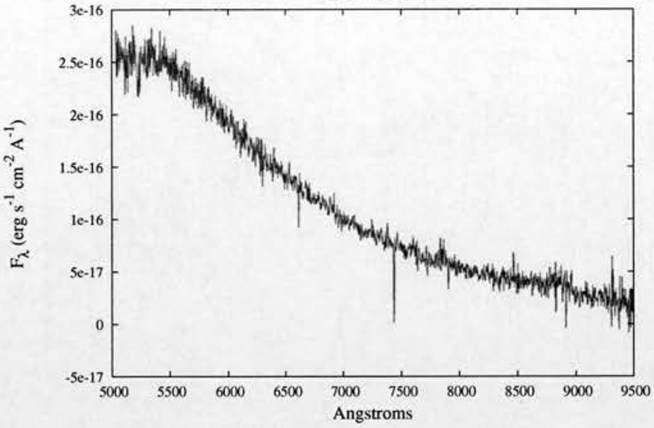

SSSJ0231+1751

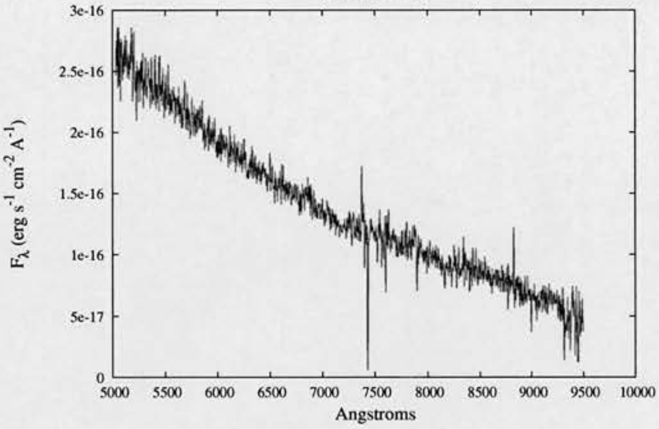

SSSJ0233+2125

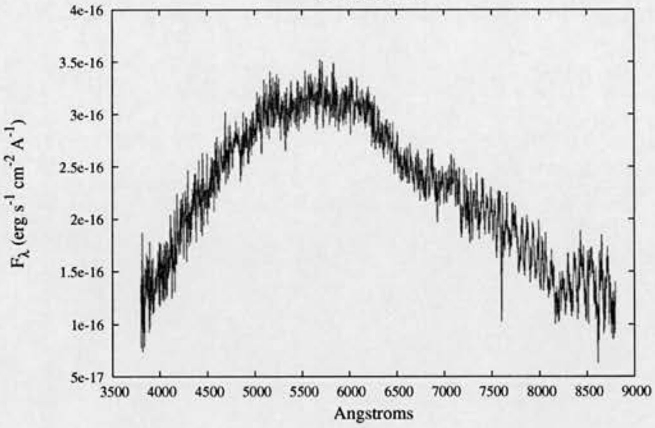

SSSJ0235+0729

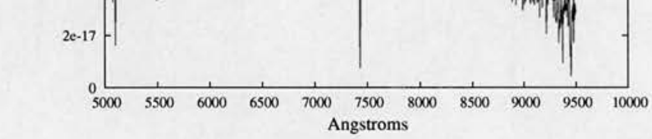

SSSJ0307+1529

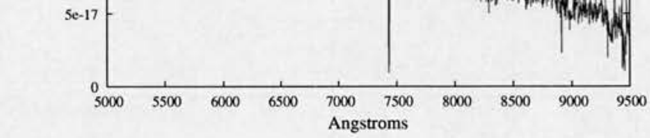

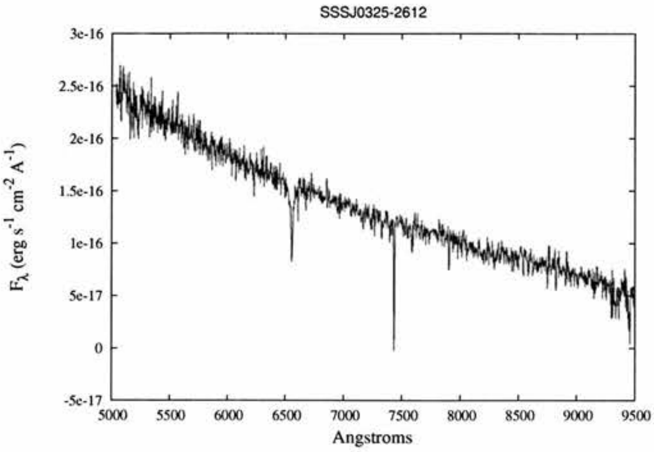
SSSJ0325-2612
F_λ (erg s^{-1} cm^{-2} A^{-1})
Angstroms
3e-16
2.5e-16
2e-16
1.5e-16
1e-16
5e-17
0
-5e-17
5000
5500
6000
6500
7000
7500
8000
8500
9000
9500

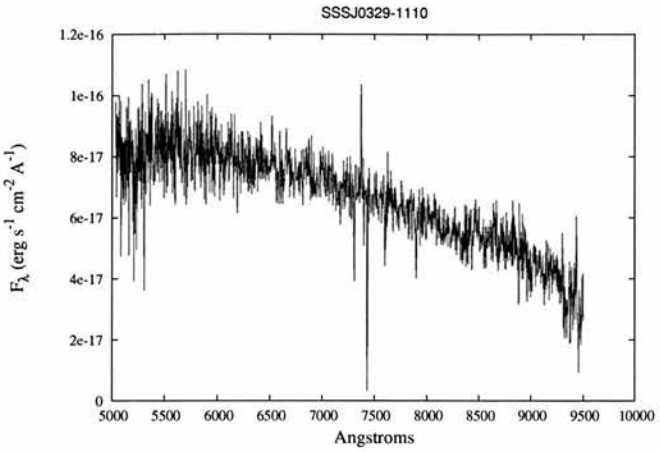
SSSJ0329-1110
F_λ (erg s^{-1} cm^{-2} A^{-1})
Angstroms
1.2e-16
1e-16
8e-17
6e-17
4e-17
2e-17
0
5000
5500
6000
6500
7000
7500
8000
8500
9000
9500
10000

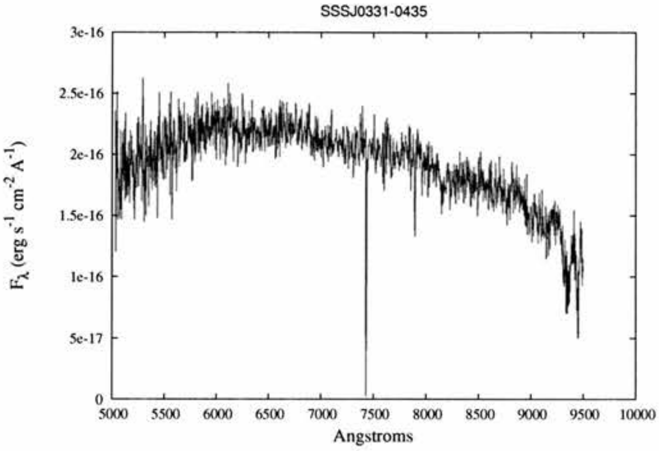
SSSJ0331-0435
F_λ (erg s^{-1} cm^{-2} A^{-1})
Angstroms
3e-16
2.5e-16
2e-16
1.5e-16
1e-16
5e-17
0
5000
5500
6000
6500
7000
7500
8000
8500
9000
9500
10000

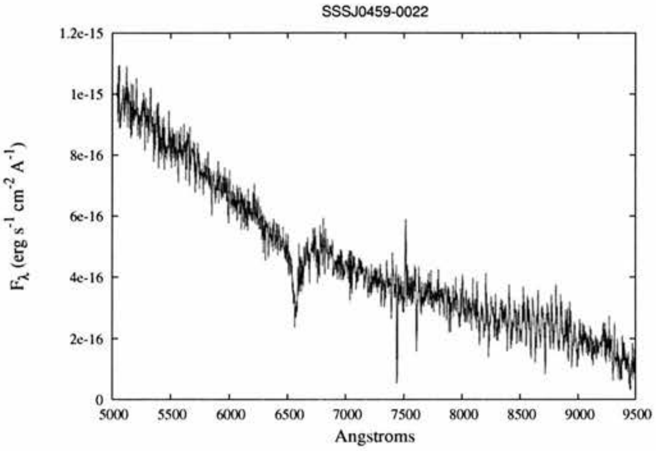
SSSJ0459-0022
F_λ (erg s^{-1} cm^{-2} A^{-1})
Angstroms
1.2e-15
1e-15
8e-16
6e-16
4e-16
2e-16
0
5000
5500
6000
6500
7000
7500
8000
8500
9000
9500

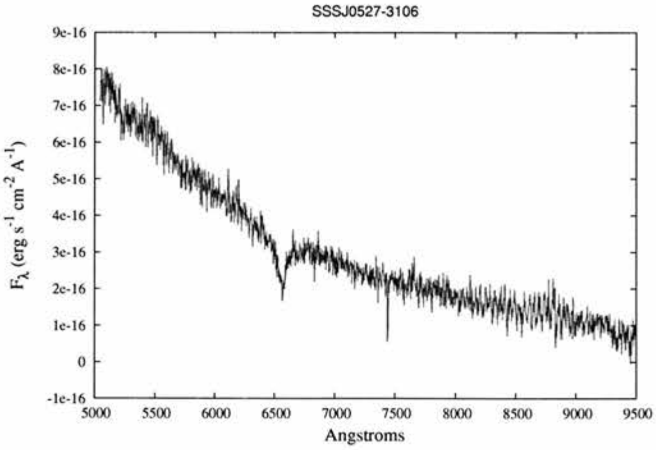
SSSJ0527-3106
F_λ (erg s^{-1} cm^{-2} A^{-1})
Angstroms
9e-16
8e-16
7e-16
6e-16
5e-16
4e-16
3e-16
2e-16
1e-16
0
-1e-16
5000
5500
6000
6500
7000
7500
8000
8500
9000
9500

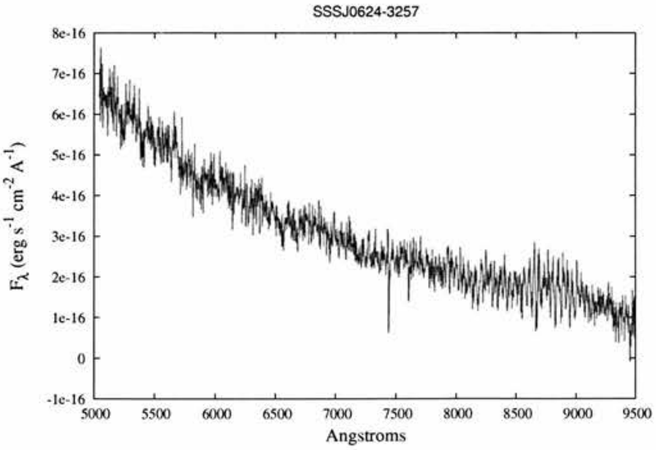
SSSJ0624-3257
F_λ (erg s^{-1} cm^{-2} A^{-1})
Angstroms
8e-16
7e-16
6e-16
5e-16
4e-16
3e-16
2e-16
1e-16
0
-1e-16
5000
5500
6000
6500
7000
7500
8000
8500
9000
9500

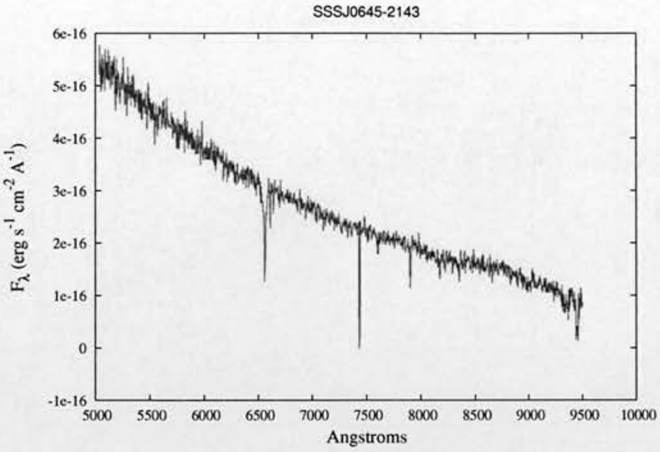
SSSJ0645-2143

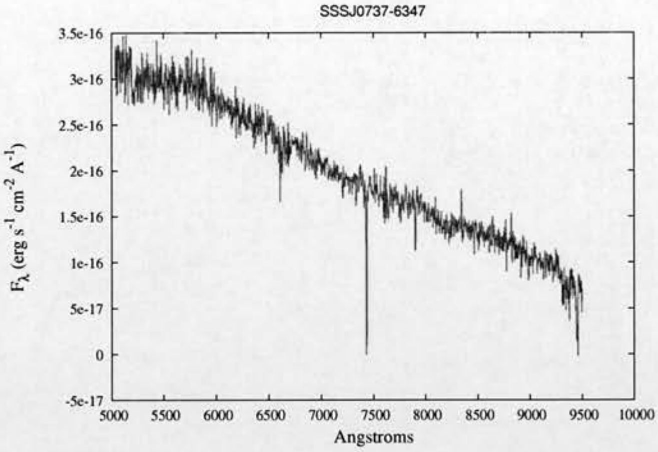
SSSJ0737-6347

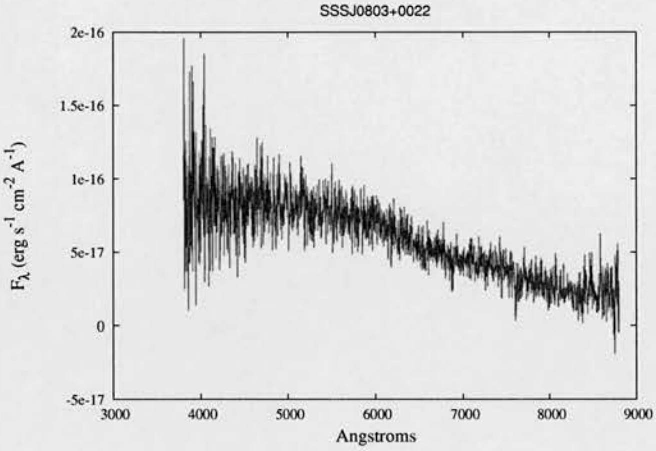
SSSJ0803+0022

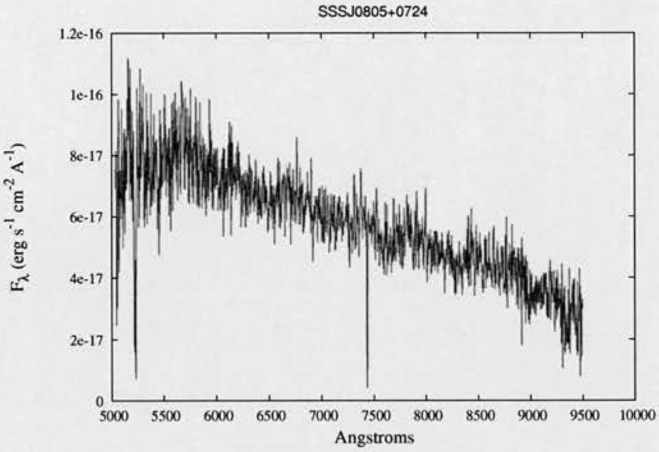
SSSJ0805+0724

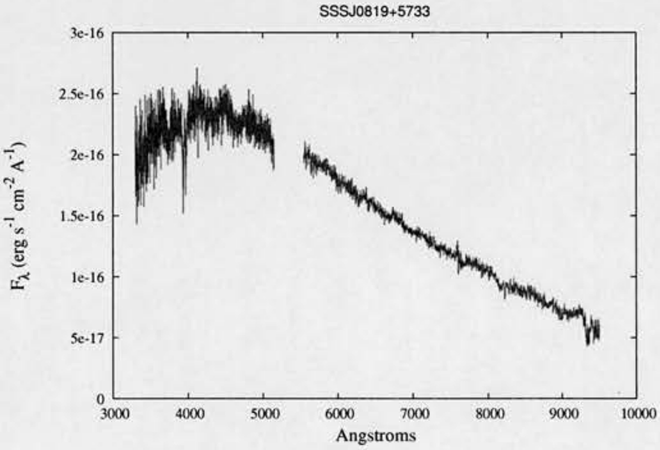
SSSJ0819+5733

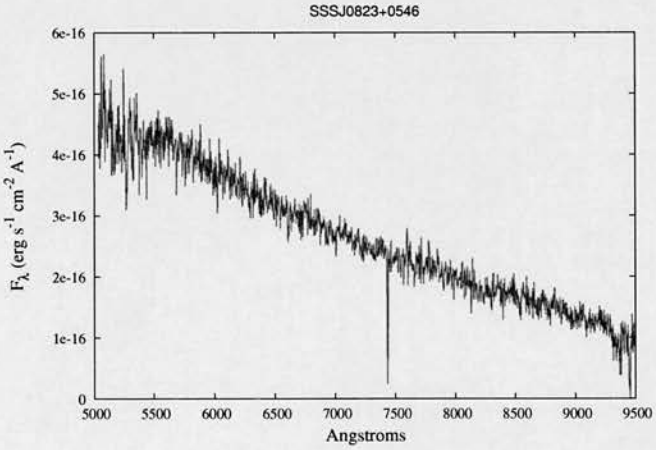
SSSJ0823+0546

SSSJ0903+0412

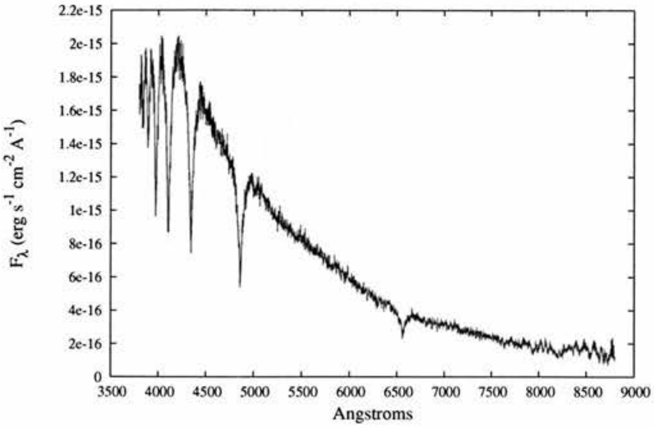

SSSJ1021-0234

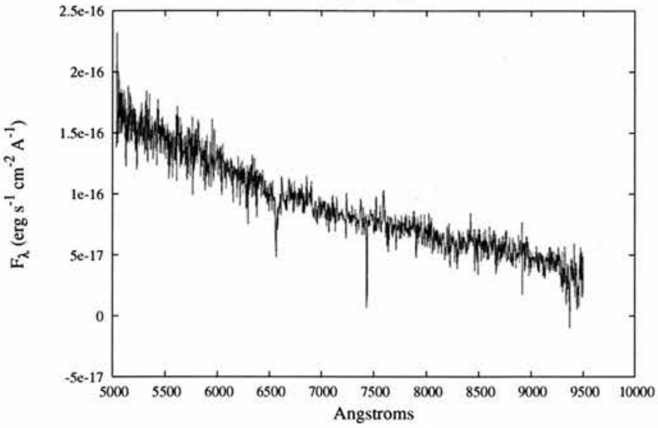

SSSJ1047+5912

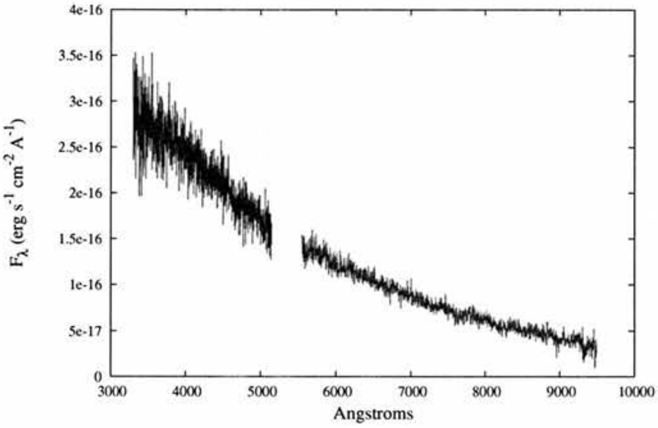

SSSJ1057+3208

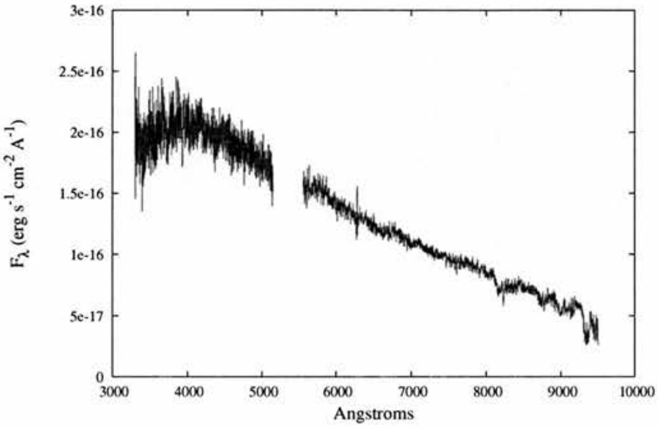

SSSJ1104+0436

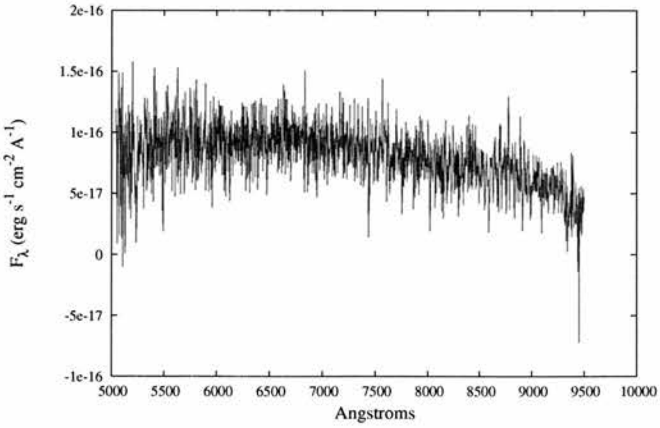

SSSJ1125+5704

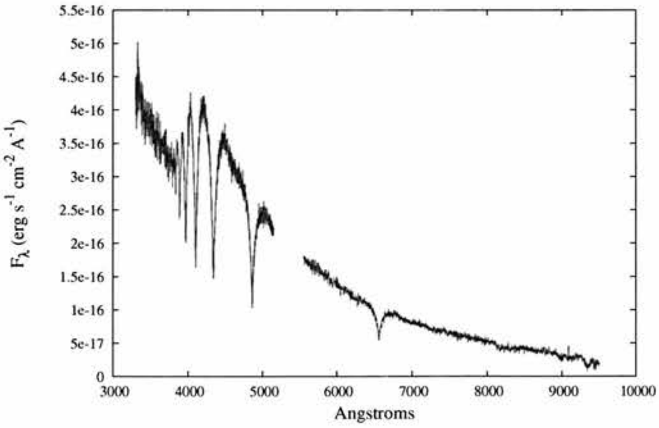

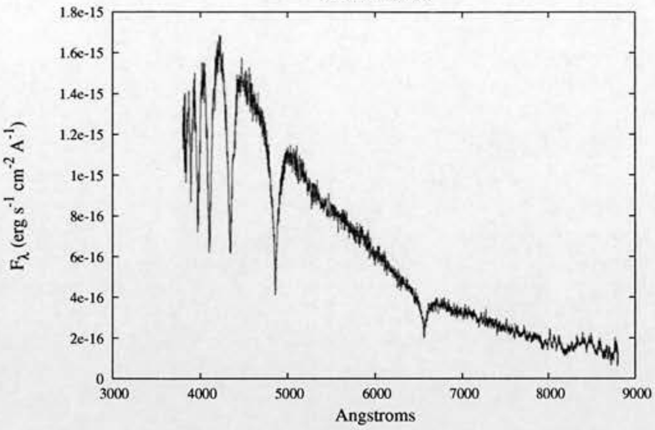
SSSJ1139+0310

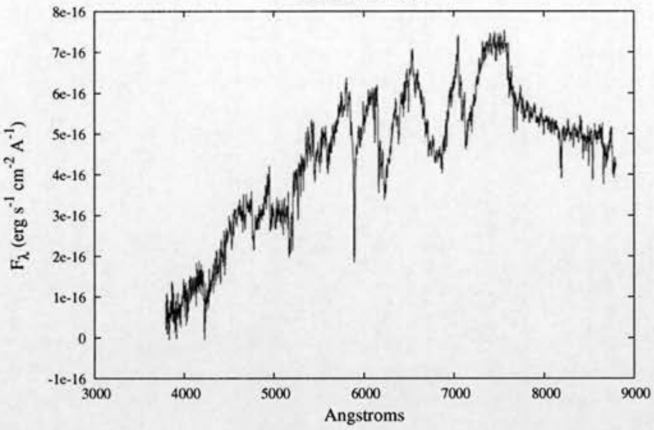
SSSJ1126+1433

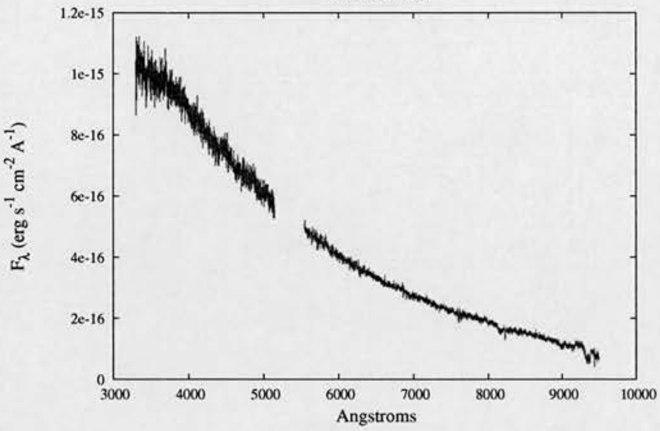
SSSJ1237+1814

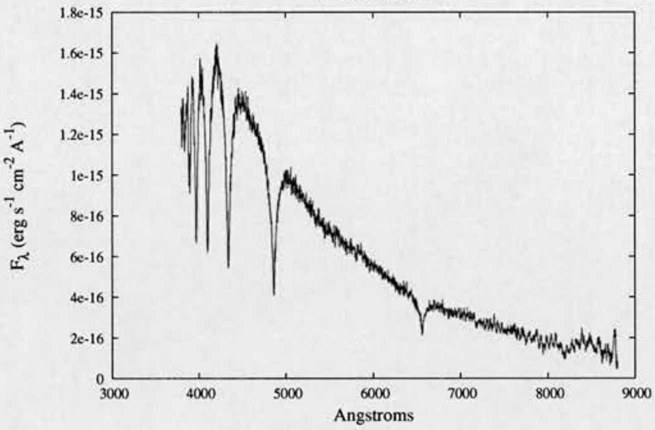
SSSJ1248+4153

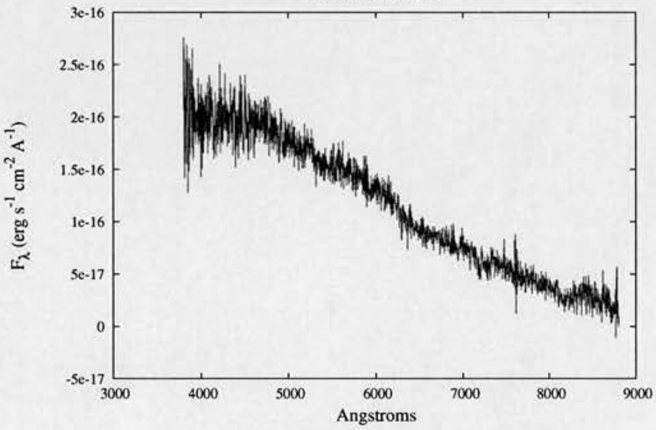
SSSJ1418-1157$_I$NT

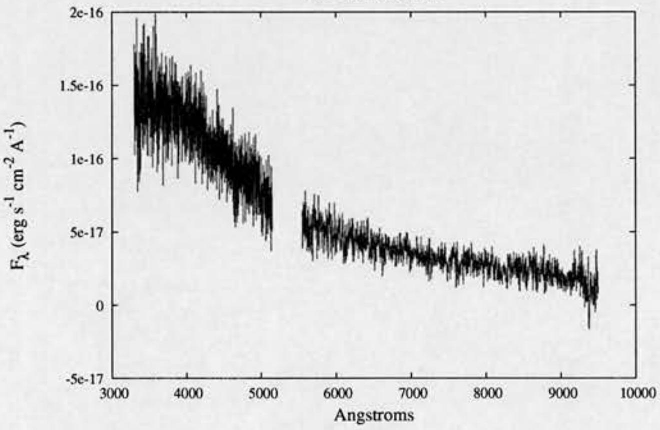
SSSJ1418-1157$_W$HT

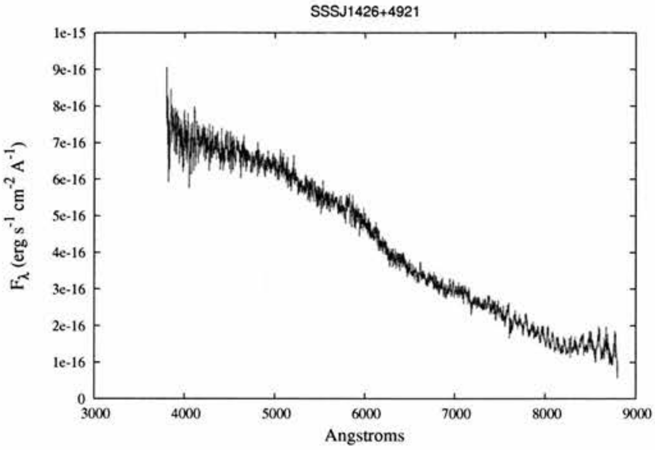
SSSJ1426+4921
F_λ (erg s^{-1} cm^{-2} A^{-1})
1e-15
9e-16
8e-16
7e-16
6e-16
5e-16
4e-16
3e-16
2e-16
1e-16
0
3000
4000
5000
6000
7000
8000
9000
Angstroms

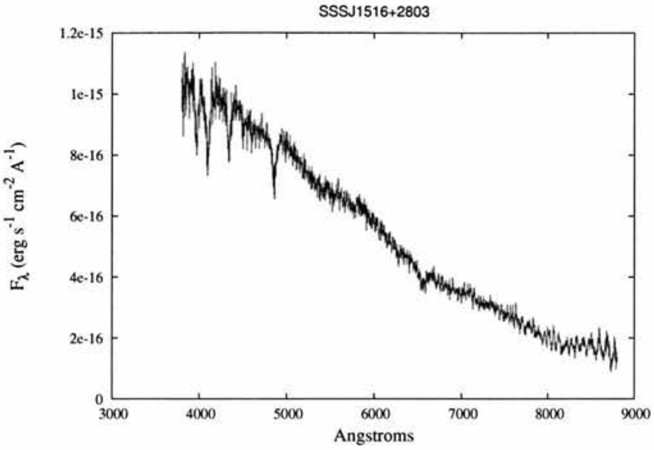
SSSJ1516+2803
F_λ (erg s^{-1} cm^{-2} A^{-1})
1.2e-15
1e-15
8e-16
6e-16
4e-16
2e-16
0
3000
4000
5000
6000
7000
8000
9000
Angstroms

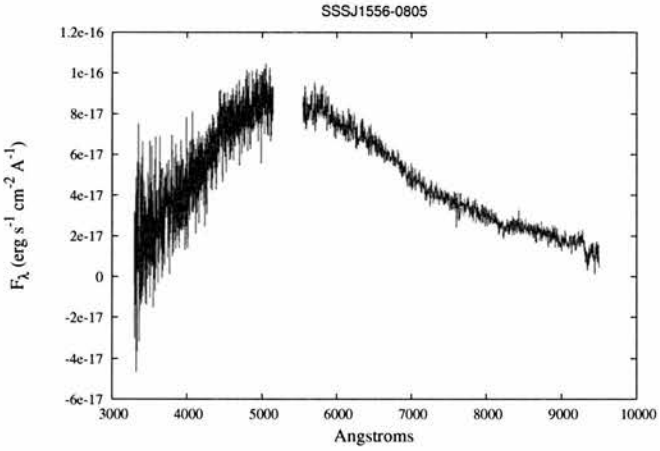
SSSJ1556-0805
F_λ (erg s^{-1} cm^{-2} A^{-1})
1.2e-16
1e-16
8e-17
6e-17
4e-17
2e-17
0
-2e-17
-4e-17
-6e-17
3000
4000
5000
6000
7000
8000
9000
10000
Angstroms

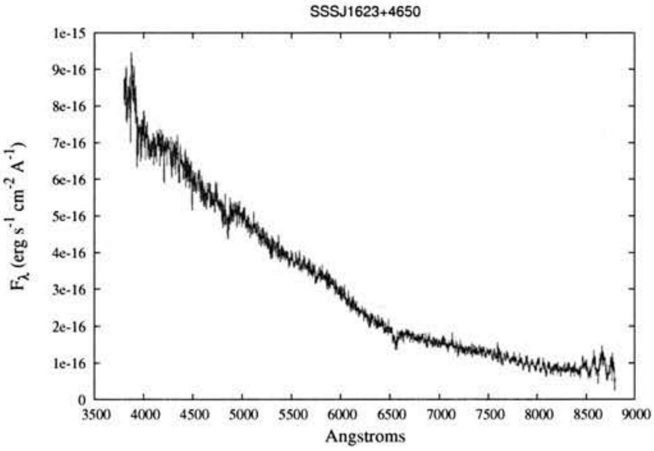
SSSJ1623+4650
F_λ (erg s^{-1} cm^{-2} A^{-1})
1e-15
9e-16
8e-16
7e-16
6e-16
5e-16
4e-16
3e-16
2e-16
1e-16
0
3500
4000
4500
5000
5500
6000
6500
7000
7500
8000
8500
9000
Angstroms

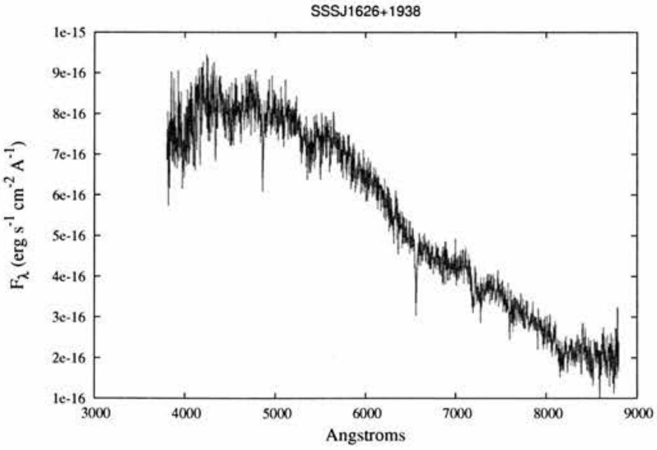
SSSJ1626+1938
F_λ (erg s^{-1} cm^{-2} A^{-1})
1e-15
9e-16
8e-16
7e-16
6e-16
5e-16
4e-16
3e-16
2e-16
1e-16
3000
4000
5000
6000
7000
8000
9000
Angstroms

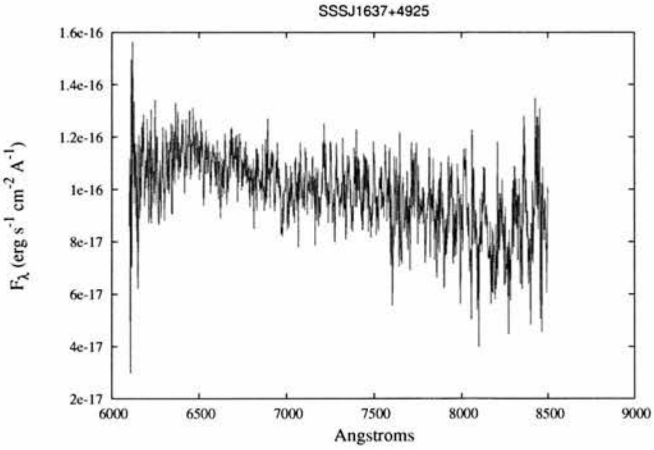
SSSJ1637+4925
F_λ (erg s^{-1} cm^{-2} A^{-1})
1.6e-16
1.4e-16
1.2e-16
1e-16
8e-17
6e-17
4e-17
2e-17
6000
6500
7000
7500
8000
8500
9000
Angstroms

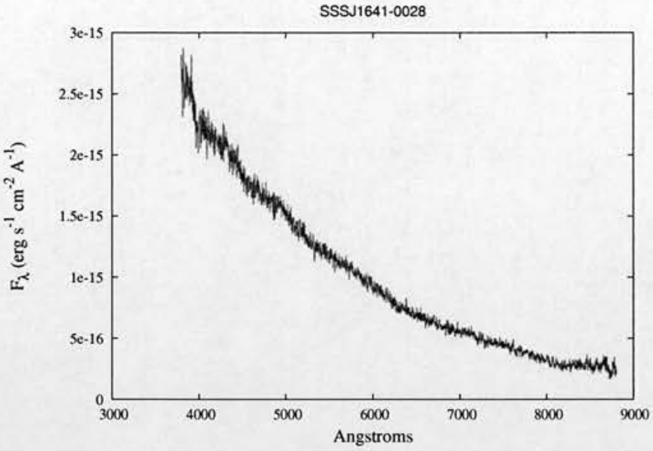
SSSJ1641-0028
F_λ (erg s^{-1} cm^{-2} A^{-1})
3e-15
2.5e-15
2e-15
1.5e-15
1e-15
5e-16
0
3000
4000
5000
6000
7000
8000
9000
Angstroms

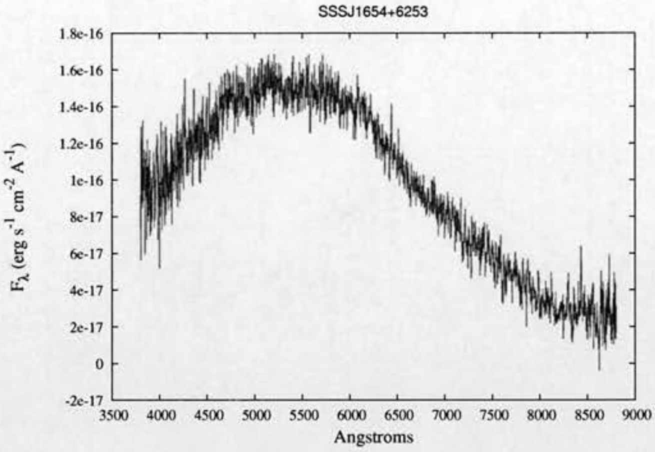
SSSJ1654+6253
F_λ (erg s^{-1} cm^{-2} A^{-1})
1.8e-16
1.6e-16
1.4e-16
1.2e-16
1e-16
8e-17
6e-17
4e-17
2e-17
0
-2e-17
3500
4000
4500
5000
5500
6000
6500
7000
7500
8000
8500
9000
Angstroms

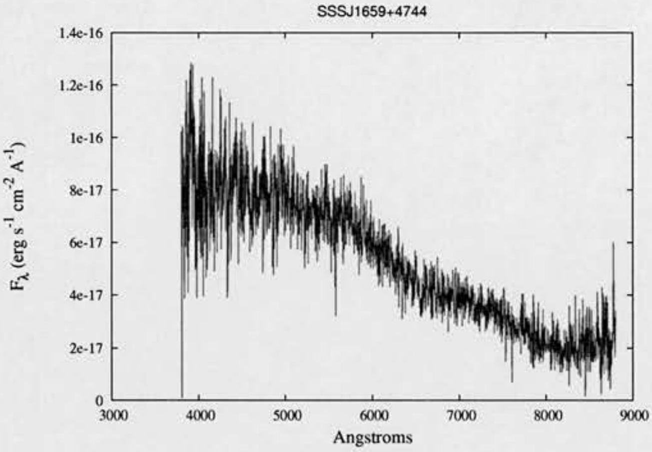
SSSJ1659+4744
F_λ (erg s^{-1} cm^{-2} A^{-1})
1.4e-16
1.2e-16
1e-16
8e-17
6e-17
4e-17
2e-17
0
3000
4000
5000
6000
7000
8000
9000
Angstroms

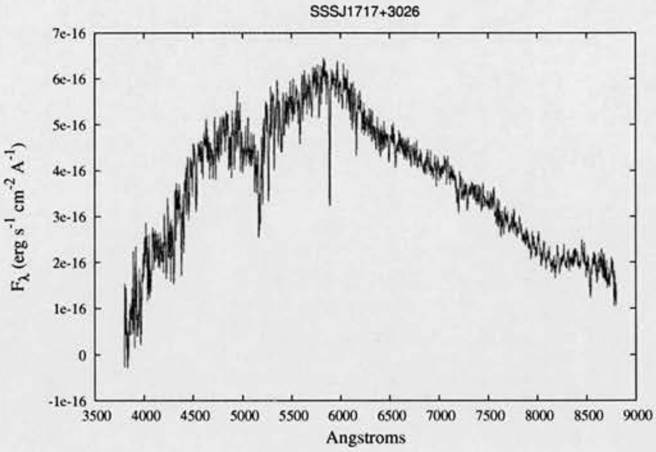
SSSJ1717+3026
F_λ (erg s^{-1} cm^{-2} A^{-1})
7e-16
6e-16
5e-16
4e-16
3e-16
2e-16
1e-16
0
-1e-16
3500
4000
4500
5000
5500
6000
6500
7000
7500
8000
8500
9000
Angstroms

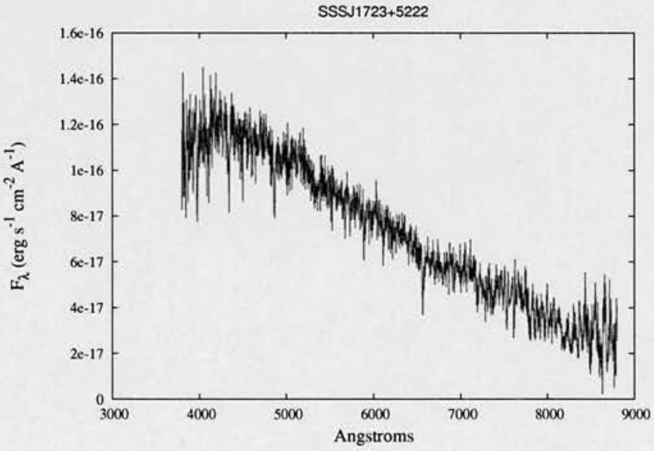
SSSJ1723+5222
F_λ (erg s^{-1} cm^{-2} A^{-1})
1.6e-16
1.4e-16
1.2e-16
1e-16
8e-17
6e-17
4e-17
2e-17
0
3000
4000
5000
6000
7000
8000
9000
Angstroms

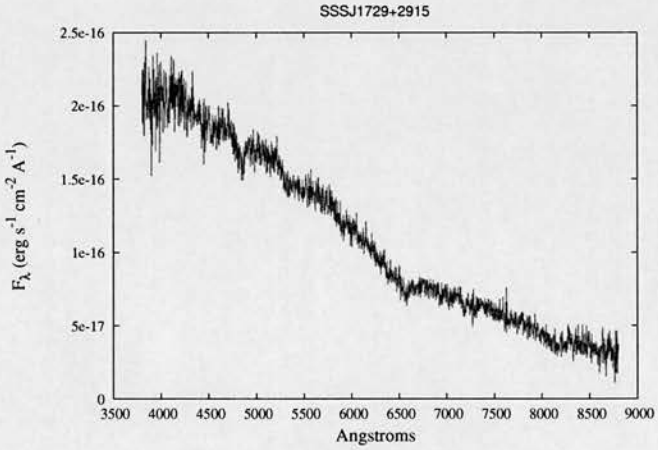
SSSJ1729+2915
F_λ (erg s^{-1} cm^{-2} A^{-1})
2.5e-16
2e-16
1.5e-16
1e-16
5e-17
0
3500
4000
4500
5000
5500
6000
6500
7000
7500
8000
8500
9000
Angstroms

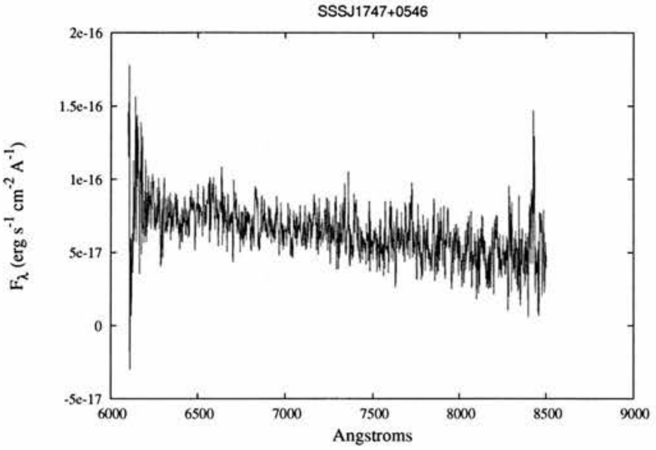
SSSJ1747+0546
F_λ (erg s^-1 cm^-2 A^-1)
2e-16
1.5e-16
1e-16
5e-17
0
-5e-17
6000
6500
7000
7500
8000
8500
9000
Angstroms

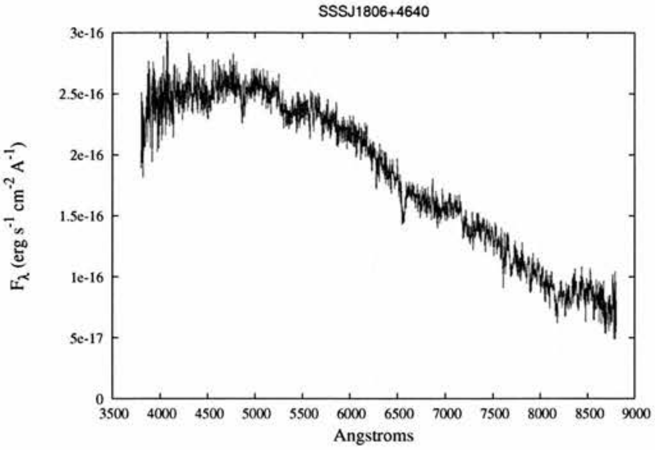
SSSJ1806+4640
F_λ (erg s^-1 cm^-2 A^-1)
3e-16
2.5e-16
2e-16
1.5e-16
1e-16
5e-17
0
3500
4000
4500
5000
5500
6000
6500
7000
7500
8000
8500
9000
Angstroms

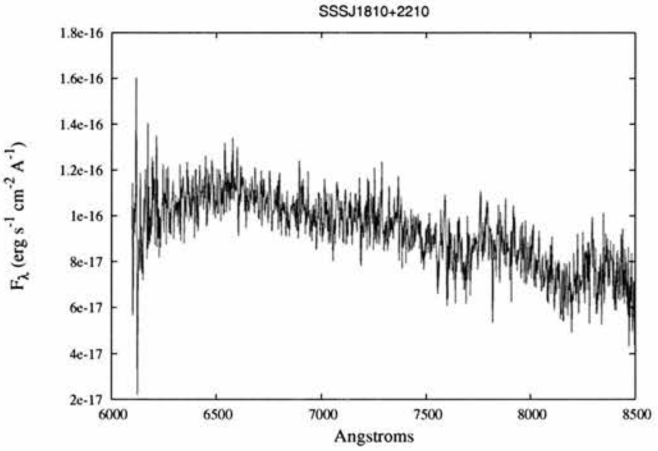
SSSJ1810+2210
F_λ (erg s^-1 cm^-2 A^-1)
1.8e-16
1.6e-16
1.4e-16
1.2e-16
1e-16
8e-17
6e-17
4e-17
2e-17
6000
6500
7000
7500
8000
8500
Angstroms

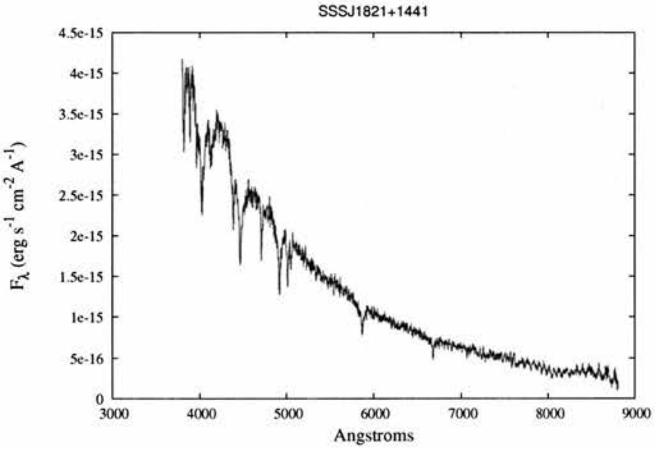
SSSJ1821+1441
F_λ (erg s^-1 cm^-2 A^-1)
4.5e-15
4e-15
3.5e-15
3e-15
2.5e-15
2e-15
1.5e-15
1e-15
5e-16
0
3000
4000
5000
6000
7000
8000
9000
Angstroms

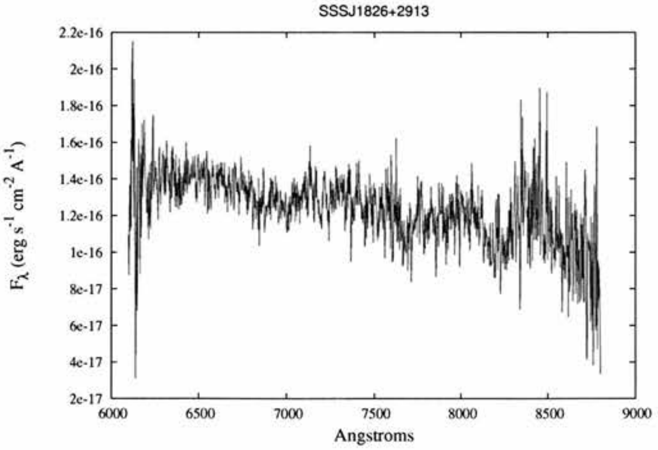
SSSJ1826+2913
F_λ (erg s^-1 cm^-2 A^-1)
2.2e-16
2e-16
1.8e-16
1.6e-16
1.4e-16
1.2e-16
1e-16
8e-17
6e-17
4e-17
2e-17
6000
6500
7000
7500
8000
8500
9000
Angstroms

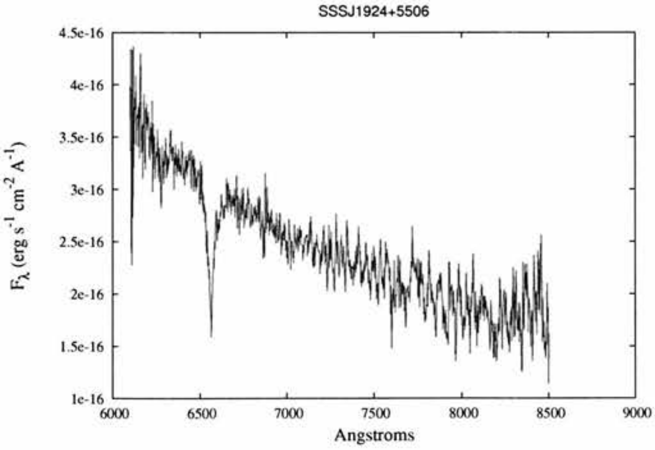
SSSJ1924+5506
F_λ (erg s^-1 cm^-2 A^-1)
4.5e-16
4e-16
3.5e-16
3e-16
2.5e-16
2e-16
1.5e-16
1e-16
6000
6500
7000
7500
8000
8500
9000
Angstroms

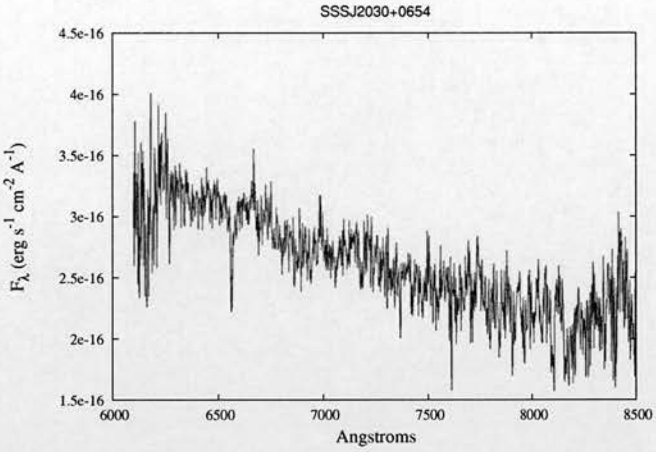

SSSJ2030+0654

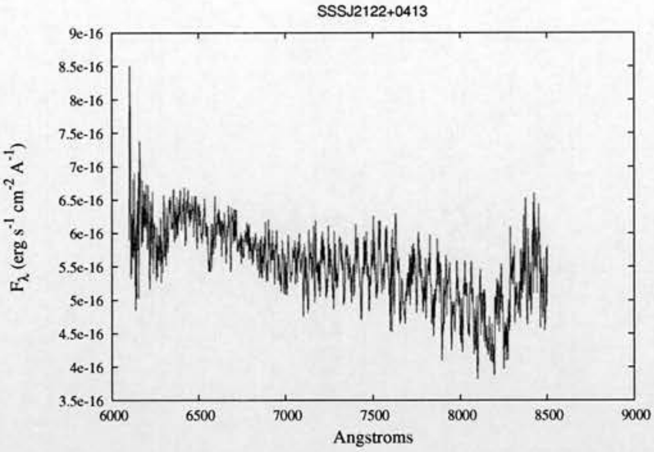

SSSJ2122+0413

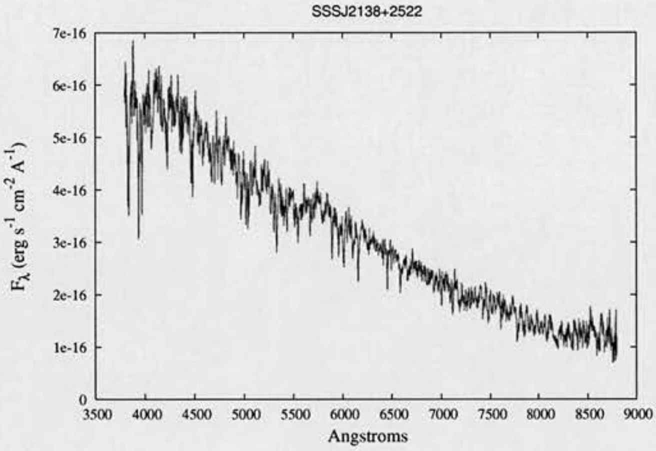

SSSJ2138+2522

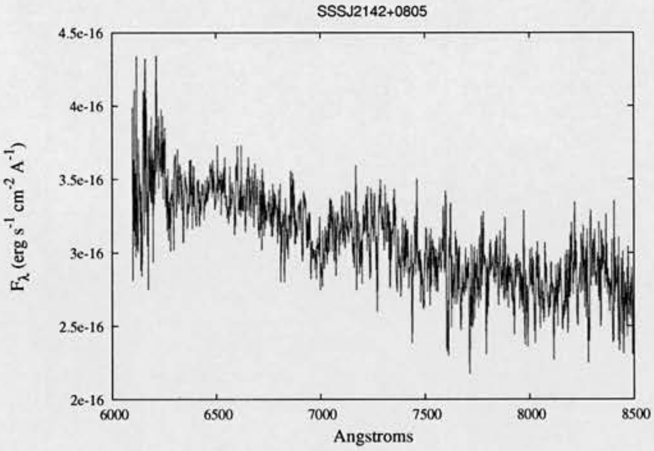

SSSJ2142+0805

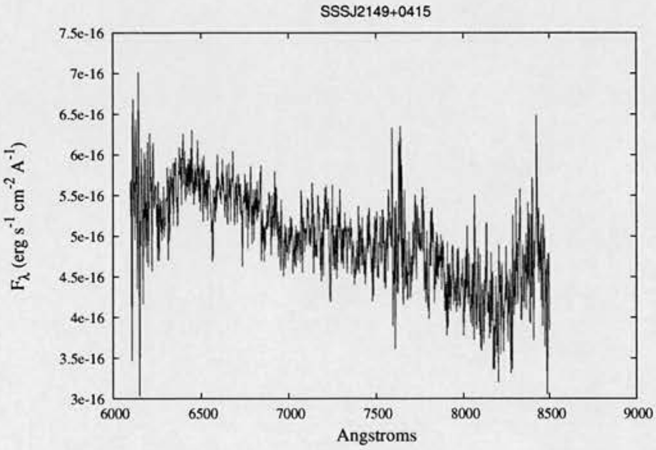

SSSJ2149+0415

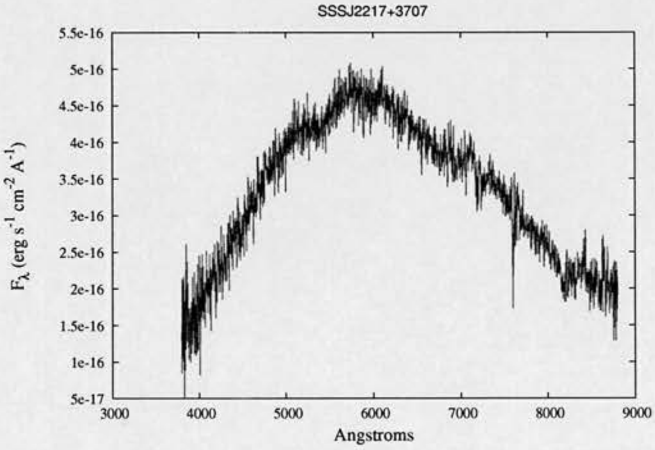

SSSJ2217+3707

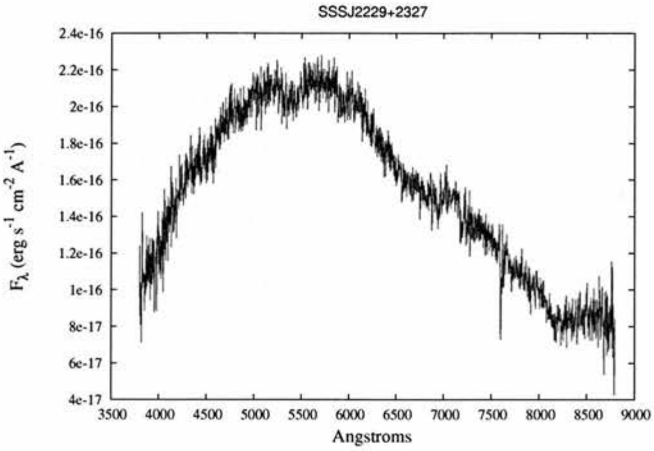

SSSJ2229+2327

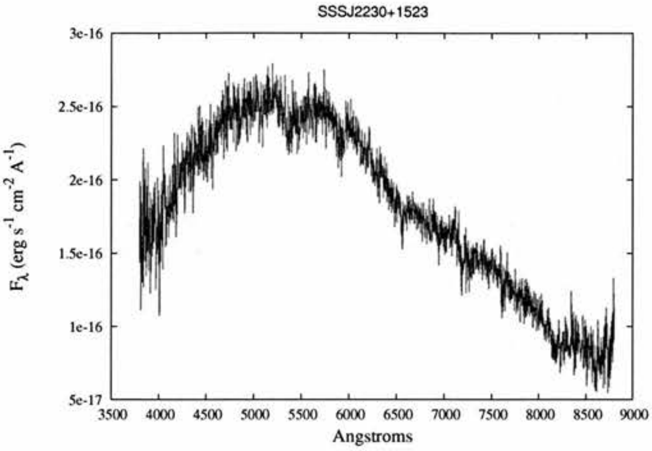

SSSJ2230+1523

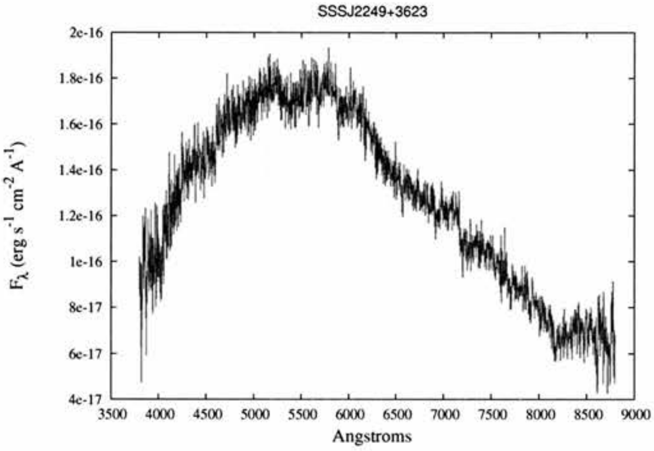

SSSJ2249+3623

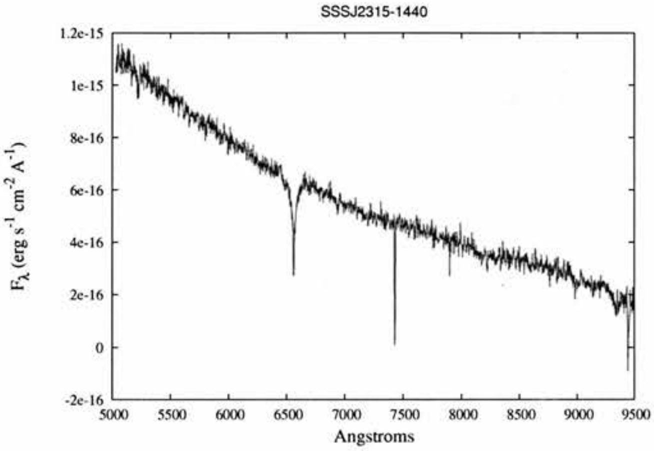

SSSJ2315-1440

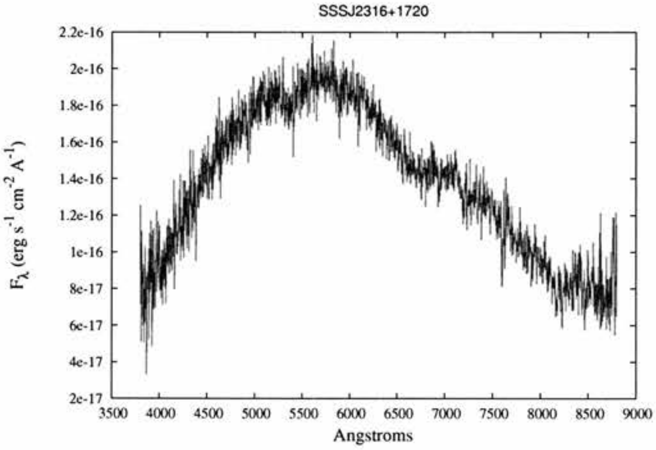

SSSJ2316+1720

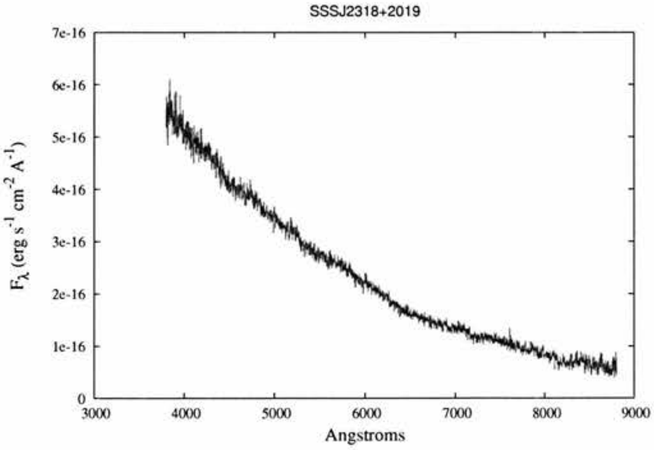

SSSJ2318+2019

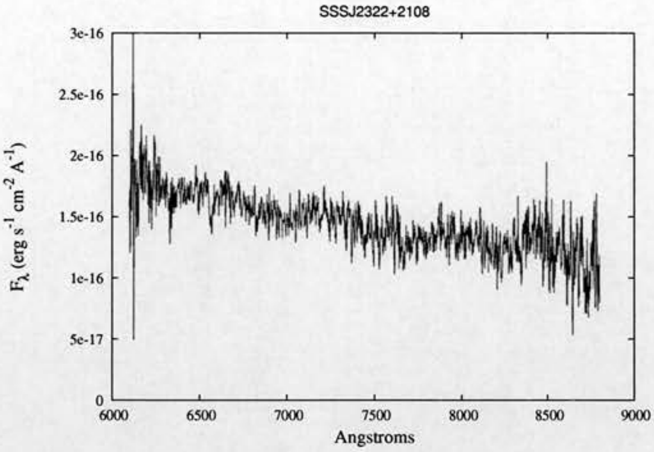
SSSJ2322+2108

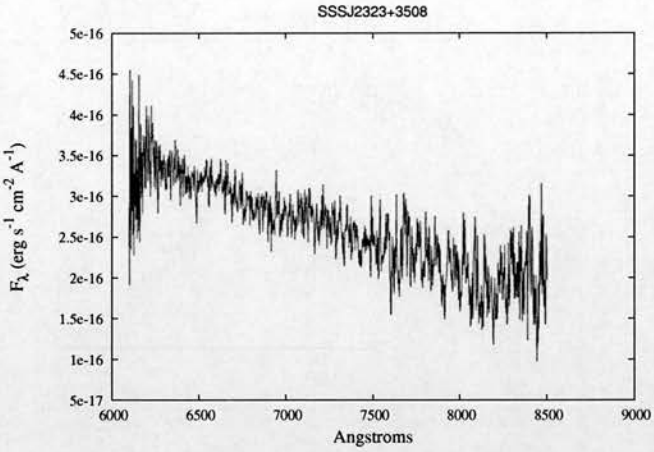
SSSJ2323+3508

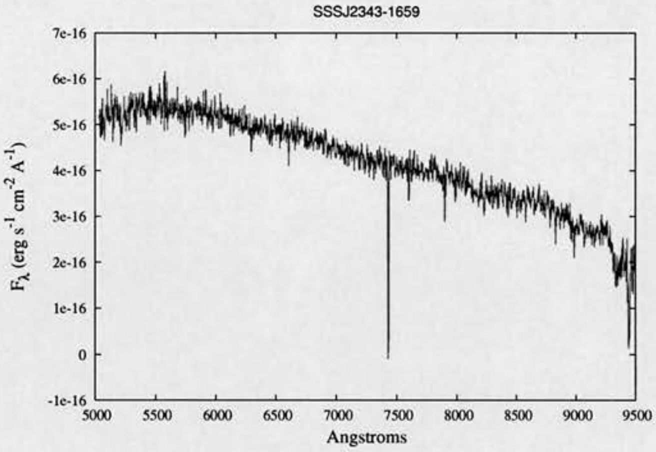
SSSJ2343-1659

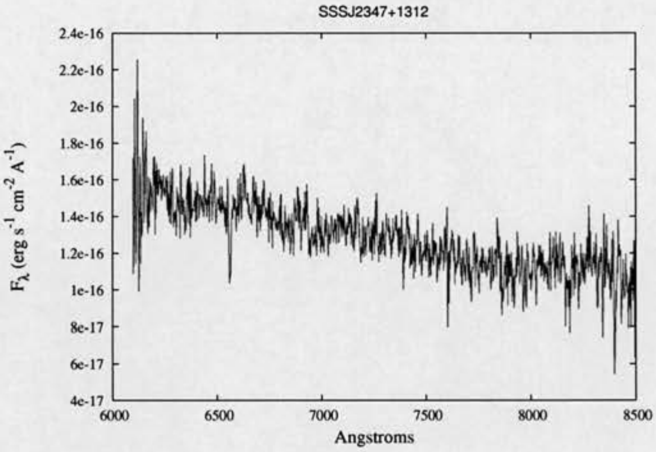
SSSJ2347+1312

Designation	$\alpha^{\dagger}$	δ	$\mu_\alpha \cos(\delta)$	μ_δ	Epoch	b_J	$b_J - r_{59F}$	$r_{59F} - i_N$	Sp. T
SSSJ0002+4614	00 02 53.9	+46 14 03	0.1993	-0.0067	1989.678	18.646	0.925	0.606	DC poor S/N
SSSJ0005+2044	00 05 25.9	+20 44 42	-0.3461	-0.2614	1991.772	18.765	0.823	0.203	DA (Hα)
SSSJ0021+2640	00 21 47.3	+26 40 36	-0.0828	-0.3054	1998.863	18.376	1.347	0.556	DC weak Hα?
SSSJ0027+0542	00 27 36.5	+05 42 06	0.2731	-0.2604	1990.79	16.964	0.930	0.446	DC weak Hα?
SSSJ0046-0147	00 46 37.5	-01 47 20	-0.0933	-0.2372	1988.842	18.255	0.759	0.512	DC poor S/N
SSSJ0055+3847	00 55 17.4	+38 47 55	-0.3976	-0.2382	1986.911	18.904	0.988	0.371	DA (Hα), poor S/N
SSSJ0113+1729	01 13 45.2	+17 29 01	0.1738	-0.0768	1989.844	19.27	0.835	0.099	DC
SSSJ0120+1231	01 20 39.7	+12 31 59	0.117	-0.2179	1989.844	19.221	1.116	0.277	DC poor S/N
SSSJ0133+2008	01 33 08.5	+20 08 13	0.2212	-0.0093	1990.719	17.798	0.501	0.204	DA
SSSJ0145+2317	01 45 19.3	+23 17 55	0.3111	-0.1035	1991.777	17.31	0.296	0.033	DC
SSSJ0206+1836	02 06 14.2	+18 36 23	0.7894	0.0969	1990.722	19.376	1.574	0.695	M
SSSJ0207+0834	02 07 57.4	+08 34 02	-0.1686	-0.1099	1991.692	19.028	0.956	0.087	DA
SSSJ0207+1111	02 07 19.3	+11 11 53	0.2824	0.1741	1991.692	19.925	1.221	-0.079	DC poor S/N
SSSJ0224-2854	02 24 32.2	-28 54 59	0.4896	-0.0372	1997.894	18.346	0.475	-0.600	LHS 1402
SSSJ0231+1751	02 31 55.7	+17 51 32	-0.1792	-0.1067	1990.785	18.288	0.145	-0.049	DC
SSSJ0233+2125	02 33 38.9	+21 25 15	0.0655	-0.2123	1990.785	18.396	1.340	0.283	DC H_2CIA?
SSSJ0235+0729	02 35 43.1	+07 29 57	-0.0041	-0.2423	1990.817	19.463	0.357	0.424	DQ
SSSJ0307+1529	03 07 04.7	+15 29 36	0.0608	-0.1737	1989.844	18.929	0.606	-0.165	DC
SSSJ0325-2612	03 25 30.0	-26 12 08	-0.0337	-0.2102	1992.989	18.127	0.589	0.013	DA

† Equinox 2000

SSSJ0329-1110	03 29 16.7	-11 10 18	0.1475	0.131	1997.75	19.518	1.029	0.102	DC weak Hα?
SSSJ0331-0435	03 31 52.5	-04 35 42	0.113	-0.258	1987.875	18.852	1.639	0.266	DC
SSSJ0459-0022	04 59 43.2	-00 22 39	0.1787	-0.2348	1999.858	15.153	0.167	0.140	DA
SSSJ0527-3106	05 27 24.4	-31 06 53	-0.1454	-0.3269	1992.766	16.058	0.030	0.050	DA
SSSJ0624-3257	06 24 25.8	-32 57 26	0.0079	-0.1981	1992.986	15.524	0.199	0.093	DC
SSSJ0645-2143	06 45 17.8	-21 43 09	0.0528	-0.2429	1995.095	17.543	0.560	0.066	DA
SSSJ0737-6347	07 37 30.7	-63 47 35	-0.2066	0.1993	1992.003	18.266	0.600	0.114	DA
SSSJ0803+0022	08 03 09.3	+00 22 38	-0.1049	-0.0413	1985.708	18.374	0.707	0.257	DC poor S/N
SSSJ0805+0724	08 05 58.9	+07 24 51	-0.0466	-0.2438	1990.911	19.773	1.009	0.898	DZ poor S/N
SSSJ0819+5733	08 19 15.2	+57 33 00	-0.1589	-0.1801	1989.976	18.199	0.539	0.217	DZ (CaII)
SSSJ0823+0546	08 23 03.9	+05 46 57	-0.2202	-0.0997	1996.883	17.917	0.960	0.154	DC
SSSJ0903+0412	09 03 16.8	+04 12 02	-0.0085	-0.0900	1986.569	16.241	-0.168	-0.037	DA
SSSJ1021-0234	10 21 31.1	-02 34 51	-0.1475	-0.1196	1986.25	18.377	0.374	-0.086	DA
SSSJ1047+5912	10 47 35.1	+59 12 51	-0.0608	-0.1831	1991.292	17.782	0.225	-0.181	DC
SSSJ1057+3208	10 57 51.1	+32 08 39	-0.0745	-0.1812	1998.39	18.371	0.289	0.123	DZ
SSSJ1104+0436	11 04 01.0	+04 36 19	0.0943	-0.385	1995.161	19.956	1.566	0.313	DC poor S/N
SSSJ1125+5704	11 25 31.2	+57 04 09	-0.0306	-0.2477	1993.319	18.003	0.017	-0.329	DA
SSSJ1126+1433	11 26 34.7	+14 33 39	0.0118	-0.0775	1991.342	18.641	0.738	0.111	M1
SSSJ1139+0310	11 39 26.7	+03 10 20	-0.0482	0.0314	1991.673	16.615	0.170	0.027	DA
SSSJ1237+1814	12 37 00.9	+18 14 59	-0.1783	-0.1382	1996.368	16.887	0.243	-0.222	DC

SSSJ1248+4153	12 48 47.6	+41 53 09	-0.0135	-0.0830	1990.147	16.295	0.019	-0.053	DA
SSSJ1418-1157	14 18 44.1	-11 57 14	-0.1798	-0.0212	1985.228	18.112	0.402	-0.129	DC
SSSJ1426+4921	14 26 59.5	+49 21 00	-0.1020	0.0316	1992.843	17.014	0.504	0.269	DC
SSSJ1516+2803	15 16 25.2	+28 03 21	-0.1018	-0.0108	1987.933	17.214	0.536	0.078	DA
SSSJ1556-0805	15 56 47.3	-08 05 60	0.3724	-0.1955	1992.48	18.8	0.960	-0.218	DC
SSSJ1623+4650	16 23 45.3	+46 50 43	-0.0214	-0.0392	1990.423	16.994	-0.004	0.058	DA
SSSJ1626+1938	16 26 26.4	+19 38 38	-0.1755	0.2155	1991.439	17.125	0.842	0.284	MS - A?
SSSJ1637+4925	16 37 32.0	+49 25 12	-0.0368	0.2377	1992.425	19.389	1.309	0.448	DC poor S/N
SSSJ1641-0028	16 41 16.5	-00 28 18	0.0427	-0.0897	1983.381	15.651	-0.032	0.186	DC
SSSJ1654+6253	16 54 01.8	+62 53 54	-0.5433	0.1301	1993.618	18.709	1.028	-0.456	LHS 3250
SSSJ1659+4744	16 59 13.6	+47 44 54	-0.0908	0.0460	1989.884	18.883	0.820	0.198	DC poor S/N
SSSJ1717+3026	17 17 47.8	+30 26 23	-0.0444	0.0313	1990.648	16.77	-0.031	0.072	sdK
SSSJ1723+5222	17 23 26.9	+52 22 43	-0.1231	-0.1743	1987.319	18.782	0.675	0.020	DA
SSSJ1729+2915	17 29 29.7	+29 15 56	-0.1672	-0.193	1993.486	18.572	0.528	0.005	DA
SSSJ1747+0546	17 47 12.4	+05 46 34	-0.1476	0.2286	1993.626	19.145	1.097	0.191	DC poor S/N
SSSJ1806+4640	18 06 02.9	+46 40 02	0.2434	0.1237	1991.602	18.254	0.665	0.638	DA
SSSJ1810+2210	18 10 34.1	+22 10 48	0.0806	-0.2651	1993.618	19.109	0.845	0.587	DC poor S/N
SSSJ1821+1441	18 21 39.0	+14 41 59	0.0424	-0.0413	1988.208	15.416	-0.290	-0.240	DB
SSSJ1826+2913	18 26 20.8	+29 13 53	0.1423	-0.2091	1989.341	19.476	1.216	0.377	DC poor S/N
SSSJ1924+5506	19 24 09.6	+55 06 47	0.0241	0.2005	1991.456	17.54	0.093	0.353	DA

SSSJ2030+0654	20 30 03.0	+06 54 55	0.1071	0.1935	1990.637	18.038	0.720	0.386	DA
SSSJ2122+0413	21 22 12.4	+04 13 59	-0.0694	-0.406	1995.586	17.909	1.176	0.452	DA poor S/N
SSSJ2138+2522	21 38 26.8	+25 22 20	0.0958	0.2396	1991.75	17.683	0.239	0.167	DZA
SSSJ2142+0805	21 42 54.5	+08 05 29	-0.0769	-0.1888	1990.706	18.22	1.096	0.619	DC poor S/N
SSSJ2149+0415	21 49 13.6	+04 15 51	0.0156	-0.2259	1995.572	17.369	1.063	0.366	DA poor S/N
SSSJ2217+3707	22 17 47.1	+37 07 50	0.462	0.0798	1986.753	18.142	1.513	0.480	weak Hα, H_2CIA?
SSSJ2229+2327	22 29 33.8	+23 27 45	0.224	-0.2085	1987.747	18.797	0.939	0.430	weak Hα, H_2CIA?
SSSJ2230+1523	22 30 55.3	+15 23 52	0.4942	0.1947	1991.706	18.379	1.070	0.287	weak Hα, H_2CIA?
SSSJ2249+3623	22 49 46.2	+36 23 25	0.3335	-0.1641	1988.532	19.052	1.183	0.436	weak Hα, H_2CIA?
SSSJ2315-1440	23 15 30.3	-14 40 05	0.1764	-0.052	1990.728	15.762	0.385	0.159	DA
SSSJ2316+1720	23 16 12.4	+17 20 46	0.3032	-0.0514	1990.814	18.972	1.210	0.550	DZA
SSSJ2318+2019	23 18 57.9	+20 19 13	0.2841	0.1375	1990.706	17.773	0.085	-0.243	DC
SSSJ2322+2108	23 22 58.1	+21 08 05	-0.2815	-0.2378	1990.706	18.781	0.889	0.316	DA poor S/N
SSSJ2323+3508	23 23 29.0	+35 08 45	0.2564	0.0286	1989.538	17.292	0.494	0.384	DC poor S/N
SSSJ2343-1659	23 43 15.2	-16 59 39	-0.2791	-0.2295	1991.68	17.899	1.177	0.342	DC
SSSJ2347+1312	23 47 01.7	+13 12 52	0.2817	0.0234	1995.82	18.594	0.912	0.325	DA poor S/N

APPENDIX D

Spectroscopic Data for Non-Catalogue Objects

In this Appendix I present astrometric, photometric and spectroscopic data, including spectral classifications where possible, for 73 objects included in my observational follow-up campaign that are *not* present in the final white dwarf catalogue. These were included in early samples before the survey limits were fixed; there are many obvious white dwarfs amongst these objects, including several white dwarf and cool main sequence star binaries, and they may be of interest to the white dwarf community.

SSSJ0006+3805

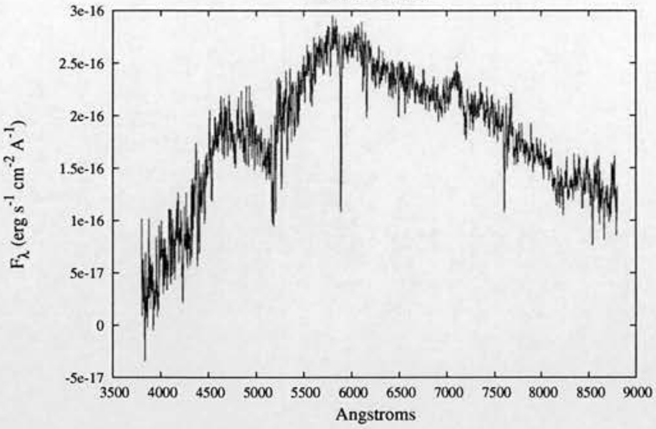

SSSJ0007+3947

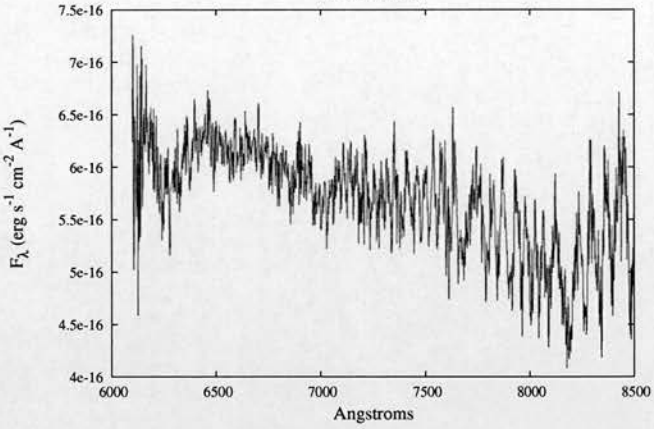

SSSJ0052+3450

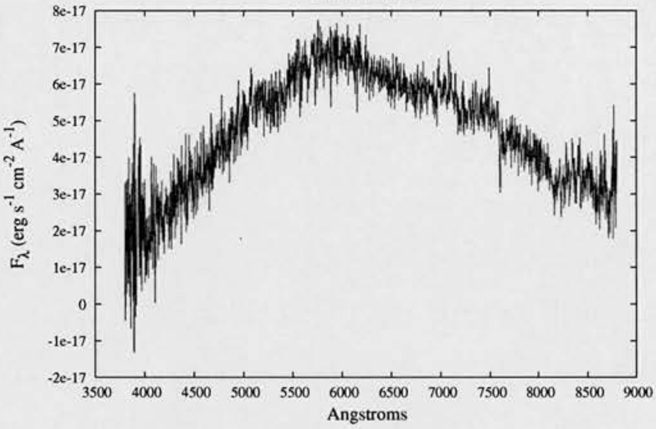

SSSJ0103-1127

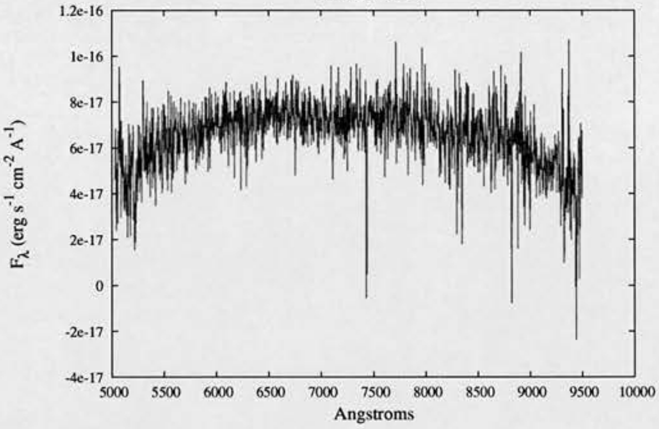

SSSJ0121-3508

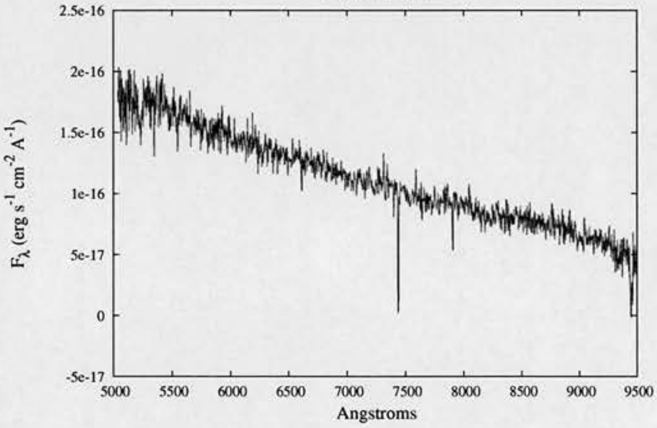

SSSJ0146+2154

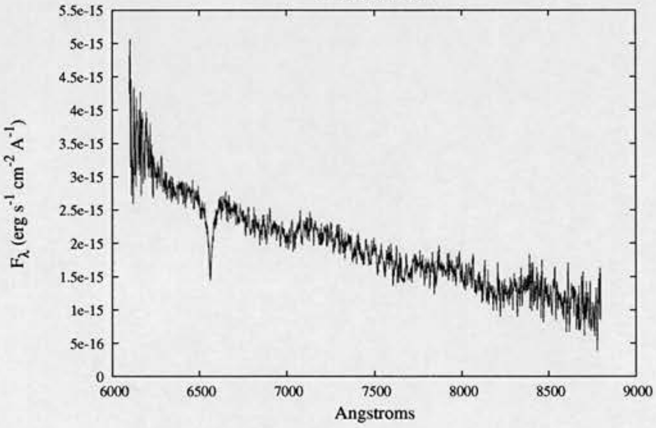

SSSJ0205-2609

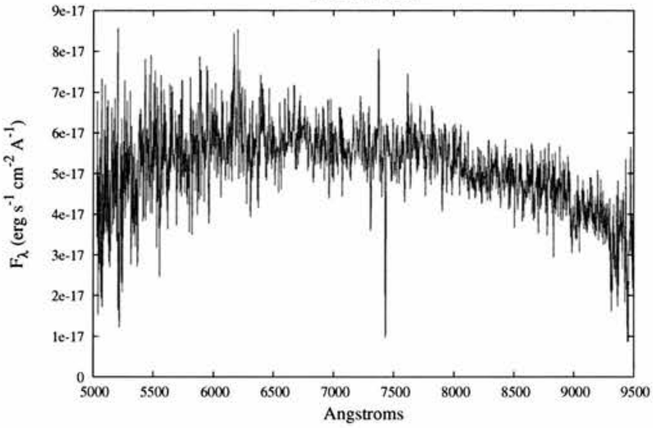

SSSJ0210+1012

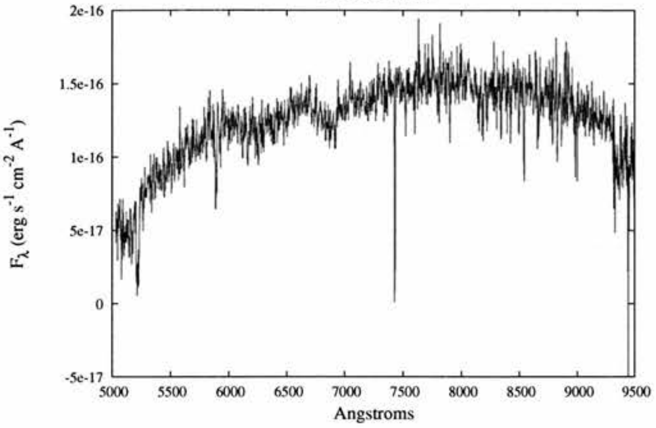

SSSJ0348-2036

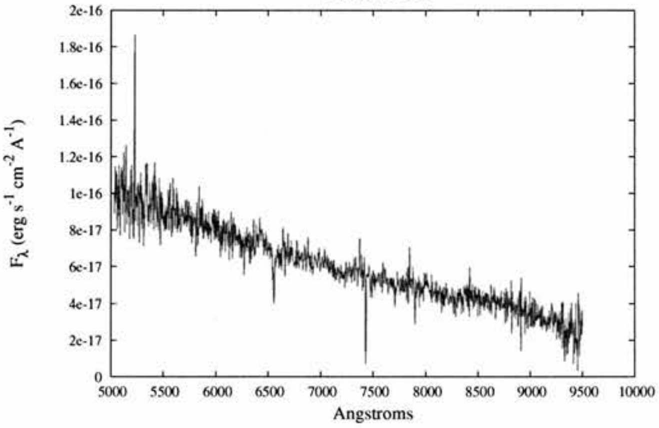

SSSJ0413-5713

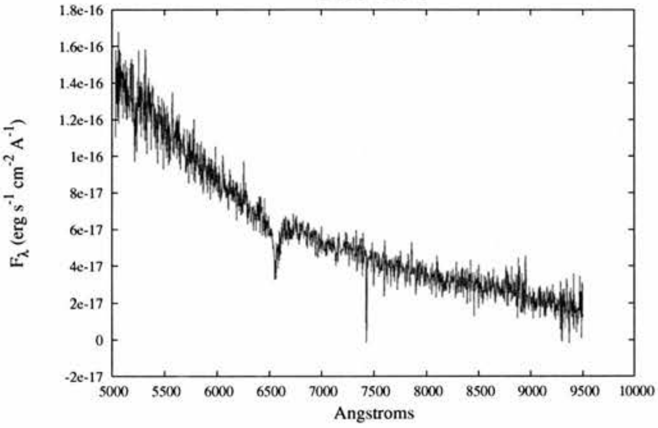

SSSJ0414+1947

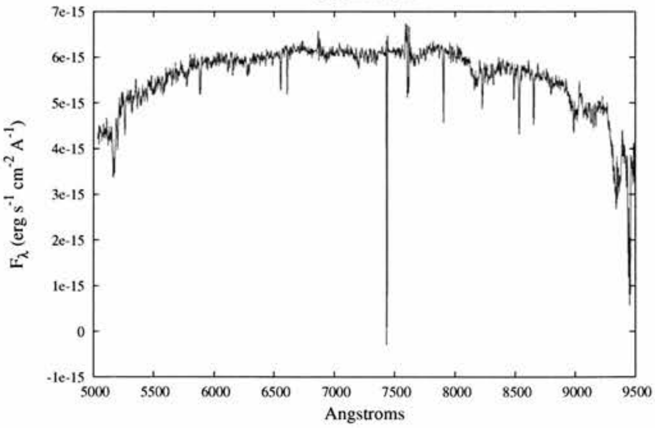

SSSJ0446+0410

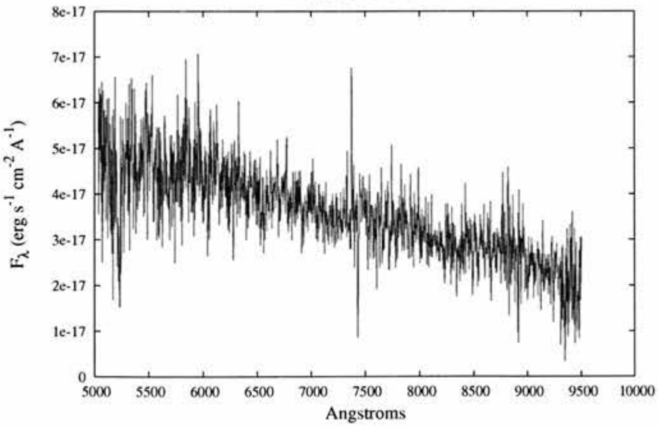

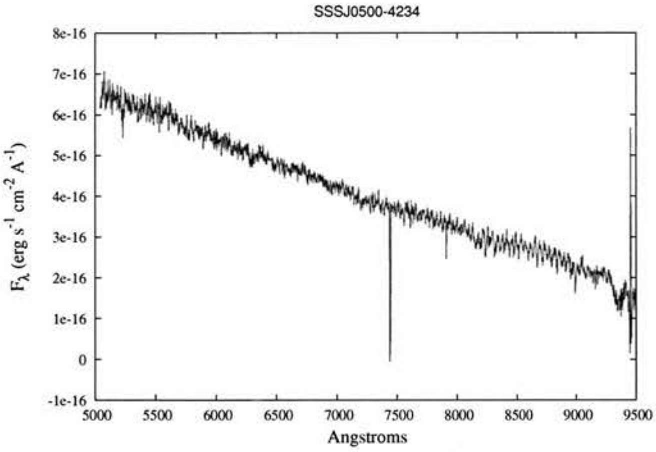
SSSJ0500-4234

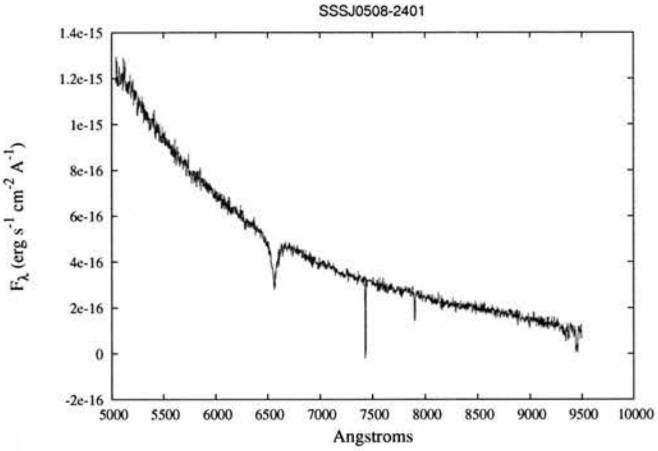
SSSJ0508-2401

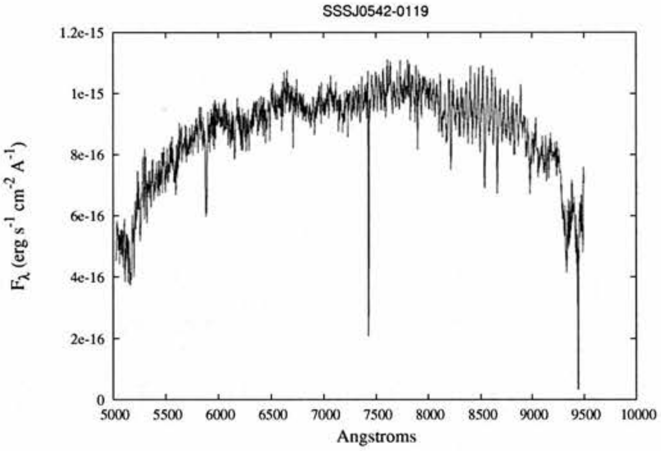
SSSJ0542-0119

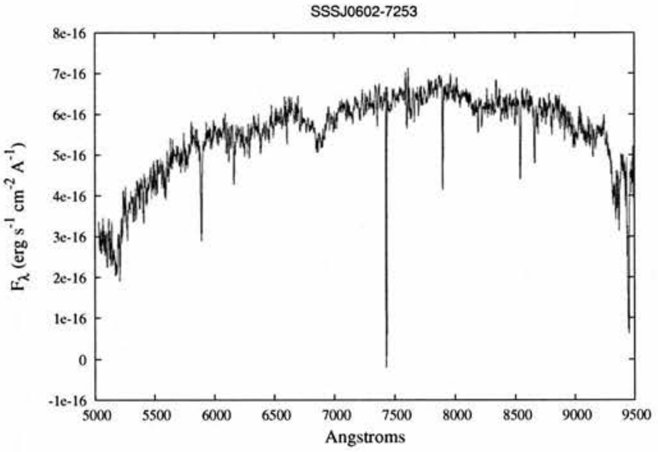
SSSJ0602-7253

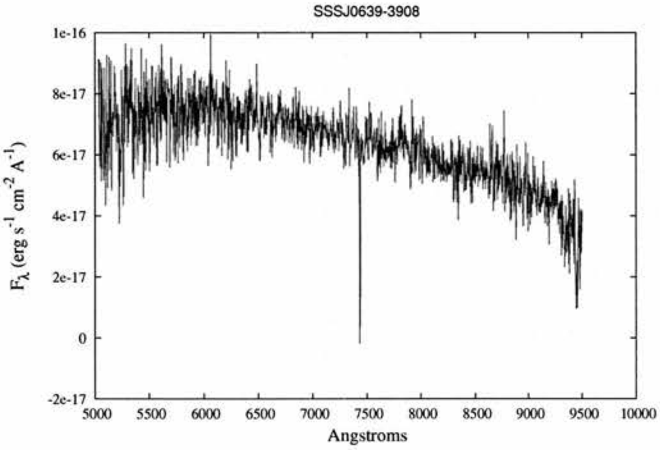
SSSJ0639-3908

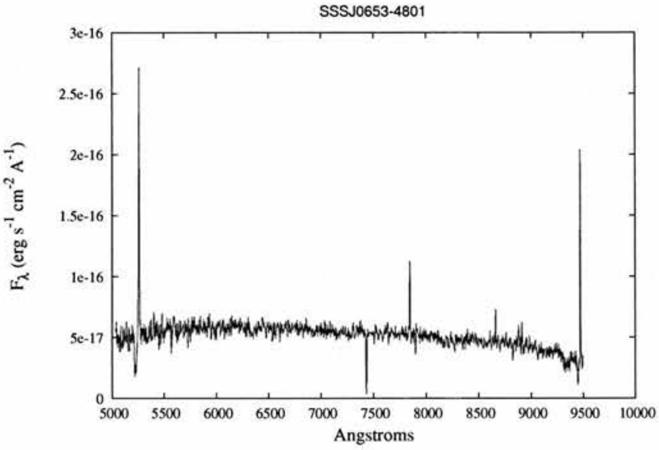
SSSJ0653-4801

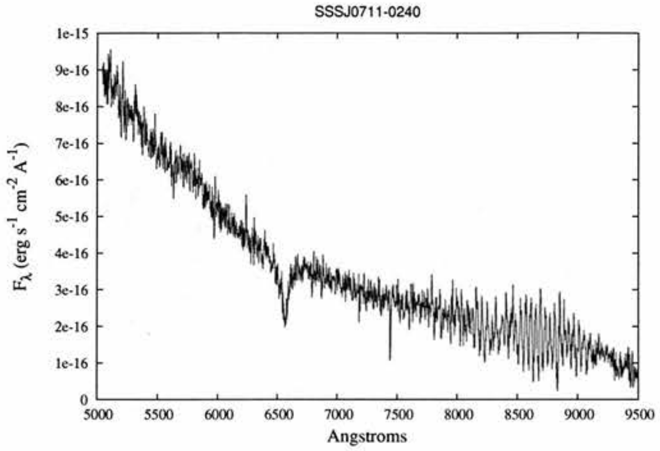
SSSJ0711-0240

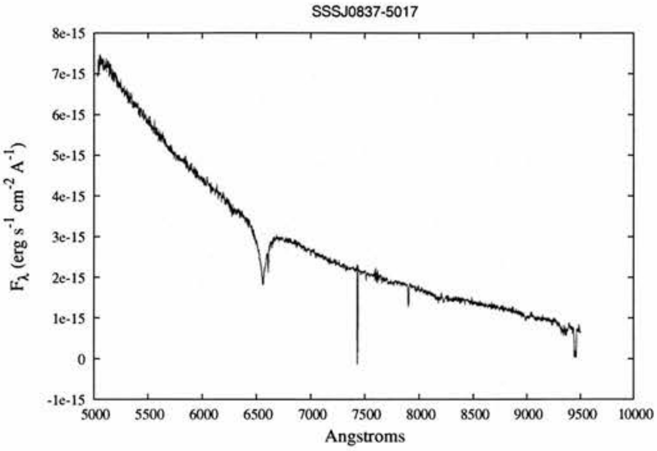
SSSJ0837-5017

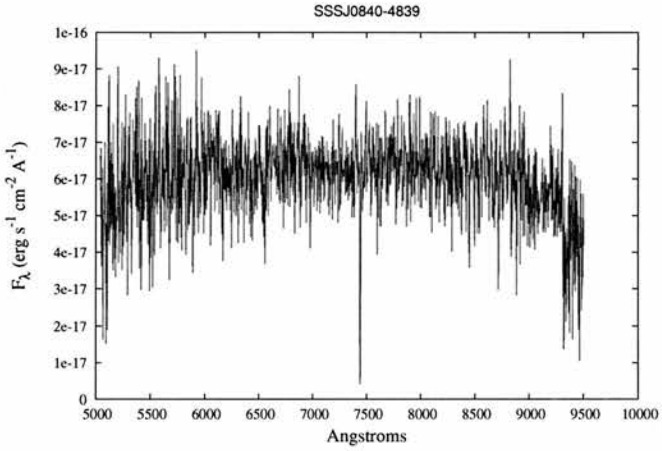
SSSJ0840-4839

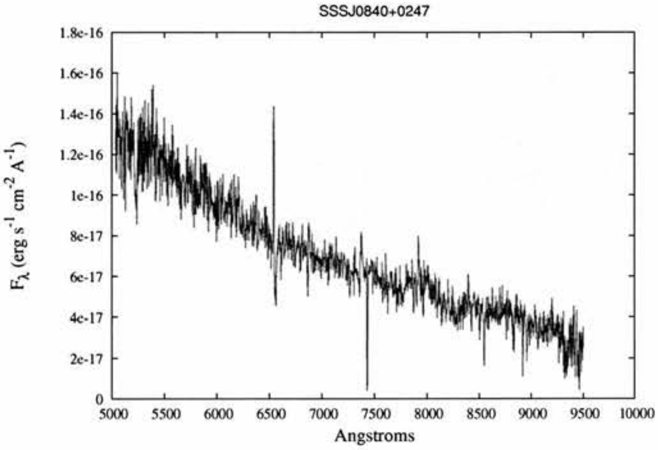
SSSJ0840+0247

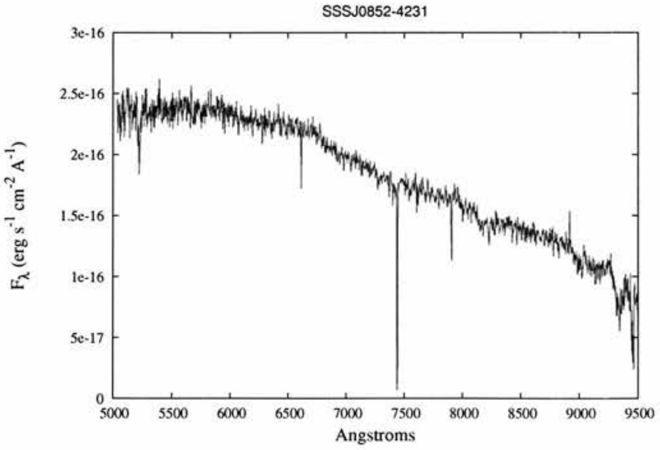
SSSJ0852-4231

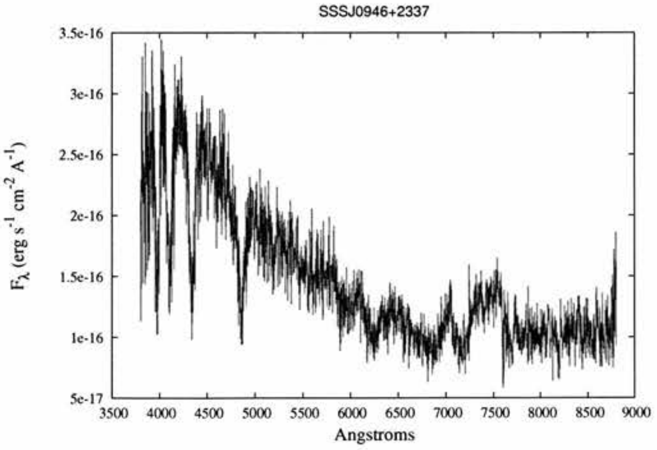
SSSJ0946+2337

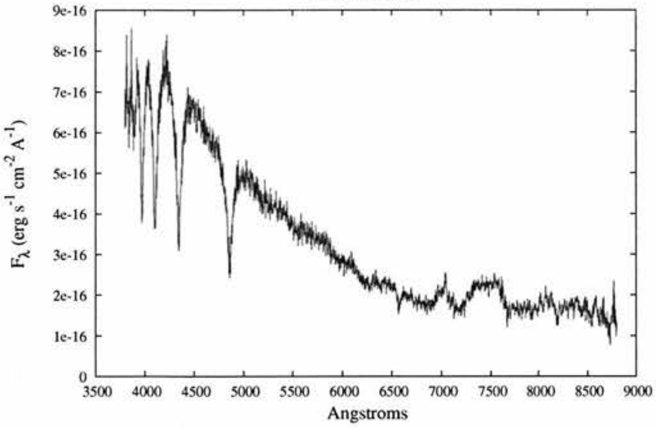
SSSJ1016-0109

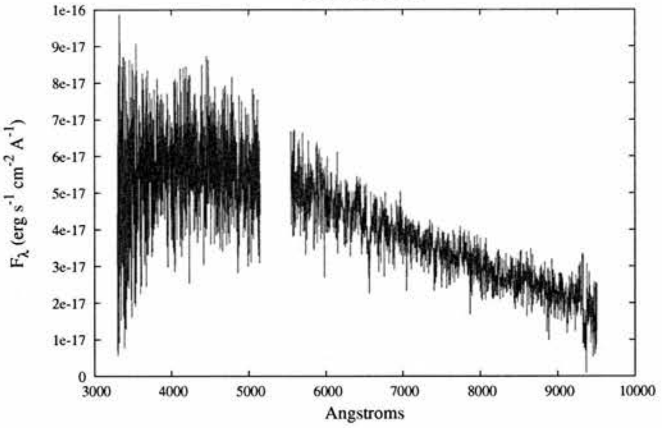
SSSJ1029+2300

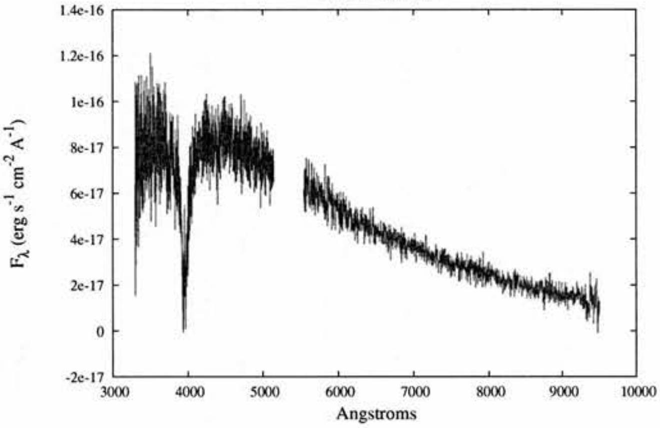
SSSJ1039+4612

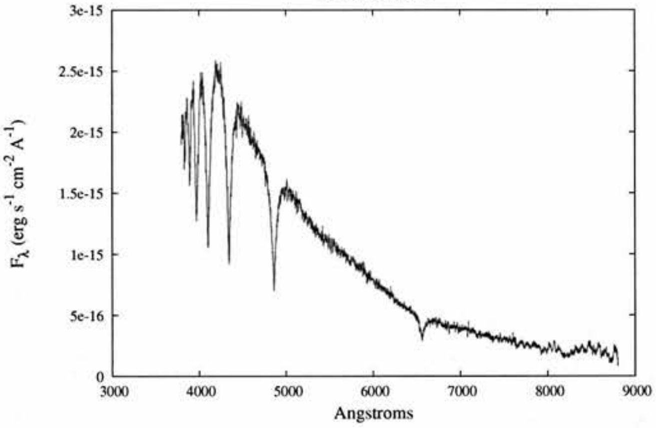
SSSJ1055+4730

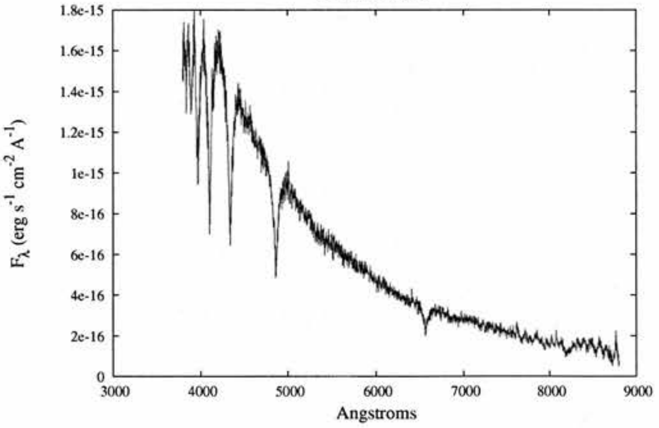
SSSJ1055+1834

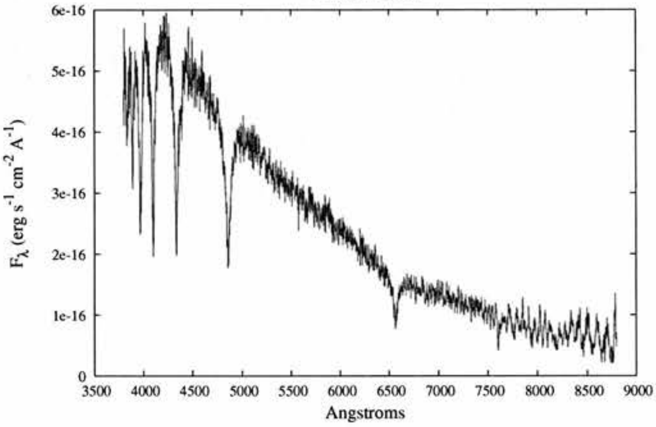
SSSJ1110+2344

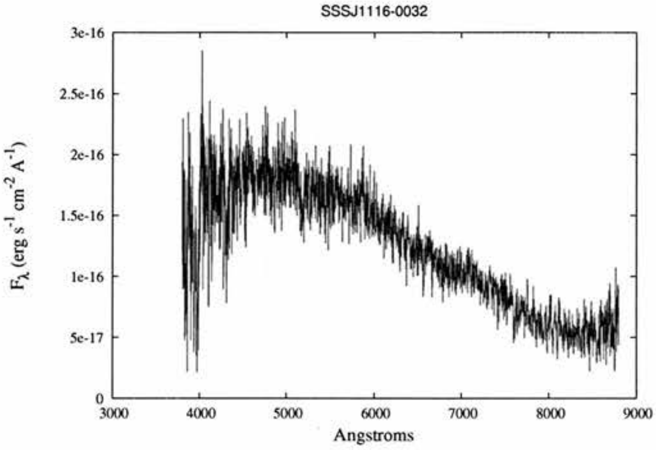
SSSJ1116-0032

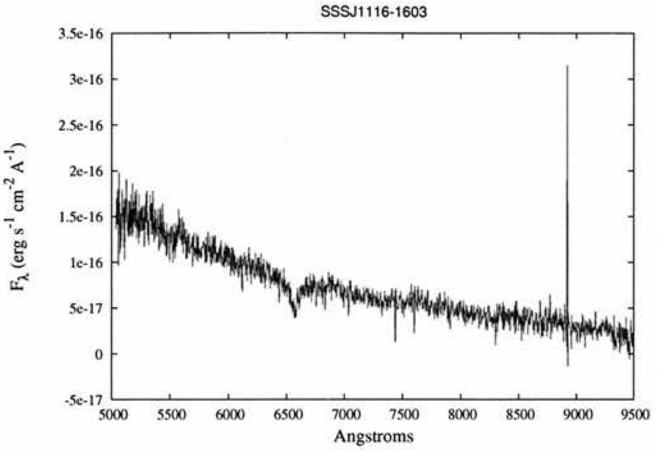
SSSJ1116-1603

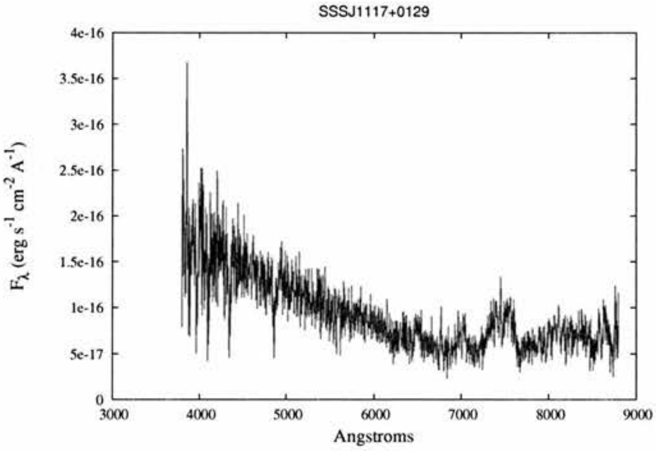
SSSJ1117+0129

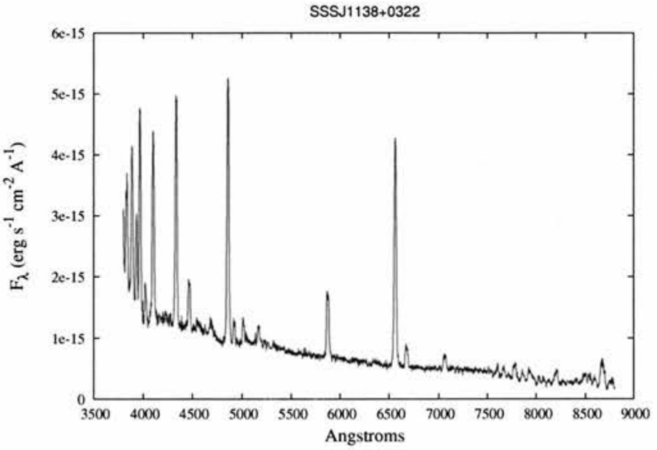
SSSJ1138+0322

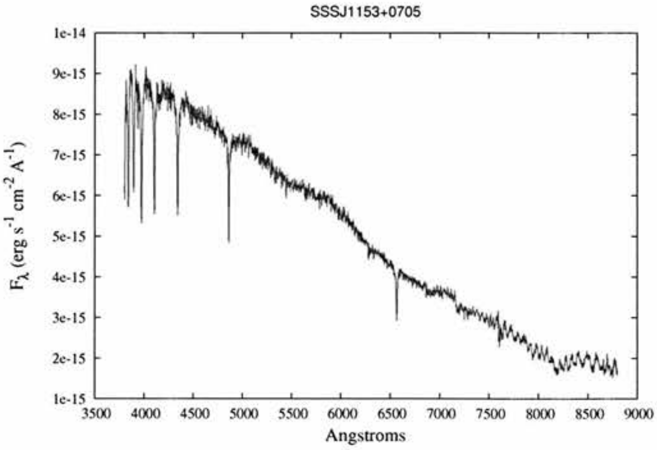
SSSJ1153+0705

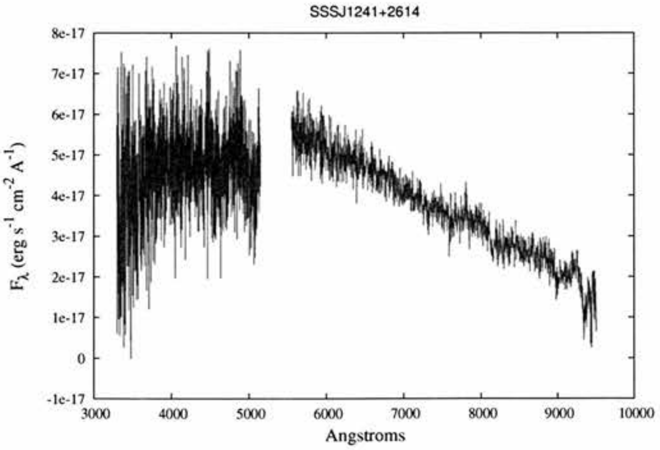
SSSJ1241+2614

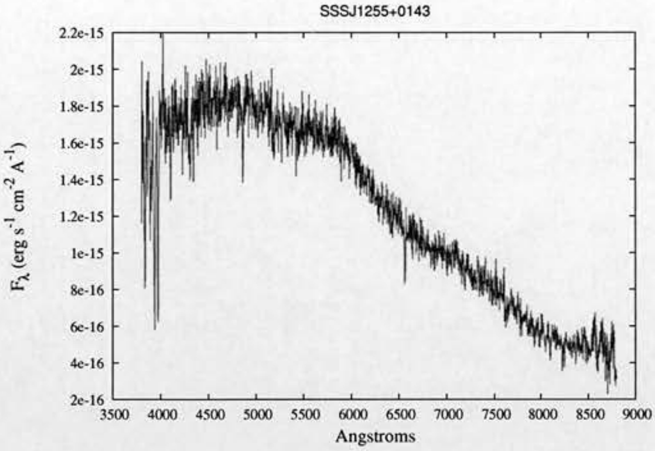
SSSJ1255+0143
F_λ (erg s^{-1} cm^{-2} A^{-1})
2.2e-15
2e-15
1.8e-15
1.6e-15
1.4e-15
1.2e-15
1e-15
8e-16
6e-16
4e-16
2e-16
3500
4000
4500
5000
5500
6000
6500
7000
7500
8000
8500
9000
Angstroms

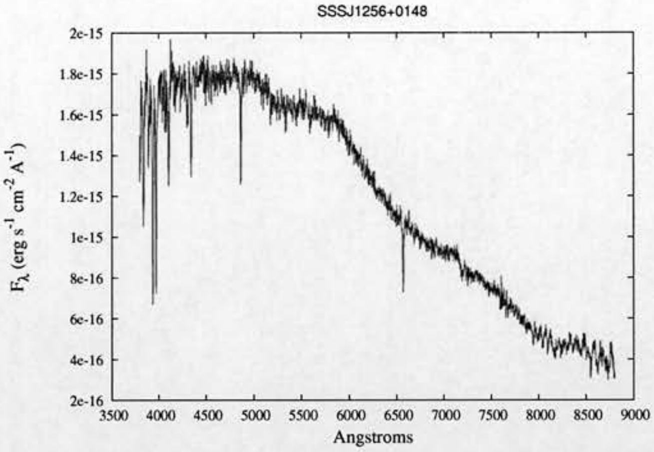
SSSJ1256+0148
F_λ (erg s^{-1} cm^{-2} A^{-1})
2e-15
1.8e-15
1.6e-15
1.4e-15
1.2e-15
1e-15
8e-16
6e-16
4e-16
2e-16
3500
4000
4500
5000
5500
6000
6500
7000
7500
8000
8500
9000
Angstroms

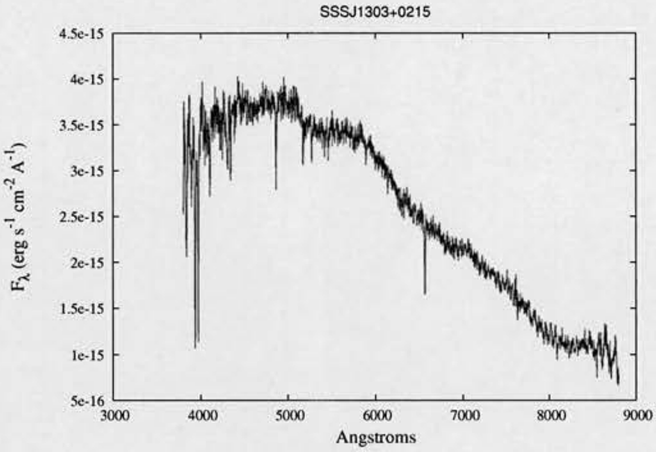
SSSJ1303+0215
F_λ (erg s^{-1} cm^{-2} A^{-1})
4.5e-15
4e-15
3.5e-15
3e-15
2.5e-15
2e-15
1.5e-15
1e-15
5e-16
3000
4000
5000
6000
7000
8000
9000
Angstroms

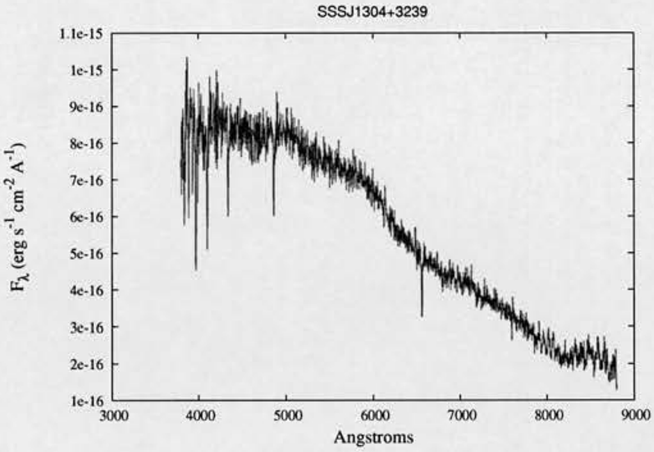
SSSJ1304+3239
F_λ (erg s^{-1} cm^{-2} A^{-1})
1.1e-15
1e-15
9e-16
8e-16
7e-16
6e-16
5e-16
4e-16
3e-16
2e-16
1e-16
3000
4000
5000
6000
7000
8000
9000
Angstroms

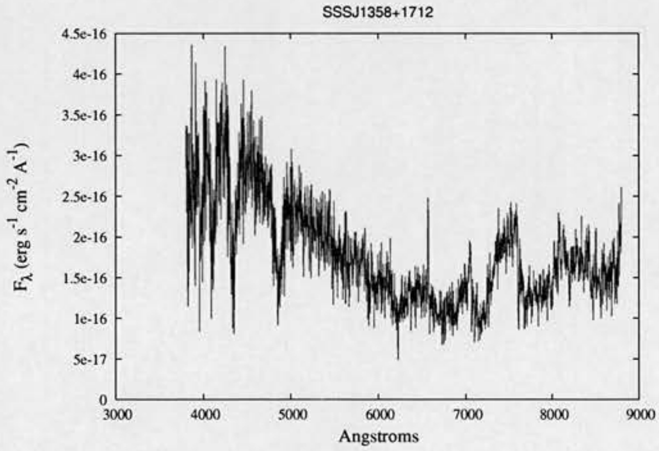
SSSJ1358+1712
F_λ (erg s^{-1} cm^{-2} A^{-1})
4.5e-16
4e-16
3.5e-16
3e-16
2.5e-16
2e-16
1.5e-16
1e-16
5e-17
0
3000
4000
5000
6000
7000
8000
9000
Angstroms

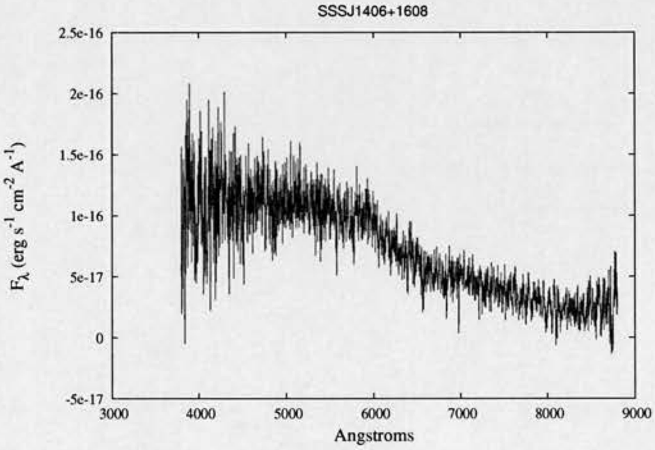
SSSJ1406+1608
F_λ (erg s^{-1} cm^{-2} A^{-1})
2.5e-16
2e-16
1.5e-16
1e-16
5e-17
0
-5e-17
3000
4000
5000
6000
7000
8000
9000
Angstroms

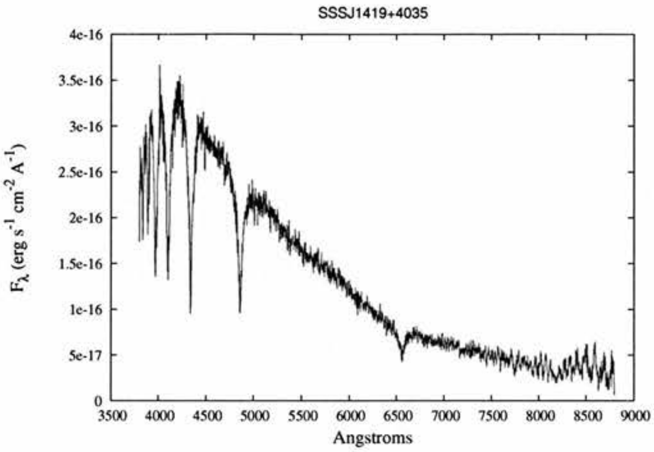
SSSJ1419+4035
F_λ (erg s^{-1} cm^{-2} A^{-1})
0
5e-17
1e-16
1.5e-16
2e-16
2.5e-16
3e-16
3.5e-16
4e-16
3500
4000
4500
5000
5500
6000
6500
7000
7500
8000
8500
9000
Angstroms

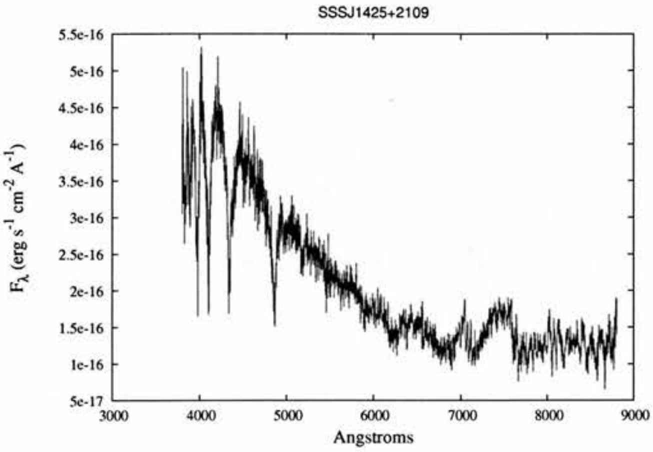
SSSJ1425+2109
F_λ (erg s^{-1} cm^{-2} A^{-1})
5e-17
1e-16
1.5e-16
2e-16
2.5e-16
3e-16
3.5e-16
4e-16
4.5e-16
5e-16
5.5e-16
3000
4000
5000
6000
7000
8000
9000
Angstroms

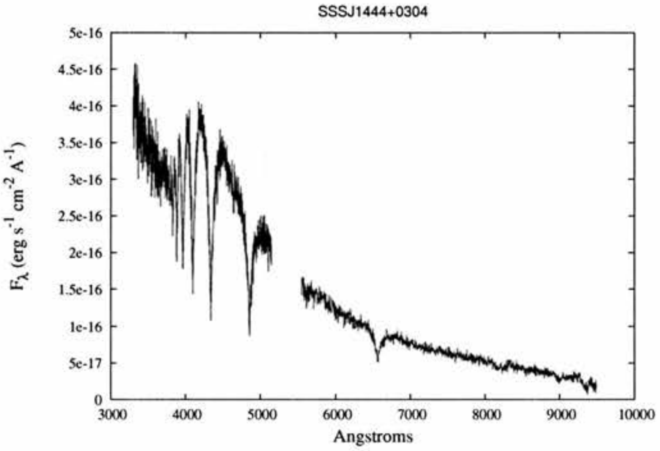
SSSJ1444+0304
F_λ (erg s^{-1} cm^{-2} A^{-1})
0
5e-17
1e-16
1.5e-16
2e-16
2.5e-16
3e-16
3.5e-16
4e-16
4.5e-16
5e-16
3000
4000
5000
6000
7000
8000
9000
10000
Angstroms

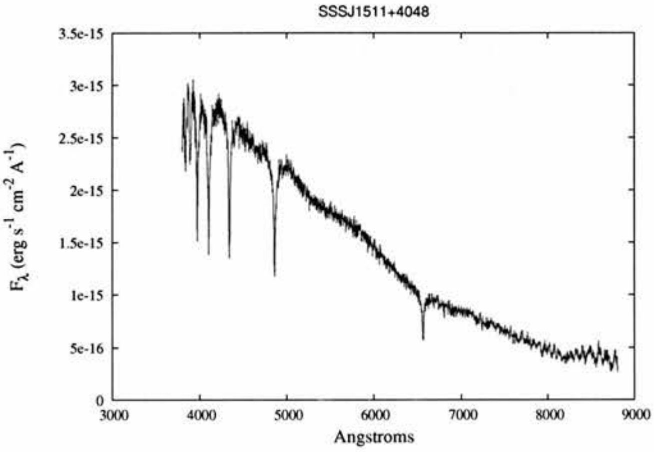
SSSJ1511+4048
F_λ (erg s^{-1} cm^{-2} A^{-1})
0
5e-16
1e-15
1.5e-15
2e-15
2.5e-15
3e-15
3.5e-15
3000
4000
5000
6000
7000
8000
9000
Angstroms

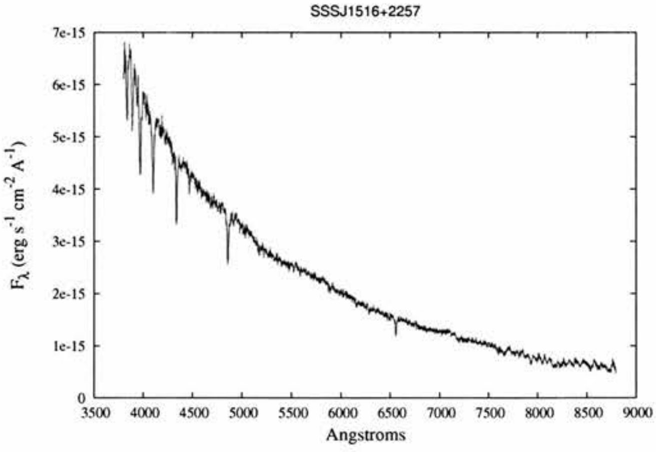
SSSJ1516+2257
F_λ (erg s^{-1} cm^{-2} A^{-1})
0
1e-15
2e-15
3e-15
4e-15
5e-15
6e-15
7e-15
3500
4000
4500
5000
5500
6000
6500
7000
7500
8000
8500
9000
Angstroms

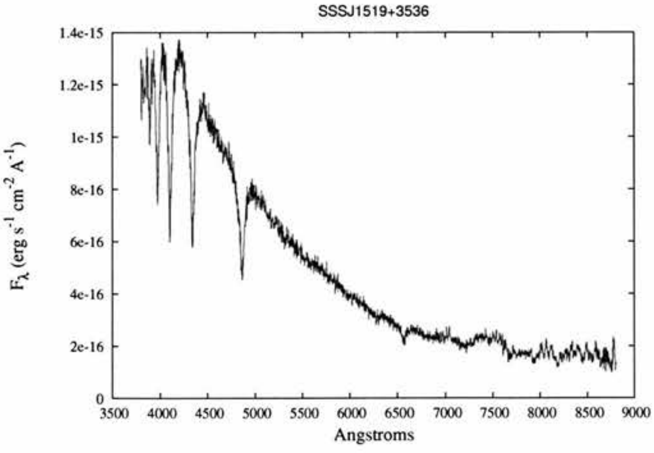
SSSJ1519+3536
F_λ (erg s^{-1} cm^{-2} A^{-1})
0
2e-16
4e-16
6e-16
8e-16
1e-15
1.2e-15
1.4e-15
3500
4000
4500
5000
5500
6000
6500
7000
7500
8000
8500
9000
Angstroms

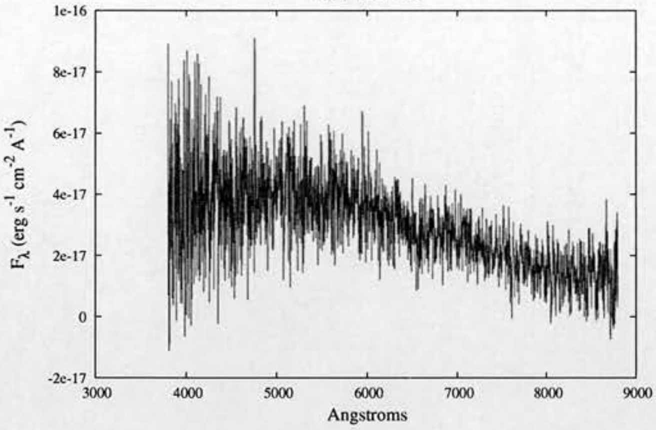
SSSJ1545+2603

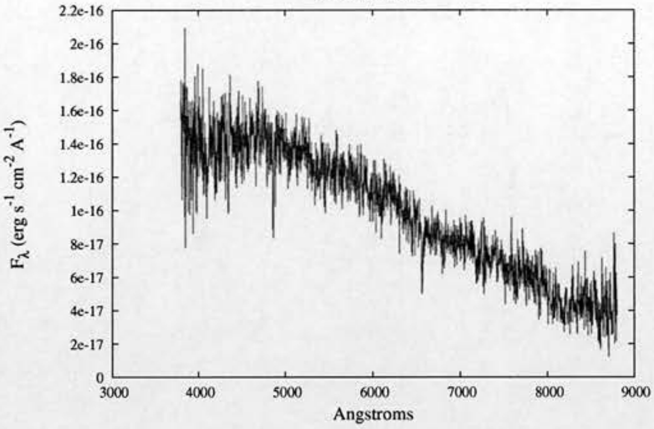
SSSJ1620+3213

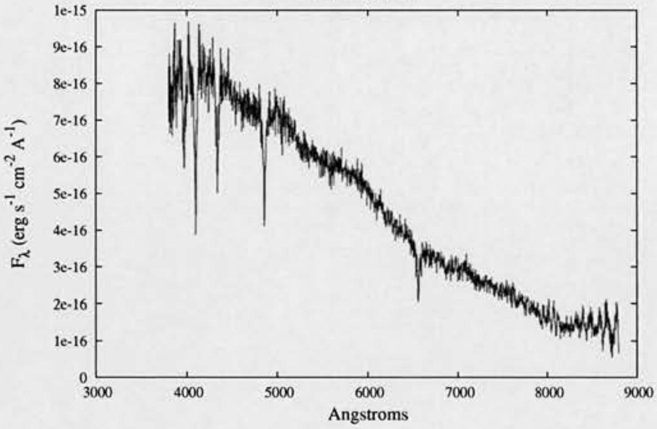
SSSJ1622+0532

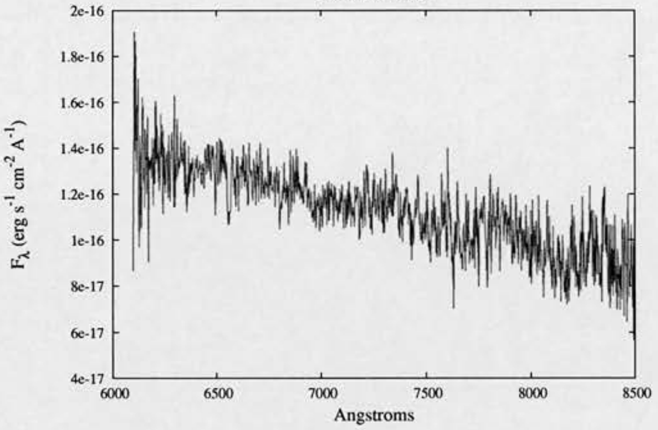
SSSJ1645+5620

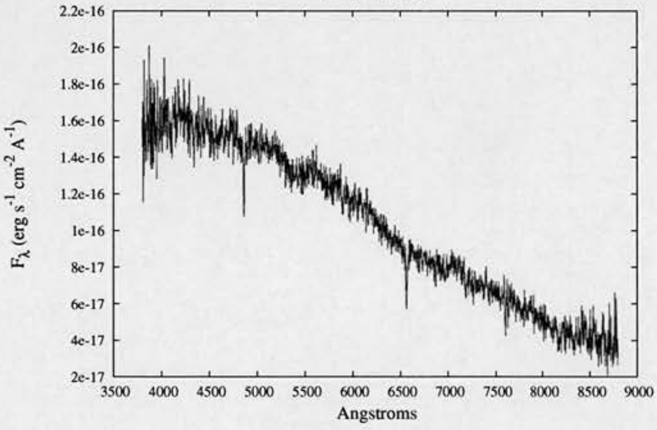
SSSJ1719+4855

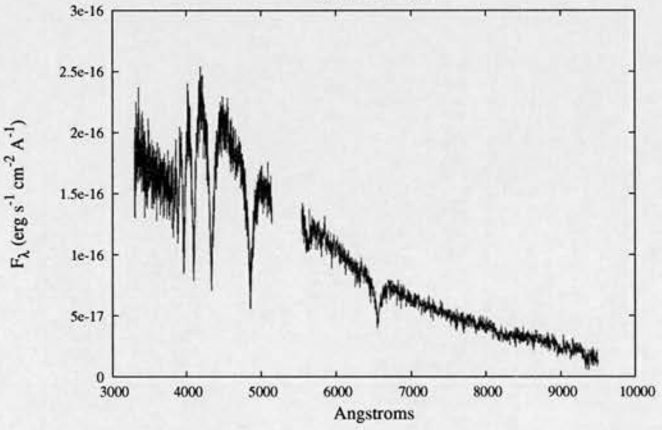
SSSJ1730+1158

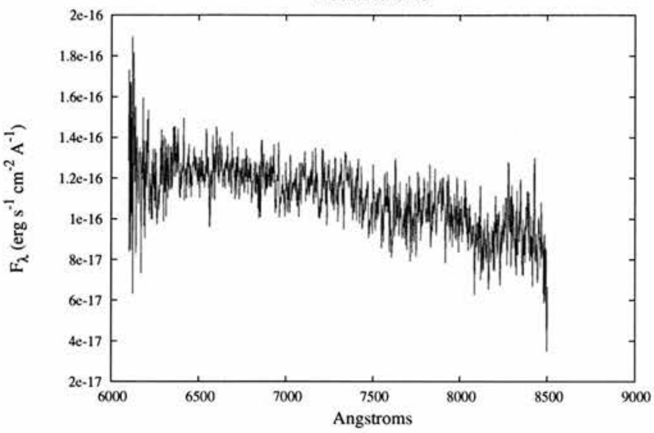
SSSJ1759+5415
F$_\lambda$ (erg s^{-1} cm^{-2} A^{-1})
2e-16
1.8e-16
1.6e-16
1.4e-16
1.2e-16
1e-16
8e-17
6e-17
4e-17
2e-17
6000
6500
7000
7500
8000
8500
9000
Angstroms

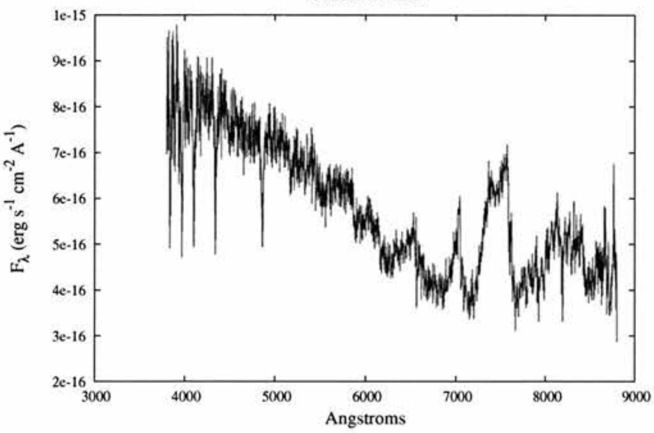
SSSJ1844+4120
F$_\lambda$ (erg s^{-1} cm^{-2} A^{-1})
1e-15
9e-16
8e-16
7e-16
6e-16
5e-16
4e-16
3e-16
2e-16
3000
4000
5000
6000
7000
8000
9000
Angstroms

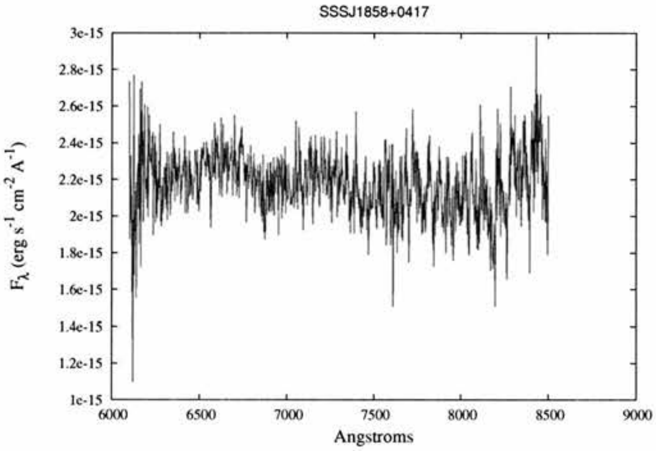
SSSJ1858+0417
F$_\lambda$ (erg s^{-1} cm^{-2} A^{-1})
3e-15
2.8e-15
2.6e-15
2.4e-15
2.2e-15
2e-15
1.8e-15
1.6e-15
1.4e-15
1.2e-15
1e-15
6000
6500
7000
7500
8000
8500
9000
Angstroms

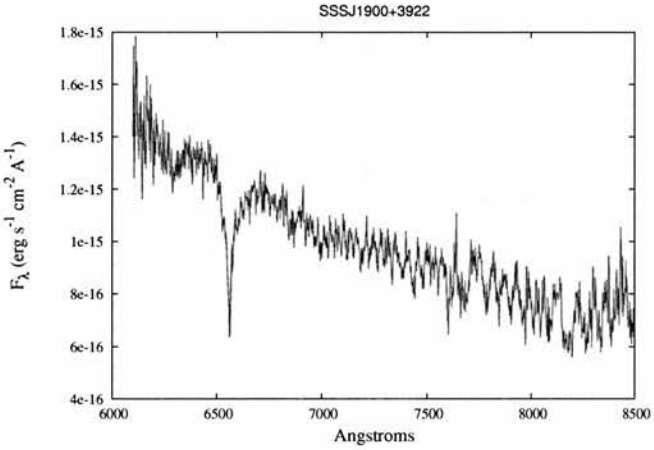
SSSJ1900+3922
F$_\lambda$ (erg s^{-1} cm^{-2} A^{-1})
1.8e-15
1.6e-15
1.4e-15
1.2e-15
1e-15
8e-16
6e-16
4e-16
6000
6500
7000
7500
8000
8500
Angstroms

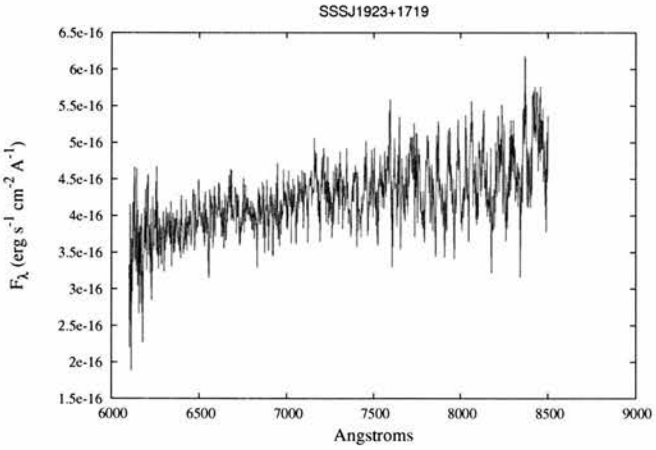
SSSJ1923+1719
F$_\lambda$ (erg s^{-1} cm^{-2} A^{-1})
6.5e-16
6e-16
5.5e-16
5e-16
4.5e-16
4e-16
3.5e-16
3e-16
2.5e-16
2e-16
1.5e-16
6000
6500
7000
7500
8000
8500
9000
Angstroms

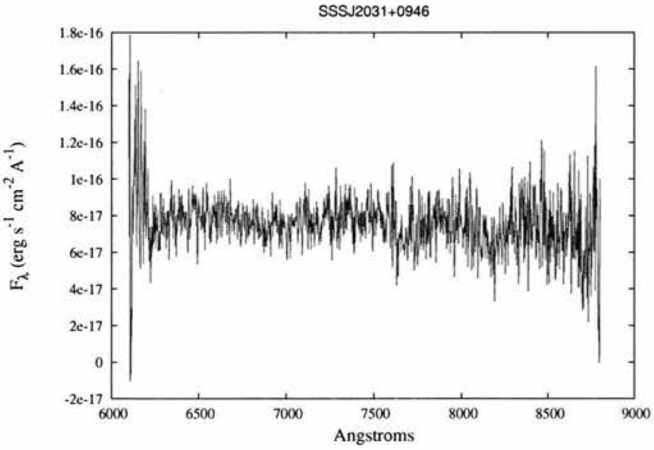
SSSJ2031+0946
F$_\lambda$ (erg s^{-1} cm^{-2} A^{-1})
1.8e-16
1.6e-16
1.4e-16
1.2e-16
1e-16
8e-17
6e-17
4e-17
2e-17
0
-2e-17
6000
6500
7000
7500
8000
8500
9000
Angstroms

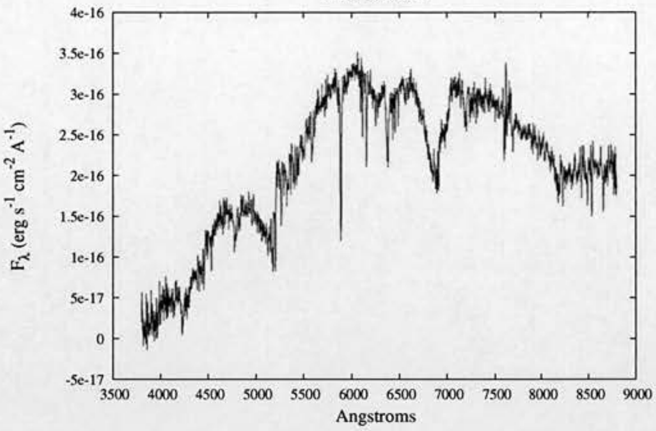
SSSJ2036+5712

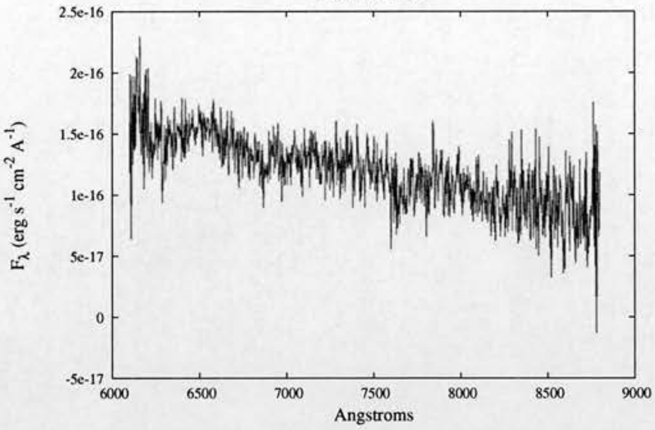
SSSJ2052+0133

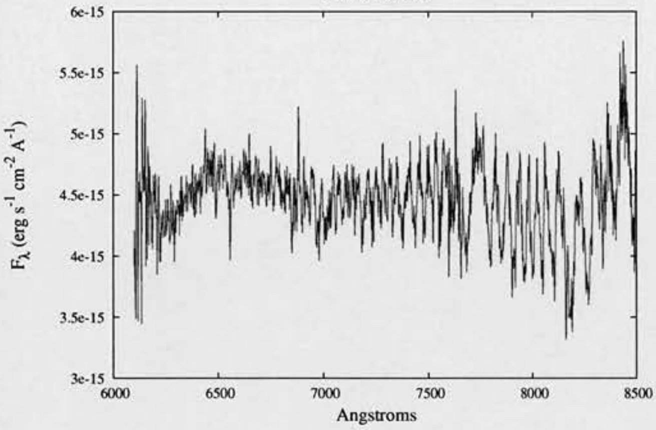
SSSJ2059+5153

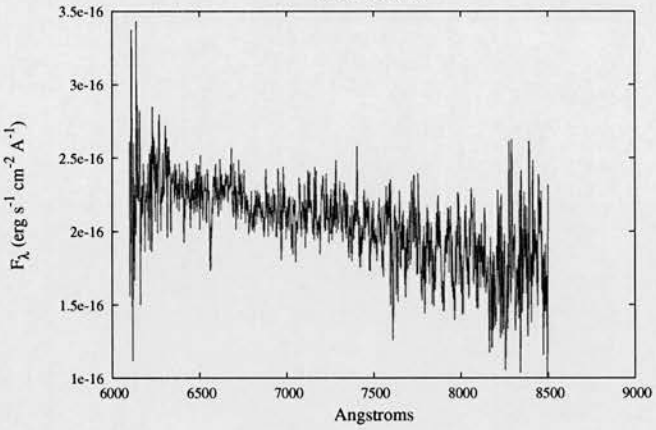
SSSJ2106+0740

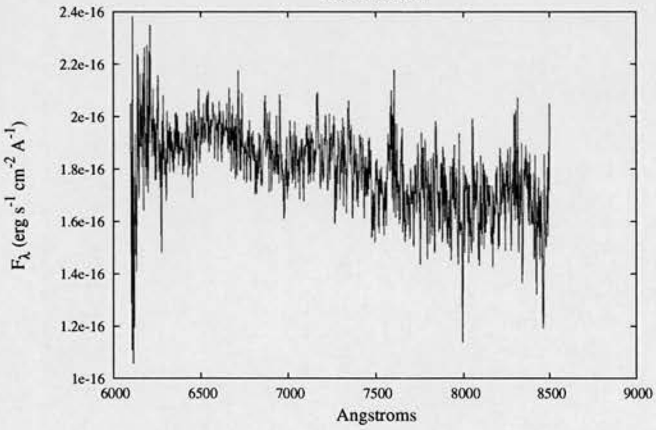
SSSJ2157+2705

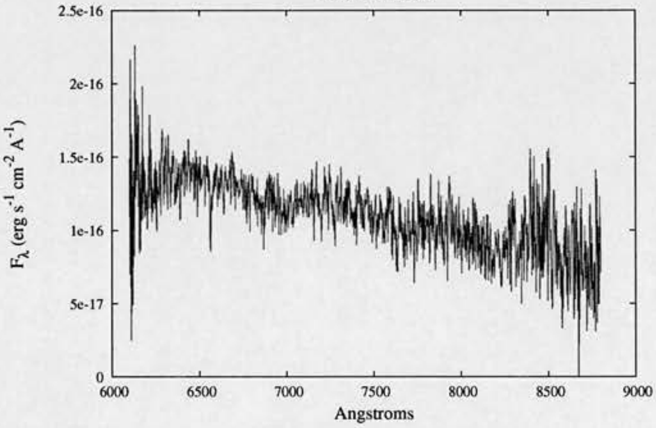
SSSJ2244+1513

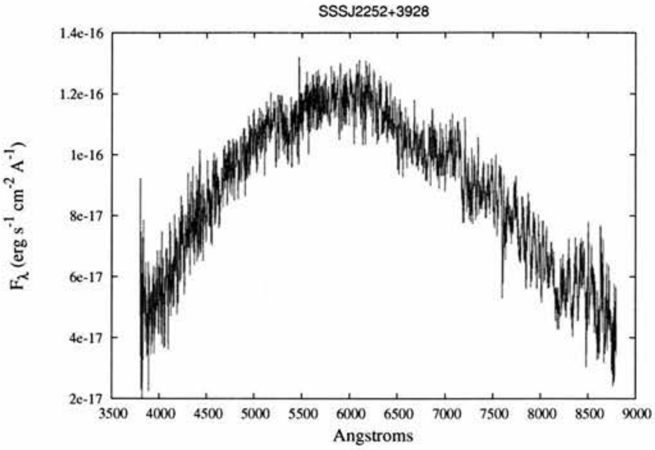
SSSJ2252+3928
F$_\lambda$ (erg s^{-1} cm^{-2} A^{-1})
1.4e-16
1.2e-16
1e-16
8e-17
6e-17
4e-17
2e-17
3500 4000 4500 5000 5500 6000 6500 7000 7500 8000 8500 9000
Angstroms

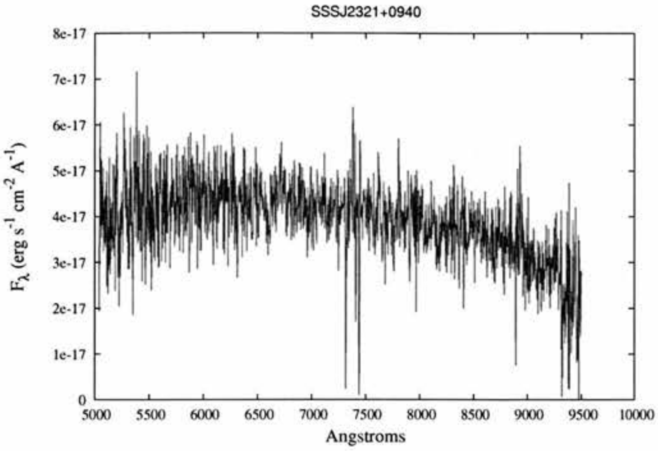
SSSJ2321+0940
F$_\lambda$ (erg s^{-1} cm^{-2} A^{-1})
8e-17
7e-17
6e-17
5e-17
4e-17
3e-17
2e-17
1e-17
0
5000 5500 6000 6500 7000 7500 8000 8500 9000 9500 10000
Angstroms

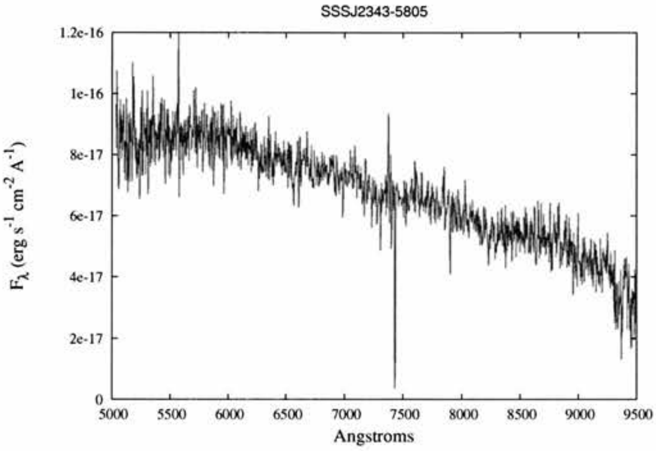
SSSJ2343-5805
F$_\lambda$ (erg s^{-1} cm^{-2} A^{-1})
1.2e-16
1e-16
8e-17
6e-17
4e-17
2e-17
0
5000 5500 6000 6500 7000 7500 8000 8500 9000 9500
Angstroms

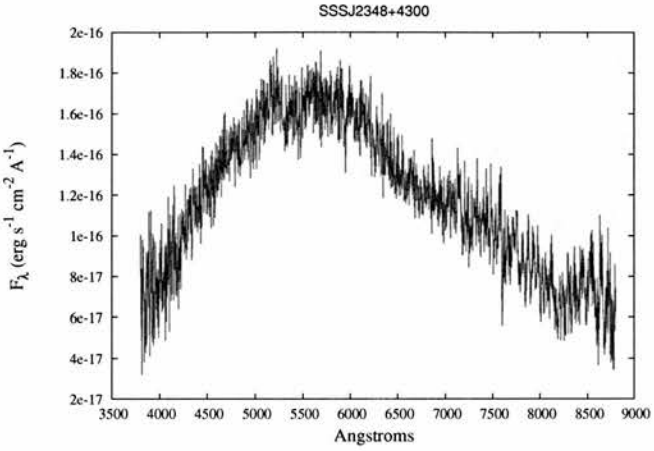
SSSJ2348+4300
F$_\lambda$ (erg s^{-1} cm^{-2} A^{-1})
2e-16
1.8e-16
1.6e-16
1.4e-16
1.2e-16
1e-16
8e-17
6e-17
4e-17
2e-17
3500 4000 4500 5000 5500 6000 6500 7000 7500 8000 8500 9000
Angstroms

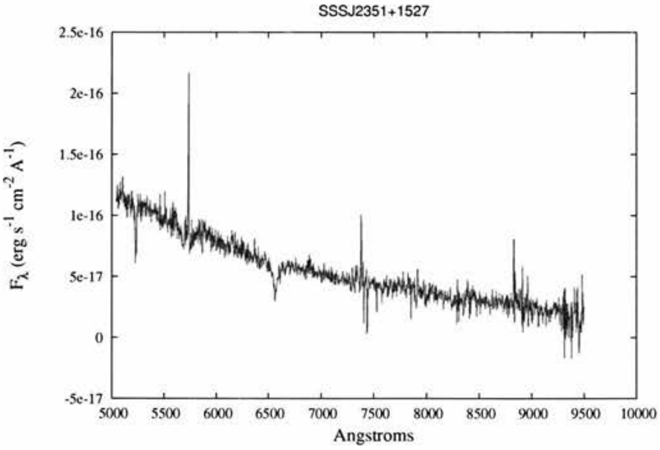
SSSJ2351+1527
F$_\lambda$ (erg s^{-1} cm^{-2} A^{-1})
2.5e-16
2e-16
1.5e-16
1e-16
5e-17
0
-5e-17
5000 5500 6000 6500 7000 7500 8000 8500 9000 9500 10000
Angstroms

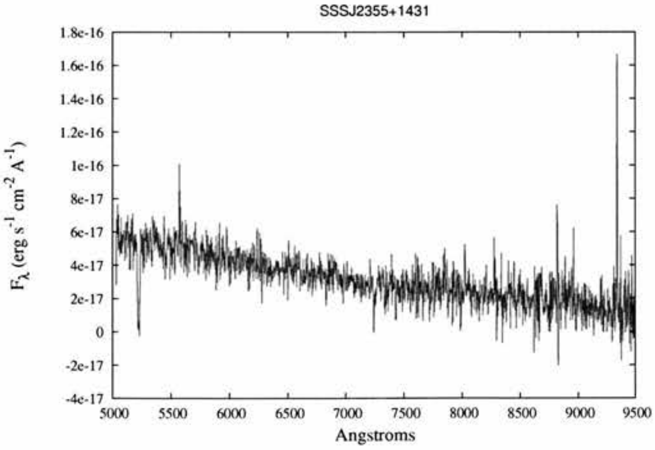
SSSJ2355+1431
F$_\lambda$ (erg s^{-1} cm^{-2} A^{-1})
1.8e-16
1.6e-16
1.4e-16
1.2e-16
1e-16
8e-17
6e-17
4e-17
2e-17
0
-2e-17
-4e-17
5000 5500 6000 6500 7000 7500 8000 8500 9000 9500
Angstroms

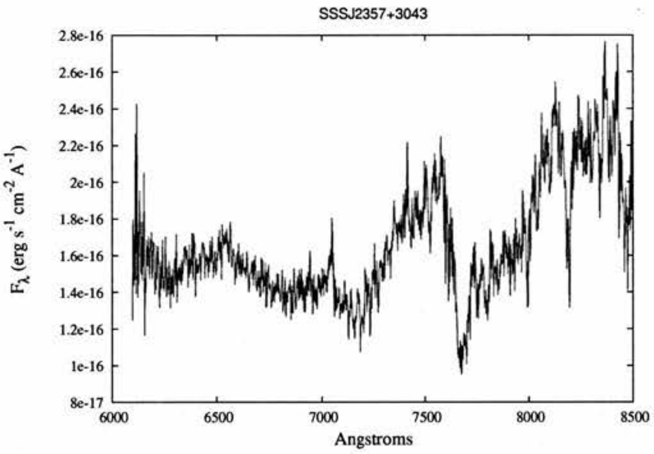
SSSJ2357+3043
F_λ (erg s^{-1} cm^{-2} A^{-1})
2.8e-16
2.6e-16
2.4e-16
2.2e-16
2e-16
1.8e-16
1.6e-16
1.4e-16
1.2e-16
1e-16
8e-17
6000
6500
7000
7500
8000
8500
Angstroms

Designation	$\alpha^{\dagger}$	δ	$\mu_\alpha \cos(\delta)$	μ_δ	Epoch	b_J	$b_J - r_{59F}$	$r_{59F} - i_N$	Sp. T
SSSJ0006+3805	00 06 04.2	+38 05 08	0.0334	-0.3176	1989.761	18.965	1.660	-1.314	MS?
SSSJ0007+3947	00 07 53.8	+39 47 33	0.3628	-0.083	1989.761	17.738	1.263	0.446	DC poor S/N
SSSJ0052+3450	00 52 46.6	+34 50 56	0.3981	-0.1529	1989.75	19.921	1.697	0.454	DC H_2CIA?
SSSJ0103-1127	01 03 53.6	-11 27 48	0.1729	-0.2244	1988.769	20.304	1.997	0.426	DC
SSSJ0121-3508	01 21 10.8	-35 08 30	0.2975	0.0888	1997.922	18.722	0.885	-0.057	DC
SSSJ0146+2154	01 46 41.5	+21 54 50	-0.1713	-0.1382	1986.694	14.907	0.098	0.203	DA
SSSJ0205-2609	02 05 27.8	-26 09 42	0.2708	0.0334	1995.822	20.463	1.559	0.014	DC poor S/N
SSSJ0210+1012	02 10 57.8	+10 12 39	0.1952	-0.2011	1991.772	20.285	1.780	0.561	MS?
SSSJ0348-2036	03 48 44.6	-20 36 31	0.1359	0.1809	1999.858	19.199	0.671	-0.229	DA
SSSJ0413-5713	04 13 09.2	-57 13 38	0.1438	-0.1391	1994.992	18.661	0.113	-0.214	DA
SSSJ0414+1947	04 14 55.8	+19 47 30	0.0912	-0.338	1989.976	14.9	1.018	0.014	MS - K?
SSSJ0446+0410	04 46 03.6	+04 10 56	0.3624	0.1944	1990.894	20.148	1.206	0.143	DC poor S/N
SSSJ0500-4234	05 00 26.8	-42 34 11	0.0763	0.3052	1998.072	17.261	0.825	0.188	DC
SSSJ0508-2401	05 08 24.5	-24 01 08	-0.0822	-0.1658	1997.85	16.418	-0.081	-0.144	DA
SSSJ0542-0119	05 42 59.0	-01 19 29	0.1176	-0.2118	1988.995	16.9	0.719	0.084	MS - K?
SSSJ0602-7253	06 02 41.5	-72 53 14	0.106	0.3094	1990.0	18.195	1.886	0.028	MS - K?

† Equinox 2000

SSSJ0639-3908	06 39 40.3	-39 08 26	-0.1828	0.2112	1994.864	19.986	1.257	0.164	DC poor S/N
SSSJ0653-4801	06 53 09.2	-48 01 54	-0.1874	0.2924	1996.202	20.434	1.597	0.281	DC
SSSJ0711-0240	07 11 48.9	-02 40 28	-0.0297	-0.1956	1986.204	16.123	0.131	-0.099	DA
SSSJ0837-5017	08 37 59.4	-50 17 47	-0.2567	0.1713	1991.107	14.153	-0.283	-0.107	DA
SSSJ0840-4839	08 40 07.2	-48 39 46	0.2842	-0.035	1991.107	20.304	1.365	0.314	DC weak Hα? poor S/N
SSSJ0840+0247	08 40 52.8	+02 47 14	-0.0151	-0.2168	1991.104	18.795	0.432	-0.052	DA + Hα emission
SSSJ0852-4231	08 52 29.6	-42 31 48	-0.3626	0.1501	1994.18	18.622	0.178	-0.373	DA Hα 6610
SSSJ0946+2337	09 46 40.4	+23 37 34	-0.0658	-0.0368	1989.962	17.277	0.287	1.297	DA+dM
SSSJ1016-0109	10 16 47.3	-01 09 07	-0.0506	-0.0123	1986.881	16.976	0.129	1.110	DA+dM
SSSJ1029+2300	10 29 30.9	+23 00 10	0.1592	-0.1044	1990.013	19.346	0.689	-0.248	DA
SSSJ1039+4612	10 39 42.1	+46 12 26	-0.2369	-0.131	1992.038	18.992	0.537	-0.352	DZ
SSSJ1055+4730	10 55 29.8	+47 30 07	-0.1035	-0.0062	1994.034	16.99	0.251	-0.306	DA
SSSJ1055+1834	10 55 38.3	+18 34 13	-0.0368	-0.0158	1994.86	16.157	-0.250	0.023	DA
SSSJ1110+2344	11 10 26.2	+23 44 08	0.0013	-0.0472	1992.207	16.985	0.019	0.390	DA
SSSJ1116-0032	11 16 29.7	-00 32 32	0.0281	-0.1649	1981.832	18.581	0.925	0.232	DC
SSSJ1116-1603	11 16 46.3	-16 03 28	0.1629	-0.1835	1993.083	18.624	0.264	-0.151	DA
SSSJ1117+0129	11 17 35.2	+01 29 39	-0.0396	0.0549	1982.325	17.675	0.435	0.917	DA+dM
SSSJ1138+0322	11 38 26.9	+03 22 08	-0.0938	-0.0678	1992.014	16.098	0.243	0.580	CV
SSSJ1153+0705	11 53 32.7	+07 05 58	0.1007	-0.1113	1996.635	14.01	0.051	0.890	DA

SSSJ1241+2614	12 41 44.0	+26 14 47	-0.1905	-0.1125	1992.339	19.326	0.937	0.381	DC
SSSJ1255+0143	12 55 15.6	+01 43 53	-0.0037	-0.0708	1984.642	15.521	-0.026	1.240	DZA
SSSJ1256+0148	12 56 11.8	+01 48 40	-0.0125	-0.0473	1984.505	15.687	-0.121	1.377	DZA
SSSJ1303+0215	13 03 06.5	+02 15 04	-0.0967	-0.0200	1984.68	14.809	-0.057	1.271	DZA
SSSJ1304+3239	13 04 02.3	+32 39 09	-0.1257	-0.0678	1991.04	17.073	0.674	0.212	DZA
SSSJ1358+1712	13 58 25.6	+17 12 06	0.0572	-0.1113	1993.343	17.568	0.390	1.606	DA+dM
SSSJ1406+1608	14 06 25.7	+16 08 28	-0.1211	-0.0436	1993.156	17.634	0.695	0.394	DA poor S/N
SSSJ1419+4035	14 19 13.1	+40 35 43	-0.0050	-0.0634	1992.834	18.066	0.284	-0.340	DA
SSSJ1425+2109	14 25 22.9	+21 09 41	-0.0602	-0.0101	1994.259	18.121	0.418	1.141	DA+dM
SSSJ1444+0304	14 44 44.4	+03 04 42	-0.1859	-0.0298	1989.247	17.143	-0.066	-0.195	DA
SSSJ1511+4048	15 11 10.0	+40 48 02	-0.1551	-0.0620	1991.243	15.865	0.394	0.293	DA
SSSJ1516+2257	15 16 40.3	+22 57 13	-0.0108	-0.0424	1987.666	15.719	-0.120	0.234	DA
SSSJ1519+3536	15 19 21.8	+35 36 26	-0.0292	0.0182	1989.166	16.67	-0.174	0.482	DA+dM
SSSJ1545+2603	15 45 02.3	+26 03 11	-0.0722	0.1224	1988.497	19.053	0.941	0.465	DC poor S/N
SSSJ1620+3213	16 20 00.9	+32 13 16	0.0306	0.2687	1989.355	18.295	0.875	-0.002	MS - A?
SSSJ1622+0532	16 22 16.3	+05 32 53	-0.1306	-0.0482	1990.328	16.786	0.351	0.146	DA
SSSJ1645+5620	16 45 02.2	+56 20 47	-0.0211	0.3649	1991.511	18.972	0.973	0.447	DA
SSSJ1719+4855	17 19 19.4	+48 55 27	-0.0879	0.431	1987.319	18.891	0.799	0.208	DA
SSSJ1730+1158	17 30 59.4	+11 58 11	-0.2251	-0.1301	1992.336	18.277	-0.122	-0.592	DA
SSSJ1759+5415	17 59 04.5	+54 15 48	-0.021	0.3046	1991.597	18.826	1.212	0.390	DA poor S/N

SSSJ1844+4120	18 44 12.7	+41 20 29	-0.0895	0.0083	1990.175	16.159	0.180	1.203	DA+dM
SSSJ1858+0417	18 58 43.1	+04 17 33	-0.0791	-0.1673	1987.581	16.104	1.084	-1.046	DA weak Hα poor S/N
SSSJ1900+3922	19 00 17.3	+39 22 36	0.0327	-0.2429	1995.475	15.755	-0.194	0.310	DA
SSSJ1923+1719	19 23 11.9	+17 19 50	-0.0376	-0.1816	1992.433	18.382	0.572	0.345	DA weak Hα Zeeman split?
SSSJ2031+0946	20 31 41.8	+09 46 06	-0.1936	0.0175	1990.64	20.128	1.850	0.059	DC poor S/N
SSSJ2036+5712	20 36 04.0	+57 12 47	-0.1383	0.2287	1990.717	19.15	1.416	0.446	sdK
SSSJ2052+0133	20 52 38.3	+01 33 26	-0.3076	-0.0722	1988.686	18.498	0.839	0.325	DC poor S/N
SSSJ2059+5153	20 59 47.3	+51 53 46	-0.5129	0.0306	1990.648	15.725	0.801	0.196	DA poor S/N
SSSJ2106+0740	21 06 22.6	+07 40 17	-0.1717	-0.2542	1987.719	18.297	0.891	0.398	DA poor S/N
SSSJ2157+2705	21 57 59.3	+27 05 16	0.3874	0.3597	1990.782	19.107	1.308	0.527	DC poor S/N
SSSJ2244+1513	22 44 43.0	+15 13 46	0.175	0.2637	1991.706	18.573	0.873	0.392	DA poor S/N
SSSJ2252+3928	22 52 57.8	+39 28 16	0.2284	0.1163	1989.75	18.968	1.037	0.470	DC, H_2CIA?
SSSJ2321+0940	23 21 41.9	+09 40 22	0.2961	0.175	1991.711	20.265	1.473	0.123	DC poor S/N
SSSJ2343-5805	23 43 45.8	-58 05 36	0.2356	-0.0758	1999.632	20.064	1.084	-0.047	DA poor S/N
SSSJ2348+4300	23 48 57.8	+43 00 42	0.1666	-0.2447	1990.642	18.5	1.104	0.626	DC
SSSJ2351+1527	23 51 01.4	+15 27 51	0.2193	-0.0178	1995.589	19.338	0.348	-0.212	DA
SSSJ2355+1431	23 55 16.5	+14 31 37	0.2397	-0.0678	1995.589	19.586	0.597	-0.117	DC
SSSJ2357+3043	23 57 45.8	+30 43 60	0.0053	-0.2028	1989.828	18.38	0.301	1.097	M8

Bibliography

Alcock, C., Allsman, R. A., Alves, D., Axelrod, T. S., Becker, A. C., Bennett, D. P., Cook, K. H., Freeman, K. C., Griest, K., Guern, J., Lehner, M. J., Marshall, S. L., Peterson, B. A., Pratt, M. R., Quinn, P. J., Rodgers, A. W., Stubbs, C. W., Sutherland, W., Welch, D. L., and The MACHO Collaboration: 1997, ApJ **486**, 697

Alcock, C., Allsman, R. A., Alves, D. R., Axelrod, T. S., Becker, A. C., Bennett, D. P., Cook, K. H., Dalal, N., Drake, A. J., Freeman, K. C., Geha, M., Griest, K., Lehner, M. J., Marshall, S. L., Minniti, D., Nelson, C. A., Peterson, B. A., Popowski, P., Pratt, M. R., Quinn, P. J., Stubbs, C. W., Sutherland, W., Tomaney, A. B., Vandehei, T., and Welch, D.: 2000, ApJ **542**, 281

Barstow, M. A., Boyce, D. D., Barstow, J. K., Forbes, A. E., Welsh, B. Y., and Lallement, R.: 2009, Ap&SS **320**, 91

Beard, S. M., MacGillivray, H. T., and Thanisch, P. F.: 1990, MNRAS **247**, 311

Bedin, L. R., King, I. R., Anderson, J., Piotto, G., Salaris, M., Cassisi, S., and Serenelli, A.: 2008a, ApJ **678**, 1279

Bedin, L. R., Salaris, M., King, I. R., Piotto, G., Anderson, J., and Cassisi, S.: 2010, ApJL **708**, L32

Bedin, L. R., Salaris, M., Piotto, G., Cassisi, S., Milone, A. P., Anderson, J., and King, I. R.: 2008b, ApJL **679**, L29

Bergeron, P.: 2001, ApJ **558**, 369

Bergeron, P. and Leggett, S. K.: 2002, ApJ **580**, 1070

Bergeron, P., Leggett, S. K., and Ruiz, M. T.: 2001, ApJS **133**, 413

Bergeron, P., Ruiz, M. T., Hamuy, M., Leggett, S. K., Currie, M. J., Lajoie, C., and Dufour, P.: 2005, ApJ **625**, 838

Bergeron, P., Ruiz, M. T., and Leggett, S. K.: 1997, ApJS **108**, 339

Bergeron, P., Wesemael, F., and Beauchamp, A.: 1995, PASP **107**, 1047

Bessell, M. S.: 1986, PASP **98**, 1303

Binney, J. and Merrifield, M.: 1998, *Galactic astronomy*

Bohlin, R. C. and Gilliland, R. L.: 2004, AJ **127**, 3508

Burleigh, M., Hogan, E., and Clarke, F.: 2006, in P. Whitelock, M. Dennefeld, & B. Leibundgut (ed.), *The Scientific Requirements for Extremely Large Telescopes*, Vol. 232 of *IAU Symposium*, pp 344–349

Calchi Novati, S., de Luca, F., Jetzer, P., and Scarpetta, G.: 2006, A&A **459**, 407

Castanheira, B. G. and Kepler, S. O.: 2009, *Journal of Physics Conference Series* **172(1)**, 012068

Chandrasekhar, S.: 1939, *An introduction to the study of stellar structure*

Chiba, M. and Beers, T. C.: 2000, AJ **119**, 2843

De Gennaro, S., von Hippel, T., Winget, D. E., Kepler, S. O., Nitta, A., Koester, D., and Althaus, L.: 2008, AJ **135**, 1

Dehnen, W. and Binney, J.: 1998a, MNRAS **294**, 429

Dehnen, W. and Binney, J. J.: 1998b, MNRAS **298**, 387

Digby, A. P., Hambly, N. C., Cooke, J. A., Reid, I. N., and Cannon, R. D.: 2003, MNRAS **344**, 583

Dufour, P., Liebert, J., Fontaine, G., and Behara, N.: 2007, Nature **450**, 522

Eisenstein, D. J., Liebert, J., Harris, H. C., Kleinman, S. J., Nitta, A., Silvestri, N., Anderson, S. A., Barentine, J. C., Brewington, H. J., Brinkmann, J., Harvanek, M., Krzesiński, J., Neilsen, Jr., E. H., Long, D., Schneider, D. P., and Snedden, S. A.: 2006, ApJS **167**, 40

Evans, D. W.: 1989, A&AS **78**, 249

Fleming, T. A., Liebert, J., and Green, R. F.: 1986, ApJ **308**, 176

Flynn, C., Holopainen, J., and Holmberg, J.: 2003, MNRAS **339**, 817

Fontaine, G., Brassard, P., and Bergeron, P.: 2001, PASP **113**, 409

Freeman, K. and Bland-Hawthorn, J.: 2002, ARA&A **40**, 487

Friedrich, S., Zinnecker, H., Brandner, W., Correia, S., and McCaughrean, M.: 2005, in D. Koester & S. Moehler (ed.), *14th European Workshop on White Dwarfs*, Vol. 334 of *Astronomical Society of the Pacific Conference Series*, pp 431–+

Garcia-Berro, E., Torres, S., Figueras, F., and Isern, J.: 2005, in E. M. Sion, S. Vennes, & H. L. Shipman (ed.), *White dwarfs: cosmological and galactic probes*, Vol. 332 of *Astrophysics and Space Science Library*, pp 15–24

Gates, E., Gyuk, G., Harris, H. C., Subbarao, M., Anderson, S., Kleinman, S. J., Liebert, J., Brewington, H., Brinkmann, J., Harvanek, M., Krzesinski, J., Lamb, D. Q., Long, D., Neilsen, Jr., E. H., Newman, P. R., Nitta, A., and Snedden, S. A.: 2004, ApJL **612**, L129

Gehrels, N.: 1986, ApJ **303**, 336

Geijo, E. M., Torres, S., Isern, J., and García-Berro, E.: 2006, MNRAS **369**, 1654

Girardi, L., Bressan, A., Bertelli, G., and Chiosi, C.: 2000, A&AS **141**, 371

Girardi, L., Groenewegen, M. A. T., Hatziminaoglou, E., and da Costa, L.: 2005, A&A **436**, 895

Goldman, B., Afonso, C., Alard, C., Albert, J., Amadon, A., Andersen, J., Ansari, R., Aubourg, É., Bareyre, P., Bauer, F., Beaulieu, J., Blanc, G., Bouquet, A., Char, S., Charlot, X., Couchot, F., Coutures, C., Derue, F., Ferlet, R., Fouqué, P., Glicenstein, J., Gould, A., Graff, D., Gros, M., Haissinski, J., Hamadache, C., Hamilton, J., Hardin, D., de Kat, J., Kim, A., Lasserre, T., Le Guillou, L., Lesquoy, É., Loup, C., Magneville, C., Mansoux, B., Marquette, J., Maurice, É., Maury, A., Milsztajn, A., Moniez, M., Palanque-Delabrouille, N., Perdereau, O., Prévot, L., Regnault, N., Rich, J., Spiro, M., Tisserand, P., Vidal-Madjar, A., Vigroux, L., Zylberajch, S., and The EROS collaboration: 2002, A&A **389**, L69

Gould, A., Flynn, C., and Bahcall, J. N.: 1998, ApJ **503**, 798

Gould, A. and Kilic, M.: 2008, ApJL **673**, L75

Grundahl, F., Clausen, J. V., Hardis, S., and Frandsen, S.: 2008, A&A **492**, 171

Hambly, N. C., Davenhall, A. C., Irwin, M. J., and MacGillivray, H. T.: 2001a, MNRAS

Hambly, N. C., Henry, T. J., Subasavage, J. P., Brown, M. A., and Jao, W.-C.: 2004, AJ **128**, 437

Hambly, N. C., Irwin, M. J., and MacGillivray, H. T.: 2001b, MNRAS

Hambly, N. C., MacGillivray, H. T., Read, M. A., Tritton, S. B., Thomson, E. B., Kelly, B. D., Morgan, D. H., Smith, R. E., Driver, S. P., Williamson, J., Parker, Q. A., Hawkins, M. R. S., Williams, P. M., and Lawrence, A.: 2001c, MNRAS

Hambly, N. C., Smartt, S. J., and Hodgkin, S. T.: 1997, ApJL **489**, L157+

Hansen, B. M. S.: 1998, Nature **394**, 860

Hansen, B. M. S. and Liebert, J.: 2003, ARA&A **41**, 465

Harris, H. C., Dahn, C. C., Vrba, F. J., Henden, A. A., Liebert, J., Schmidt, G. D., and Reid, I. N.: 1999, ApJ **524**, 1000

Harris, H. C., Gates, E., Gyuk, G., Subbarao, M., Anderson, S. F., Hall, P. B., Munn, J. A., Liebert, J., Knapp, G. R., Bizyaev, D., Malanushenko, E., Malanushenko, V., Pan, K., Schneider, D. P., and Smith, J. A.: 2008, ApJ **679**, 697

Harris, H. C., Munn, J. A., Kilic, M., Liebert, J., Williams, K. A., von Hippel, T., Levine, S. E., Monet, D. G., Eisenstein, D. J., Kleinman, S. J., Metcalfe, T. S., Nitta, A., Winget, D. E., Brinkmann, J., Fukugita, M., Knapp, G. R., Lupton, R. H., Smith, J. A., and Schneider, D. P.: 2006, AJ **131**, 571

Hawley, S. L., Gizis, J. E., and Reid, I. N.: 1996, AJ **112**, 2799

Herwig, F., Blöcker, T., Langer, N., and Driebe, T.: 1999, A&A **349**, L5

Hogan, E., Burleigh, M. R., and Clarke, F. J.: 2009, MNRAS **396**, 2074

Holberg, J. B.: 2009, *Journal of Physics Conference Series* **172(1)**, 012022

Holberg, J. B., Barstow, M. A., Bruhweiler, F. C., Cruise, A. M., and Penny, A. J.: 1998, ApJ **497**, 935

Ibata, R. A., Richer, H. B., Gilliland, R. L., and Scott, D.: 1999, ApJL **524**, L95

Iben, I. J. and Laughlin, G.: 1989, ApJ **341**, 312

Isern, J., García-Berro, E., Torres, S., and Catalán, S.: 2008, ApJL **682**, L109

Jeffery, E. J., von Hippel, T., Jefferys, W. H., Winget, D. E., Stein, N., and De Gennaro, S.: 2007, ApJ **658**, 391

Johnson, J. A., Butler, R. P., Marcy, G. W., Fischer, D. A., Vogt, S. S., Wright, J. T., and Peek, K. M. G.: 2007, ApJ **670**, 833

Jones, L. R., Fong, R., Shanks, T., Ellis, R. S., and Peterson, B. A.: 1991, MNRAS **249**, 481

Jordan, S.: 2007, in R. Napiwotzki & M. R. Burleigh (ed.), *15th European Workshop on White Dwarfs*, Vol. 372 of *Astronomical Society of the Pacific Conference Series*, pp 139–+

Kalirai, J. S., Bergeron, P., Hansen, B. M. S., Kelson, D. D., Reitzel, D. B., Rich, R. M., and Richer, H. B.: 2007, ApJ **671**, 748

Kalirai, J. S., Saul Davis, D., Richer, H. B., Bergeron, P., Catelan, M., Hansen, B. M. S., and Rich, R. M.: 2009, ApJ **705**, 408

Kepler, S. O., Kleinman, S. J., Nitta, A., Koester, D., Castanheira, B. G., Giovannini, O., Costa, A. F. M., and Althaus, L.: 2007, MNRAS **375**, 1315

Kilic, M., Brown, W. R., and McLeod, B.: 2010, ApJ **708**, 411

Kilic, M., Munn, J. A., Harris, H. C., Liebert, J., von Hippel, T., Williams, K. A., Metcalfe, T. S., Winget, D. E., and Levine, S. E.: 2006, AJ **131**, 582

Kilic, M., von Hippel, T., Mendez, R. A., and Winget, D. E.: 2004, ApJ **609**, 766

Kippenhahn, R. and Weigert, A.: 1994, *Stellar Structure and Evolution*

Knox, R. A., Hawkins, M. R. S., and Hambly, N. C.: 1999, MNRAS **306**, 736

Koester, D. and Chanmugam, G.: 1990, *Reports on Progress in Physics* **53**, 837

Kong, D. and Zhu, Z.: 2008, *Chinese Astronomy and Astrophysics* **32**, 360

Kroupa, P.: 2001, MNRAS **322**, 231

Krzesinski, J., Kleinman, S. J., Nitta, A., Hügelmeyer, S., Dreizler, S., Liebert, J., and Harris, H.: 2009, A&A **508**, 339

Leggett, S. K., Ruiz, M. T., and Bergeron, P.: 1998, ApJ **497**, 294

Liebert, J., Dahn, C. C., and Monet, D. G.: 1988, ApJ **332**, 891

Liebert, J., Dahn, C. C., and Monet, D. G.: 1989, in G. Wegner (ed.), *IAU Colloq. 114: White Dwarfs*, Vol. 328 of *Lecture Notes in Physics, Berlin Springer Verlag*, pp 15–23

Lindegren, L.: 2010, in *IAU Symposium*, Vol. 261 of *IAU Symposium*, pp 296–305

Lineweaver, C. H.: 1999, *Science* **284**, 1503

Liu, J.: 2009, MNRAS **400**, 1850

Magnier, E. A., Liu, M., Monet, D. G., and Chambers, K. C.: 2008, in W. J. Jin, I. Platais, & M. A. C. Perryman (ed.), *IAU Symposium*, Vol. 248 of *IAU Symposium*, pp 553–559

Martin, B. R.: 1971, *Statistics for physicists*

McCook, G. P. and Sion, E. M.: 1999, ApJS **121**, 1

Mendez, R. A. and Guzman, R.: 1998, A&A **333**, 106

Méndez, R. A. and Minniti, D.: 2000, ApJ **529**, 911

Meng, X., Chen, X., and Han, Z.: 2008, A&A **487**, 625

Metcalfe, N., Shanks, T., Fong, R., and Jones, L. R.: 1991, MNRAS **249**, 498

Monteiro, H., Jao, W., Henry, T., Subasavage, J., and Beaulieu, T.: 2006, ApJ **638**, 446

Moos, H. W., Sembach, K. R., Vidal-Madjar, A., York, D. G., Friedman, S. D., Hébrard, G., Kruk, J. W., Lehner, N., Lemoine, M., Sonneborn, G., Wood, B. E., Ake, T. B., André, M., Blair, W. P., Chayer, P., Gry, C., Dupree, A. K., Ferlet, R., Feldman, P. D., Green, J. C., Howk, J. C., Hutchings, J. B., Jenkins, E. B., Linsky, J. L., Murphy, E. M., Oegerle, W. R., Oliveira, C., Roth, K., Sahnow, D. J., Savage, B. D., Shull, J. M., Tripp, T. M., Weiler, E. J., Welsh, B. Y., Wilkinson, E., and Woodgate, B. E.: 2002, ApJS **140**, 3

Mullally, F., Reach, W. T., De Gennaro, S., and Burrows, A.: 2009, ApJ **694**, 327

Napiwotzki, R., Christlieb, N., Drechsel, H., Hagen, H., Heber, U., Homeier, D., Karl, C., Koester, D., Leibundgut, B., Marsh, T. R., Moehler, S., Nelemans, G., Pauli, E., Reimers, D., Renzini, A., and Yungelson, L.: 2003, *The Messenger* **112**, 25

Napiwotzki, R., Karl, C. A., Nelemans, G., Yungelson, L., Christlieb, N., Drechsel, H., Heber, U., Homeier, D., Koester, D., Leibundgut, B., Marsh, T. R., Moehler, S., Renzini, A., and Reimers, D.: 2007, in R. Napiwotzki & M. R. Burleigh (ed.), *15th European Workshop on White Dwarfs*, Vol. 372 of *Astronomical Society of the Pacific Conference Series*, pp 387–+

Noh, H. and Scalo, J.: 1990, ApJ **352**, 605

Oegerle, W. R., Jenkins, E. B., Shelton, R. L., Bowen, D. V., and Chayer, P.: 2005, ApJ **622**, 377

Oppenheimer, B. R., Hambly, N. C., Digby, A. P., Hodgkin, S. T., and Saumon, D.: 2001, *Science* **292**, 698

Oswalt, T. D., Smith, J. A., Wood, M. A., and Hintzen, P.: 1996, Nature **382**, 692

Perlmutter, S., Aldering, G., Goldhaber, G., Knop, R. A., Nugent, P., Castro, P. G., Deustua, S., Fabbro, S., Goobar, A., Groom, D. E., Hook, I. M., Kim, A. G., Kim, M. Y., Lee, J. C., Nunes, N. J., Pain, R., Pennypacker, C. R., Quimby, R., Lidman, C., Ellis, R. S., Irwin, M., McMahon, R. G., Ruiz-Lapuente, P., Walton, N., Schaefer, B., Boyle, B. J., Filippenko, A. V., Matheson, T., Fruchter, A. S., Panagia, N., Newberg, H. J. M., Couch, W. J., and The Supernova Cosmology Project: 1999, ApJ **517**, 565

Press, W., Flannery, B., Teukolsky, S., and Vetterling, T.: 2007, *Numerical Recipes: The Art of Scientific Computing*, Cambridge University Press, Cambridge (UK) and New York, 3rd edition

Reed, B. C.: 2006, JRASC **100**, 146

Reid, I. N.: 2005, ARA&A **43**, 247

Robin, A. C., Reylé, C., Derrière, S., and Picaud, S.: 2003, A&A **409**, 523

Rocha-Pinto, H. J., Scalo, J., Maciel, W. J., and Flynn, C.: 2000, A&A **358**, 869

Rose, W. K.: 1998, *Advanced Stellar Astrophysics*

Rowell, N. R., Hambly, N. C., and Bergeron, P.: 2009, *Journal of Physics Conference Series* **172(1)**, 012001

Rowell, N. R., Kilic, M., and Hambly, N. C.: 2008, MNRAS **385**, L23

Ruiz, M. T. and Bergeron, P.: 2001, ApJ **558**, 761

Salaris, M., Dominguez, I., Garcia-Berro, E., Hernanz, M., Isern, J., and Mochkovitch, R.: 1997, ApJ **486**, 413

Salim, S., Rich, R. M., Hansen, B. M., Koopmans, L. V. E., Oppenheimer, B. R., and Blandford, R. D.: 2004, ApJ **601**, 1075

Savitzky, A. and Golay, M. J. E.: 1964, *Analytical Chemistry* **36**, 1627

Schmidt, M.: 1959, ApJ **129**, 243

Schmidt, M.: 1968, ApJ **151**, 393

Stobie, R. S., Ishida, K., and Peacock, J. A.: 1989, MNRAS **238**, 709

Subasavage, Jr., J. P.: 2010, in *American Astronomical Society Meeting Abstracts*, Vol. 215 of *American Astronomical Society Meeting Abstracts*

Tinney, C. G., Reid, I. N., and Mould, J. R.: 1993, ApJ **414**, 254

Tremblay, P. and Bergeron, P.: 2008, ApJ **672**, 1144

van Loon, J. T., Boyer, M. L., and McDonald, I.: 2008, ApJL **680**, L49

Weber, M. and de Boer, W.: 2009, *ArXiv e-prints*

Weidemann, V.: 2000, A&A **363**, 647

Winget, D. E., Hansen, C. J., Liebert, J., van Horn, H. M., Fontaine, G., Nather, R. E., Kepler, S. O., and Lamb, D. Q.: 1987, ApJL **315**, L77

Wood, M. A.: 1995, in D. Koester & K. Werner (ed.), *White Dwarfs*, Vol. 443 of *Lecture Notes in Physics, Berlin Springer Verlag*, pp 41–+

Wood, M. A. and Oswalt, T. D.: 1998, ApJ **497**, 870

Zioutas, K., Andriamonje, S., Arsov, V., Aune, S., Autiero, D., Avignone, F. T., Barth, K., Belov, A., Beltrán, B., Bräuninger, H., Carmona, J. M., Cebrián, S., Chesi, E., Collar, J. I., Creswick, R., Dafni, T., Davenport, M., di Lella, L., Eleftheriadis, C., Englhauser, J., Fanourakis, G., Farach, H., Ferrer, E., Fischer, H., Franz, J., Friedrich, P., Geralis, T., Giomataris, I., Gninenko, S., Goloubev, N., Hasinoff, M. D., Heinsius, F. H., Hoffmann, D. H., Irastorza, I. G., Jacoby, J., Kang, D., Königsmann, K., Kotthaus, R., Krčmar, M., Kousouris, K., Kuster, M., Lakić, B., Lasseur, C., Liolios, A., Ljubičić, A., Lutz, G., Luzón, G., Miller, D. W., Morales, A., Morales, J., Mutterer, M., Nikolaidis, A., Ortiz, A., Papaevangelou, T., Placci, A., Raffelt, G., Ruz, J., Riege, H., Sarsa, M. L., Savvidis, I., Serber, W., Serpico, P., Semertzidis, Y., Stewart, L., Vieira, J. D., Villar, J., Walckiers, L., and Zachariadou, K.: 2005, *Physical Review Letters* **94(12)**, 121301